# THE EFFECTS OF NOVEL SURFACE TREATMENTS ON THE WEAR AND FATIGUE PROPERTIES OF STEEL AND CHILLED CAST IRON

by

Jason William Carroll

A dissertation submitted in partial fulfillment
of the requirements for the degree of
Doctor of Philosophy
(Materials Science and Engineering)
in The University of Michigan
2012

Doctoral Committee:

Professor J. Wayne Jones, Chair
Professor John W. Halloran
Professor John E. Allison
Assistant Professor Samantha H. Daly

## DEDICATION

This dissertation is dedicated my high school drafting teacher Jeff Baldwin, whose hard-nose, disciplined, no-nonsense approach to teaching was oddly a safe-haven in the turbulent teenage years of my life. His personality and teaching methods are sorely lacking in our society today, and we are all the poorer for it.

To Professor Judith Todd who first introduced a poorly mannered and equally poorly dressed eighteen year old to the wonders of metallurgy. Her patience, kindness, humor, and love for her field and students are without equal.

Finally, to Amanda, Henry, Adam, and Roger – my best friends and companions on the silly, mystic journey called life.

## ACKNOWLEDGMENTS

A special thanks to Chris Torbet for his knowledge and candid discussions about ultrasonic fatigue. His easy going competence is refreshing and added greatly to my dissertation. I would also like to thank Brock Spigelmeyer, Jim Pietraski, and Mitesh Kamdar whom I have worked with on tappet design and wear problems for the past six years. Their intellects and joy in learning and playing in the lab made my work enjoyable.

## Table of Contents

## LIST OF FIGURES

## LIST OF TABLES

# CHAPTER 1

# Problem Introduction

## 1.1 Problem Overview

Internal combustion engines used in transportation applications are usually designed to run to, or preferably past, a set time between overhauls (TBO) which is usually between 150,000-200,000 miles for car engines and 2000 hours for general aviation engines. In order to achieve this, engine manufacturers need to continue to develop new materials and processing methods for engine components that experience significant wear due to rolling and/or sliding contact: parts such as camshafts, gears, rocker arms, cylinders, and piston rings. Cam and gear surfaces experience some of the highest stresses anywhere in the engine due to the small contact loading areas and high material stiffness, which result in finite part lives. Optimization of these contact surfaces to lengthen TBO of the engine is one of the hurdles for engine manufacturers in extending the life of their products as well as reducing emissions and fuel consumption.

A critical engine subsystem that has seen significant improvements over the past century is the valve train, specifically, the camshaft and tappet. A cam is an element of the camshaft and follower mechanical system that compels the movement of the follower (tappet) by direct contact [1]. An example of an engine camshaft and tappet combination is shown in Figure 1.1a. The tappet is usually a rolling element although some solid tappets are still in use. The motion of the follower is the result of the surface contour (profile) of the cam [1]. The cam profile is analogous to a line of computer code that instructs the computer on what action to take next. In the case of automobile or general aviation internal combustion engines, the cam is a shaft with lobes on it which the tappet follows as the shaft rotates. Figure 1.1b shows an example of a flat tappet running on a carburized steel cam lobe in an engine.

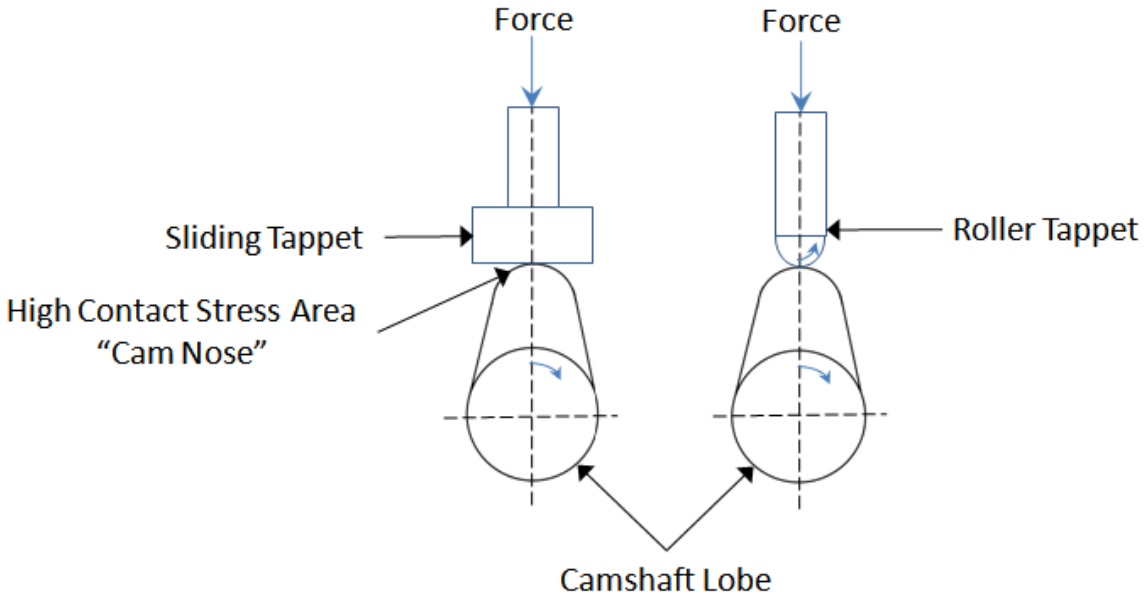


(a)

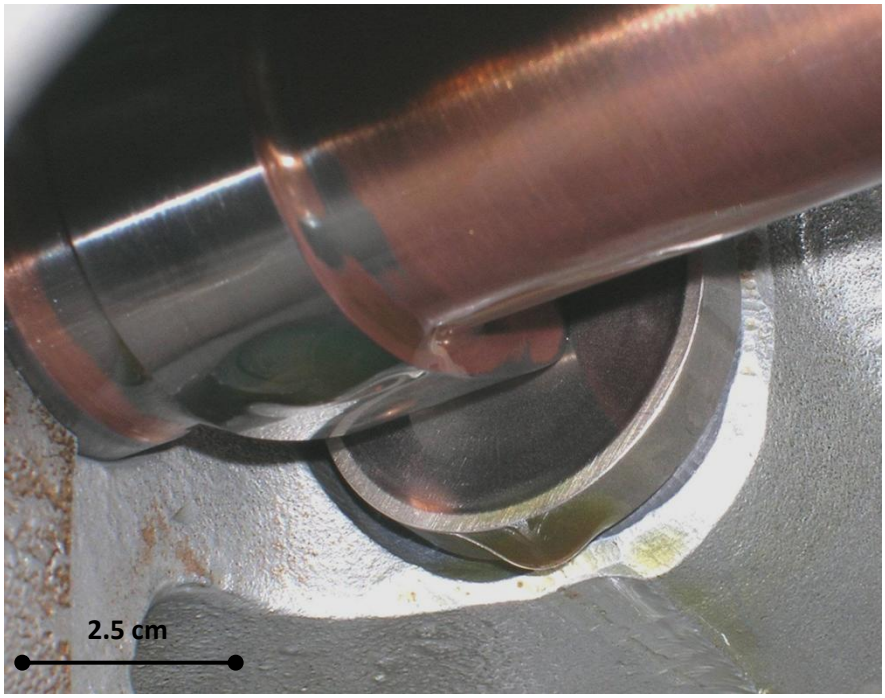


(b)

Figure 1.1 (a) Camshaft lobe configurations: sliding and roller type. The tappet is stationary and is usually loaded either from a rocker arm/push-rod configuration or with a rocker configuration. The roller tappet is more in use today, although sliding lifters are still used in many high performance automobile and aircraft engines. (b) Example of a sliding tappet running against a rotating camshaft lobe.

The motion of the tappets controls the opening and closing of the intake and exhaust valves, which in turn, control the inlet of fuel and air into the cylinders and exhaust gases out of the cylinders after combustion (Figure 1.2). The camshaft is an influential component that governs how the engine can perform, and the choice of camshaft lobe shape has a large effect on engine performance [1]. Also, since the camshaft is the "braincenter" of the IC engine, it must be durable under a combination of torsional, bending, and contact loading, as failure of the camshaft will result in failure of the engine to operate at peak performance, or at all. When camshaft lobes fail it is usually a result of contact fatigue which manifests itself as pitting and spalling, where large amounts of material break off due to cracking, resulting in a sharp, non-linear increase in the wear rate and eventual destruction of the lobe lift. An example of a typical failed tappet and cam lobe is shown in Figure 1.3. An example of how these failures occur in common carburized SAE 8620 camshafts with a sliding, chilled cast iron tappet is discussed in the following section.

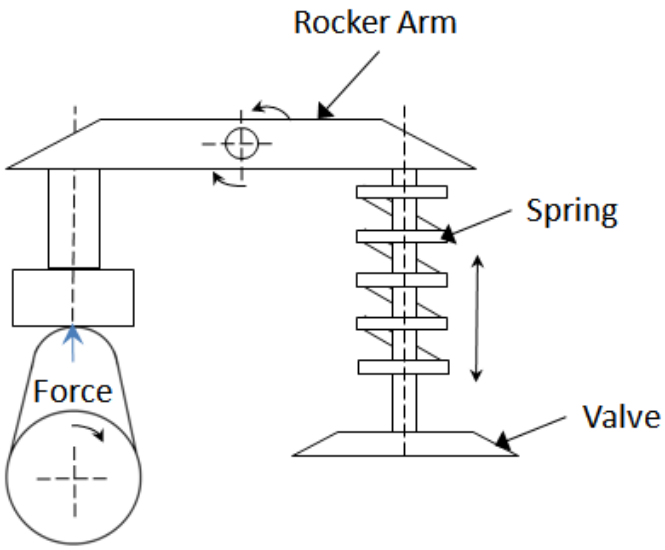


Figure 1.2 Valve train schematic. The cam lobe and tappet load the rocker arms which then opens the valve. The spring controls the rate of valve opening.


(a)


(b)

Figure 1.3 Typical surface condition of a (a) spalled tappet, (b) camshaft lobe.

## 1.2 Cam Lobe Failure on a SAE 8620 Carburized Steel Camshaft

A carburized SAE 8620 steel camshaft with a 60 HRC case hardness is described here to illustrate the typical failure mode of camshafts loaded by flat tappets after approximately $1x10^6$ cycles (1 cycle = 1 revolution) of sliding contact load. SAE 8620 steel is a medium carbon low-alloy steel with approximately 0.20 wt % carbon. In the carburized zone, the carbon content is approximately 1.0 wt % carbon, which after hardening and tempering results in a tempered martensitic microstructure with uniform carbides (Figure 1.4). For typical camshafts, the depth of the carburized zone is approximately 1-1.5mm. An intake valve cam on the camshaft is shown in Figures 1.5a-b. Two areas of discoloration and cracking were observed on the top of the lobe (Figure 1.5a) separated by an angle of approximately 68 degrees: the highest stresses occurring at these locations on the lobe. Light microscope and scanning electron microscope (SEM) images of one of the discolored and cracked areas on the lobe revealed severe spalling (Figures 1.5b and 1.6a, b). The cracks appeared to initiate at the surface of the lobe and extend diagonally below the surface until they turn roughly parallel to the surface at a depth of approximately 50 μm. No obvious secondary phases or inclusions were observed at the ends or along the cracks. In addition to the main cracks seen running diagonally to the surface, many secondary cracks were also observed emanating from the main cracks. These smaller cracks appeared to run in approximately the same direction as the main cracks. A closer view of one of the longer cracks seen in Figures 1.7 revealed that there may be a layer of material approximately 5 μm deep at the surface of the lobe that appears to be plastically deformed.

This type of surface contact failure is typical of cam lobes and gear teeth. It is generally referred to as contact fatigue in scientific studies. More commonly it is termed spalling and pitting in engineering practice. Camshafts typically experience this type of failure as they see high contact stress and boundary lubrication conditions throughout their lives. The boundary lubrication regime allows for asperity contact which can locally increase friction, temperature, and wear. Chen [2] studied cam and tappet wear and found surface fatigue to be the dominant mode of failure. Contact fatigue and the mechanisms that cause it will be explored further.

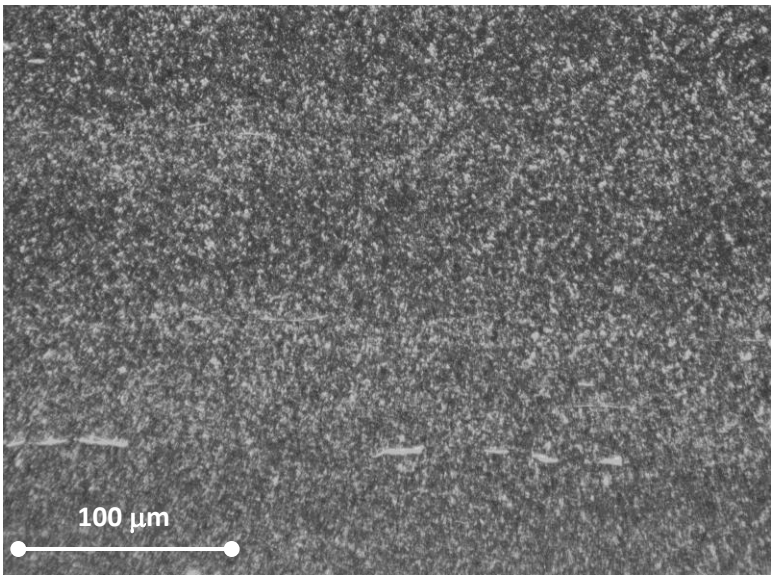


Figure 1.4 An example of the tempered martensitic microstructure present in the case hardened zone of carburized SAE 8620 steel.

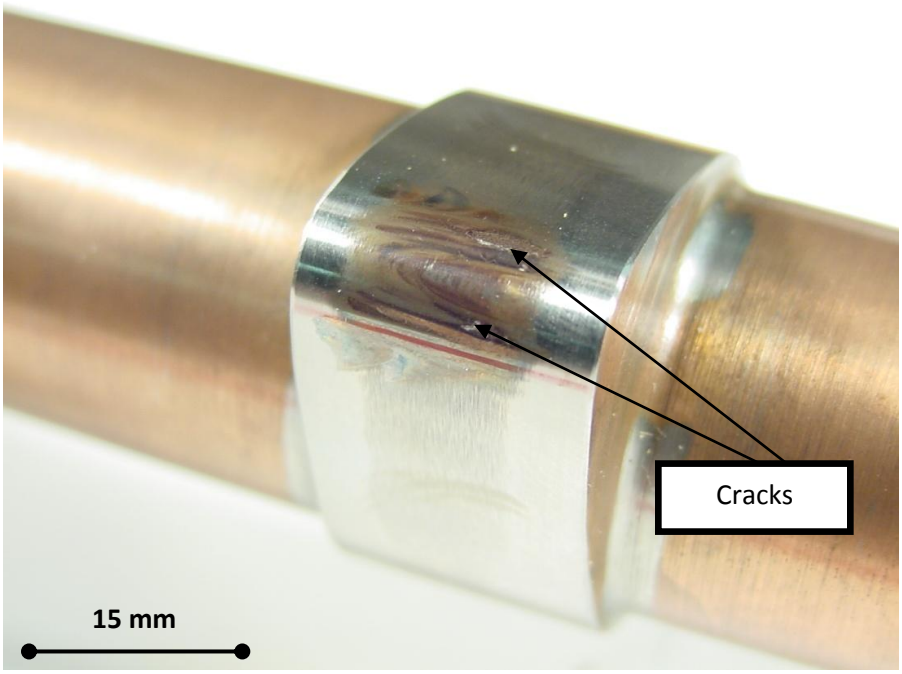


(a)

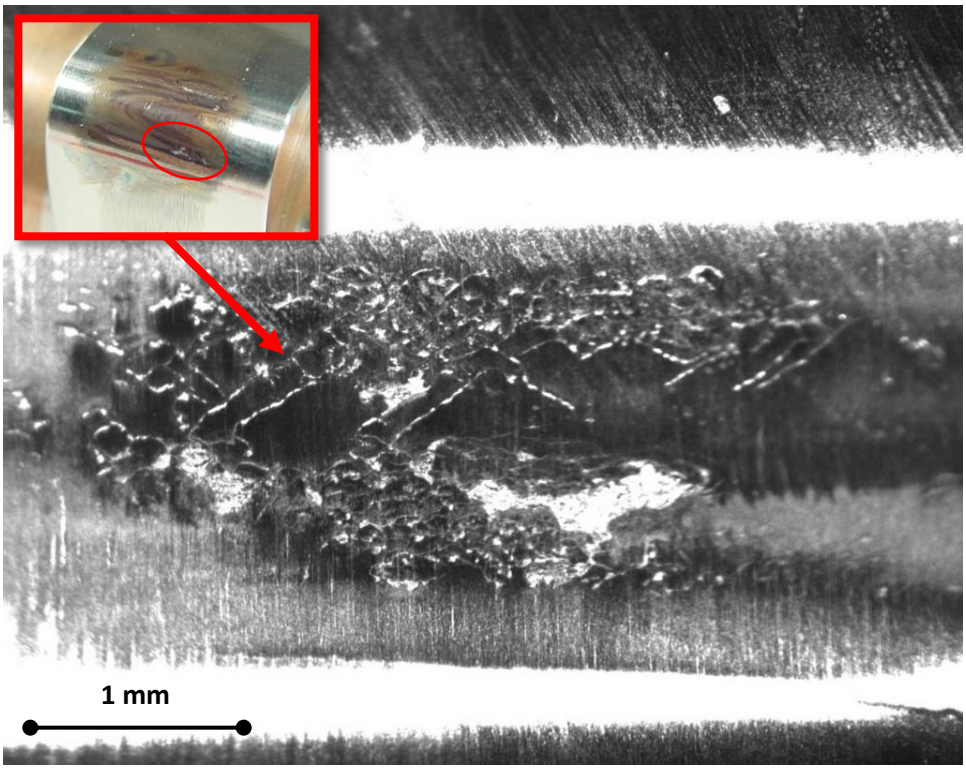


(b)

Figure 1.5 A camshaft lobe exhibiting the early stage of contact fatigue failure. (a) The lobe exhibiting two discolored areas with cracking observed in both areas. The locations of the cracks were at the highest contact stress locations on the lobe. (b) Light macrograph of one of the damaged areas on the lobe.

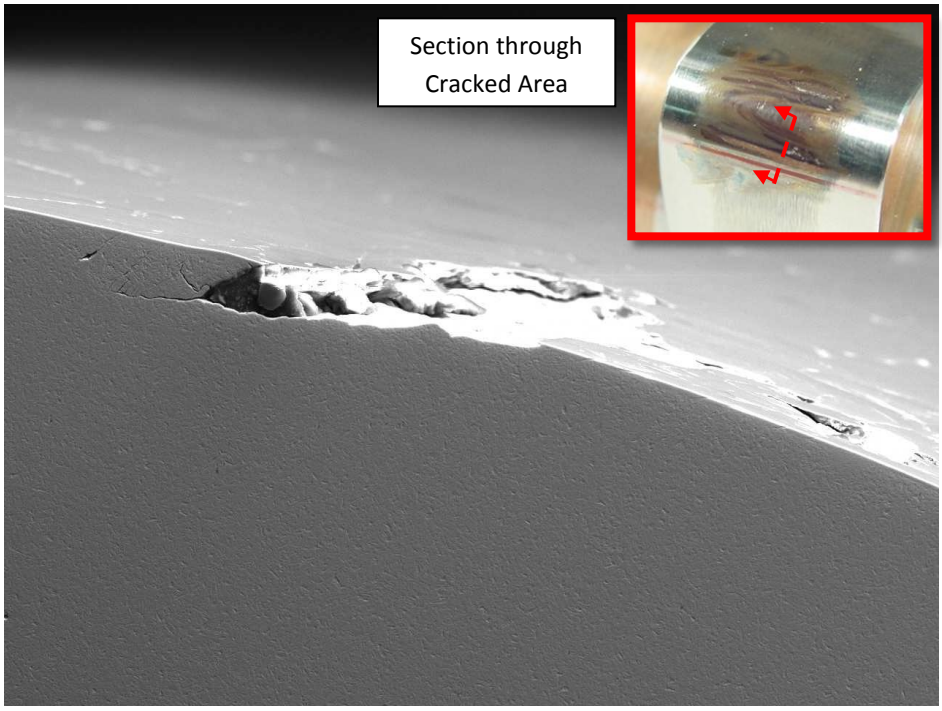


(a)

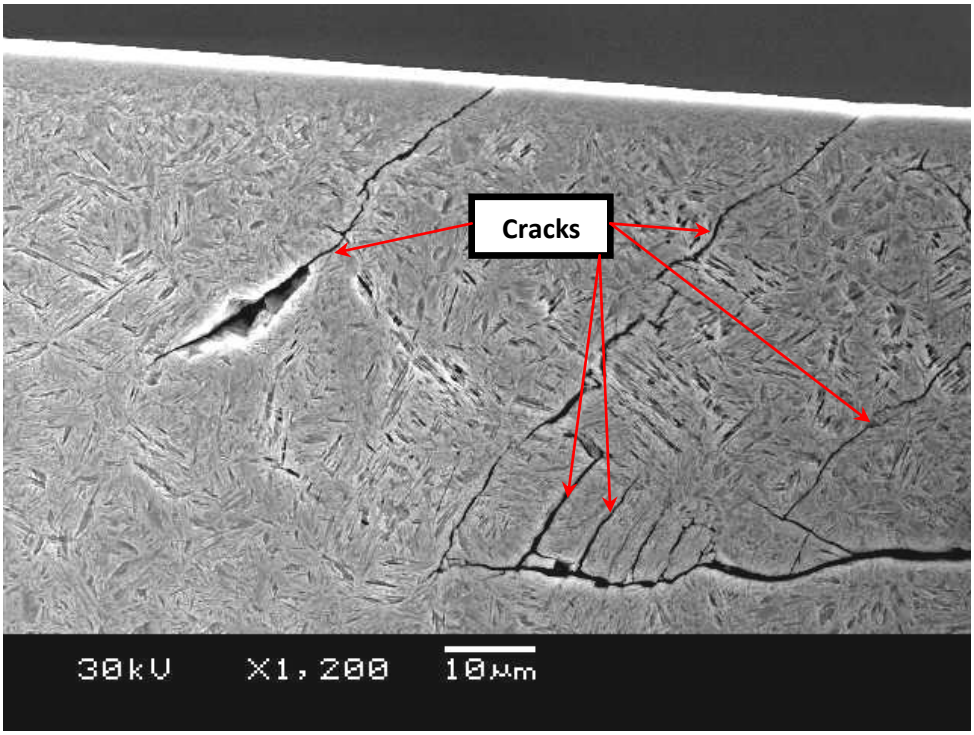


(b)

Figure 1.6 (a) SEM photomicrograph of the damaged area on the cam lobe with the cross-sectioned sampled tilted to show the contact surface. (b) Higher magnification view of the etched cross-section through the cracked area on the camshaft lobe.

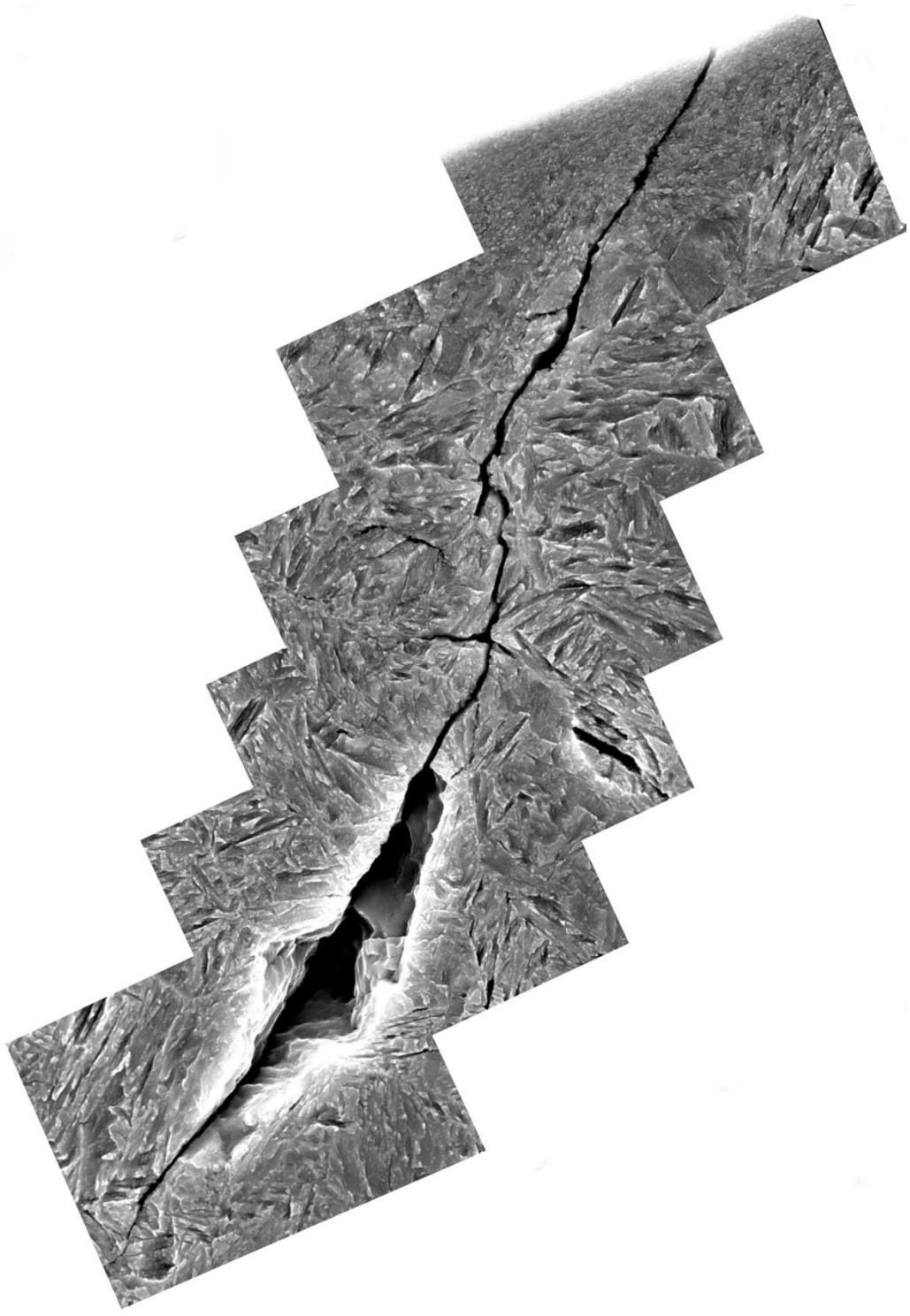

Figure 1.7 Collage of a large crack seen in Figures 1.6.

## 1.3 The Foundations of Contact Fatigue

### 1.3.1 The Different Modes of Contact Fatigue

Since most cam lobes fail by contact fatigue, the mechanical designer needs to determine what mode of contact fatigue will control crack initiation, propagation, and subsequent wear deterioration of the rolling or sliding surface. A method to analyze this problem was developed in the 1980s by Ponter et al. [3] They created what can be referred to as a contact fatigue mechanism map, an example of which is shown in Figure 1.8, where $p_{max}/k$ is the maximum contact pressure divided by the yield strength in simple shear of the material which is used to define the shakedown limits of the material as a function of friction.

If residual stresses introduced by plastic deformation lead to a steady-state elastic response, the system has experienced "elastic shakedown". Further, if the material is plastically deformed but the cycle of plasticity is closed – no gain of strain with each cycle – the system has experienced "plastic shakedown". Finally, if the plastic deformation cycle is open, the material will "ratchet" also known as "incremental collapse" gaining a net strain with each cycle until the material fails. Examples of each mode of contact fatigue are shown in Figure 1.9. Ponter et al. used the kinematical shakedown theorem of Koiter [4] to model the shakedown limits in rolling contact and rolling contact with sliding. He assumed an elastic-perfectly plastic material with a yield surface of:

$$F(\sigma_{ij}) = k^2 \qquad (1.1)$$

Where $F$ is either the Tresca or Von Mises homogeneous function and $k$ is the yield stress in simple shear. For any work state of stress $\sigma_{ij}^*$ that lies within yield, i.e. $F(\sigma_{ij}^*) \leq k^2$, Koiter's maximum work inequality holds: $(\sigma_{ij}^* - \sigma_{ij})d\varepsilon_{ij}^p \leq 0$, where $\sigma_{ij}$is the stress at yield associated with the plastic strain increment $d\varepsilon_{ij}^p$ : $d\varepsilon_{ij}^e$ being the elastic strain. Ponter et al. then studied the cases of incremental collapse without alternating plasticity which can lead to ratcheting fatigue and alternating plasticity without incremental collapse which can lead to low-cycle fatigue; both occurring

when the shakedown limit is exceeded. The mathematical descriptions for both are given in [3]. The result of their work can be seen in Figure 1.8. "Surface" and "subsurface" notations in Figure 1.8 are meant to indicate where failure will initiate. Below a COF of 0.3, the maximum shear stress occurs below the surface, resulting in cracks initiating subsurface. Above a COF of 0.3, the maximum shear stress occurs at the surface, and thus, cracks initiate there. The dashed line in Figure 1.8 represents the lower bound to the elastic shakedown limit of the material. When the maximum normalized contact pressure, ($p_{max}$/k) for any value of friction is in the area labeled "elastic", no plastic flow occurs for any number of contact fatigue cycles. In the area labeled "elastic shakedown", plastic flow occurs initially until the development of residual stresses suppresses further plastic flow. In the plastic shakedown area, a closed cycle of plastic straining is developed just below the surface of contact. Since the strained area is contained within an elastic field of the surrounding material, the progressive accumulation of plastic strain is suppressed. In the ratcheting zone, plastic strain can accumulate and lead to failure.

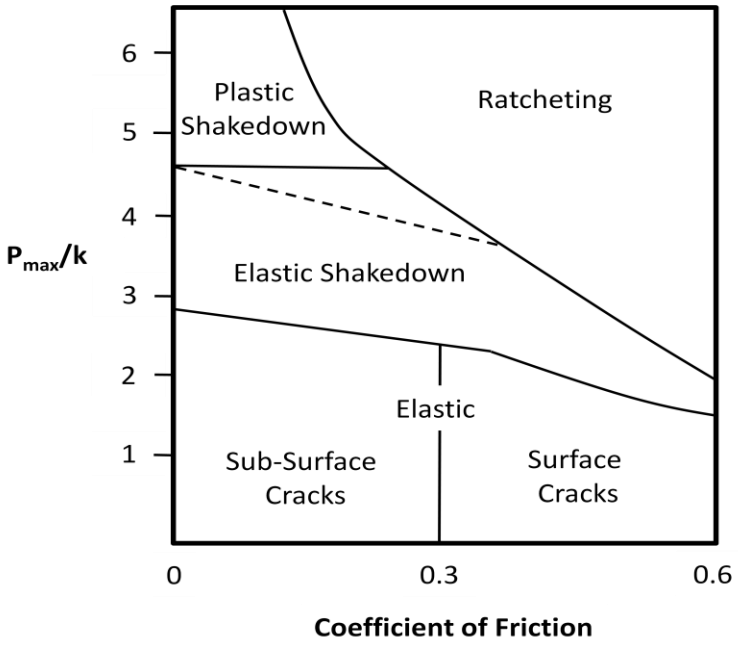


Figure 1.8 Fatigue mechanism diagram for sliding or rolling contact [3]. $p_{max}$/k is the maximum contact pressure divided by the shear yield strength of the metal.

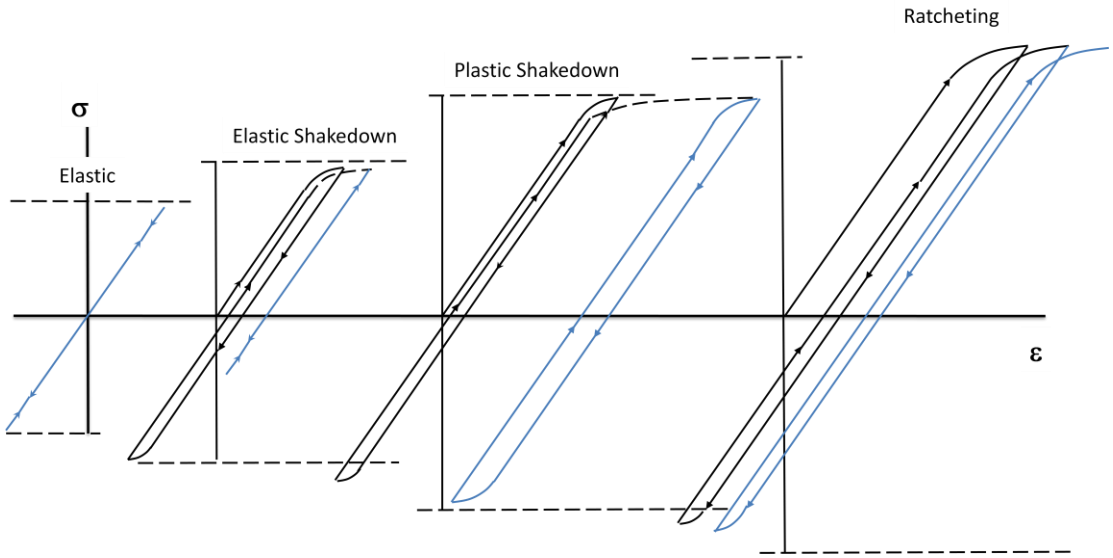


Figure 1.9 Different contact fatigue modes: elastic, elastic shakedown, plastic shakedown and ratcheting.

Using axial fatigue as an analogy, the work of Ponter et al. helps a designer know what type of contact fatigue they will encounter; low-cycle fatigue which would include plastic shakedown and ratcheting, or high to very high cycle fatigue, which could include elastically shaken-down materials and elastic contact loading. Knowing what type of contact fatigue will control the life of the part allows the designer to pick the correct monolithic or composite material design to resist a given fatigue mechanism in much the same way one would under axial or bending fatigue conditions. Since some materials work better under low rather than high stress amplitudes and vice-versa, Ponter's method is important for rolling and sliding wear design.

### 1.3.2 The Metallurgical Response to Contact Loading

Once the contact fatigue mode is understood, it is then important to understand metallurgically what ***actually*** is controlling fatigue, be it ductility of the material; inclusion size, type, and morphology; a slip mechanism such as the Bauschinger effect for some higher stressed metals; or some other mechanism. The word "actually" is used as Ludema states in his book [5] that mathematical wear models do not provide a general context for solving wear problems due to the multi-control and noise variable reality of wear. Many researchers today are working to solve this

problem by approaching wear from a nano and atomic scale as well as using thermodynamics to explain the evolution of surfaces under contact loading [6-8]. From an empirical standpoint, a similar approach will be attempted in this dissertation.

Two of the most important contact fatigue mechanisms are low cycle fatigue resulting from a closed cycle of plastic deformation above the elastic shakedown limit, or open-cycle ratcheting fatigue above the plastic shakedown limit. Some of the earliest known studies on this type of contact fatigue began in the 1970s, prior to Ponter's work, with the introduction of what is now widely referred to as the *delamination theory of wear*.

#### 1.3.2.1 The Delamination Theory of Wear

The delamination theory of wear was introduced in 1973 by Suh at MIT [9-17]. Since that time, many mechanisms have been postulated by the theory to account for how the coefficient of friction affects the wear rate, where the external energy applied through sliding contact is transferred, why some hard metals wear faster than soft ones, how microstructures affect wear rates, and how the initial roughness and waviness of the surface affect the wear rate and wear phenomena [12].

Suh's delamination theory of wear can be summarized as follows [12]:

(1) When two sliding surfaces come into contact, normal and tangential loads are transmitted through the contact points by adhesive and plowing actions. Asperities of the softer surface are easily deformed and some are fractured by the repeated loading action. A relatively smooth surface is generated, either when these asperities are deformed or when they are removed. Once the surface becomes smooth, the contact is not just an asperity-to-asperity contact, but rather an asperity-plane contact; each point along the softer surface experiences cyclic loading as the asperities of the harder surface plow it.

(2) The surface traction exerted by the harder asperities on the softer surface induces plastic shear deformation that accumulates with repeated loading.

(3) As the subsurface deformation continues, cracks are nucleated below the surface. Crack nucleation very near the surface is not favored because of a triaxial state of highly compressive stress that exists just below the contact regions.

(4) Once cracks are present (owing either to the crack nucleation process or to pre-existing voids), further loading and deformation causes cracks to extend and to propagate, joining neighboring ones. The cracks tend to propagate parallel to the surface at a depth governed by material properties and the coefficient of friction.

(5) When these cracks finally shear to the surface (at certain weak positions) long and thin wear sheets "delaminate". The thickness of a worn sheet is controlled by the location of the subsurface crack growth, which is controlled by the normal and the tangential loads at the surface.

The first in the sequence of events can be well described using Hertzian contact mechanics. For sliding contact of a smooth sphere on a smooth semi-infinite flat surface – a very common contact geometry – analytical equations developed by Hamilton and Goodman [18, 19] give explicit equations for the normal and tangential stress fields under sliding as a function of the coefficient of friction. Their analysis gave the boundary stresses as:

$$\sigma_z = -\frac{3P}{2\pi a^3}(a^2 - x^2 - y^2)^{\frac{1}{2}} \qquad (1.2)$$

$$\tau_{zx} = -\frac{3Q}{2\pi a^3}(a^2 - x^2 - y^2)^{1/2} \qquad (1.3)$$

$$\tau_{yz} = 0 \qquad (1.4)$$

Where *P* is the normal load and *Q* is the frictional force. The contact radius *a* is given as:

$$a = \left\{\frac{3\pi P R_1 R_2}{4(R_1 + R_2)}\left[\frac{1 - \nu_1^2}{\pi E_1} + \frac{1 - \nu_2^2}{\pi E_2}\right]\right\}^{1/3} \qquad (1.5)$$

For plastic yielding analysis, the Von Mises yield parameter, $\sqrt{J_1}$ , is used, where $J_1$ is given as:

$$J_1 = \frac{1}{6}\left\{\left(\sigma_x - \sigma_y\right)^2 + (\sigma_x - \sigma_z)^2 + (\sigma_z - \sigma_x)^2\right\} + {\tau_{xy}}^2 + {\tau_{yz}}^2 + {\tau_{zx}}^2 \qquad (1.6)$$

Examples of the resulting stress field in the direction of sliding as a function of friction are given in Figure 1.10. As friction increases, the stress state become unsymmetrical and the maximum tensile and compressive stress increase significantly. Also, as friction increases the highest value of the Von-Mises yield parameter ($J_1$), increases and moves toward the surface, intersecting it at a coefficient of friction of approximately 0.3 (see Figures 1.11 and 1.12). This is the same result that yielded the transition from subsurface to surface initiated contact fatigue seen in Ponter's work as Figure 1.8.

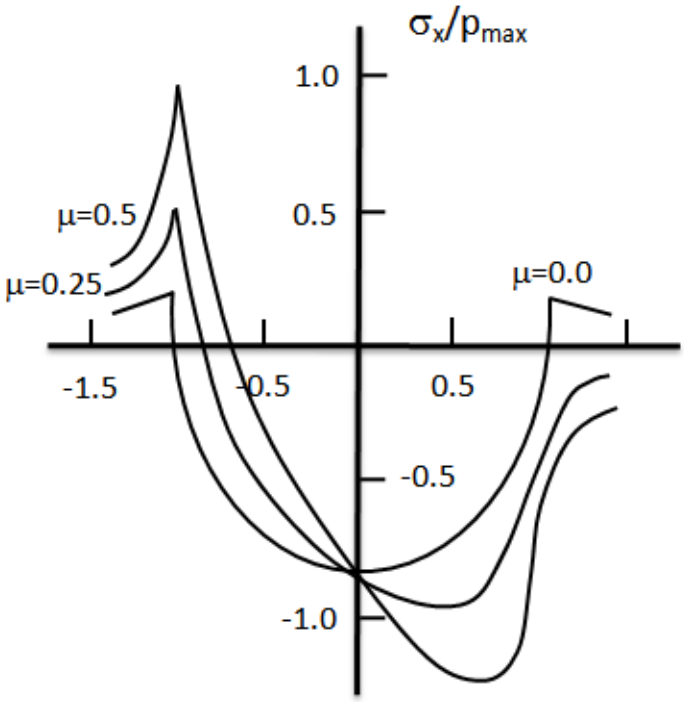


Figure 1.10 x-directed stress (Pa) field (stress in the direction of sliding) divided by the maximum contact pressure as a function of friction. As friction increases the stress increases and the symmetry of stress around contact zone diminishes.

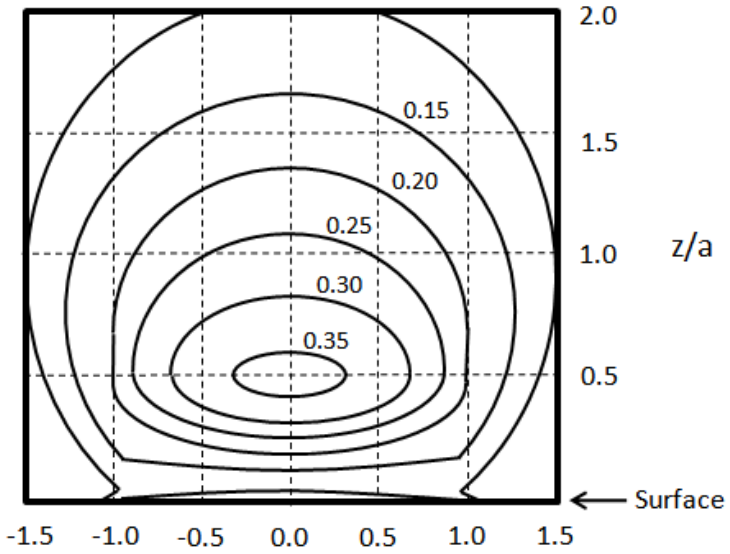


Figure 1.11 Lines of constant Von-Mises yield criterion divided by the maximum contact pressure ($J^{1/2}/p_{max}$) for a coefficient of friction of 0 calculated from the analytical model of Hamilton and Goodman. Note that the highest amplitude line occurs below the surface.

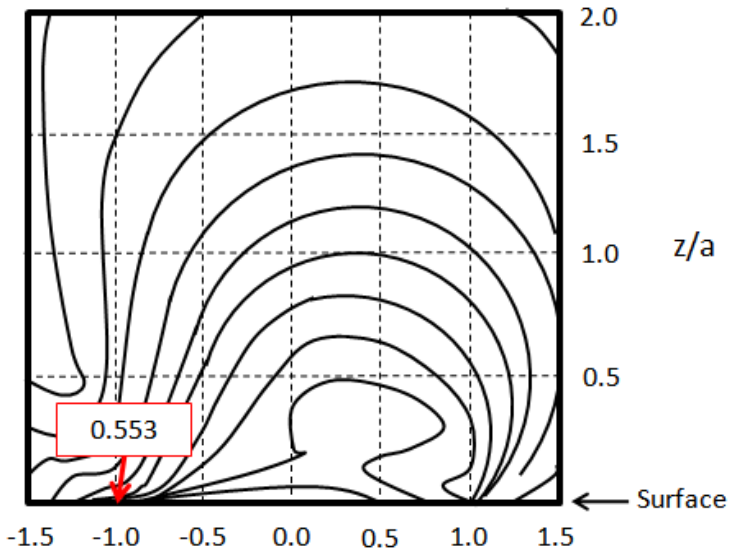


Figure 1.12 Lines of constant Von-Mises yield criterion divided by the maximum contact pressure ($J^{1/2}/p_{max}$) for a coefficient of friction of 0.5. The highest amplitude line now occurs on the surface at the back of the sliding contact zone.

Equations describing the more advanced situation of rough surfaces in contact as well as various contact geometries can be found in [20]. When the surface becomes the

likely location for crack initiation in a thin layer of highly deformed material, a so-called "tribological layer" [25], the works by Jahanmir and Suh [12, 13], Rigney and Hirth [21], and Kapoor and coworkers [22-28] offer useful models for estimating the role of surface plastic deformation on the wear properties of a particular material and will be discussed further. Suh and Sridharan [10] provided a model of how friction relates to the wear rate by relating the work done in deforming the surface to the coefficient of friction. Jahanmir and Suh [12] modeled the mechanics of subsurface void nucleation. Both models relate the stress fields as can be determined from Hamilton and Goodman's model to friction and, subsequently to crack nucleation at metallurgical features such as inclusions. Rigney and Hirth created a simpler model for determining the coefficient of friction (or conversely, the thickness of the deformed surface layer), accounting for the plastic work done in the near-surface region, which they described in terms of work hardening, recovery and the microstructure existing during steady state sliding. Their model was: $\mu = \frac{wt\tau\epsilon}{L}$ where w is the width of the wear track, t the thickness of the deformed surface region, $\tau$ the shear stress, $\varepsilon$ the average net strain per cycle, and L the normal load. They also provide mathematical models for making friction independent of the load to be in agreement with Amonton's Law ($\mu$=F/L). Their model provides good agreement with various empirical results.

#### 1.3.2.2 Ratcheting Fatigue – Kapoor's Method

Kapoor's model was specific to the mechanism of ratcheting fatigue and the competitive nature between low-cycle fatigue and ratcheting modes in controlling the life of a material in contact. His empirical model of ratcheting has wide applications to contact fatigue problems in both rolling and sliding contact.

Ratcheting fatigue, often called cyclic creep or incremental collapse, describes the process of strain accumulation in a material subjected to open cycles of plastic strain leading to failure of the material after the total plastic strain accumulation is greater than some critical upper bound value strain $\varepsilon_c$ [22, 23]. Ratcheting will occur if a material subjected to plastic deformation does not experience elastic or plastic

shakedown. Shakedown occurs when the residual stresses created during past loading cycles are not overcome by the applied stress field resulting in an entirely elastic or closed cyclic plastic deformation [22]. A typical stress pattern for a rolling/sliding contact with a coefficient of friction of 0.5 is given in Figure 1.13. Because a shear stress is superimposed on an alternating compressive and tensile stress state in sliding contact, the overall stress state is not symmetric, leading to ratcheting in the direction of sliding. For many problems ratcheting is normal as there is no material mechanism to resist the asymmetrical stress field leading to the accumulation of strain in the sliding direction. In three-dimensional point contacts, the undeformed material surrounding the material trying to ratchet can suppress the continued plastic deformation leading to a closed-cycle of plastic deformation: plastic shakedown. Shakedown limits have been found to change slightly when strain hardening is considered, with the largest change seen above a coefficient of friction of 0.3. However, the difference is not very large: a reduction of the shakedown limit of approximately 14% at $\mu$=0 and 0.3. Manson and Halford also provide a good overview of ratcheting as a mechanism of low-cycle axial fatigue showing how it manifests itself in stress-controlled and strain-controlled problems [29]. In a stress-controlled state a cyclically hardening material will experience stabilization in strain, reaching a nearly elastic response. A softening material will experience an increased rate of ratcheting in the direction of the mean stress until failure, if the maximum stress is high enough. Examples of both are given in Figure 1.14.

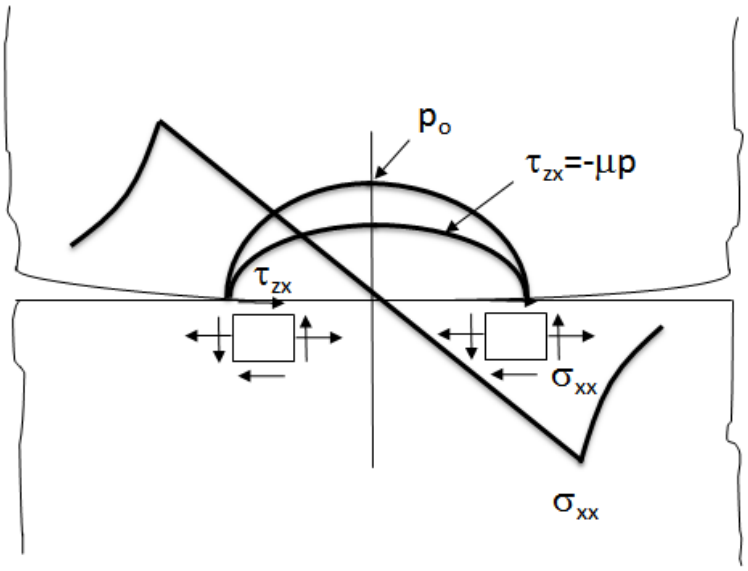


(a)

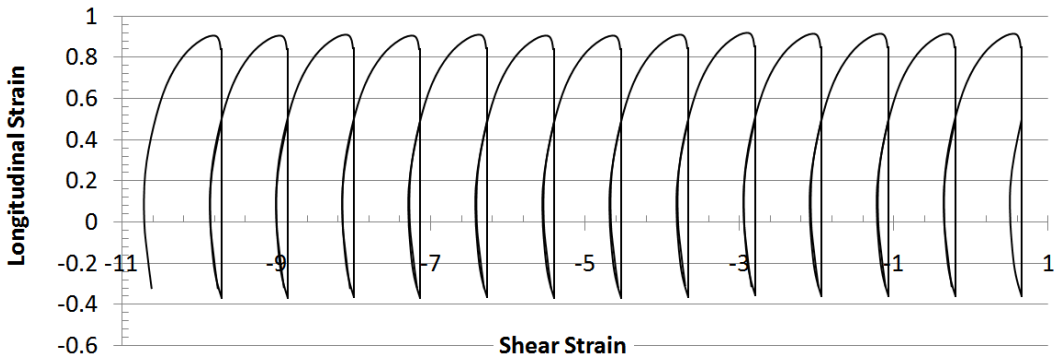


(b)

Figure 1.13 Stress state for a sliding contact with a coefficient of friction of 0.5. The stress state is asymmetrical which leads to ratcheting in the direction of the slider motion [22].

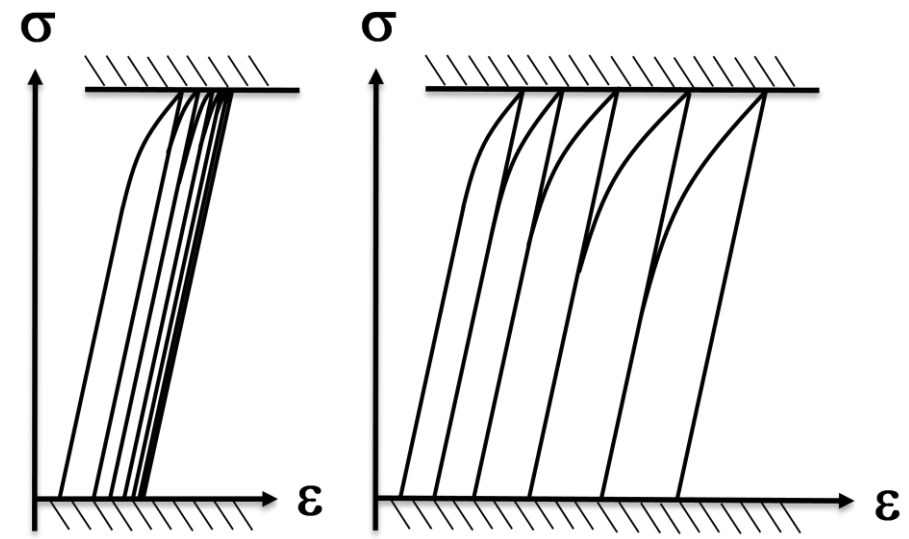


Figure 1.14 Ratcheting in force control in strain hardening (left diagram) and softening materials (right diagram) [26]. The strain softening materials experience a runaway ratcheting response.

When the load case and the coefficient of friction lie in the ratcheting region in Figure 1.8, then the material would be expected to fail via ratcheting fatigue. Kapoor [22] created the first in-depth model for ratcheting fatigue in sliding or rolling contact motivated by the various experimental results of Suh et al. [9], and Kuo and Rigney [30]. Kapoor theorized that ratcheting fatigue and low-cycle fatigue, as described by Challen, Halling, Oxley and co-workers [31-32], are competing mechanisms for failures in wear problems, with the mechanism with the lowest cycles to failure being the dominant mode.

Kapoor proposed a simple experiment to show the effect of a ratcheting strain superimposed on a fully reversed axial plastic strain. A typical ratcheting curve is shown in Figure 1.15. Ratcheting will usually occur over three stages, the first being a strain hardening stage where the ratcheting rate decreases. The second is a steady state region with a nearly constant ratcheting rate. The third is a tensile overload stage typical of ductile failure of tensile specimens. Kapoor argued that both ratcheting as shown in Figure 1.15 and low-cycle fatigue mechanisms are occurring at the same time and are competitive in controlling the fatigue life. Whichever occurs first controls material life. For ratcheting, the total number of cycles to failure can be given as:

$$N_r = {\varepsilon_c}/{\Delta\varepsilon_r} \qquad (1.7)$$

where $\varepsilon_c$ is the total strain to failure and $\Delta\varepsilon_r$ the total ratcheting strain range. For low-cycle fatigue, the number of cycles to failure is given by the Coffin-Manson relationship,

$$N_f = \left(\frac{2C}{\Delta\varepsilon_f}\right)^{1/n} \qquad (1.8)$$

Examples of the strain based fatigue curves are given in Figure 1.16. For a given fatigue strain $\Delta\varepsilon_f$, and ratcheting strain $\Delta\varepsilon_r$, the number of cycles to failure can be read from the curves. Ratcheting will control the fatigue life if the alternating ratcheting strain results in failure at a lower number of cycles than caused by the alternating fatigue strain. If the alternating strain controls fatigue, ratcheting can be made to control the fatigue life by increasing the ratcheting strain level.

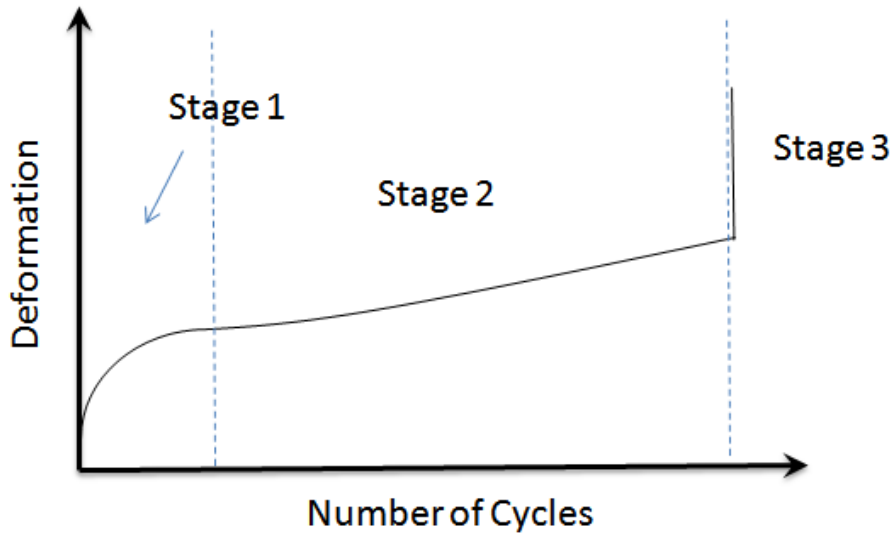


Figure 1.15 A typical ratcheting curve. The curve has three stages: an initial strain hardening state where the ratcheting rate decreases, a steady-state region, and a final ductile overload stage [22].

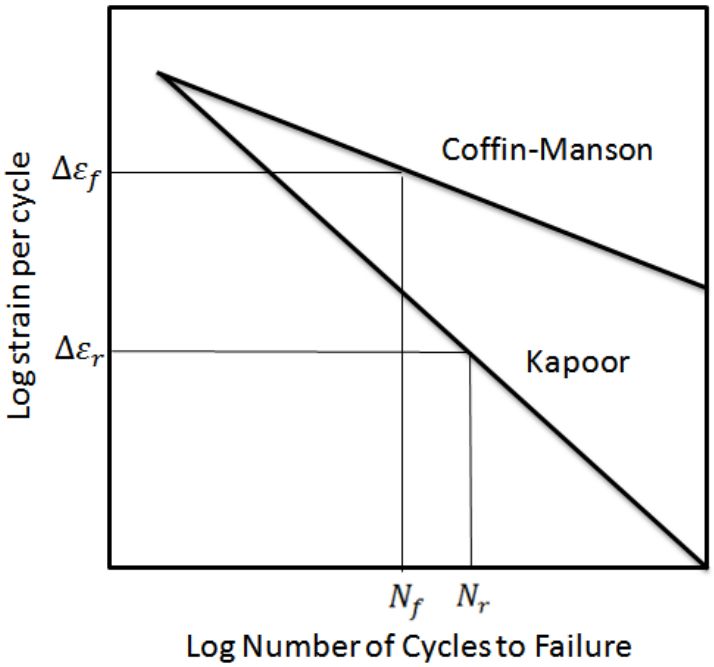


Figure 1.16 Ratcheting and low-cycle fatigue curves, showing the competitive nature proposed by Kapoor between the two strain fields [22].

In comparing his model to the works of Challen et al. and Bower and Johnson [34-35], Kapoor found that ratcheting seemed to control life in both cases. Challen et al. modeled friction and wear as the result of asperity interaction and deformation [33]. They assumed that low-cycle fatigue controls the wear rate as a function of continued shear straining of the softer asperity. Challen et al. determined the number of cycles to failure using the Coffin-Manson equation. Kapoor's work suggests that the best way to model contact stress problems above the plastic shakedown limit is to know the ratcheting rate of the material and the critical stress to failure. Kapoor and Johnson [26, 27] first used the ratcheting theory to predict the formation of extruded slivers from hard asperity contact (Figure 1.17). They made detailed mathematical analysis of asperity contact stresses to predict the $p_{max}/k$ ratio and show that ratcheting occurs and leads to the sliver formation. Yang and Torrance [36] made a similar analysis using the ratcheting theory to calculate the Archard wear rates of 5083 aluminum, 60:40 brass and OFHC copper. They found the theory to accurately predict the wear rates of these materials

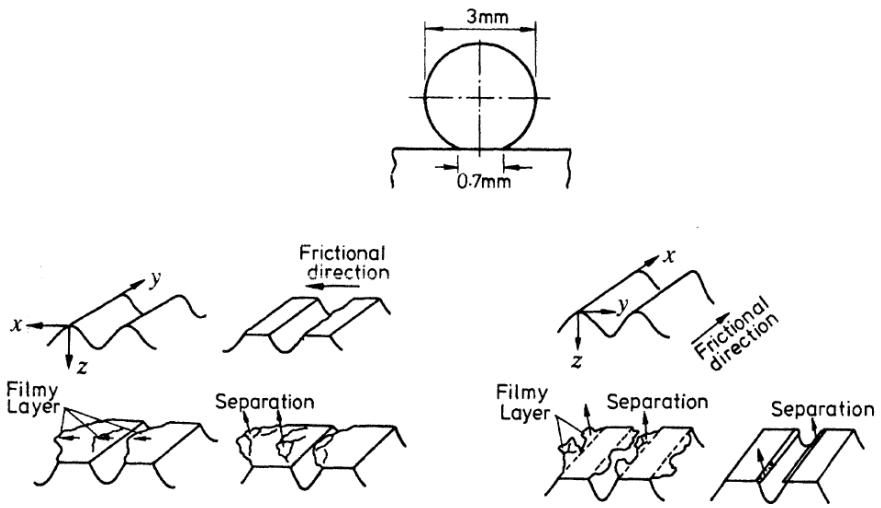


Figure 1.17 Sliver formation from hard asperity contact. The slivers are caused by ratcheting which leads to the incremental extrusion of the slivers and eventual separation from the softer material [25].

Kapoor and Franklin [25] used the ratcheting model to model wear by proposing that a thin layer near the surface of the material in contact controls the life. They named the plastically deformed layer the *Tribological Layer*. They claimed in their work that linear elastic fracture mechanics (LEFM) approaches to solving contact fatigue problems suffer from three distinct drawbacks. First, it does not explain the initiation of cracks. Secondly, it predicts that cracks propagate in Mode II whereas in laboratory experiments cracks turn at an angle and propagate in Mode I. Lastly; the crack is in a heavily plastically deformed region, invalidating the assumptions of LEFM. Therefore, calculating the accumulated plastic flow in the tribological layer can lead to a determination of the cycles to failure should the material experience an open cycle of shear strain. Once the strain in the tribological layer reaches the critical strain $\varepsilon_c$ the layer will crack leading to a delamination such as the ones described by Suh [9]. Therefore, the properties of the material no longer depend on the bulk properties but rather on the properties in the tribological layer where the hardness can increase or decrease due to strain hardening or softening, hard particle mixing, chemical changes, or other microstructural changes. Also, the stress-strain response in the tribological layer would likely be very different than the bulk due to texture formation as well as dislocation dynamics such as dislocation cell formation. Finally, under the high compressive hydrostatic pressure present in contact problems, the

strain to failure would likely increase in the tribological layer due to the suppression of void nucleation of the type described by Suh [16], leading to an increase in life under ratcheting fatigue conditions.

Ringsberg et al. [28], Tyfour et al. [24] have also successfully used the ratcheting theory to describe contact fatigue failure in rolling and rolling/sliding contact fatigue in rail steels. They used the accumulated total ratcheting strain, measured using the $tan\beta$ method shown in Figure 1.18, in the direction of sliding as a function of contact load cycles as the parameter to measure the amount of ratcheting. The total strain was estimated as:

$$\Delta\varepsilon_r = tan\beta = \sqrt{(\Delta\tilde{\varepsilon})^2 + \left(\Delta\tilde{\gamma}/\sqrt{3}\right)^2} \qquad (1.9)$$

Where $\Delta\tilde{\varepsilon}$ is the average ratcheting axial strain and $\tilde{\gamma}$ the average ratcheting shear strain.

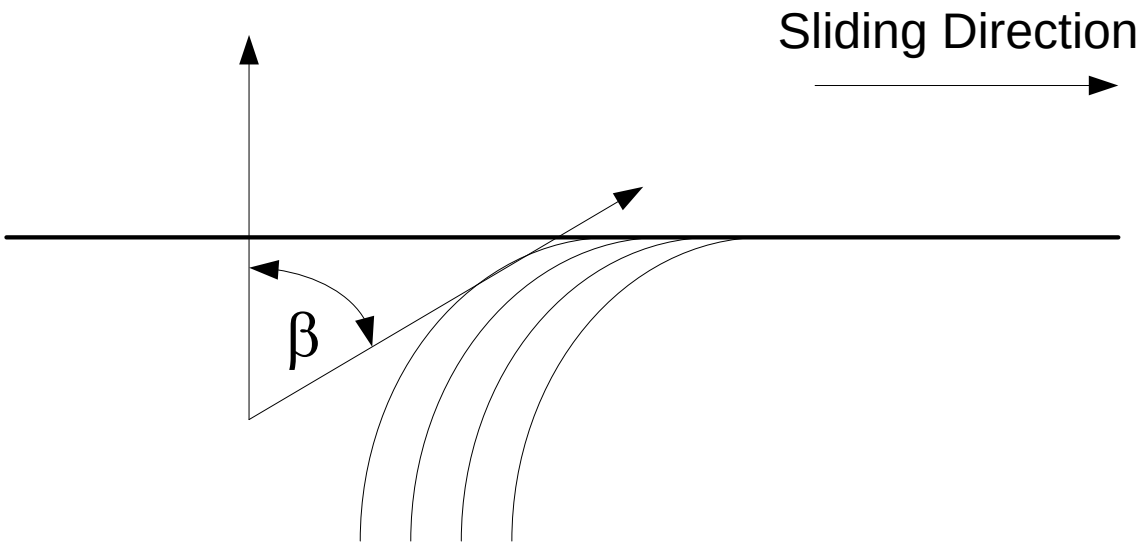


Figure 1.18 Total ratcheting strain measurement method from Tyfour [24]. The tangent of β is taken as the shear strain at a given number of cycles.

They proposed that failure will occur once the accumulated plastic strain exceeds a critical strain $\varepsilon_c$. The plastic strain per cycle is given as $\Delta Rd = C\frac{P_r}{k_{eff}}$ where $P_r$ is the

difference between the actual $p_{max}$/k ratio at the plastic shakedown limits at a given constant coefficient of friction and $k_{eff}$ is the hardness at the given cycle. The value of $k_{eff}$ varies if the material strain hardens or softens with load cycles. C is a material constant that is independent of stress which can be experimentally determined as the slope of the plot of $P_r$ multiplied by the number of cycles at that load and the total ratcheting strain, $tan\beta$.

#### 1.3.2.3 Stress Calculations for General Ratcheting Fatigue

The ratcheting fatigue approach requires that the strain per cycle be calculated. Using the explicit stress equations for a sliding sphere on a flat surface derived by Hamilton and Goodman coupled with the bulk elastic properties of the solid, the strain components and principal strains and directions can be calculated, making it possible to calculate the shear strain for pin-on disk testing of materials as well as similar loading applications. To calculate the accumulated plastic shear strain in circular contact, the nonlinear kinematic hardening model developed for line contacts by Bower and Johnson [34] can be used to predict ratcheting strain accumulation as a function of cycles and therefore, the ratcheting strain rate. For surface plastic flow their model uses the equations for stress:

$$\sigma_{xx} = \begin{cases} -2\mu p_o\, x/a, & |x| \le a \\ -2\mu\left[p_o\, x/a \pm \{(x/a)^2 - 1\}^{1/2}\right], & |x| \ge a \end{cases} \qquad (1.10)$$

$$\tau_{zx} = \begin{cases} -\mu p_o\{1 - (x/a)^2\}^{1/2} & |x| \le a \\ 0 & |x| \ge a \end{cases} \qquad (1.11)$$

With the principal shear stress in the plane of deformation given as:

$$\tau = \left\{\frac{1}{4}(\sigma_{xx} - \sigma_{zz})^2 - \tau_{zx}^2\right\}^{1/2} = \mu p_o \qquad (1.12)$$

μ is the coefficient of friction, $a$ is the radius of the contact area and $p_o$is the contact pressure. Therefore, the surface will yield when $\mu p_o = k$, where $k$ is again the shear yield strength. Above this load parameter, continued deformation occurs. Under sliding loading the material experiences a cycle of nonproportional load or

compressive, shear, tension which results in an unsymmetrical cycle of stress and explains the accumulating plastic flow experienced in sliding contact. To model this load situation, Bower and Johnson used the method of Armstrong and Frederick [37]:

$$d\varepsilon^p = \frac{\sqrt{3}}{2}\frac{1}{h}\langle\frac{\sqrt{3}}{2}\frac{\sigma' - X'}{k} : d\sigma\rangle\frac{\sigma' - X'}{k} \qquad (1.1)$$

Where h is the hardening modulus given by: $h = c - \frac{\sqrt{3}}{2k}\gamma_1[(X - Y):(\sigma' - X')]$ where $v = \langle u\rangle$ denote $v = u$ if $u > 0$ (plastic loading) and $v = 0$ if $u \leq 0$ (elastic unloading). Integration gives the accumulating plastic strain.

#### 1.3.2.4 Competing Contact Fatigue Models

More recently, the ratcheting model, enhanced by a consideration of multiaxial-critical plane fatigue initiation proposed by Jiang and Sehitoglu [38-40], appears to be more widely accepted [41]. The Jiang and Sehitoglu model accounts for both ratcheting and multiaxial fatigue effects. Ratcheting is calculated using a similar method to Bower et al. [34]. Multiaxial loading is accounted for in the multiaxial fatigue criterion (*FP* = multiaxial fatigue parameter):

$$FP = \frac{\Delta\varepsilon}{2}\sigma_{max} + J\Delta\gamma\Delta \qquad (1.14)$$

Where $\Delta\varepsilon$ is the normal strain range, $\sigma_{max}$ is the maximum normal stress, $J$ is a material dependent constant, $\Delta\gamma$ is the shear strain range, and $\Delta\tau$ is the shear stress range. All of the stress and strain parameters are on the critical plane which is defined as the plane of maximum FP. The first term is a mean stress term. The relationship between fatigue parameter and fatigue life is given as:

$$(FP - FP_o)^m N_f = C \qquad (1.15)$$

Where $FP_o$, m, and C are material constants. The fatigue damage per cycle can then be calculated as:

$$\frac{dD_f}{dN} = \frac{1}{N_f} = \frac{(FP - FP_o)^m}{C} \qquad (1.16)$$

Where $D_f$ is the fatigue damage that is less than or equal to 1. To accommodate ratcheting, Jiang and Sehitoglu proposed that the ratcheting damage per cycle be given as:

$$\frac{dD_r}{dN} = \frac{|d\gamma_r/dN|}{\gamma_{crit}} \qquad (1.17)$$

Where $\gamma_{crit}$ is a material constant representing the ductility of the material. The sum of both damage terms is taken as the total damage per cycle of loading.

The multiaxial model is based on the critical plane models based on the works of Guest [42, 43], Brown and Miller [44], Socie and Bannatine [45] and Socie and Shield [46]. The book by Socie and Marquis [47] offers a more in-depth discussion of these and other relevant strain and energy based multiaxial fatigue models. The critical plane model incorporates the effects of both normal and shear stresses on fatigue crack initiation, which helps to explain why cracks can form at various angles in contact problems.

### 1.3.3 Crack Nucleation

#### 1.3.3.1 Void Nucleation as Described by the Delamination Theory of Wear

Surfaces experiencing rolling and/or sliding contact almost invariably suffer from some degree of plastic deformation. Plastic deformation under sliding contact and its role in void nucleation was described for the delamination theory of wear by Jahanmir and Suh [12]. Jahanmir and Suh linked the plastic deformation caused by sliding wear in the contact surface to void nucleation and crack initiation for the first time. They found that void nucleation can only occur in a small region below the sliding contact where the presence of a hydrostatic compressive stress field is diminished but plastic deformation is still above the shakedown limit in order to nucleate a void. They assumed that voids nucleate at inclusions or phase boundaries when the radial stress component exceeds a critical tensile stress when inclusions are large enough to satisfy the energy criterion for crack nucleation. However, smaller inclusions do not satisfy the energy criterion. Therefore, it is a necessary but not sufficient condition for void nucleation. Jahanmir and Suh found that for small particles less than 1 μm in size, the stress criterion created by Ashby that is based on

dislocation interaction with the particle is the most useful. For larger particles, continuum mechanics is more suitable. The Jahanmir and Suh model assumes a particle size above 1 μm and that nucleation occurs when the tensile stress at the interface of the particle and the matrix equals the interfacial strength. Their analysis found that void nucleation around hard particles happens easily but that crack propagation from the voids is slow. Therefore, for metals under wear conditions where void nucleation can occur easily, crack propagation may be the rate-controlling step. This would be typical for medium strength steels. Steels such as SAE 52100 in a hardened condition where nucleation is much more difficult would likely have void nucleation as the rate-controlling step.

One major drawback of Jahanmir and Suh's model is that many materials used for high contact stress applications such as bearing quality SAE 52100 steel or carburized SAE 8620 steel are very clean: containing only small and uniformly distributed oxides, silicates, metallic carbo-nitrides, and sulphide inclusions in a tempered martensitic matrix where crack nucleation would be more likely to occur at smaller inclusions due to dislocation pile-ups or other atomic level interactions at the inclusion-matrix interface. Also, due to the high yield strength and flow resistance of these steels, plastic flow is minimized and confined to the surface for coefficients of frictions greater than approximately 0.3.

#### 1.3.3.2 Crack Nucleation as Described by the Ratcheting Fatigue Theory

Crack nucleation is considered to occur when the cumulative ratcheting strain $\Delta\varepsilon_r$ equals the critical strain $\varepsilon_c$. Unlike the general delamination theory of wear and the various fracture mechanics studies on crack propagation in fretting fatigue, the ratcheting theory assumes that crack nucleation is the life controlling mechanism and therefore controls the number of cycles to failure. Hence, no fatigue crack growth models have been created to describe the crack propagation of ratcheting induced cracks.

#### 1.2.2.3 Fatigue Crack Nucleation under Elastic, High-Cycle Fatigue Conditions

Eid and Thomason's [48] work on the nucleation of fatigue cracks in low-alloy steel under high cycle fatigue conditions (≈5 x $10^6$ cycles) detailed the role of aluminum oxide inclusions in the crack initiation process in steel. They found that aluminum oxide inclusions are a source of fatigue cracks due to the high stress concentration at the pole points on the inclusion/matrix interface. However, they found that in the high-cycle regime, the local stress field is considerably lower than that required to cause localized plastic deformation in the matrix, which implies that that fatigue cracks will not form so long as the aluminum oxide inclusions remain undamaged and firmly bonded to the matrix. Wang et al. [49] found similar results to Eid and Thomason in SAE 52100 steel. They found that subsurface inclusions were the most potent fatigue crack nucleation sites and that for various low-alloy steels multiple endurance limits or none at all was observed for various low-alloy steels. D. Wang et al. [50] found that in the absence of subsurface inclusions, fatigue cracks nucleated as cleavage cracks along prior austenitic grain boundaries. They found that the fatal crack initiated at subsurface inclusions even though small cracks had previously formed at carbide interfaces on the surface of the test samples. They conjectured in their work that in high-strength low-ductility steels like SAE 52100, the formation of a hole due to a debonded inclusion causes a stress concentration that cannot be mitigated through plasticity and thus leading to crack initiation. They used the dislocation dipole model create by Lin [51] to explain crack initiation. More recent work in the very high cycle regime such as that of Marines et al. [52] found that the endurance limit dropped approximately 150-200 MPa over $10^7$ cycles with cracks initiating primarily at oxide inclusions above $10^8$ cycles. Melander and Olund [53, 54] have shown the effect of titanium carbo-nitride, Ti(C,N), and aluminum oxide (Al, O) inclusions in both axial and rolling contact fatigue. They found that un-cracked Ti(C,N) inclusions are the most dangerous followed by cracked Ti(C,N) and then cracked aluminum oxides in affecting the fatigue life in both axial and rolling contact for all but the shortest cracks (~2 μm). The difference in potency was attributed to the high crack energy release rates associated with a crack for the alumina case and the sharp edge of the Ti(C,N) inclusion. By creating SAE 52100 bearing steels with

increasing amounts of nitrogen, Melander and Olund showed that the statistical median fatigue life between $10^6$ and $10^7$ cycles decreases dramatically with an increase in nitrogen from 58-118 ppm. The amount of fatigue failures with Ti(C,N) inclusions at the origin was found to increase with nitrogen content in line with the decreasing fatigue life.

Other authors have extensively described the role of inclusions in elastic, high cycle fatigue. Cogne et al. [55], Brooksbank and Andrews [56-59], and Atkinson and Shi [60] provide good overviews of the affect of inclusion type (carbo-nitrides versus oxides and sulphides) on fatigue life of steels that correlate well with very high cycle fatigue failures. Other than the work of Melander and Olund, very few, if any, authors have shown any significant experimental and theoretical basis for the differences that specific inclusions play in rolling or sliding contact fatigue; although much work has been done for over a century to improve the cleanliness of steels with a subsequent increase in wear life. Most of the work, such as that of Monnot, Heritier, and Cogne [61] show how specific inclusions affect axial or rotating beam fatigue life and attempt to analogously relate the results to contact.

### 1.3.4 Crack Propagation

Fleming and Suh [17] developed the first theoretical model for subsurface crack propagation in sliding wear assuming the propagation controls the wear rate. Their work sought to create a theoretical construct for the delamination theory of wear and was a follow-up paper to the crack initiation model developed by Jahanmir and Suh. They assumed that all cracks are in plane strain and initially running parallel to the surface of contact. They also assumed that the crack would only propagate in the tensile zone of the contact stress field, staying closed within in the compressive region. They assumed a simple model in polar coordinates for the subsurface stress at a preexisting crack,

$$\sigma_{rr} = \frac{-2F}{\pi r} cos(\alpha + \theta)$$
$$\sigma_{r\theta} = 0$$
$$\sigma_{\theta\theta} = 0, \qquad (1.18)$$

Where F is the applied load at an angle $\alpha$ to the surface. They then calculated stress intensity factors at the crack based on the stress model and applied the Paris crack propagation law integrated into a calculation of worn volume. The model suffers from the fact that there exists little material property data for highly deformed material. Also, the assumption that the crack only propagates in tension has been shown by many to not be so.

These works were the first to try to describe the crack propagation during sliding contact using linear elastic fracture mechanics. In order for crack propagation to be useful in modeling the wear rate of a material it must be assumed that crack propagation is the rate controlling process. This assumption is a fair one for many ferrous alloys that have high hardness and low fracture toughness such as hardened steels. The obvious question in using LEFM in studying crack propagation in and around plastically deformed surfaces is whether the assumptions intrinsic to LEFM are invalid in this case. Fleming and Suh answered this problem by breaking the contact zone into compressive and tensile regions. The compressive region being the region in front of the sliding contact as explained in the papers by Hamilton and Goodman for spherical contact on flat surfaces, and tensile behind. Fleming and Suh assumed that in the compressive region the crack was closed and in the tensile region residual stresses suppressed plastic deformation leaving an elastic stress field that meets the requirements of LEFM. These conditions are no longer valid for open cycles of shear strain above the shakedown limit where ratcheting fatigue operates. Therefore, assuming a material below the shakedown limit, fracture mechanics would likely be a valid approach for trying to model crack propagation for sliding wear problems as long as the varied material properties are accounted for. Fleming and Suh's model results in the calculation of approximate stress intensity factors for cracks parallel to the contact surface. The model determines stress intensities at different values of the critical crack depth and critical crack length. They summarized that the stress intensity factor and the critical crack depth *d* increased with increasing coefficient of friction and that residual stresses do not affect the propagation of cracks in sliding wear.

The work by Hills and Ashelby [62] extended the work of Fleming and Suh by showing that crack growth can occur by two growth mechanisms not just the one in the tensile region as claimed by Fleming and Suh. The first growth mechanism occurred just before the rider arrives at the flaw, consisting of a mode II stress intensification with a light clamping force between the crack faces. The second growth mechanism consists of mode I and II components behind the slider similar to that found by Fleming and Suh. Hills and Ashelby claimed that Fleming and Suh's model underestimated the crack growth rate due to a lack of the additional growth mechanism and that they did not include force contributions from many contacting asperities. They found that the majority of crack propagation occurs in the first growth mechanism due to shear.

Rosenfield [63] claimed in his work that the elastic field assumption for crack propagation in Fleming and Suh's work was highly unrealistic but might be appropriate if the work hardened layer responds to stress in a linear fashion although not elastically. However, he mentioned that the crack size of many contact fatigue cracks are on the order of the microstructural size and thus LEFM may still not be adequate to model crack propagation under sliding wear. Rosenfield's model agrees with much of the results of Fleming and Suh but differs from them by focusing on the compressive region ahead of the asperity contact and the frictional contact between the crack faces. Like Hills and Ashelby, Rosenfield supports the claim that crack growth of cracks parallel to the contacting surface are dominated by mode II-shear. Rosenfield modeled the combined uniform shear-compression stress intensity factor by using the work of Swedlow:

$$K_{II} = \left(\sigma_{xy} - tan\beta\sigma_{xy}\right)(\pi a)^{1/2} \qquad (1.19)$$

where $\tan\beta$ is the friction force between the crack faces.

More recent modeling of cracks under conditions of rolling fatigue by Goshima et al. [64, 65] allow for calculation of mode I, II, and III crack growth and also kinking under conditions of heating, crack face friction, and crack hydraulic fluid pressure. His models accurately predict many crack situations found in experiments on contact

fatigue in metals under both rolling and sliding conditions. The only drawback is that the model requires complex numerical procedures to solve for the crack growth path and growth rate. Giannakopoulos, Lindley and Suresh et al. [66-69] sought to overcome numerical model complexity by introducing simple stress intensity models that connect certain conditions of contact mechanics with fracture mechanics via asymptotic matching. The equivalence was made possible by identifying geometries of cracked specimens that are analogous to stress singularities in contact mechanics, such as the edge of a cylinder pressed into a flat or a rounded end cylinder into a flat. Theoretically one could find a similar equivalence in sliding contact of a sphere on a flat like it typically found for pin-on-disk wear testers. However, there is no singularity in the pressure field for contact of that type. However, in a practical sense, the ball will typically wear in pin-on-disk testing at high contact stresses and low cycles or at low contact stress and low cycles of load. Therefore, the work by Giannakopoulos, Lindley and Suresh et al. could possibly be extended to cases of spherical contact and thus facilitate a analytical method for calculating fatigue initiation and crack growth in two-dimensional plane strain. Assuming this is possible, the mode I and mode II stress intensity factors for a three-dimensional crack analogue of a punch contacting a flat surface are given as:

$$K_I = \frac{P}{2a\sqrt{\pi a}} \qquad (1.20)$$

$$K_{II} = \frac{Q}{2a\sqrt{\pi a}} \qquad (1.21)$$

Giannakopoulos et al., postulated that a crack will initiate and advance in a direction along which the local mode II stress intensity factor amplitude, $\Delta k_2$, vanishes. Using the formulation by Cotterell and Rice [70] for kinked cracks, the local $k_1$ and $k_2$ stress intensities are related to the remote $K_I$ and $K_{II}$ stress intensities and the angle of the crack by the following:

$$\begin{aligned} k_1 &= a_{11}(\phi)K_I + a_{12}(\phi)K_{II} \\ k_2 &= a_{21}(\phi)K_I + a_{22}(\phi)K_{II} \end{aligned} \qquad (1.22)$$

where to a first order approximation

$$a_{11}(\phi)=\frac{1}{4}\left(3\cos\frac{\phi}{2}+\cos\frac{3\phi}{2}\right)$$
$$a_{12}(\phi)=-\frac{3}{4}\left(\sin\frac{\phi}{2}+\sin\frac{3\phi}{2}\right)$$
$$a_{21}(\phi)=\frac{1}{4}\left(\sin\frac{\phi}{2}+\sin\frac{3\phi}{2}\right)$$
$$a_{22}(\phi)=\frac{1}{4}\left(\cos\frac{\phi}{2}+3\cos\frac{3\phi}{2}\right) \qquad (1.23)$$

To solve for initial crack angle, $\phi_{in}$, Giannakopoulos et al. suggested setting $k_2$ equal to 0 after substituting the remote stress intensity factors and dimensionless factors into one another. Since there is no additional applied load on the sample as was the case in the work by Giannakopoulos et al., the crack should grow in the initial crack direction until it turns due to tensile fluid pressure on the crack face until a secondary crack forms along the original crack and opens toward the surface.

## 1.4 Problem Summary and Dissertation Topics

Typically cam and/or tappet failure analyses like the one discussed previously are difficult as both part surfaces are extremely damaged making it hard to determine the root mechansim of the failure: abrasion, adhesion, low-cycle/ratchetting fatigue, or elastic-high cycle fatigue. The cam analyzed in this chapter had very low time on it making the failure mechanism determinable. The cracked cam surface indicated that cracks initiated at the cam surface and were most likely caused by the contact fatigue mechanisms described previously. In this case, the studies that comprise the delamination theory of wear, as well as more recent works on ratcheting and multiaxial contact fatigue would apply. Analysis of the contact stress and coefficient of friction of the cam suggests that the contact fatigue occurred under elastic, low-stress amplitude conditions. Therefore, the effects of inclusions and other microstructural features such as prior austenitic grain boundaries, carbides, etc in initiating and effecting crack propagation need to be considered. However, in contact

fatigue wear failure analyses, the ability to find a small inclusion or microstructural feature on a crack surface is nearly impossible. Usually the likely crack initiation feature can only be inferred as a possible failure mechanism due to finding other similar features near the crack. Therefore, to design a cam and/or tappet surface to resist low-stress amplitude contact fatigue wear failure at lives approaching $10^8$ to $10^9$ cycles, tests need to be able to determine how plastic deformation and microstructual discontinuities such as inclusions affect the life of the material. Traditionally, in wear testing, tribometers are used to test how materials wear. Unfortunately, normal tribometers have many shortcomings such as the wear of the counter body during testing which reduces the contact pressure and stresses. Also, tribometers must be operated at low speeds to reduce the potential for overheating or an oil must be used to reduce the coefficient of friction which reduces heat generation as well as acting to carry heat away from the contact interface. The use of oil can have a positive effect of reducing the contact stress fields as well as a negative effect of forming corrosive byproducts after repeated use which may help to initiate and/or enhance surface deterioration. The bottom line is that short tests using tribometers usually produce good results if one is interested in low-cycle or ratcheting fatigue failures in materials only expected to survive $10^3$ to $10^5$ cycles. If a designer is interested in engineering materials to last for $10^8$ to $10^9$ cycles, tribometers do little more than validate a materials resistance to abrasion and adhesion under specific loading and boundary conditions: classic Archard linear wear model [71]. Most designers follow a philosophy of the "harder the better" in order to resist adhesion and abrasion to achieve long life designs [72]. Although this philosophy is relevant in most cases, it ignores discrete contact fatigue related wear failures occurring at low $p_{max}/k$ ratios and low friction. It could be argued in some cases that the surface is wearing fast enough, even in the case of very hard materials, to eliminate the potential for a fatigue crack to initiate due to the material not having time to build up enough cycles. However, in many critical wear applications such as cams and tappets, oil is introduced to the system in order to slow down or stop the adhesion and abrasion wear mechanisms. Therefore, it is not out of the realm of possibility that many wear

failures like the cam failures described previously are the result of discrete elastic contact fatigue.

Therefore, this dissertation will seek to answer the following questions in order to create a thorough design methodology for creating contact fatigue resistance surfaces:

1. What is the contact fatigue controlled mechanism and failure difference between unhardened and laser hardened SAE 8620, 4140, or 52100 with various pre-heat treatments? How does laser hardening affect the contact fatigue life and by what mechanism?
2. Does coating a hardened SAE 52100 with a layered CrN and hydrogenated diamond-like-carbon or an electroless nickel-phosphorus-polytetrafluoroethylene infused coating affect the axial stress-life fatigue limit of the steel? How do the mechanisms controlling axial fatigue relate to elastic contact fatigue?
3. Does coating a SAE 52100 and a chilled cast iron with a layered CrN and hydrogenated diamond-like-carbon increase the contact fatigue life of the materials? If so, by what mechanisms?
4. Can an ultrasonic wear tester be created that can simulate contact lifetimes on the order of $10^8$ cycles SAE 52100 steel and chilled cast iron coated with a layered CrN and hydrogenated-amorphous hydrogenated diamond-like-carbon. Will the results from the tester allow for the development of a quantitative-empirical model for wear depth calculation that is can also predict wear for traditional tribometers.

## 1.5 References


1. H.A. Rothbart; Cam Design Handbook; McGraw-Hill Handbooks; (2004)
2. F. Chen. A Textbook on Mechanics and Design of Cam Mechanisms, Pergamon Press, (1982).
3. A. Ponter, A. Hearle and K. Johnson. Application of the kinematical shakedown theorem to rolling and sliding point contacts. J. Mech. P. Solids, 33, 4, pp. 339-362, 1985
4. W. Koiter, Koninkl. Ned. Ak. Wetenschap B59, 24, 1956.
5. K. Ludema. Friction, wear, lubrication: a textbook in tribology. CRC Press, L.L.C. 1996
6. B. Bhushan. Nanotribology of Ultrathin and Hard Amorphous Carbon Films. Tribology of Diamond-Like Carbon Films. C. Donnet and A. Erdemir (eds). Springer, 2008
7. C. Lee, Q. Li, W. Kalb, X-Z. Liu, H. Berger, R.W. Carpick, J. Hone. *Frictional Characteristics of Atomically Thin Sheets.* Science, 328, www.sciencemag.org 2010
8. R.W. Carpick, Controlling friction. Science**,** 313, pp. 184-185, 2006
9. N. Suh. An overview of the delamination theory of wear. Wear, 44, pp. 1-16. 1977
10. N. Suh and P. Sridharan. Relationship between the coefficient of friction and the wear rate of metals. Wear, 34, pp. 291-299, 1975.
11. S. Jahanmir, N. Suh and E. Abrahamson. Microscopic observations of the wear sheet formation by delamination. Wear, 28, pp. 235-249, 1974
12. S. Jahanmir and N. Suh. Mechanics of subsurface void nucleation in delamination wear. Wear, 44, pp. 17-38, 1977
13. N. Suh, N. Saka, and S. Jahanmir. Implications of the delamination theory on wear minimization. Wear, 44, pp. 127-134, 1977
14. S. Jahanmir. The relationship of tangential stress to wear particle formation mechanisms. Wear, 103, pp. 233-252, 1985

15. N. Saka, A. Eleiche, and N. Suh. Wear of metals at high sliding speeds. Wear, 44, pp. 109-125, 1977
16. S. Jahanmir, N. Suh and E. Abrahamson. The delamination theory of wear and the wear of a composite surface. Wear, 32, pp. 33-49, 1975
17. J. Fleming and N. Suh. Mechanics of crack propagation in delamination wear. Wear, 44, pp. 39-56, 1977
18. G. Hamilton, L. Goodman, Journal of Applied Mechanics 33(2), pp. 371-376, 1966
19. G. Hamilton. Proceedings of the Institution of Mechanical Engineers Part C- Journal of Mechanical Engineering Science, 197, pp. 53-59, 1983
20. K.L. Johnson. Contact Mechanics. 2000
21. D. Rigney, J. Hirth. Wear, 53, pp. 345-370, 1979
22. A. Kapoor. A Reevaluation of the life to rupture of ductile metals by cyclic plastic strain. Fatigue and Fracture of Engineering Materials and Structures, 17, 2, pp. 201-219, 1994
23. A. Kapoor, K. Johnson. Proc of the Royal Society London A, 445, pp. 367-381, 1994
24. W. Tyfour, J. Beynon, A. Kapoor. Wear, 197, pp. 255-265, 1996
25. A. Kapoor and F.J. Franklin. Tribological Layers and the Wear of Ductile Metals. Wear, 245, pp. 204-215. 2000. J. Ringsberg. Cyclic Ratcheting and failure of a pearlitic rail steel. Fatigue and Fracture Engineering Materials and Structure, 23 (9), pp. 747-758, 2000
26. A. Kapoor, K.L. Johnson Wear 186-187 (1995) pp. 86-91, 1995
27. A. Kapoor Wear 212, pp. 119-130, 1997
28. J.W. Ringsberg. Cyclic ratchetting and failure of a pearlitic rail steel. Fatigue and Fracture of Engineering Materials and Structure, 23 (9): pp 747-758, 2000
29. S.S. Manson and G.R. Halford. Fatigue and Durability of Structural Materials. ASM International. 2006
30. S. Kuo and D. Rigney. Sliding behavior of aluminum. Materials Science and Engineering A157, pp. 141-143, 1992

31. J. Halling. A Contribution to the Theory of Mechanical Wear. Wear, 34, pp. 239-249, 1975
32. B. Hockenhull, E. Kopalinsky, and P. Oxley. An investigation of the role of low cycle fatigue in producing surface damage in sliding metallic friction. Wear, 148, pp. 135-146. 1991
33. J. Challen, P. Oxley and B. Hockenhull. Prediction of Archard's Wear Coefficient for Metallic Sliding Friction Assuming a Low-Cycle Fatigue Wear Mechanism. Wear, 1, pp. 275-288. 1986
34. A. Bower and K. Johnson. The influence of strain hardening on cumulative plastic deformation in rolling and sliding contact. J. Mech. P. Solids, 37, 4, pp. 471-493, 1989
35. A. Bower. Cyclic Hardening Properties of Hard-Drawn Copper and Rail Steel. J. Mech. Phys. Solids., vol 37, No. 4, pp. 455-470. 1989
36. Y. Yang and A. Torrance, Wear by plastic ratcheting- an experimental evaluation. Wear, 196, pp. 147-155, 1996
37. P. Armstrong. C. Frederick. CEGB Report RD/B/N73 1, 1966
38. Y. Jiang and H. Sehitoglu. Modeling of cyclic ratcheting plasticity: Part 1. Development of constitutive equations. ASME Journal of Applied Mechanics, 63, pp. 720-725. 1996
39. Y. Jiang and H. Sehitoglu. Modeling of cyclic ratcheting plasticity: Part 2. Implement of the new model and comparison of theory with experiments. ASME Journal of Applied Mechanics, 63, pp. 726-733. 1996
40. Y. Jiang and H. Sehitoglu. A Model for Rolling Contact Fatigue. Wear, 224, pp. 38-49, 1999
41. W. Tyfour, J. Beynon, A. Kapoor, The steady state wear behavior of pearlitic rail steel under dry rolling-sliding conditions, Wear, 180 pp. 79-89, 1995
42. J. Guest, On the strength of ductile materials under combined stress, Philosophical Magazine, Vol. 1900, pp. 69–132.
43. J. Guest, Recent research on combined stress, Proceedings, Institution of Automobile Engineers 35 pp. 33–72. 1940

44. M. Brown, K. Miller, A theory for fatigue failure under multiaxial stress–strain conditions, Proc. Instn. Mech. Engr. 187, pp. 745–755. 1973
45. D. Socie, J. Bannantine, Bulk deformation fatigue damage models, Materials Science and Engineering A 103, pp. 3–13. 1988
46. D. Socie, T. Shield, Mean stress effects in biaxial fatigue of Inconel 718, ASME Journal of Engineering Materials and Technology 106, pp. 227–232. 1984
47. D. Socie, G. Marquis. Multiaxial Fatigue. Society of Automotive Engineers, 2000
48. N. Eid, P. Thomason, Acta Metallurgica, 27, pp. 1239-1249, 1979
49. Q. Wang, C. Bathias, N. Kawagoishi, Q. Chen. Effect of inclusion on subsurface crack initiation and gigacycle fatigue strength. Int. Journal of Fatigue, 24, pp. 1269-1274, 2002
50. D. Wang, H. Hua, M. E. Fine and H. S. Cheng, Fatigue crack initiation and fracture in 52100 steel, Materials Science and Engineering A
51. M. Lin, M. Fine, T. Mura. Acta Metall., 34(4), pp.619-628, 1986
52. I. Marine-Garcia, P. Paris, H. Tada, C. Bathias. Int Journal of Fatigue, 29, pp. 2072-2080, 2007
53. A. Melander, P. Olund. Materials Science and Technology. Vol. 15, pp. 555-562, 1999
54. A. Melander. International Journal of Fatigue, 19, 1, pp. 13-24, 1996
55. J. Cogne, B. Heritier, J. Monnot, Clean Steel 3, Balatonfured, Hungary, 2-4 June 1986, The Institute of Metals, pp. 26-31. 1987
56. D. Brooksbank, K. Andrews, Journal of the Iron and Steel Institute, 206 (6), pp. 595-599. 1968
57. D. Brooksbank, K. Andrews, Journal of the Iron and Steel Institute, 207 (4), pp. 474-483. 1969
58. D. Brooksbank, Journal of the Iron and Steel Institute, 208 (5), pp.495-499. 1970
59. D. Brooksbank, K. Andrews, Journal of the Iron and Steel Institute, 210 (4), pp. 246-255. 1972

60. H. Atkinson and G. Shi. Progress in Materials Science 48, pp. 457–520, 2003
61. J. Hoo Ed. Effect of Steel Manufacturing Processes on the Quality of Bearing Steels. STP987, ATSM, 1988
62. D. Hills, D. Ashelby, Wear, 54, pp. 321 – 330, 1979
63. A. Rosenfield. Wear, 61, pp. 125-132, 1980
64. T. Goshima. Journal of Thermal Sciences. 26, pp. 615-639, 2003
65. T. Goshima and L.M. Keer. Trans ASME J. Lubric. Tech. Vol 112, no. 2, pp 382-391, 1990
66. B. Conner, T. Lindley, T. Nicholas, and S. Suresh. Int. Journal of Fatigue. Vol 26. pp. 511-520, 2004
67. A. Giannakopoulos, T. Lindley, and S. Suresh Acta Materialia. Vol 46. No. 9. pp. 2955-2968, 1998
68. A. Giannakopoulos, T. Venkatesh, T. Lindley, and S. Suresh. Acta Materialia. Vol 47 No. 18. pp. 4653-4664, 1999
69. A. Giannakopoulos, T. Lindley, and S. Suresh. Acta Materialia. Vol 46. No. 9. pp. 2955-2968, 1998
70. B. Cotterell, J. Rice, Int. J. Fract., 1980, 16, pp. 155. 1980
71. J. Archard. Journal of Applied Physics, Vol. 24, No. 8, pp. 981-988, 1953
72. E. Rabinowicz. Friction and Wear of Materials, John Wiley and Sons, 1995

# CHAPTER 2

## Very High Cycle Fatigue Behavior of Hydrogenated Diamond-Like-Carbon and Electroless Nickel-Polytetrafluoroethylene Coated SAE 52100

### 2.1 Introduction

Many engineering systems such as camshafts and bearings experience contact load cycles up to and in excess of 100 million ($10^8$) cycles, however, laboratory and verification testing will usually end significantly below that due to time, cost, and equipment constraints. This results in discrete contact failure modes, typical of high cycle contact fatigue, being impossible to detect, which can lead to non-conservative design and a lack of understanding of the true controlling variables of surface degradation. Also, many researchers in recent years have found that the assumption of an endurance limit no longer holds at very high cycles of loading beyond $10^8$ [1-4]. Low amplitude loading at or above $10^8$ cycles can lead to fatigue failures, typically at inclusions, porosities, supergrains, or other internal microstructural features. This is a very important concern as an analogous situation exists for some contact fatigue problems, as was first described by Lundberg and Palmgren in the 1940s and Chiu (1971) [5]; specifically those in the elastic loading regime [6]. The elastic response of materials to contact loading is usually the result of low values of sliding friction and contact load in higher strength materials like bearing steel where internal features such as inclusions can control the fatigue life or where hard films are used. Lundberg and Palmgren simultaneously showed that the contact life of a rolling element can be modeled as a curve similar to a Basquin-Wohler curve typical of axial fatigue testing.

$$L_{10} = \left(\frac{C_r}{P_{eq}}\right)^p \qquad (2.1)$$

Where $L_{10}$ is the 90% lifetime of a bearing, $C_r$ is basic dynamic load rating or capacity of a bearing and is defined as the load that a bearing can carry for 1 million inner-race revolutions with a 90% probability of survival; $P_{eq}$ is the equivalent bearing load; and $p$ is the load-life exponent. Equation 2.1 was derived from the work of Lundberg and Palmgren to connect the probability of survival of a bearing to the

contact stress, number of cycles, and volume of material stressed. The form of equation 2.1 suggests, as is now widely known and well accepted, that contact fatigue can occur at very high cycles of load under nominally elastic contact conditions.

Therefore, the ability to test prospective materials to be used in mechanical devices experiencing contact loading at low stress amplitudes with expected lives of $10^8$ cycles or greater is an important issue for the designer. This becomes a difficult task if a normal tribometer, which usually run at speeds around 10-40 Hz, is used. If higher frequency tests are used the ability to control heating, fretting, lubrication conditions, and/or match the exact environment of the part or system being verified is difficult. Therefore, most lab wear testing is performed below 100Hz. This results in a test taking anywhere from approximately 11.5 days at 100 Hz to 58 days for 20 Hz tests in order to reach $10^8$ cycles. This makes understanding contact fatigue failures resulting from elastic high cycle to very high cycle contact fatigue mechanisms difficult to observe and understand.

A potentially better way to examine contact fatigue at high cycles of load is to expand on the work of Cogne et al. [7, 8], who argued that axial fatigue mechanisms can be correlated to contact fatigue problems. The mechanisms which control axial fatigue life in long life, elastic loading regimes also play significant roles in the elastic contact fatigue life, the major difference being the volume of material that experiences sufficient stress to nucleate and propagate a crack. The difference in stressed volume likely reduces the possible effect that large inclusions or other microstructural features can have on the fatigue life. Melander and Olund [9, 10] have recently shown the effect of titanium carbo-nitride, Ti(C,N), and aluminum oxide ((Al, O)) inclusions in both axial and rolling contact fatigue. They found that un-cracked Ti(C,N) inclusions are the most dangerous followed by cracked Ti(C,N) and then cracked aluminum oxides in affecting the fatigue life in both axial and rolling contact for all but the shortest cracks (~2 μm). The difference in potency was attributed to the high crack energy release rates associated with a crack for the alumina case and the sharp edge of the Ti(C,N) inclusion. By creating SAE 52100 bearing steels with increasing amounts of nitrogen, Melander and Olund showed that

the statistical median fatigue life between $10^6$ and $10^7$ cycles decreases dramatically with an increase in nitrogen from 58-118 ppm. The amount of fatigue failures with Ti(C,N) inclusions at the origin was found to increase with nitrogen content in line with the decreasing fatigue life.

There has been a significant increase in the use of ultrasonic loading techniques to test the axial fatigue properties of materials since Cogne's paper was written, [11]. Now there is a possibility to directly investigate microstructurally relevant mechanisms associated with axial very high cycle fatigue properties and attempt to relate them to elastic contact fatigue. The technique can be used to understand the elastic wear properties of high strength steels or hard thin films; or more importantly, steels coated with hard thin films, which are becoming more ubiquitous in engine and other power system applications. The effects of thin films on the fatigue properties of steels has been studied with results showing, increased, decreased, and equal fatigue lives in previous studies. One of the main reasons for the mixed results is that the stress levels for the fatigue testing varied, resulting in some tests measuring global plasticity-driven fatigue (low-cycle fatigue) to local plasticity-driven fatigue (high-cycle fatigue). The tests which resulted in failures in the low cycle regime tended to show increased fatigue strength with the addition of coatings [12, 13] while the failures in the high-cycle range generally showed no benefit [14]. No studies to date have been reported for the effect of thin films on the very high cycle fatigue properties of steels.

In this chapter, ultrasonic axial fatigue testing of a hardened SAE 52100 coated with an electroless nickel-phosphorus-polytetrafluoroethylene (Ni-PTFE) coating and hardened SAE 52100 with two different hydrogenated diamond-like-carbon (DLC) coatings will be studied. The chapter will focus on determining if hard thin films affect fatigue life at $10^8$ cycles and to determine the underlying mechanisms controlling fatigue failures in the very high cycle regime. Wear of DLC coated SAE 52100 steel and cast iron at very high wear cycles ($10^8$) using ultrasonic techniques will be studied in Chapter 4. A discussion on the effectiveness of using axial fatigue results for designing contact fatigue resistant surfaces will be presented in Chapter 5.

## 2.2 Experimental Methods

Barstock SAE 52100 was heat treated by normalizing for 3 hours at 900°C in air, austenitized for 3 hours at 840°C followed by an oil quench and tempering at 230°C for 3 hours to achieve a tempered martensitic microstructure with uniform carbides (<1μm diameter) and uniform hardness in the range of 58-60 HRC. The heat treated barstock was then machined into 34 samples per Figure 2.1 for ultrasonic testing. Eight additional samples were machined per ASTM E466 with a diameter of 12.7 mm, gage length of 15.24 mm, and gage diameter of 5.08 mm for traditional axial fatigue testing. All samples were then electropolished to promote better adhesion of the coatings. Three sets of samples were then coated. The first set consisted of heat treated and electropolished SAE 52100 coated with a bond layer of chromium nitride (CrN) to a thickness of 1-2μm with a top layer of a tungsten doped hydrogenated DLC (a-C:H:W) (DLC A) at a thickness of 3-4μm. The second also consisted of heat treated and electropolished SAE 52100 coated with a bond layer of chromium nitride (CrN) to a thickness of 1-2μm with a top layer of a tungsten doped hydrogenated DLC and DLC (a-C:H:W−a-C:H) (DLC B) at a thickness of 3-4μm. The last set of samples consisted of heat treated and electropolished SAE 52100 coated with a nickel-phosphorous polytetrafluoroethylene (Ni-PTFE) coating applied via an electroless plating process similar to that called for in AMS 2404. The Ni-PTFE coating was chosen as it is a versatile coating where the hardness of the nickel can be controlled by the amount of phosphorous present. In low phosphorous coatings the hardness can approach 60 HRC making for a wear resistant surface similar to hardened steel. The addition of PTFE particles in the electroless bath results in a homogeneous distribution of spherical PTFE particles throughout the final coating thickness. The particles act as a low friction tribolayer resulting in lower contact stresses due to lower friction. A schematic of the Ni-PTFE coating on SAE 52100 as well as a photomicrograph showing the coating on SAE 52100 are given in Figures 2.2a-b. A simplified ternary phase diagram for the $sp^2$ and $sp^3$ bonding and hydrogen system is shown in Figure 2.3a. The diagram shows the typical values of the bond types and hydrogen present in hydrogenated DLCs. Figure 2.3b gives a schematic of the bond layer and coating thicknesses with Figure 2.3c showing an example of a a-

C:H:W sample of heat treated SAE 52100 with a tempered martensitic microstructure.

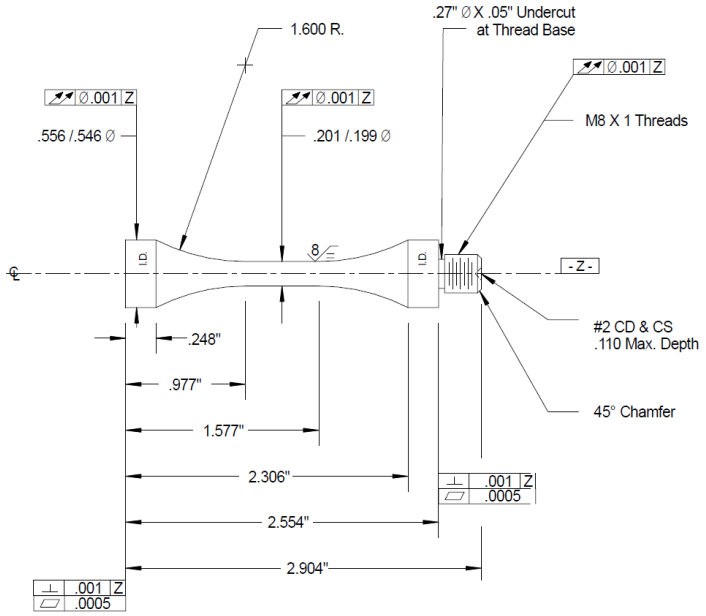


Figure 2.1 Ultrasonic fatigue sample engineering drawing.

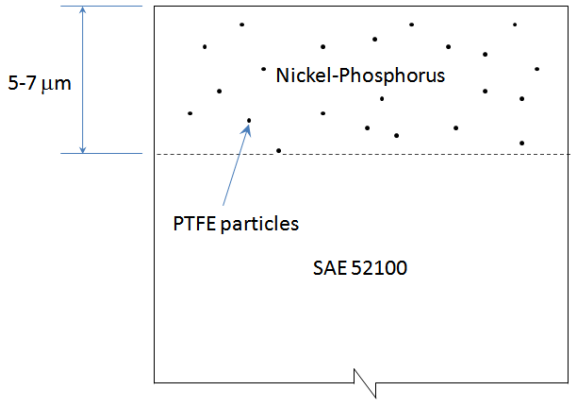


(a)

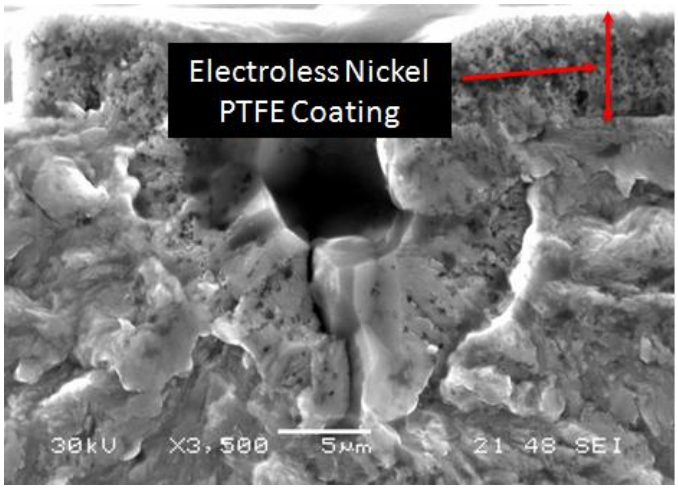


(b)

Figure 2.2 (a) Schematic of the Ni-PTFE coating on heat treated SAE 52100 steel. (b) Photomicrograph of the Ni-PTFE on a fractured SAE 52100 sample. The coating is shown following along the contour of a surface hole in the base steel

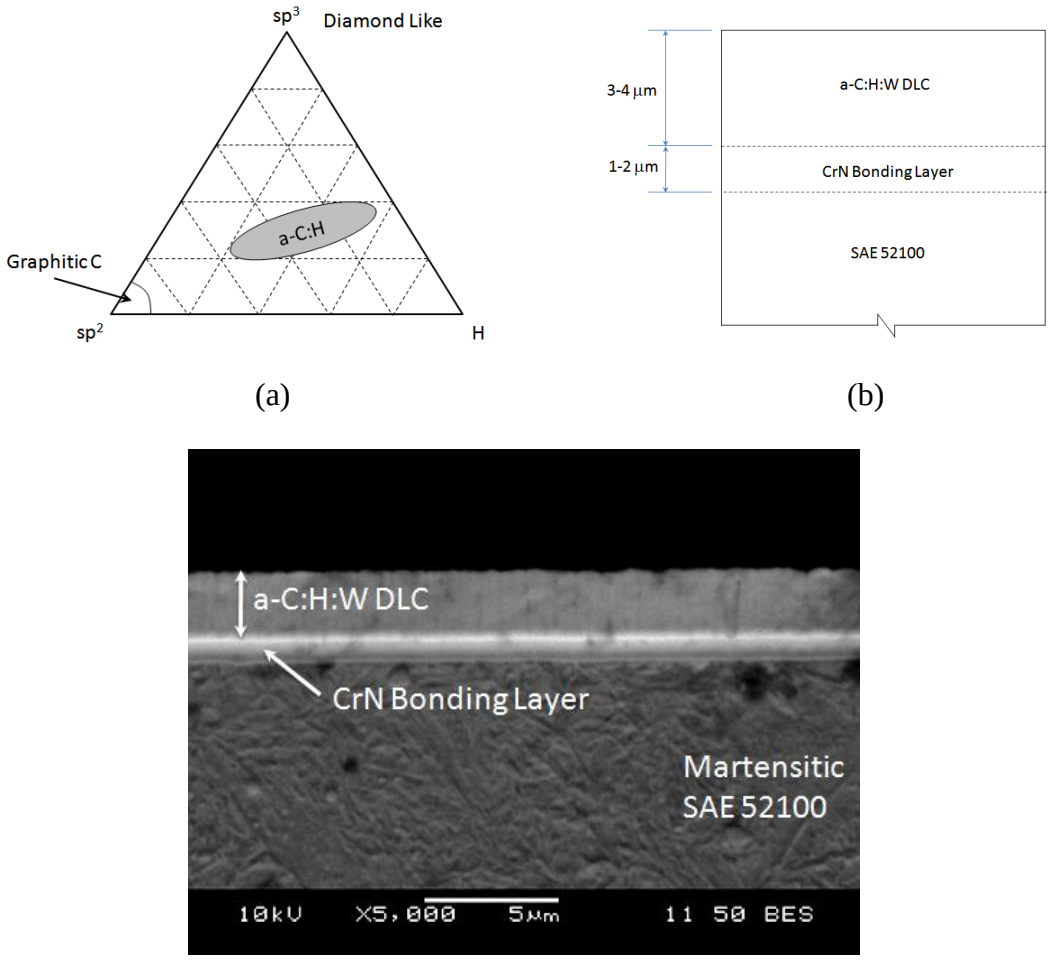


Figure 2.3 (a) Ternary phase diagram of the carbon sp2, sp3, hydrogen phase diagram showing the typical ratio of the bonds types and hydrogen in hydrogenated DLCs. (b) Schematic of the DLC coating and CrN bond layer on heat treated SAE 52100 steel. (c) Photomicrograph of the tempered martensitic microstructure of SAE 52100 coated with a CrN bonded a-C:H:W DLC.

Ultrasonic fatigue testing was performed using the ultrasonic fatigue test equipment shown in Figure 2.4. The eight samples prepared per ASTM E466 were tested using a servohydraulic MTS 810 load frame. For ultrasonic testing a piezoelectric ultrasonic transducer was used to generate the mechanical driving force from an electrical signal at 20 kHz. The large diameter end of an amplification horn was connected to the transducer and the small end had a lambda rod connected to it. The length of the lambda rod is equal to the wavelength corresponding to a frequency of 20 kHz. The other end of the lambda rod had one end of the specimen connected to it. The horn,

lambda-rods and the specimen are all designed so that these individual components are in resonance at a frequency close to 20 kHz. In turn, the assembled system is in resonance at 20 kHz with displacement antinodes at both ends of the specimen. An ultrasonic generator/controller provides frequency and displacement amplitude control during the fatigue test [15]. The ultrasonic test is displacement controlled. Figure 2.5 shows the general strain amplitudes along the sample length.

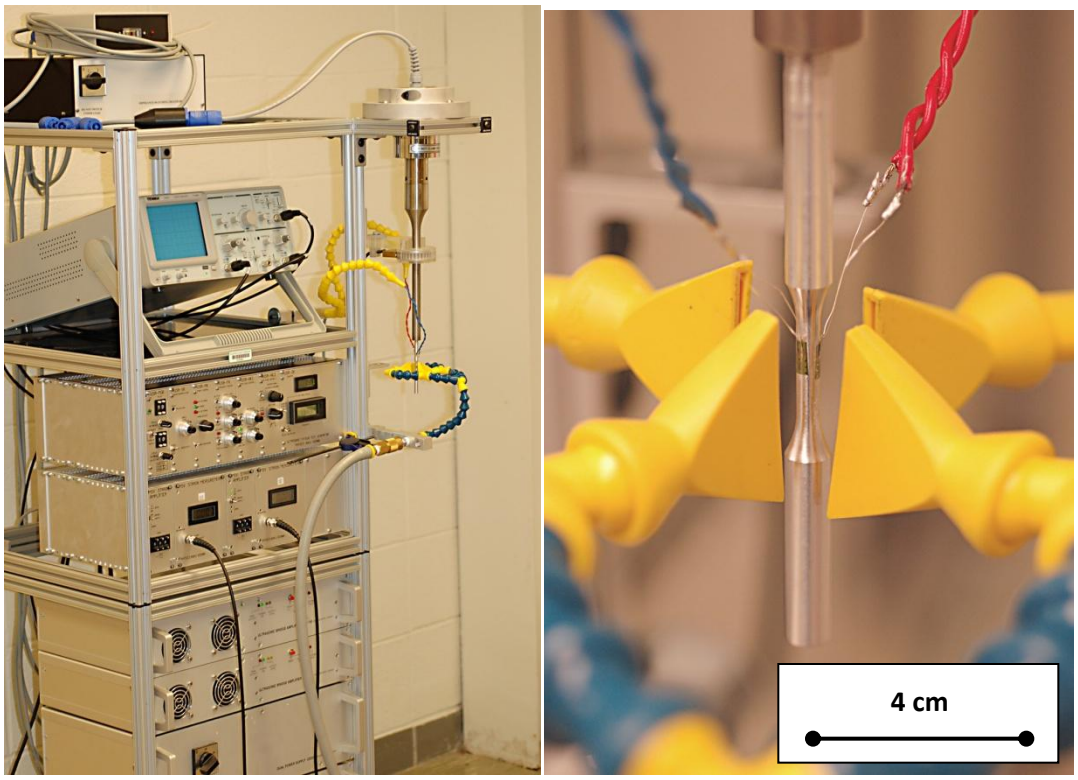


Figure 2.4 Ultrasonic fatigue equipment

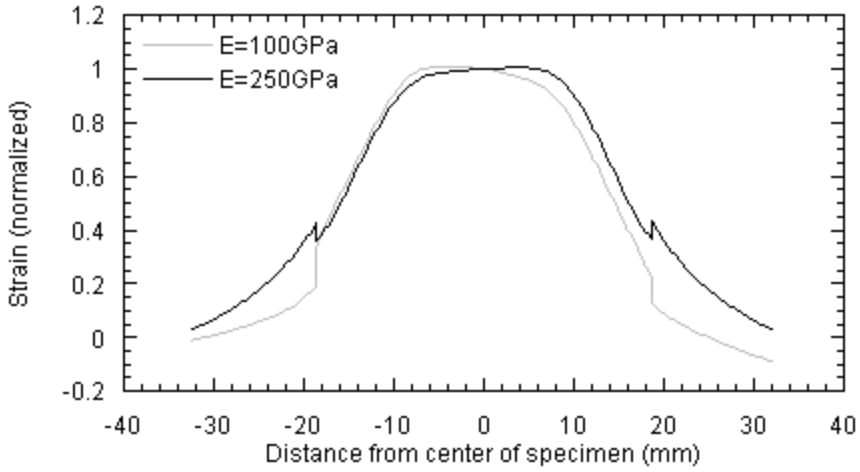


Figure 2.5 Normalized strain distribution along the ultrasonic sample [15]

Ultrasonic testing was carried out using a step fatigue testing method with a 50 MPa step and an R value of -1. If a sample failed before $10^8$ cycles, the stress was stepped down by 50 MPa for the next sample. If a sample survived, the stress was stepped up 50 MPa and a subsequent $10^8$ cycle ran at the new stress. This was repeated, if needed, at incrementally higher stresses until the sample eventually failed. If a sample did not fail, the retested sample was assumed to be a new sample for analysis in order to maximize the number of data points. Servohydraulic fatigue testing was carried out on an MTS 810 loadframe using load control at stresses of 1200-1400 MPa. All samples were loaded until failure at an R value of 0.01.

## 2.3 Results

## 2.4 Fatigue Testing

The complete results from the fatigue testing are shown in Figure 2.6. The data are categorized by the frequency at which each sample was tested as well as the stress ratio R. The graph can be modeled with a typical power law fatigue curve with decreasing curvature at lower maximum stress. Four data points tested at 20 kHz were found to lie significantly to the left of the mean fit line at 800 and 850 MPa.

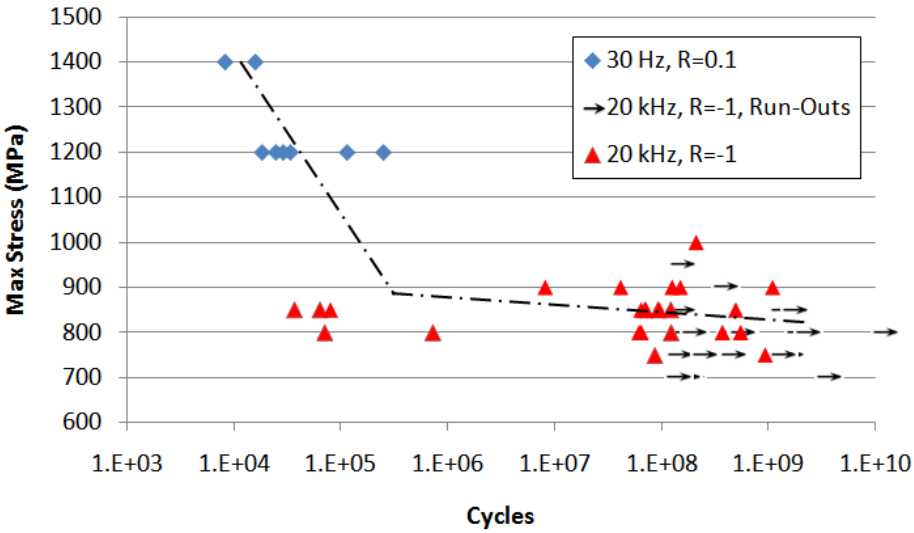


Figure 2.6 Fatigue data including run-outs (censored) data. The data are shown as a function of the frequency and stress ratio R. All ultrasonically tested samples were run at 20 kHz and R value of -1. The servohydraulically tested were all run at 30 Hz and an R ratio of 0.1

The location of the fatigue origins was analyzed using scanning electron microscopy to determine if the origin was "surface" indicating that the origin location was in the SAE 52100 steel with some part or all of the origin intersecting the steel surface. Subsurface origins were defined as origins where the inclusion at the origin was completely below the surface of the steel substrate (greater than half of the inclusion diameter from the surface). The locations of all fatigue origins for the ultrasonically loaded samples are depicted in Figure 2.7. Four origins intersected the steel surface and are thus shown as circles on the steel/coating interface. An example of a surface fatigue origin is shown in Figure 2.8a, b.

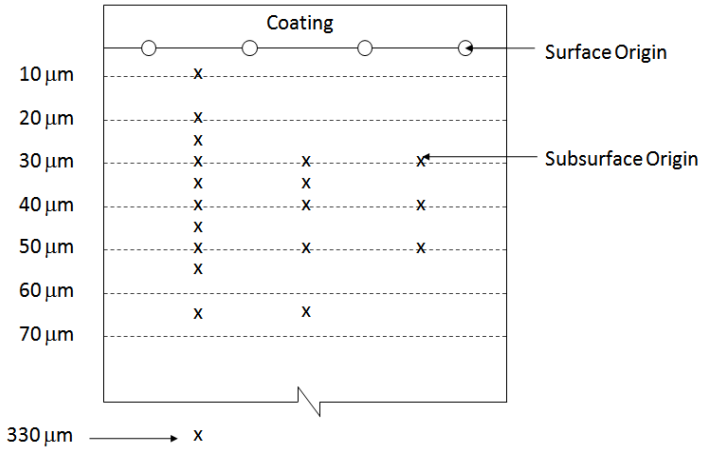


Figure 2.7 Map of the location of fatigue failures from ultrasonic loading. The 'x' represents failures at subsurface inclusions; the four circles indicate that the fatigue origin intersected the surface of the SAE 52100 and that the morphology of the origin was a hole with or without an inclusion present.

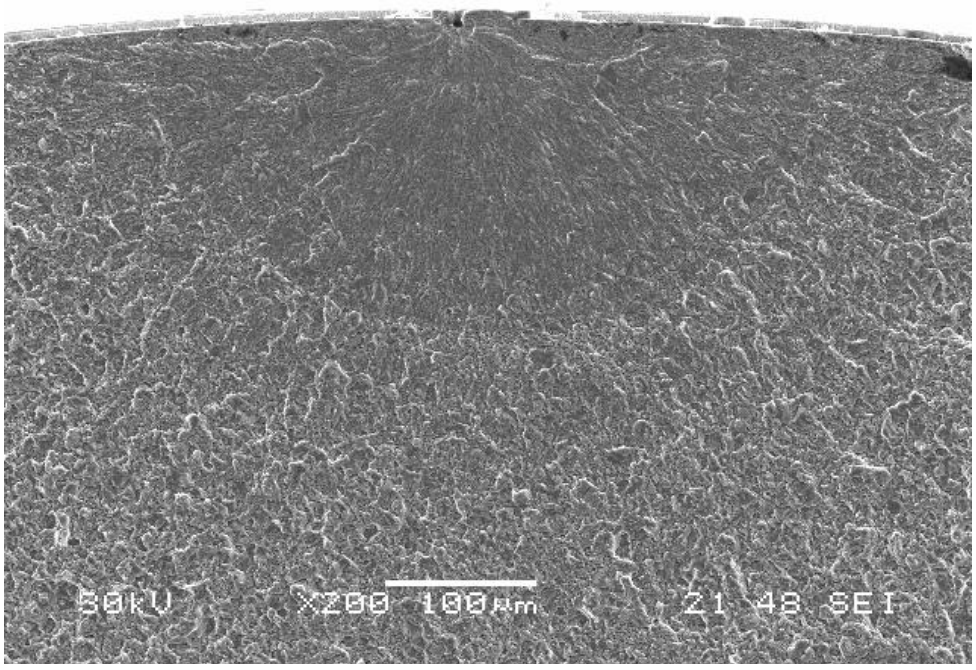


(a)

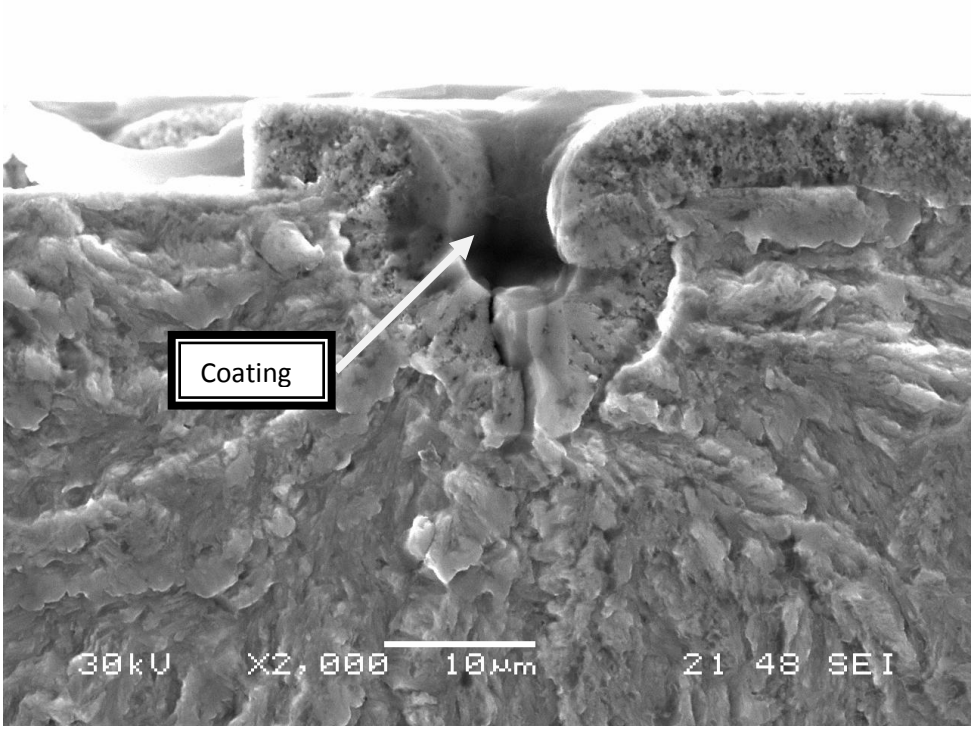


(b)

Figure 2.8 Surface fatigue origin in an electroless Ni-PTFE coated sample, (a) showing the origin and propagation zone, and (b) the coating in the surface hole, indicating that the hole was present prior to coating.

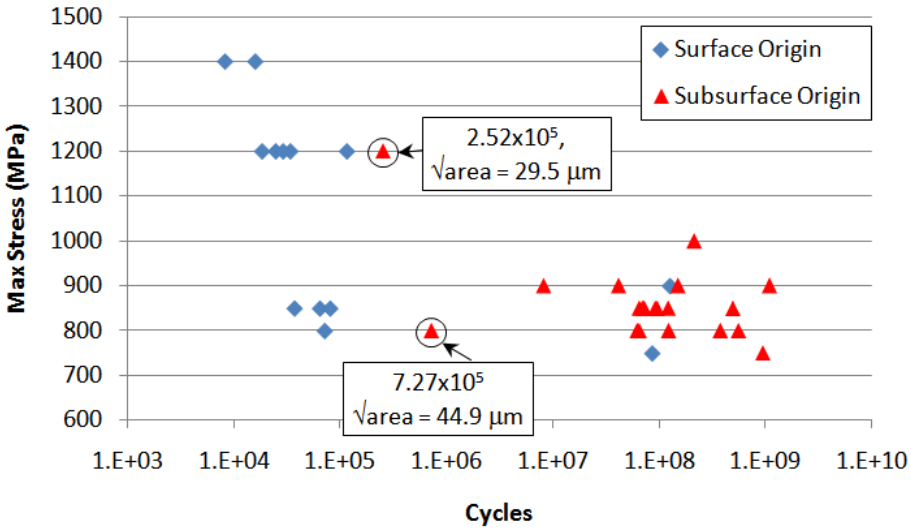


Figure 2.9 Fatigue data of failed samples by origin location. The three samples at 850 MPa and one sample at 800 MPa with short fatigue lives had surface origins. Two samples with short fatigue lives but subsurface origins were found to have the two largest inclusions at the fatigue origin of all of the samples.

A plot of the fatigue data from Figure 2.6 as a function or origin location is shown in Figure 2.9. The plot shows that the four outliers from Figure 2.6 were the samples with surface origins. Two other data points were also analyzed as they were had subsurface fatigue origins with the lowest fatigue lives of all samples failing from subsurface origins. The first data point was from a sample tested at 30 Hz and 1200 MPa. The inclusion had a projected square root area of 29.5 μm and was the only sample tested at 1200 or 1400 MPa which failed from a subsurface origin. The inclusion was the second largest observed at all of the subsurface fatigue origins. The second sample was tested at 20 kHz and 800 MPa. It failed at $7.27 \times 10^5$ with a projected square root area inclusion size of 44.9 μm. The inclusion was the largest observed at all of the subsurface fatigue origins. Both inclusions are shown in Figures 2.10a-c.

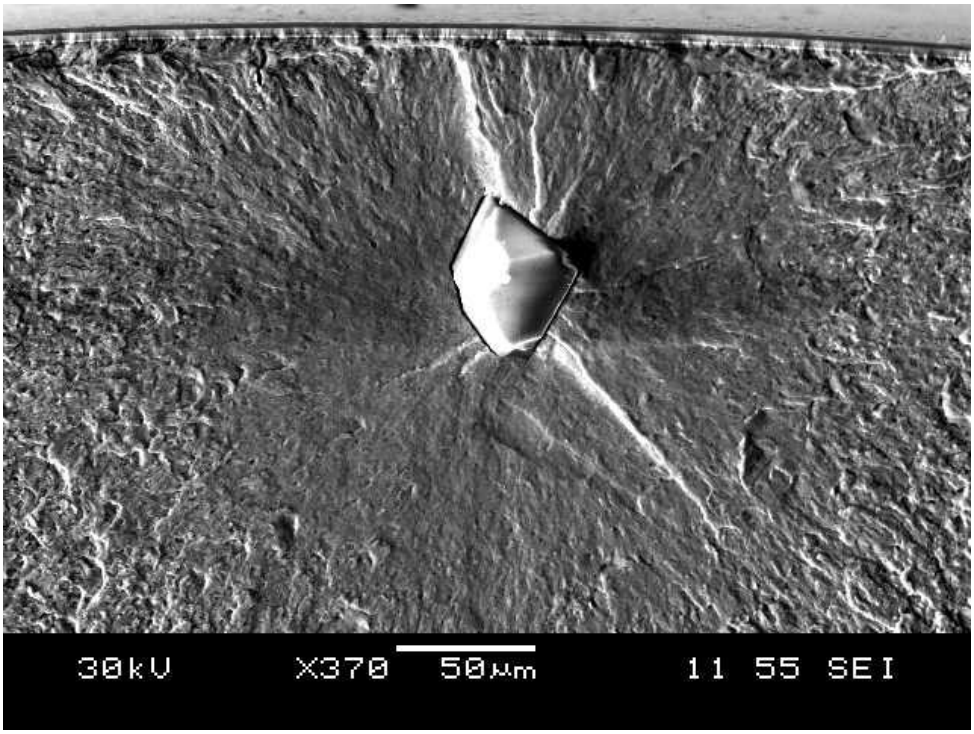


(a)

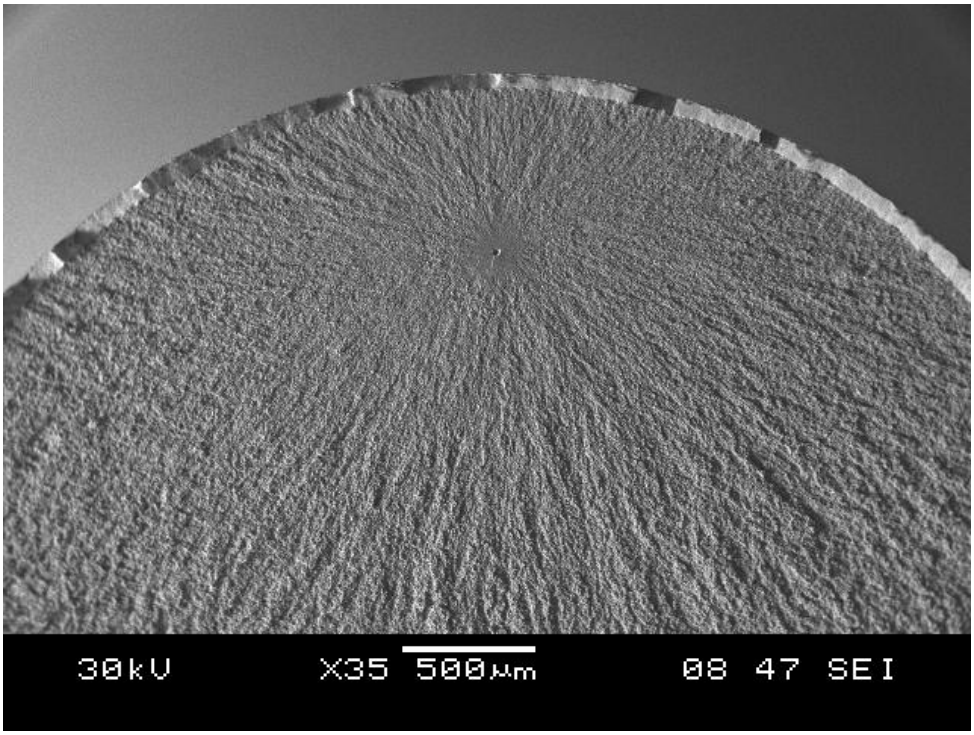


(b)

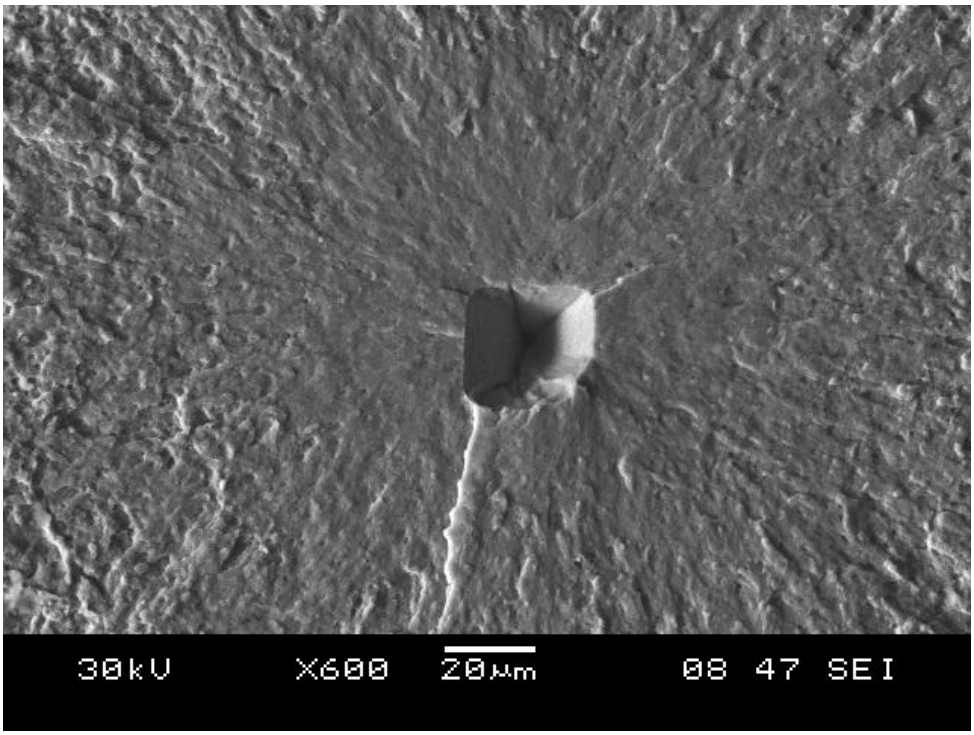


(c)

Figure 2.10 Scanning electron microscope photomicrograph of the largest inclusions found at a fatigue origin. (a) The inclusion was an aluminum oxide. The sample failed at 800 MPa and $7.27 \times 10^5$ cycles. (b, c) The inclusion was not found on either half of the fractured sample. The sample failed at 1200 MPa and $2.52 \times 10^5$ cycles.

A histogram of the square root area sizes of all inclusions is shown in Figure 2.11. The fit curve is a Weibull distribution. The median square root area was 11.8 μm with a left skew due to the outlying large inclusion sizes.

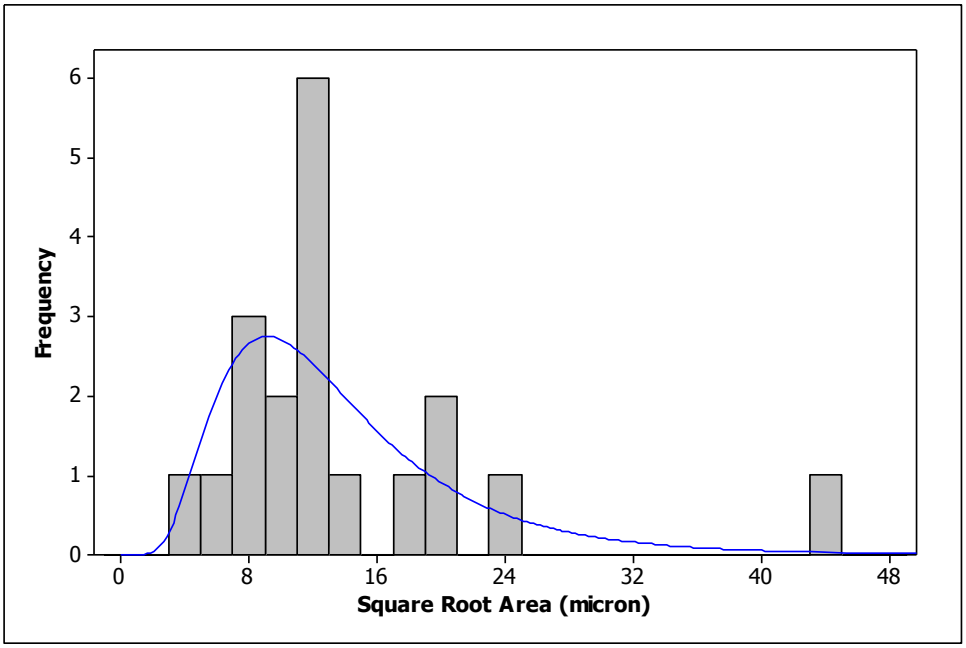


Figure 2.11 Histograms of the square root area size in μm of the inclusions present at the subsurface fatigue origins.

The inclusions were analyzed to determine if the type affected the fatigue life. Each inclusion was analyzed using energy dispersive spectroscopy (EDS). Two different inclusion types were observed. The first was an aluminum oxide containing magnesium and calcium (Al, O); the EDS spectrum is given in Figure 2.12a. The second inclusion was a metallic carbonitride inclusion that primarily contained titanium as a nitride former, but also contained the nitride forming elements chromium and niobium [Ti(C,N)]. The EDS spectrum is given in Figure 2.12b. Examples of the each inclusion type on the fracture surface of failed fatigue samples are given in Figures 2.13 through 2.16.

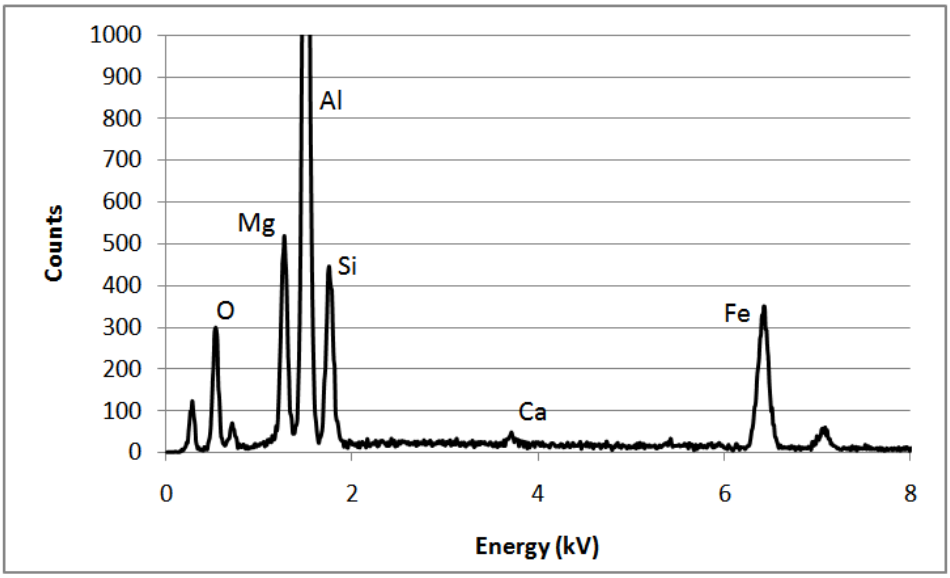


(a)

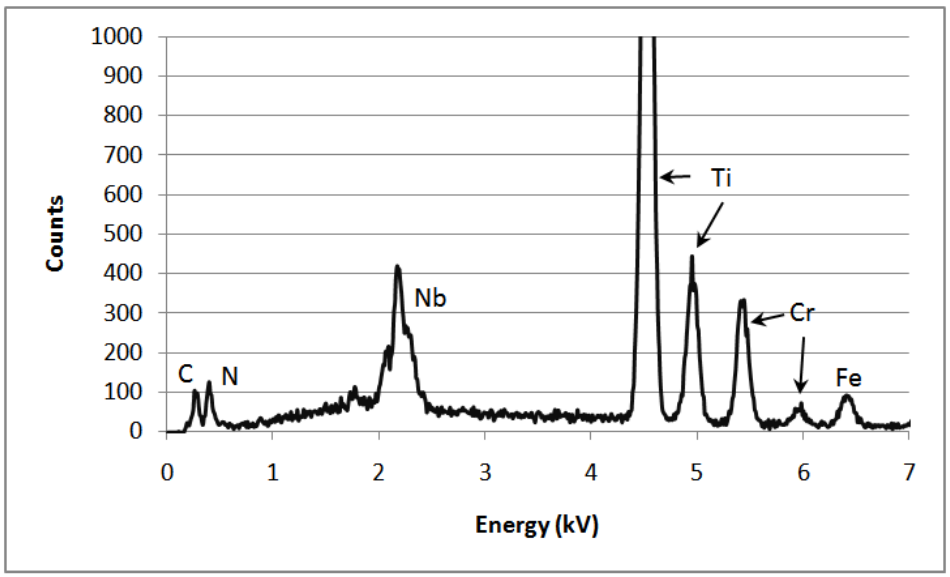


(b)

Figure 2.12 (a) Energy dispersive spectrometry (EDS) results for the typical oxide inclusion found at the fatigue origins of many of the failed samples, (b) EDS spectra for the typical Ti(C,N) inclusion.

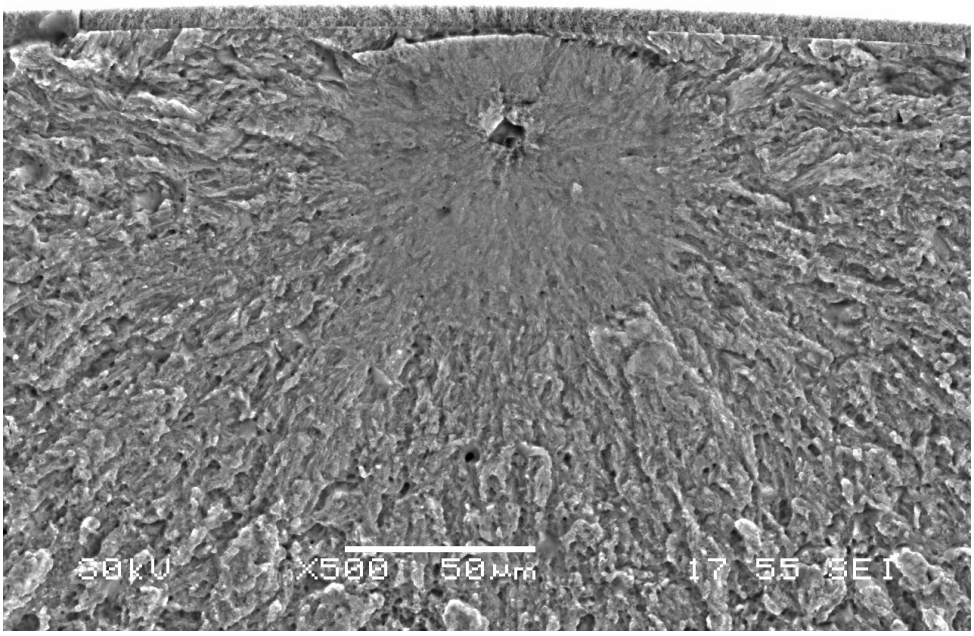


(a)

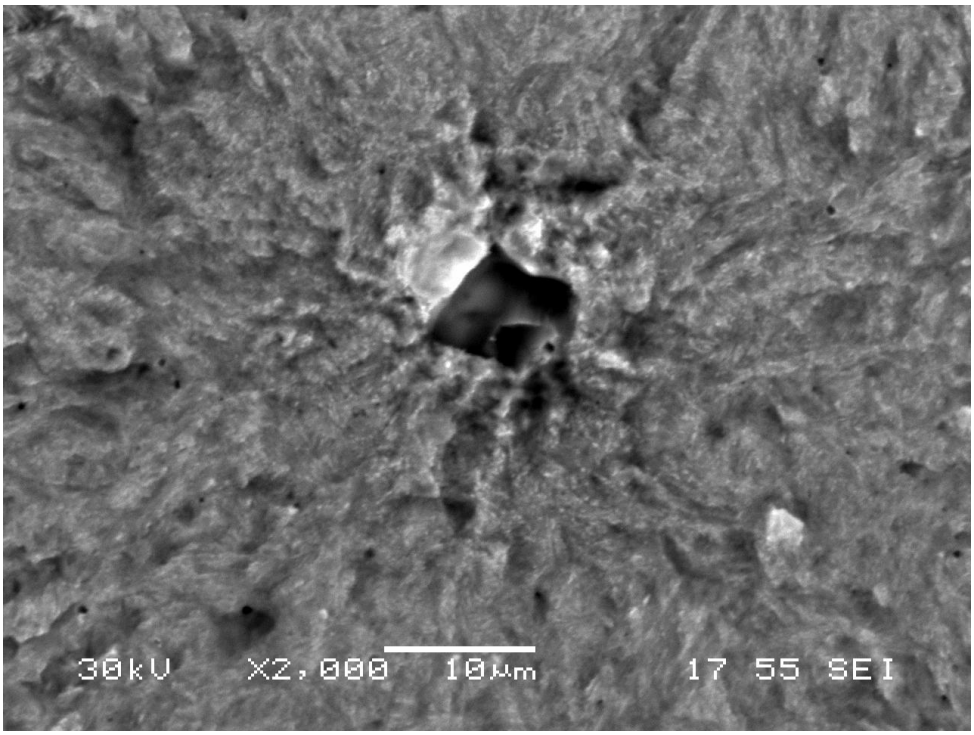


(b)

Figure 2.13 (a, b) Scanning electron microscope photomicrographs of the a Ti(C,N) inclusion at the fatigue origin area of a Ni-PTFE coated sample. The sample failed at a stress of 850 MPa and $9.28 \times 10^7$ cycles.

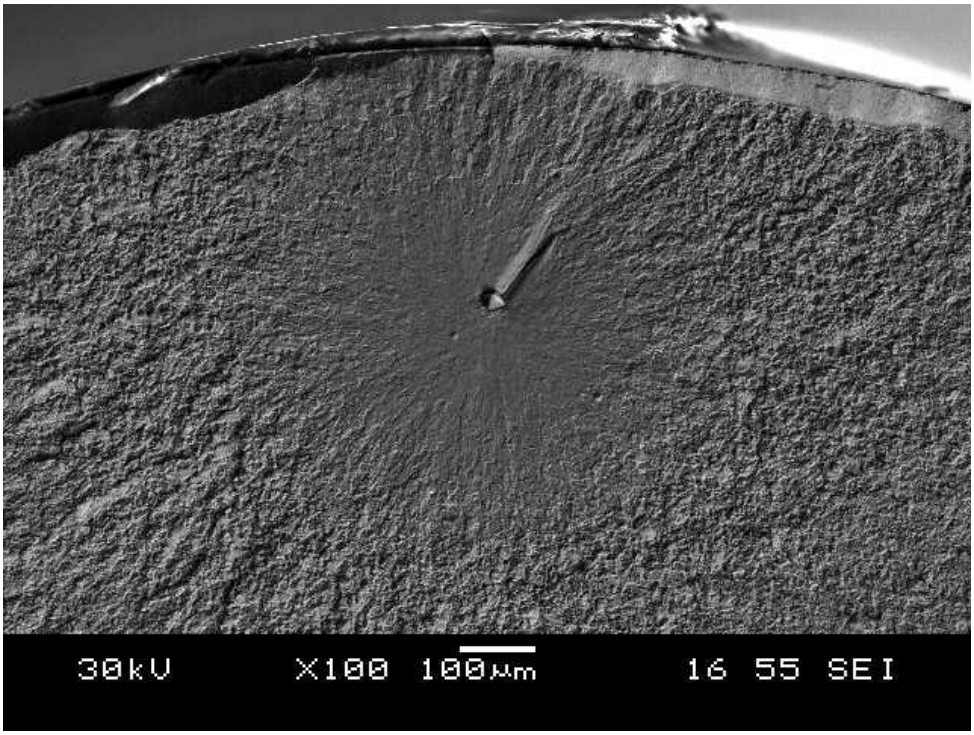


(a)

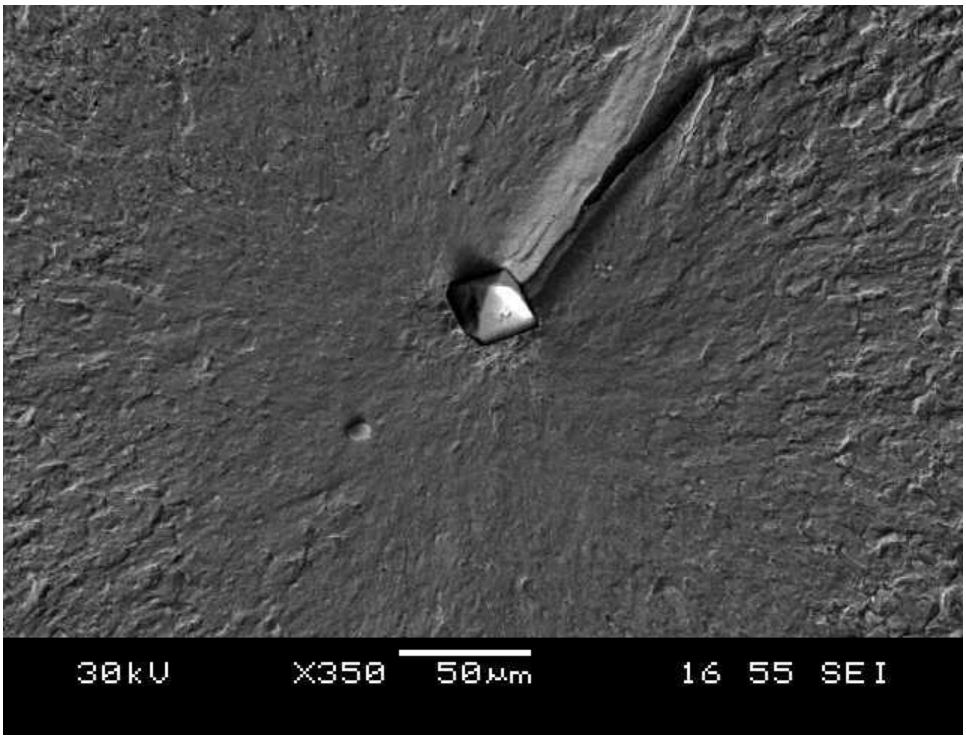


(b)

Figure 2.14 (a, b) Scanning electron microscope photomicrographs of an (Al, O) inclusion at the fatigue origin area of a DLC A coated sample. The sample failed at a stress of 850 MPa and $1.22 \times 10^8$ cycles.

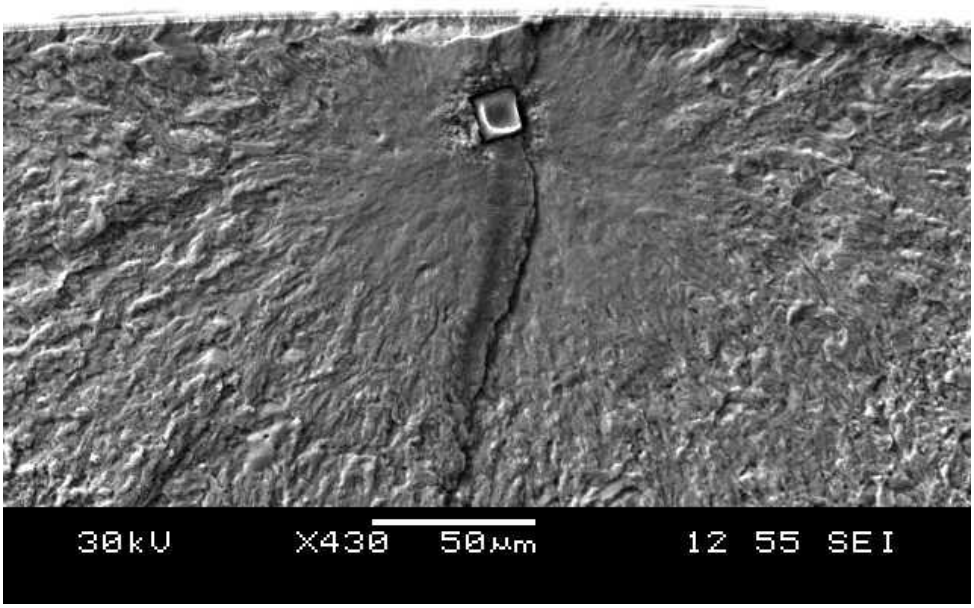


(a)

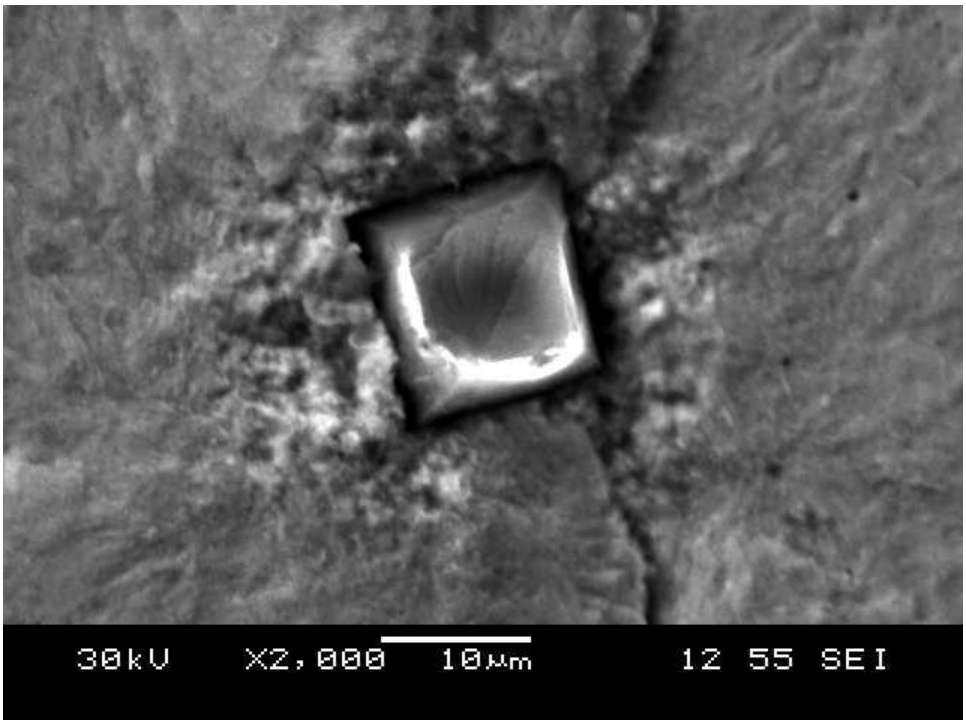


(b)

Figure 2.15 (a, b) Scanning electron microscope photomicrographs of an (Al, O) inclusion at the fatigue origin area of a DLC A coated sample. The sample failed at a stress of 850 MPa and $7.26 \times 10^7$ cycles.

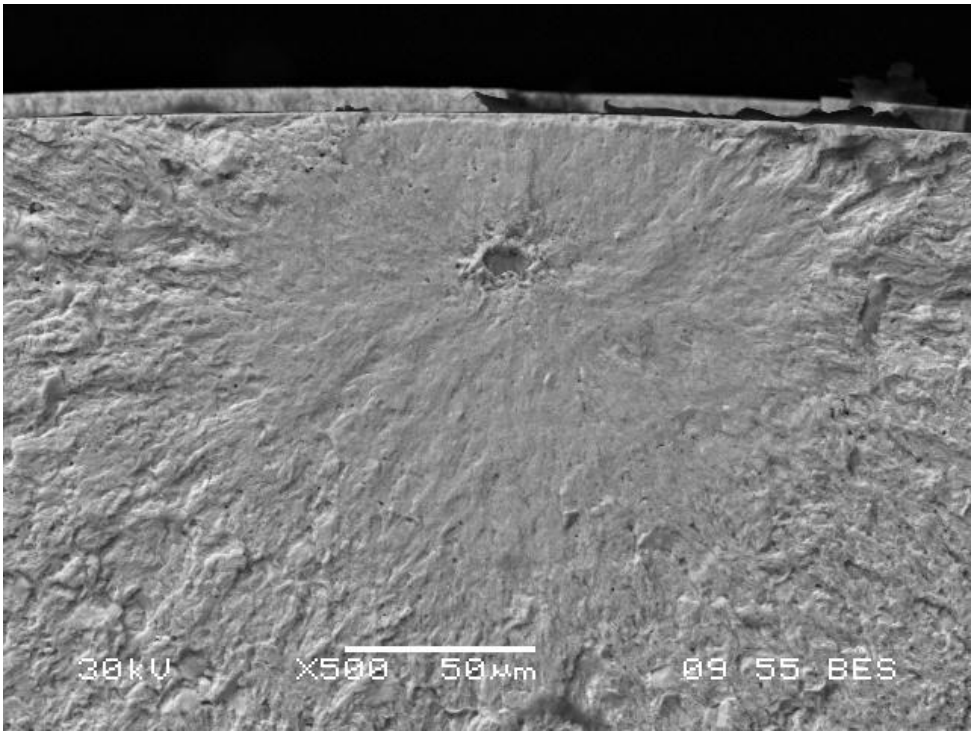


(a)

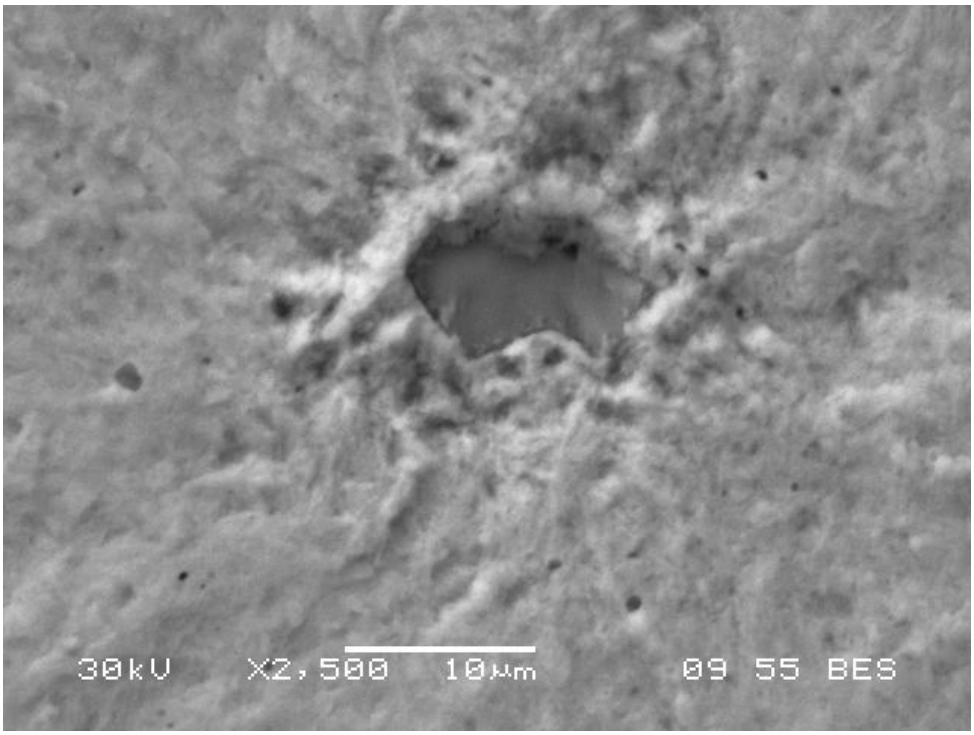


(b)

Figure 2.16 (a, b) Scanning electron microscope photomicrographs of the a Ti(C,N) inclusion at the fatigue origin area of a Ni-PTFE coated sample. The sample failed at 850 MPa and $5.01 \times 10^8$ cycles.

The histogram shown in Figure 2.11 was then replotted as separate histograms for each inclusion type (Figure 2.17). The median square root area for the Ti(C,N) inclusions was 7.6 μm versus 11.4 μm for the (Al, O) inclusions. The variance of the Ti(C,N) inclusions was also significantly lower than that of the (Al, O) inclusions.

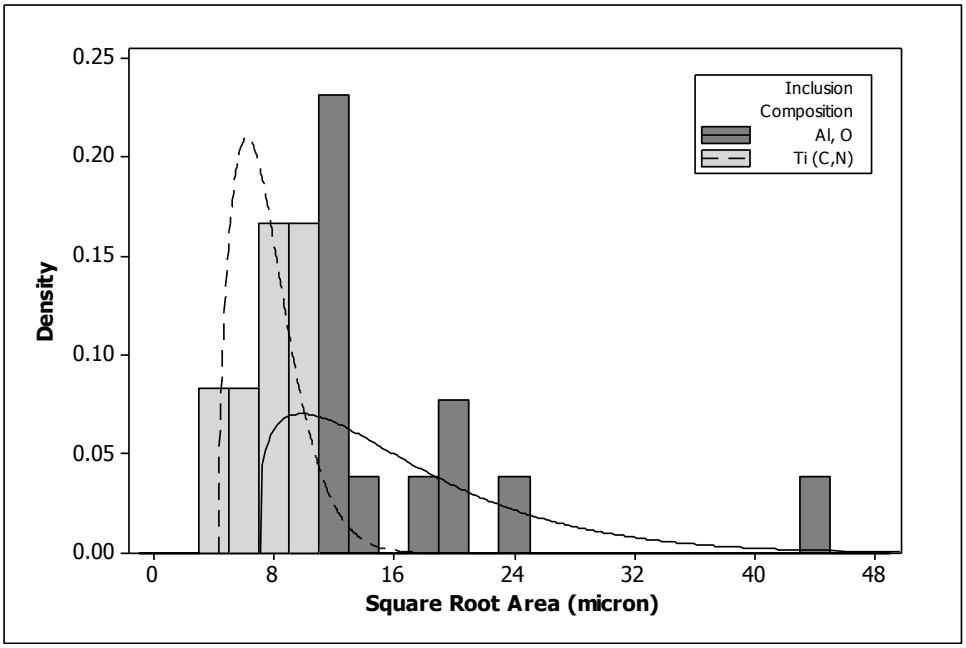


Figure 2.17 Histograms of the square root area size in μm of the different inclusion types. The median size and variance of the Ti(C,N) inclusions is significantly smaller than that of the oxide inclusions.

No significant difference in fatigue life was observed between the inclusion types even though the Ti(C,N) inclusions are considerably smaller. The fatigue data from Figure 2.6 were plotted in Figure 2.18 with only the samples with subsurface origins and inclusions present shown. The data are separated by inclusion type. Therefore, there is likely another mechanism working to increase the stress intensity, or local stress, at the smaller Ti(C,N) inclusions to be similar in magnitude to the larger (Al, O) inclusions.

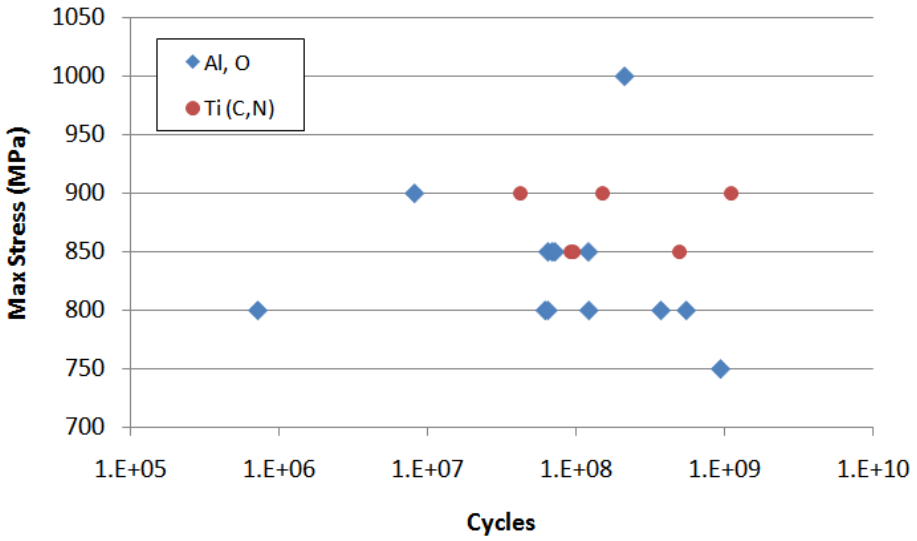


Figure 2.18 Fatigue data from Figure 2.6 with only the samples with subsurface fatigue origins and inclusions present shown. The data are separated by inclusion type. No significant difference is fatigue life was found.

### 2.4.1 Fracture Mechanics Analysis

The finding that the fatigue origin location is significant in Figure 2.9 is not unusual as the stress intensity for surface origins at inclusions, holes, or other defects is higher for these origins than for subsurface origins of the same size [1-3]: the stress intensity factor being approximately 30% larger [17].

#### 2.4.1.1 Fracture Mechanics Analysis of Failed Samples with Subsurface Fatigue Origins

To analyze the differences in inclusion types and the effect on fatigue life, the size of each inclusion was measured and the stress intensity was calculated using Murakami's method, which assumes that the inclusion behaves as a preexisting crack [17-20]. The square root area in equation 2.2 was determined by measuring the projected surface area directly using a scanning electron microscope and measurement software.

$$\Delta K = 0.5\Delta\sigma\sqrt{\pi\sqrt{area}} \qquad (2.2)$$

The stress intensity values by sample and inclusion type are given in Table 2.1. A 2t hypothesis test was run on the resulting stress intensity values. If the fatigue lives of

the samples with (Al, O) or Ti(C,N) inclusions had similar fatigues lives at a given stress level, then their stress intensities should also be similar, based on Murakami's method shown in equation 2.2. Murakami based the stress intensity value of subsurface defects, such as inclusions, on the projected square root area of the defect and the global stress. Based on the results of the 2t tests; and following Murakami's analysis, the Ti(C,N) inclusions are predicted to have a significantly (p-value = 0.003) lower mean stress intensity than the oxide inclusions: 2.11 MPa*$m^{1/2}$ for the Ti(C,N) inclusions versus 2.95 MPa*$m^{1/2}$ for the oxide inclusions. This suggests that inclusion type must be considered a key variable for modeling the fatigue behavior in addition to stress, projected fatigue origin size and fatigue origin location.

In addition to the stress intensity values at the inclusions, the stress intensity values at what are known as the fine granular area (FGA) and fish-eye were calculated. FGA is a term used to describe an area of subcritical crack growth around an internal inclusion. FGA formation is theorized to be a result of polygonization followed by micro-debonding initiation and coalescence [21], or due to hydrogen embrittlement [17], or a separation of boundaries between carbide particles and the matrix [22]. However, there is no consensus on this. The fish-eye represents the smooth crack propagation region which includes the inclusion, FGA, and the smooth propagation zone up to overload fracture. Figure 2.19 shows a cross-section (top view) and plane (side) view of the inclusion origin which depicts the FGA. Figure 2.20 shows an example of an FGA (rough area around the inclusion) and fish-eye in a failed sample. The stress intensity values for each are calculated using equation 2.2 where the projected square root area size of the FGA and fish-eye, including the area of the inclusion, are used. The stress intensity values at of the FGAs and fish-eyes for each sample that failed at subsurface inclusions are also given in Table 2.1.

The mean value of the fine granular area (FGA) and fish-eye stress intensity values by inclusion type were calculated and are given in Table 2.2 along with p-values for 2t tests between the inclusion types. The average stress intensities of 2.95 MPa$*m^{1/2}$ for the oxide inclusions and 2.11 MPa$*m^{1/2}$ for the Ti(C,N) inclusions were below the mean values of the threshold stress intensity values given in [15, 21-24] of 4-6

$MPa*m^{1/2}$ for the heat treated steel. The presence of FGAs is consistent with crack propagation below $\Delta K_{th}$. The average stress intensity factors of the FGAs was 3.7 $MPa*m^{1/2}$ for the oxide inclusions and 3.3 $MPa*m^{1/2}$ for the Ti(C,N) inclusions which are in the range found in [15, 21-24]. The average stress intensity factor of the fish-eye/overload interface was 8.3 $MPa*m^{1/2}$ for the oxide inclusions and 7.8 $MPa*m^{1/2}$ for the Ti(C,N) inclusions which are close to that found in [16] but for stress ratios closer to 0.1 than -1 which was primarily used in this study. Hypothesis testing was carried out on the stress intensity data for FGAs, and fish-eye/overload interfaces to determine if the inclusion type at the fatigue origin resulted in stress intensities above those predicted by others using only the FGA and fish-eye size. Results of these analyses are given in Table 2.2. The probability value (p-value = 0.003) is less than 0.05 for a standard 2t test, indicating that the population mean stress intensity at the FGA is possibly also controlled by the inclusion type assuming a normal variance of the stress intensity at the inclusion. This is consistent with the hypothesis that the same mechanism which increases the stress intensity values around the Ti(C,N) inclusion is still active multiple inclusion diameters away from the inclusion boundary.

Finally, the inclusion type was found to have no significance on the stress intensity values of the fish-eye/overload interfaces (p-value = 0.229). The independence of stress intensity value at the fish-eye/overload interfaces suggests that the mechanism which increases the stress intensity values around the Ti(C,N) inclusion and FGA is exhausted at significant distances away from the inclusion and FGA.

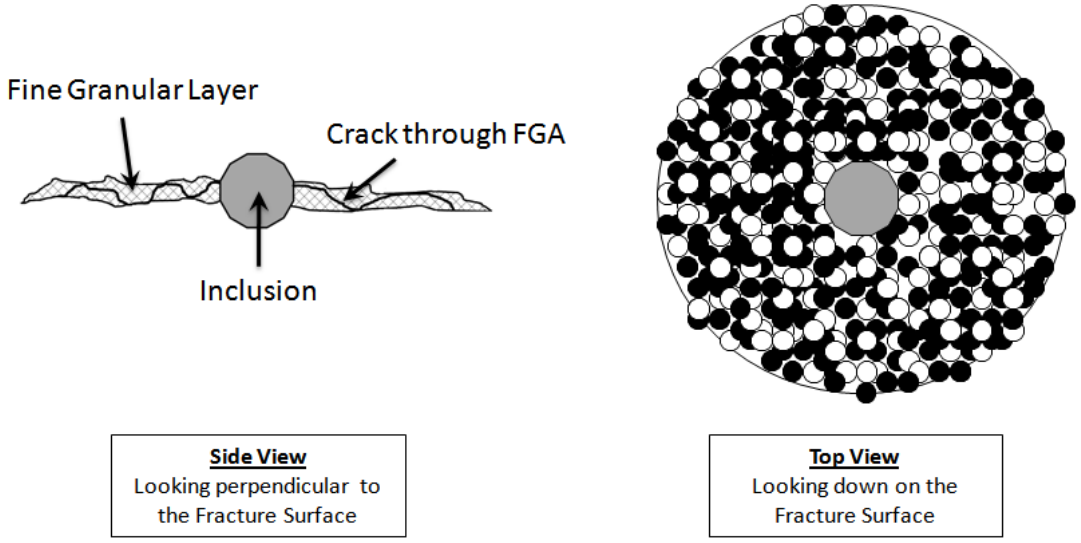


Figure 2.19 Schematic of the fine granular area (FGA) after complete crack formation. The FGA thickness is on the order of 400 nm [16]. The black and white circles on the top view represent microdebonding in the FGA.

Table 2.1 Inclusion composition and stress intensity by coating type with stress intensity value adjusted for inclusion type (only the Ti(C,N) values changed by definition).

| Coating Type | Inclusion Composition | $\Delta K_{Inclu}$ (MPa*m$^{1/2}$) | $\Delta K_{FGA}$ (MPa*m$^{1/2}$) | $\Delta K_{Fish}$ (MPa*m$^{1/2}$) |
|---|---|---|---|---|
| DLC 41 | (Al, O) | 3.1 | 3.5 | 7.2 |
| DLC 41 | (Al, O) | 2.4 | 3.7 | 7.7 |
| DLC 41 | (Al, O) | 3.2 | 3.5 | 7.9 |
| DLC 41 | (Al, O) | 3 | 3.4 | 7.5 |
| DLC 41 | (Al, O) | 3.7 | no FGA | 9.9 |
| DLC 40 | (Al, O) | 2.4 | 4.1 | 7.5 |
| DLC 40 | Ti(C,N) | 2.4 | 3.4 | 7.4 |
| DLC 41 | (Al, O) | 2.5 | 3.7 | 8.4 |
| DLC 41 | (Al, O) | 2 | 3.9 | 7.3 |
| DLC 40 | (Al, O) | 2.4 | 3.5 | 7.6 |
| DLC 40 | (Al, O) | 2.6 | 3.7 | 8.2 |
| DLC 40 | (Al, O) | 2.6 | 4.0 | 9.1 |
| DLC 40 | (Al, O) | 4.8 | 4.4 | 11.7 |
| Ni-PTFE | Ti(C,N) | 2.2 | 3.3 | 8.0 |
| Ni-PTFE | (Al, O) | 2.4 | 3.3 | 7.8 |
| Ni-PTFE | Ti(C,N) | 1.7 | 3.4 | 7.6 |
| Ni-PTFE | Ti(C,N) | 2 | 3.3 | 7.1 |
| Ni-PTFE | Ti(C,N) | 2.6 | 3.3 | 8.5 |
| NT-07 | Ti(C,N) | 1.8 | 3.4 | 8.1 |

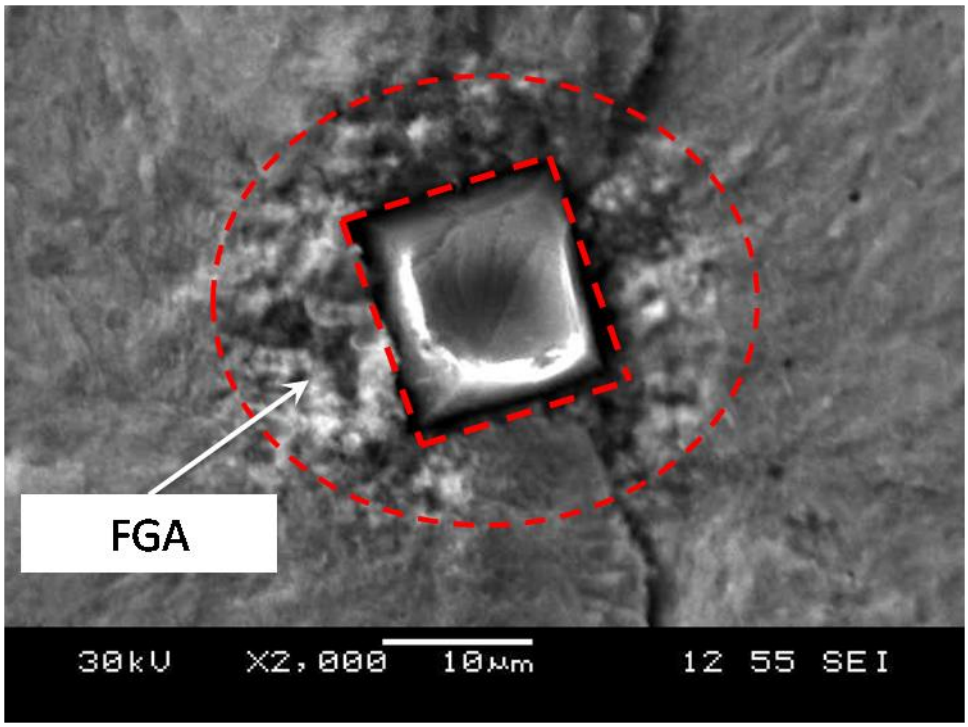


(a)

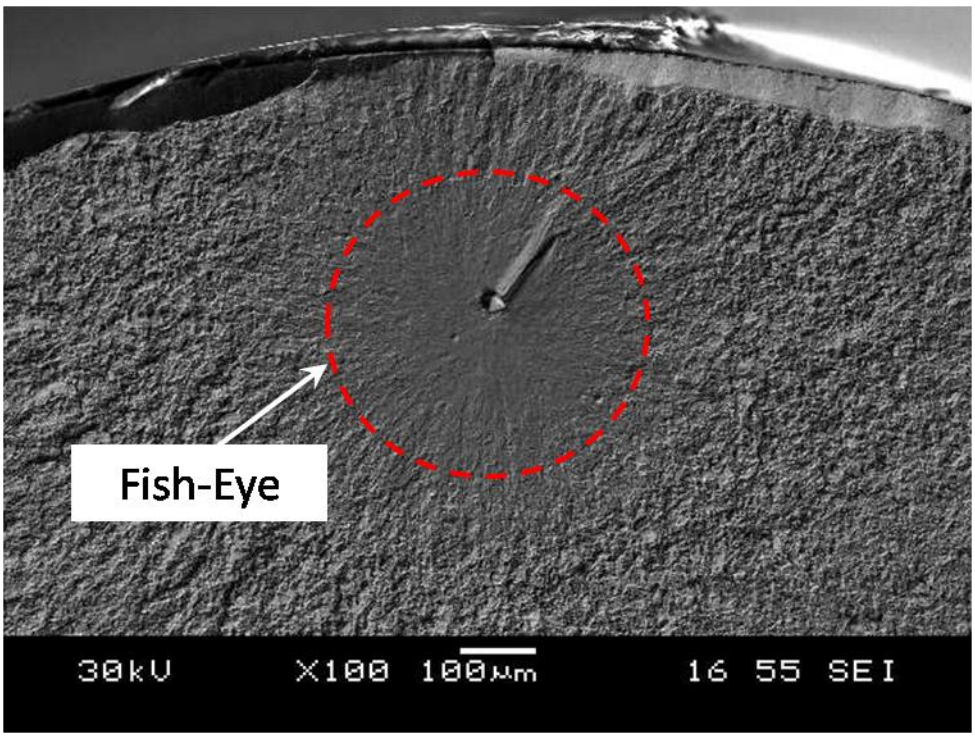


Figure 2.20 Example of a (a) FGA (area between the two red dashed lines and (b) fish-eye.

Using the model of Paris et al. [25, 26] based on the Paris-Hertzburg law and the work of Hertzburg [27] on crack propagation in monolithic metal alloys, the stress intensity threshold for crack growth within the fish eye was theoretically calculated as equation 2.3.

$$\frac{\Delta K_{eff}}{E\sqrt{b}} = 1 \qquad (2.3)$$

Here it is assumed, as Paris et al. did, that the crack is initially at size $a_o$ with no crack closure, corresponding to equation 2.3 and growing from an initial defect equal to the radius of the inclusion. Using equation 2.3, assuming a Burgers vector (b in equation 2.1) magnitude of approximately 0.3 nm, and an elastic modulus of the SAE 52100 steel of 210 GPa, the stress intensity would be equal to about 3.6 MPa√m which is very close to the mean stress intensity values calculated at the FGA boundaries for both inclusion types. Since the yield point in a single grain is nominally equal to the stress needed to irreversibly move a dislocation it is also not surprising that Hertzburg's [27] crack threshold equation 2.3 for closure free crack extension fits to the failure data well.

Based on the results discussed thus far, stress, inclusion type, and fatigue origin location are significant factors controlling the fatigue life of the coated steel. None of the three coatings on the SAE 52100 substrates were found to affect fatigue life. All samples with subsurface fatigue origins had FGAs associated with them, except one sample which had a large oxide inclusion with a calculated stress intensity above the threshold defined by equation 2.3 for long crack growth. Fish-eyes were observed for all subsurface fatigue origins. The inclusion type had a significant effect on the stress intensities at the inclusion and FGA boundaries. The stress intensity for stress and inclusion size alone, equation 2.2, doesn't completely describe the stress intensity at the Ti(C,N) inclusions and FGAs around these inclusions. A mechanism associated with the inclusion type that increases the stress intensity above that determined by stress and inclusion size alone is therefore likely active.

Table 2.2 Inclusion composition and stress intensity by coating type with stress

| Inclusion Composition | Mean $\Delta K_{FGA}$ (MPa*$m^{1/2}$) | Mean $\Delta K_{Fish}$ (MPa*$m^{1/2}$) |
|---|---|---|
| (Al, O) | 3.71 | 8.29 |
| Ti(C,N) | 3.34 | 7.77 |
| | | |
| p-value | 0.003 | 0.229 |

#### 2.4.1.2 Accounting for the Inclusion Type Difference in the Stress Intensity Values

To better understand how differences in inclusion types and size affect the fatigue strength, the number of cycles to failure were plotted as a function of the stress intensity for the (Al, O) and Ti(C,N) inclusions separately. It can be seen that the Ti(C,N) inclusions result in failures in approximately the same number of cycles but at lower ΔK values than that of the oxide inclusions (Figure 2.21) based on the Murakami analysis. Statistically, the difference is not as pronounced (p-value = 0.256) as it is visually. This is most likely due to the large variation in inclusion sizes and thus stress intensity for the (Al, O) inclusions, and secondly due to the small number of samples found with Ti(C,N) inclusions. A large variation in oxide inclusion size was also seen in previous work [9].

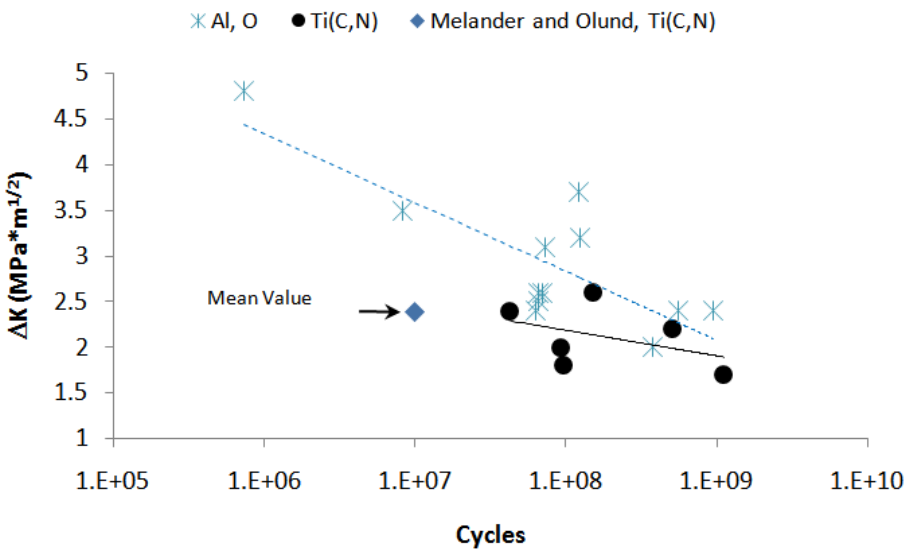


Figure 2.21 The stress intensity at the inclusion before crack propagation versus the number of cycles. The Ti(C,N) inclusion failed at lower stress intensity at a given number of cycles than did the oxide inclusions. The mean value for the Ti(C,N) from [9] is also shown. The size distribution of the Ti(C,N) from [9] was symmetrical about the mean, with the majority of Ti(C,N) inclusions having a size of ~9 μm.

To deal with the difference, the use of the Irwin energy model for crack growth under the assumption of plane strain is proposed. The crack energy release rate G for plane strain conditions is given as:

$$G = (1 - v^2)\, K^2/E$$

and

$$K = \sigma_Y(\pi a)^{1/2}$$

*K* represents the short crack fatigue growth threshold stress intensity factor. Combined, these equations result in the following equation if the crack length is taken to be equivalent to the square root area of the higher energy release rate inclusion:

$$\sqrt{area}_{Type} = \frac{EG}{\pi\sigma_Y^2(1 - v^2)} \qquad (2.4)$$

In this study, G (N/m) is defined as the difference in the crack energy release rate between a typical aluminum oxide inclusion and a Ti(C,N) inclusion [9]. In this case,

the square root area is associated with the inclusion type, and not with its size as it is in equation 2.2. Assuming the elastic modulus is 210 GPa, a yield strength of 1000 MPa, and Poisson's ratio of 0.3, the square root area associated with the inclusion type can be calculated at various stress levels for the coated SAE 52100 samples. To simplify the analysis, G is assumed to be constant at 0.075 N/mm as given in [9] regardless of the inclusion size. Since the inclusion sizes do not vary much for the Ti(C,N) inclusions and the difference in the energy release rate assuming elastic or elastoplastic is approximately constant for crack sizes of around 0.005 mm or greater [9], this should be a safe assumption. Melander and Olund found that Ti(C,N) can have a higher driving force for crack growth even above aluminum oxides inclusions so long as the oxide inclusion is not cracked. None of the oxide inclusions at fatigue origins were found cracked in this study, which suggests that the Ti(C,N) inclusions are likely to be more potent.

It is proposed that this square area be added to that given by Murakami in equation 2.2 resulting in the following generalized formula.

$$\Delta K = 0.5\Delta\sigma\sqrt{\pi\left(\sqrt{area}_{Size} + \sqrt{area}_{Type}\right)} \qquad (2.5)$$

Equation 2.5 can now be used to reanalyze the results in Figure 2.21 which graphically depict the difference in the stress intensity between the oxide and Ti(C,N) inclusions. The modified stress intensities are given in Table 2.3 and shown plotted against those for the aluminum oxide inclusions in Figure 2.22. The stress intensities now better overlap, unlike in the unmodified results in Figure 2.21.

If use is made of the equivalence formula between crack energy release rate and mode I stress intensity, it is found that the square root area is approximately equal to the plastic zone radius and/or critical crack length defined by Tanaka et al. [33] for short cracks. This is the same parameter (intrinsic crack length) used by El Haddad, Topper, and Smith [34].

$$G = (1 - v^2)\, K^2/E$$

$$G = (1 - v^2)\, K^2/E \qquad (2.6)$$

$$\sqrt{area}_{Type} \approx \frac{1}{\pi}\left(\frac{K}{\sigma}\right)^2 \qquad (2.7)$$

$$r_p = \frac{1}{\pi}\left(\frac{K}{\sigma_Y}\right)^2, \qquad for\ plane\ stress \quad (2.8)$$

$$r_p = \frac{1}{3\pi}\left(\frac{K}{\sigma_Y}\right)^2, \qquad for\ plane\ strain \quad (2.9)$$

$$a_o = \frac{1}{\pi}\left(\frac{K}{\sigma_e}\right)^2, \qquad Tanaka\ et\ al.\ [33] \quad (2.10)$$

It is therefore likely that the difference between the inclusion types can be explained as a increased driving force at Ti(C,N) inclusions. The increase is caused by the stress concentrating effect of the sharp edge of the inclusion as well as the smaller residual compressive stresses around the Ti(C,N) inclusions than those around the aluminum oxide inclusions [9]; making it easier to initially propagate a short crack away from the inclusion.

It is interesting to note that the slope of logarithmic trend lines for both inclusions types in Figure 2.21 suggests that the difference in stress intensity values decreases as stress decreases (higher number of cycles to failure). This makes sense if the plastic zone size indeed helps control the initial sub-threshold short crack growth at small inclusions, and would suggest that the difference in stress intensity values between the inclusion types will disappear at low enough stress levels (high enough cycles). If logarithmic regression equations for both inclusion types in Figure 2.21 are set equal to each other, it is found that equality occurs at approximately $2 \times 10^9$ cycles; suggesting that the additional inclusion type effect is overcome by the size affect between $10^9$ to $10^{10}$ cycles. It is also interesting to note the resemblance that the curves in Figure 2.21 have to those for steels as found in Barsom and Rolfe [35]. They determined that there exists a strong correlation between the total stress intensity range divided by the square root of the notch tip radius and the number of cycles to fatigue. Their method is a simple method for applying stress concentration

methods to cracks; therefore, the similarity to the failed coated SAE 52100 data and the work of Melander and Olund are not surprising. In different ways, both account for (stress concentration [35] versus fracture mechanics [9]) the driving force for crack formation and extension. The convergence of differences in fatigue strength of different inclusion types as the stress decreases is therefore most likely a statement of the fact that if the local stress at the inclusion, (which would include size, geometric, and residual stress effects), is below the yield point of the grain adjacent to the inclusion, no fatigue can take place.

Table 2.3 Inclusion composition and stress intensity by coating type with stress intensity value adjusted for inclusion type (only the Ti(C,N) values changed by definition).

| Specimen # | Inclusion Composition | Cycles | $\Delta K_{inclu}$ (MPa*m$^{1/2}$) | $\Delta K_{inclu}$ Adj (MPa*m$^{1/2}$) |
|---|---|---|---|---|
| 40-02 | Ti(C,N) | 4.19E+07 | 2.4 | 3 |
| NT-03 | Ti(C,N) | 5.01E+08 | 2.2 | 2.8 |
| NT-05 | Ti(C,N) | 1.11E+09 | 1.7 | 2.5 |
| NT-06 | Ti(C,N) | 9.28E+07 | 2.0 | 2.7 |
| NT-07 | Ti(C,N) | 1.52E+08 | 2.6 | 3.2 |
| NT-08 | Ti(C,N) | 9.68E+07 | 1.8 | 2.5 |

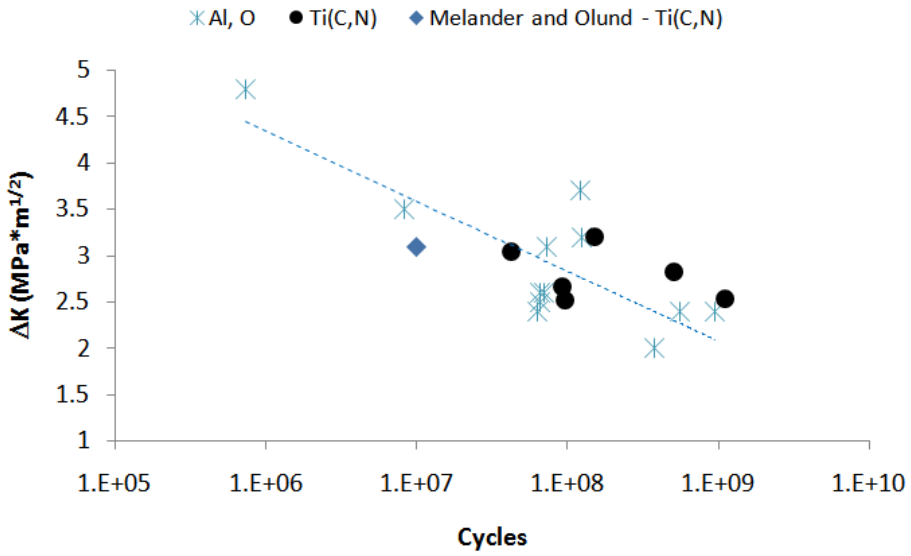


Figure 2.22 Adjusted stress intensity values corrected for crack energy release rate based on inclusion type. G is held constant at 0.075 N/mm for all ΔK corrections.

The dependence of the FGA and inclusion stress intensity values is hypothesized to be due to the influence of the stress state around the inclusion. Cogne et al. [7], Brooksbank and Andrews [36-39], and Atkinson and Shi [40] provide good overviews of the affect of inclusion type on fatigue life of steels; however, Melander and Olund's work directly suggests that the difference is likely due to there still being a difference in crack energy release rate between a Ti(C,N) inclusion and oxide inclusion as the crack grows, although, the difference approaches zero as the crack grows larger [9] – likely explaining a lack of difference in stress intensity values between inclusion types at the fish-eye/overload boundaries.

### 2.4.2 Fatigue Life Modeling

Since the life of the coated SAE 52100 samples is most likely the result of the stress, inclusion size, and inclusion type and not the coating, it is useful to develop a model for the fatigue life of the material. In contact loading of thin films, if the loading is high enough and the coating too thin, the base material will see significant stress. Thin hard coatings are typical as most coatings, like DLCs, develop increasing amount of residual tensile stress as the thickness increases, resulting in poor adherence. Therefore, there is a tendency for spalling of the coating caused by base material cracking prior to failure of the coating. The effect of inclusions in the small stressed volume below the coating is therefore important to proper modeling of a thin-film on steel experiencing contact loading.

The fatigue life as it relates to stress, material strength, and defect size can be modeled using a modified Basquin equation as given in equation 2.11.

$$\sigma_a = \sigma_f'\left(2N_f\right)^b \qquad (2.11)$$

Where $\sigma_a$ is the alternating stress, $\sigma_f'$ is the fatigue strength coefficient and b is the Basquin exponent. The work of Liu et al. [28] developed and outlined four methods for determining the fatigue strength coefficient and the Basquin exponent. The methods are outlined in Table 2.4.

Table 2.4 Basquin equation coefficients

| *Author* | $\sigma_f^{'}$ | $b$ |
|---|---|---|
| Liu et al. [28, 29] | $1.12\frac{(Hv+120)^{9/8}}{\left(\sqrt{area}_{\text{int}}\right)^{1/8}}$ | $\frac{1}{3}\log\left(1.35(Hv+120)^{-\frac{1}{16}}\left(\sqrt{area}_{\text{int}}\right)^{-\frac{1}{48}}\right)$ |
| Tanaka and Akiniwa [30] | $\frac{2}{\sqrt{\pi}}\left(\frac{4}{C_A(m_A-2)}\right)^{\frac{1}{m_A}}\left(\sqrt{area}_{\text{int}}\right)^{\frac{1}{m_A}-\frac{1}{2}}$ | $-\frac{1}{m_A}$ |
| Chapetti et al. [31] | $2.5\frac{(Hv+120)}{\left(\sqrt{area}_{\text{int}}\right)^{1/6}}$ | $-\frac{1}{48}$ |
| Mayer et al. [32] | $(2C)^{\frac{1}{n}}\left(\sqrt{area}_{\text{int}}\right)^{-1/6}$ | $-\frac{1}{n}$ |

The first method created by Liu et al. and described in [28] takes into account the effect of hydrogen on the formation of the FGA. Hydrogen has been proposed as a possible cause of FGA formation by Murakami et al. [16]. Liu's model also uses Murakami's equation for the threshold stress intensity value [17]

$$\Delta K_{th} = 1.8x10^{-3}(Hv + 120)\left(\sqrt{area}\right)^{1/3} \qquad (2.12)$$

When combined with Murakami's stress intensity equation for internal defects, results in a fatigue life equation that only differs from Murakami's in the magnitude of the constant: 2 versus 1.56.

$$2\frac{(Hv + 120)}{\left(\sqrt{area}\right)^{1/6}}, \qquad Liu\ et\ al.\ [28] \qquad (2.13)$$

$$1.56\frac{(Hv + 120)}{\left(\sqrt{area}\right)^{1/6}}, \qquad Murakami\ [17] \qquad (2.14)$$

When hydrogen is included in the model equation 2.13 takes the following form:

$$2.7\frac{(Hv + 120)^{15/6}}{\left(\sqrt{area}\right)^{3/6}}, \qquad (2.15)$$

Liu et al. [28] derived their values for the Basquin equation using equations 2.13 and 2.15 by assuming at $10^6$ cycles the alternating stress is given by equation 2.13 and at $10^9$ cycles the alternating stress equals equation 2.15 resulting in the values given in Table 2.3. The other three models are described in detail in [28]. Tanaka and Akiniwa [30] assume that crack propagation follows the Paris law inside the FGA. Chapetti et al. [31] uses the notion that longer fatigue lives correlate to larger FGAs. Mayer et al. [32] uses the notion that there exists a linear relationship between the quotient of the alternating stress and the endurance limit and the number of cycles to failure in a double logarithmic form. The constants for both the Tanaka and Akiniwa and Mayer equations were determined experimentally and are provided in their papers.

A linear relationship was found for the stress intensity at the inclusion versus the logarithm of lifetime divided by the square root area of the inclusion (Figure 2.23). A statistical correlation (Table 2.5) between the log stress intensity versus log cycles and log cycles divided by square root area for the failed samples from this study found the correlation to be very strong as was seen in [30]. Since the correlations were satisfactory, Tanaka and Akiniwa and Mayer's methods were used to calculate the strength of the fractured samples using the Basquin approach.

Table 2.5 Correlation analysis of the stress intensity at the inclusion versus the log number of cycle and log number of cycles divided by the square root area of the inclusion.

| Author | Analysis Method | Pearson | P-value |
|---|---|---|---|
| Tanaka and Akiniwa [30] | Log ΔK (Inclusion) vs Log Cycles | -0.805 | 0 |
| | Log ΔK (Inclusion) vs Log Cycles/area$^{1/2}$ | -0.876 | 0 |

The coefficients $m_a$ and C for our data, using the Tanaka and Akiniwa [30] model, were found graphically to be 7.3 and $4.39 \times 10^{-11}$, respectively (Figure 2.24). The coefficients for the model of Mayer et al. [32] were also found graphically with n=11.64, and $C=1.53 \times 10^{44}$ (Figure 2.25)

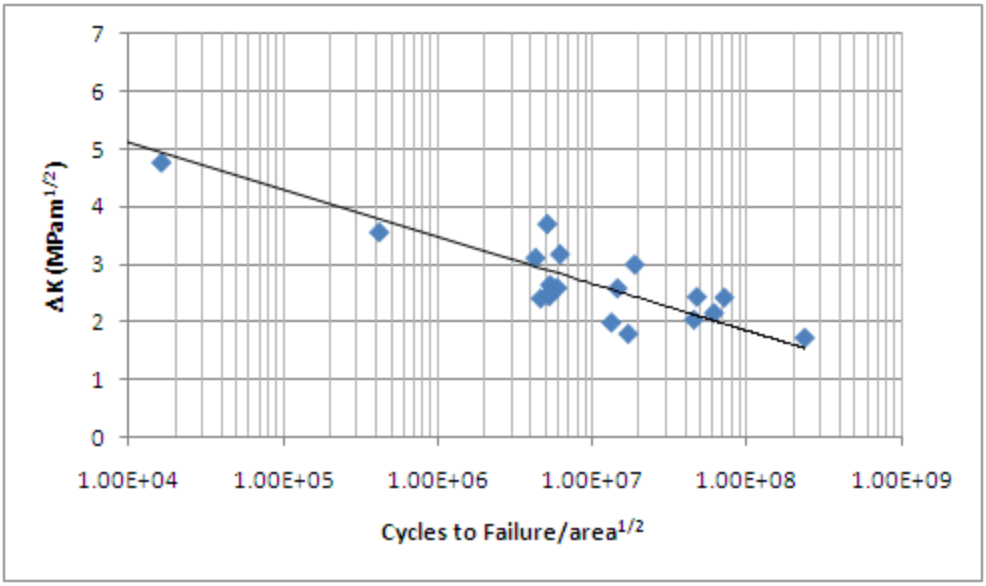


Figure 2.23 The stress intensity at the inclusion versus the cycles to failure divided by the square root area of the inclusion.

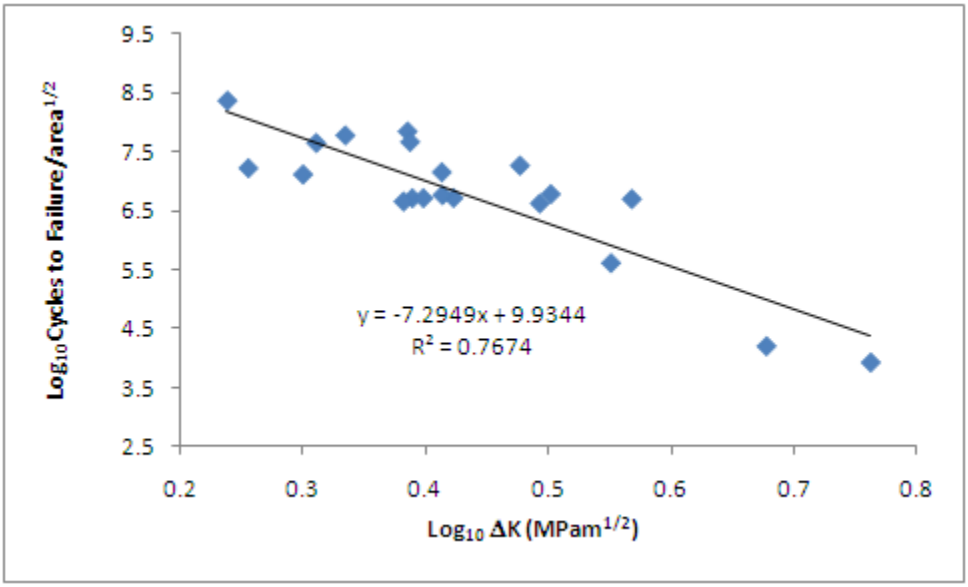


Figure 2.24 Analysis to determine the coefficients for the model of Tanaka and Akiniwa [30].

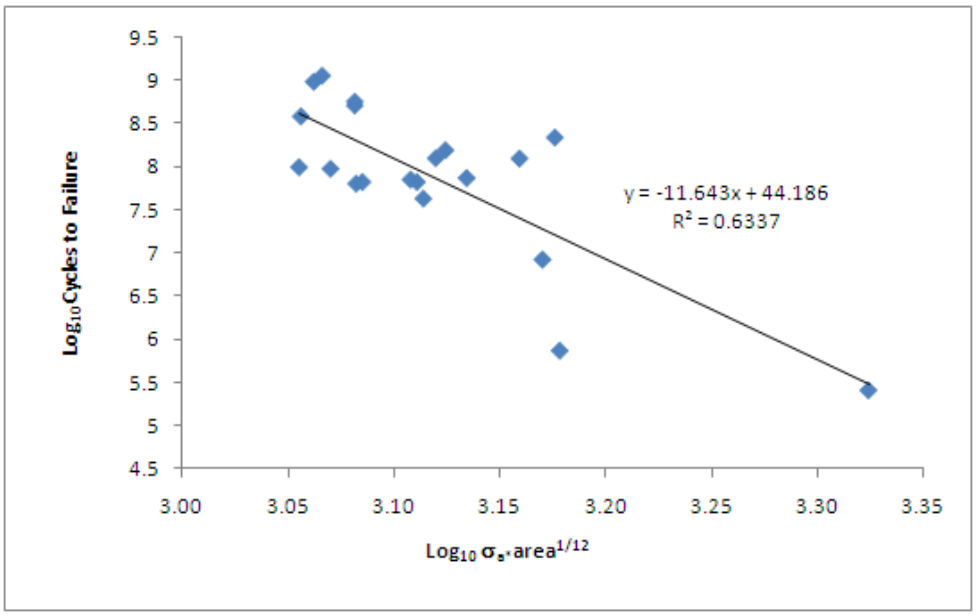

Figure 2.25 Analysis to determine the coefficients for the model of Mayer et al. [32].

To analyze the appropriateness of the Murakami [17] and Liu [28] equations for fatigue strength, the fracture stress for each sample was divided by the stress ratio R adjusted fatigue strength given by equations (2.16) through (2.18). A plot of the results is given in Figure 2.26.

$$1.56\frac{(Hv+120)}{(\sqrt{area})^{1/6}}\left[\frac{1-R}{2}\right]^{\alpha} \qquad (2.16)$$

$$\alpha = 0.226 + Hv \times 10^{-4} \qquad (2.17)$$

$$2.0\frac{(Hv+120)}{(\sqrt{area})^{1/6}}\left[\frac{1-R}{2}\right]^{\alpha} \qquad (2.18)$$

The Murakami equation more closely matches the fatigue data in this study with Liu's giving a less conservative prediction. Both equations appear to accurately model the result above approximately $10^5$ cycles.

Plots of the fatigue strength based on the four models given in Table 2.4 and using the smallest and largest inclusion sizes are given in Figures 2.27–2.28. The four models were chosen because they can be adjusted for material hardness, inclusion size and

type unlike statistical models using probability density functions only. For the Tanaka and Akiniwa [30] model, their coefficients were used as the ones from the failed specimens from this study underestimated the strength significantly. Chapetti's and Liu's models modeled the fatigue data very well at all stress levels tested. Mayer's was accurate above $10^7$ cycles as was Tanaka and Akiniwa's with the exception that their range was very large.

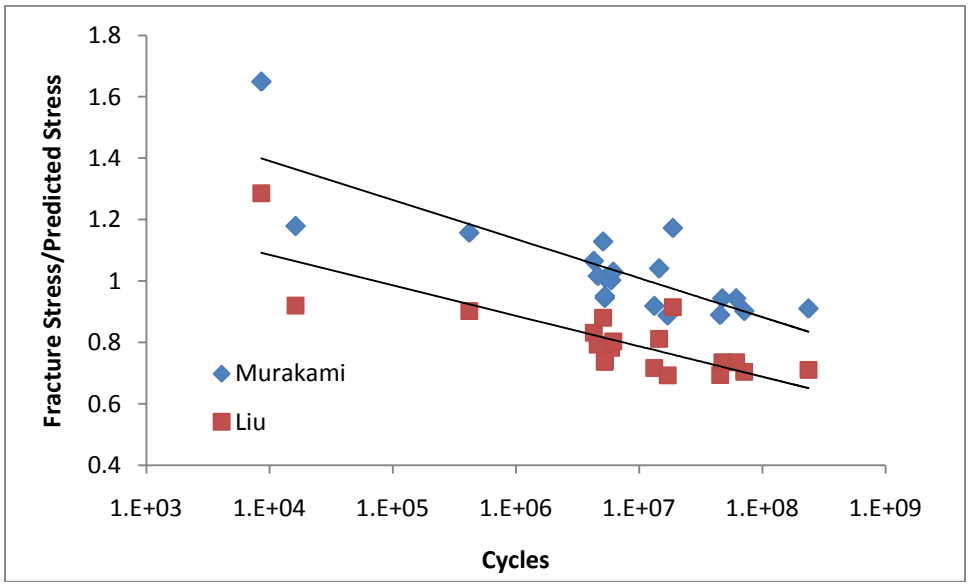


Figure 2.26 Ratio of failure stress to calculated strength using the equations of Murakami and Liu.

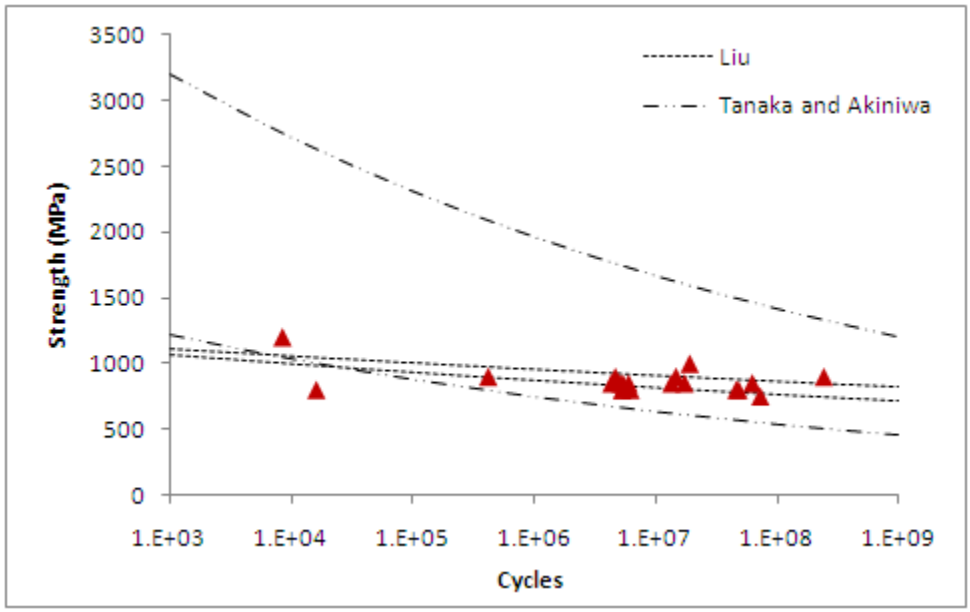


Figure 2.27 Predicted fatigue strength based on the methods of Liu et al. and Tanaka and Akiniwa.

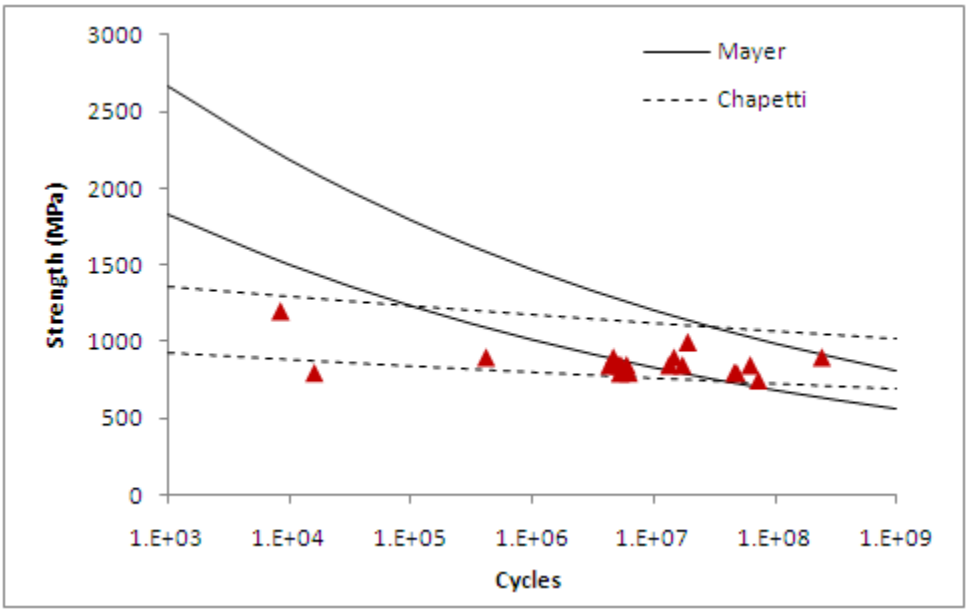

Figure 2.28 Predicted fatigue strength based on the methods of Mayer et al. and Chapetti et al.

The observed differences in correlation methods shown in Figures 2.27 and 2.28 as well as Table 2.5, used to find the unknown parameters, is important as it suggests that both the Tanaka and Akinawa [30] and Mayer [32] methods may suffer in accuracy based on the prescribed method of regression modeling. The models of Liu et al. [28, 29] and Chapetti et al. [31] do not have this problem since they are much more in the form of the original Murakami strength formula.

The modeling methods based on the method of Murakami, especially those of Chapetti [31] and Liu et al. [28, 29] were very useful when modeling the coated SAE 52100 data, and are extremely useful when modeling with limited samples: a typical issue in industrial design applications. These models, which were based on Murakami's model, allow for the adjustment based on inclusion type as well as size and stress on the part or sample. This allows for a better modeling of the variation in fatigue life caused by these variables. Chapetti and Liu's are considered the most useful in that they are simple and at least in this study, appear to be very accurate. Also, the use of extreme value statistical methods such as the Gumbel distribution suggested by Murakami are very useful in accounting for extreme sized inclusions

and volume of material stressed which is very helpful for design engineers trying to control failure rates to maintain a reliable product in contact mechanical design. It is also useful from a quality control perspective as the Murakami's method can be used in replacement of less quantitative inclusion rating methods such as ASTM E45. The only caution is that Murakami's and other models known to this author do not account for the potency of the inclusion type at the fatigue origin.

## 2.5 Conclusions

1. The addition of diamond like carbon and electroless nickel with Teflon coatings to hardened and tempered SAE 52100 bearing steel had no affect on the fatigue life.
2. Different inclusion types can affect the stress intensity value, and therefore the fatigue life at both the inclusion and FGA, but does not significantly affect the stress intensity at the fish-eye/overload interface.
3. The difference in stress intensity values between Ti(C,N) and alumina inclusions was due to the higher driving force for crack extension at the Ti(C,N) inclusions [9].
4. A correction factor can be added to the Murakami equation to account for inclusion type instead of just inclusion size. However, above $2 \times 10^9$ cycles the correction factor approaches zero.
5. Chapetti's [31] and Liu et al. [28] modeling methods accurately predicted the fatigue strength of the failed coated SAE 52100 samples. Both models allow for inclusion type correction which could make them more accurate in modeling the fatigue strength.

## 2.6 References


1. C. Bathias. Fatigue and Frac Engng Mater Struct, 25, (1999), p 559-565
2. I. Marines, X. Bin, C. Bathias. Int Journal of Fatigue, (2003), p. 1101-1107
3. C. Bathias, L. Drouillac, P. Le Francois. Int Journal of Fatigue, 25, (2001), p. S143-S151
4. H. Mughrabi. Fatigue and Frac Engng Mater Struct, 22, (1999), p 633-641
5. F. Sadeghi, B. Jalahmadi, T. Slack, N. Raje, N. Arakene, Journal of Tribology, 131, (2009)
6. A. Ponter, A. Hearle, K. Johnson. J Mech Phys Solids, 33, 4, (1985), p. 339-362
7. Cogne, J.Y., Heritier, B. & Monnot, J. 1987. Clean Steel 3, Balatonfured, Hungary, 2-4 June 1986, The Institute of Metals, pp. 26-31.
8. Ultrasonic fatigue: proceedings of the First International Conference on Fatigue and Corrosion Fatigue Up to Ultrasonic Frequencies. Metallurgical Society of AIME, 1982, J. Wells ed.
9. A. Melander, P. Olund. Materials Science and Technology. Vol. 15, pp. 555-562, (1999)
10. A. Melander. International Journal of Fatigue, 19, 1, pp. 13-24, (1996)
11. VHCF-4. Ed J. Allison, J.W. Jones, J. Larsen, R. Ritchie. TMS, (2007)
12. K. Kim, C. Suh, R. Murakami, C. Chung, Surface and Coatings Technology, 171, pp. 15-23, (2003)
13. J. Schaufler, K. Durst, T. Haas, R. Nolte, H. Hoppel, M. Gocken. International Journal of Fatigue, pp. 1-7, (2012)
14. S. Baragetti, F. Tordini, International Journal of Fatigue, 29, pp. 1832-1838, (2007)
15. A. H. Salem, C. J. Torbet, A. Shyam, T. M. Pollock, J. W. Jones
16. T. Sakai. Fourth International Conference on High Cycle Fatigue. TMS, pp. 3-12, (2007)
17. Y. Murakami. Metal Fatigue: Effect of Small Defects and Nonmetallic Inclusions. Elsevier (2002)

18. Y. Murakami, T. Nomoto, T. Ueda, Fatigue Fract. Eng. Mater. Struct. 22 (1999) pp. 81-590.
19. Y. Murakami, T. Nomoto, T. Ueda, Y. Murakami, Fatigue Fract. Eng. Mater. Struct. 23 pp. 893-902, (2000)
20. Y. Murakami, T. Nomoto, T. Ueda, Y. Murakami, Fatigue Fract. Eng. Mater. Struct. 23 pp. 903-910, (2000)
21. T. Sakai, Y. Sato, and N. Oguma. Fatigue and Frac Engng Mater Struct, 25, pp. 765-773, (2002)
22. K. Shiozawa, L. Lu, S. Ishikawa. Fatigue Fract Engng Mater Struct, 24, pp. 781-790, (2001)
23. T. Sakai, N. Oguma, and H. Horada. Fourth International Conference on High Cycle Fatigue. TMS, (2007) p 129-136
24. T. Sakai, B. Lian, Takeda, K. Shiozawa, Y. Ochi, M. Nakajima, T. Nakamura. International Journal of Fatigue. 32, pp. 497-504. (2010)
25. P. Paris, I. Marine-Garcia, R. Hertzburg. Proceedings of Very High Cycle 3. Warrendale, Pa. TMS (2004)
26. I. Marine-Garcia, P. Paris, H. Tada, C. Bathias. Int Journal of Fatigue, 29, pp. 2072-2080, (2007)
27. R. Hertzburg. Materials Science and Engineering A190, pp 25-32, (1995)
28. Y. Liu, Y. Li, S. Li, Z. Yang, S.Chen, W. Hui, Y. Weng. International Journal of Fatigue 32, pp. 1351–1357, (2010)
29. Y. Liu, Z. Yang, Y. Li, S. Chen, S. Li, W. Hui. Materials Science and Engineering A, 497, pp 408-415, (2008)
30. K. Tanaka, Y. Akiniwa. Fatigue Fract Eng Mater Struct, 25, pp. 775-784, (2002)
31. M. Chapetti, T. Tagawa, T. Miyata. Materials Science and Engineering A, 356, pp 236-244, (2008)
32. H. Mayer, W. Haydn, R. Schuller, S. Issler, B. Furtner, H. Bacher. International Journal of Fatigue, 31, pp. 242-249, (2009)
33. K. Tanaka, Y. Nakai, M. Yamashita. International Jounral of Fracture, 17, pp. 519-533, (1981)

34. M. El Haddad, T. Topper, K. Smith. Engineering Fracture Mechanics, 11, pp. 573-584, (1979)
35. J. Barsom, S. Rolfe. Fracture and Fatigue Control in Structures. 3rd Ed. ASTM, (1999)
36. Brooksbank, D. & Andrews, K.W. 1968. Journal of the Iron and Steel Institute, 206 (6), pp. 595-599.
37. Brooksbank, D. & Andrews, K.W. 1969. Journal of the Iron and Steel Institute, 207 (4), pp. 474-483.
38. Brooksbank, D. 1970. Journal of the Iron and Steel Institute, 208 (5), pp.495-499.
39. Brooksbank, D. & Andrews, K.W. 1972. Journal of the Iron and Steel Institute, 210 (4), pp. 246-255.
40. H. Atkinson and G. Shi. Progress in Materials Science 48 (2003) 457–520

# CHAPTER 3

## Wear of Diamond-Like-Carbon (DLC) Coatings on SAE 52100 and Chilled Cast Iron

### 3.1 Introduction

The need for very high cycle wear data is becoming increasingly important as more advanced materials are being used to reduce friction, decrease emissions, and extend the lives of automotive components, especially those of the internal combustion engine. One need not look farther than the Stern Review on the Economics of Climate Change [1] or the U.S. Department of Energy's report on how we will face the energy challenges of the 21$^{st}$ century [2] to understand the human and financial need for advanced materials. In mechanical devices which will experience high stress contact loading, these advanced materials are typically hard thin films that are expected to see millions, if not billions, of cycles of load over their lifetime. Currently, there are few if any legitimate tests for simulating wear over the life of devices designed to last that long. This makes it difficult for a designer to understand the controlling mechanisms of wear in the very high cycle regime at or above $10^8$ cycles. The first published application of a very high cycle wear test that could quickly get to $10^8$ cycles was performed by Mason et al at Bell Labs [3-4] in the 1950s to understand how wire spring relays wear over billions of cycles of wear. Since then, most works at higher frequencies of load have focused on very small amplitude fretting <10 μm [4-7]. However, most of these tests were performed below 1.5 kHz and only approached $10^6$ cycles of wear [5]. Spaltmann et al [8] showed how an ultra-high frequency tribometer operating at 40kHz can be successfully used to obtain wear data for hard coatings above $10^8$ cycles.

Conventional tribometers usually operate in the range of 500 RPM on the low end to 50000 RPM for higher speed rolling contact machines. These tribometers are usually for evaluating short time wear performance of a material to resist abrasion, adhesion, or low-cycle fatigue wear mechanisms. Because of the lack of high frequency testers, little data exist to help designers determine the best coatings, manufacturing and quality processes, coating thicknesses, and other parameters when selecting coatings

for designs. Therefore, there exists a need to further develop wear testing methods that provide data in the range of $10^8$ cycles and greater.

This chapter describes the development of an ultrasonic wear tester and the results from wear testing of an amorphous-hydrogenated diamond-like carbon (DLC) coated on chilled cast iron and SAE 52100 bearing steel. An analytical equation to predict wear depth as a function of cycles and contact load will also be developed based on modeling of the test results. Wear depth results from ultrasonic wear testing will be compared to results from a conventional low-frequency tribometer to determine the adequacy of the analytical model to predict wear depth under ultrasonic and conventional test rates.

## 3.2 Experimental Methods

### 3.2.1 Material

The material used in the study was hardened and tempered SAE 52100 bearing steel with a tempered martensitic microstructure and a chilled cast iron with composition as shown in Table 3.1. Examples of the microstructure in the chilled zone of the cast iron are shown in Figure 3.1 The cast iron was poured onto a room temperature steel chill plate coated with graphite in order to harden the surface to ~60 HRC and result in a surface microstructure consisting of a mixture of massive iron carbides and fine pearlite with small amounts of martensite and bainite. The diamond-like carbon coating is an Oerlikon Balzers Balinit DLC Star multilayer coating consisting of an initial layer of chromium nitride that is graded to a final pure amorphous-hydrogenated a-C:H-DLC (DLC) layer.

Table 3.1 Chemical Composition of the chilled cast iron.

| Element | Composition (Weight % ) |
|---|---|
| Total Carbon (TC) | 3.45 |
| Silicon (Si) | 2.32 |
| Nickel (Ni) | 1.49 |
| Manganese (Mn) | 0.91 |
| Molybdenum (Mo) | 0.84 |
| Chromium (Cr) | 0.75 |
| Copper (Cu) | 0.07 |
| Iron | Remainder |

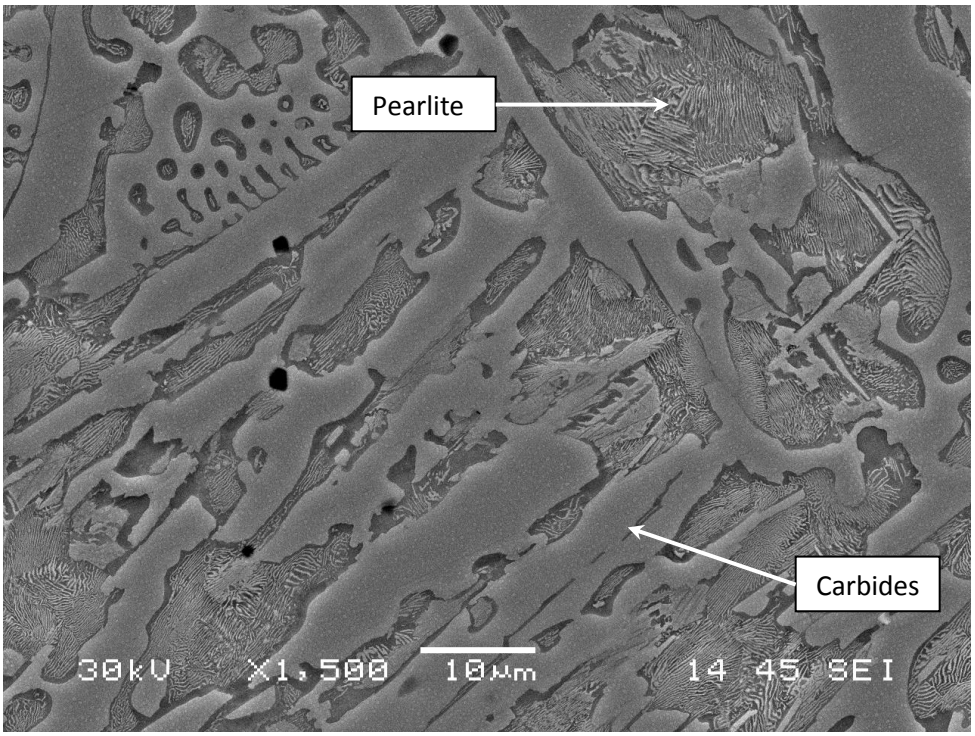


Figure 3.1 A scanning electron microscope photomicrograph of the microstructure in the chilled area of the cast iron. The microstructure consists of massive iron carbides in a matrix of pearlite.

### 3.2.2 Wear Testers

An ultrasonic wear tester was developed by converting the vertically oriented ultrasonic tester described in Chapter 2. For wear testing, the equipment was configured as shown in Figure 3.2a-b. The ultrasonic machine (UT) is a closed loop system that operates at a resonant frequency of approximately 20 kHz. The system can adjust the frequency continuously as the system resonance drifts slightly during testing. The drift is usually less than 0.5-1.0 kHz. In this study the frequency was set at 19.6 Hz. The displacement or linear translation amplitude was measured using a non-contact fiber optic sensor. Load was applied by adjusting a counterweight on the rear of the set-up and adding dead weights at the zero-displacements nodes of the ultrasonic horn. The UT is driven by a piezoelectric generator, which is typical for UT equipment used in nondestructive testing and other applications. It is novel with respect to the amplifier which allows for relatively large displacements, used in axial fatigue testing of dogbone shaped fatigue samples.

The ultrasonic wear testing system simulates component wear by controlling the contact pressure (stress) and translation speed by controlling the normal weight on the ball and the frequency and displacement of testing, respectively. The displacement range for all tests was 60 μm (120 μm travel per cycle). The contact load was applied via a 4.763 mm diameter diamond ball with a modulus of elasticity of approximately 850 GPa. A schematic of the wear test system in given in Figure 3.2c

Low frequency tribometry was performed using a Microphotonics pin on disk tribometer using a 3.175 mm diameter silicon nitride ball as the counterbody. A load of 30N was stationary and applied directly on the center axis of the ball with the DLC coated disk rotating below the ball.

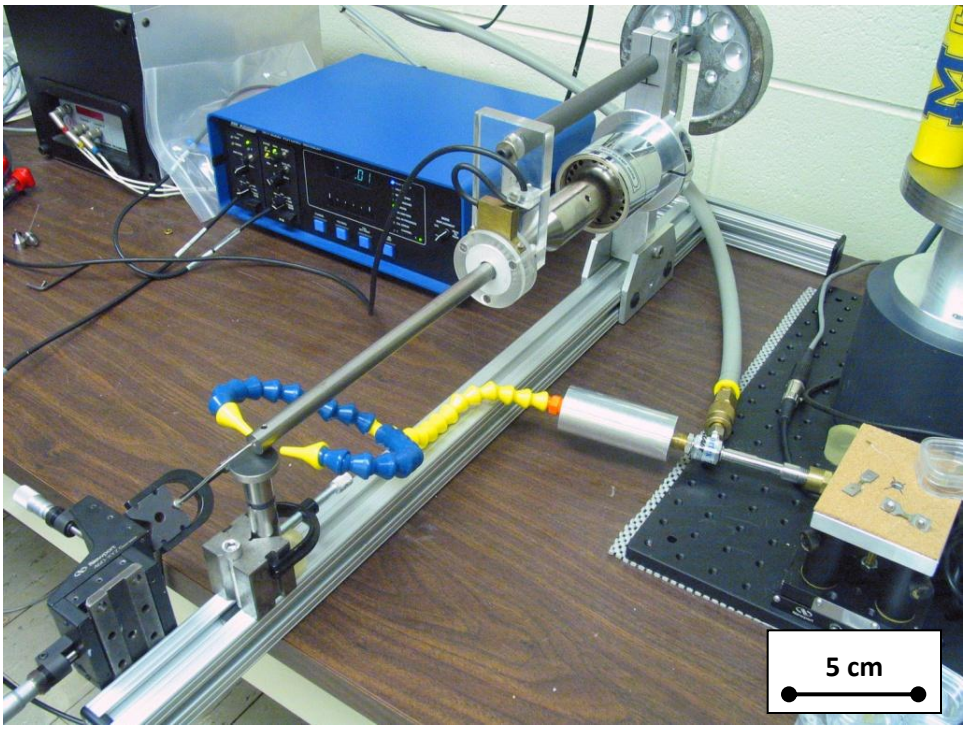


(a)

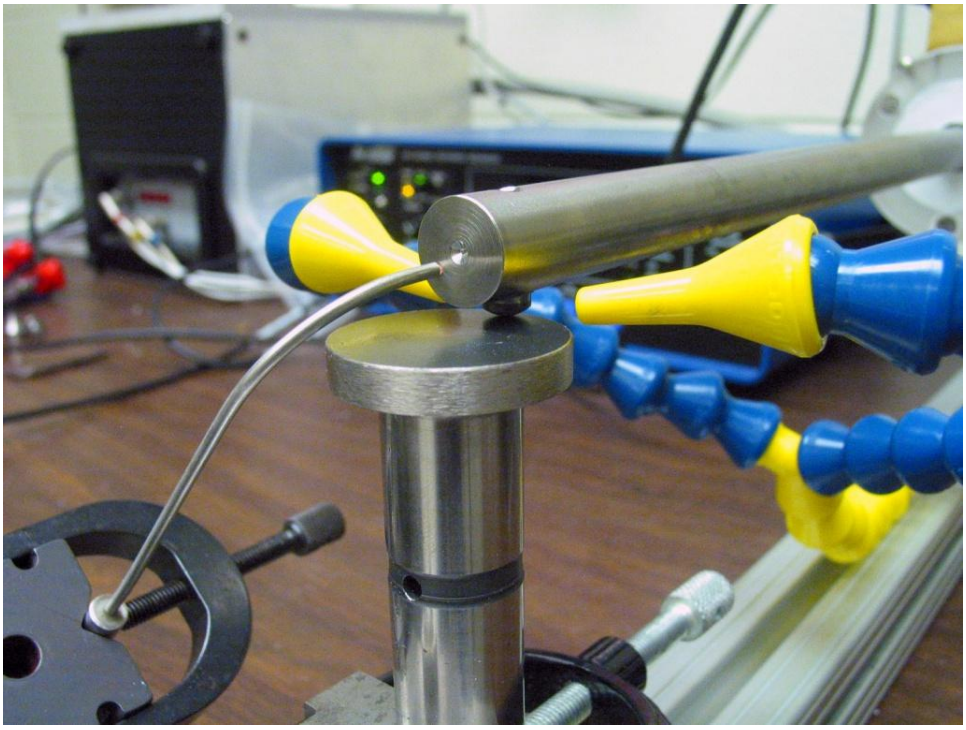

(b)

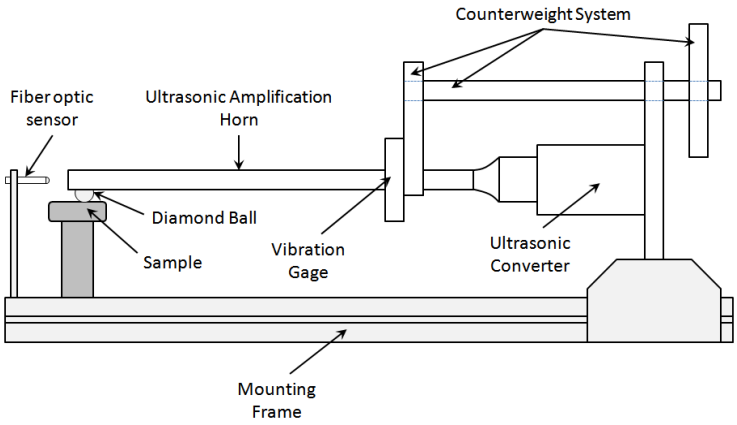


(c)

Figure 3.2 (a, b) The ultrasonic test equipment used for the very high wear testing. (c) A schematic of the ultrasonic wear testing system.

### 3.2.3 Wear Measurement

The wear depth of all samples was measured using a ST400 Optical Profiler from Nanovea. The scanning parameters are given in Table 3.2. The depth resolution was 12 nm, depth accuracy 60 nm, and the lateral resolution 1.3 μm.

Table 3.2 Optical profilometer settings

| Measurement | 3D scans | Line scans |
|---|---|---|
| **Probe** | 400μm | 400μm |
| **Acquisition rate** | 100 Hz | 100 Hz |
| **Averaging** | 1 | 1 |
| **Measured surface** | 1mm x 1mm | 25mm |
| **Step size** | 3μm x 3μm | 3μm |
| **Scanning Mode** | Constant speed | Constant speed |

### 3.2.4 Raman Spectroscopy

The measurements were performed using a "LabRam" J-Y Spectrometer. A helium-neon (He-Ne) laser (632.8 nm wavelength) and a 600 gr/mm grating were used for the measurements. The measurements were performed using backscattering geometry ($180^0$) with an Olympus BX40 microscope. The measurements were repeated with an argon ($Ar^+$) ion laser (514.5 nm wavelength) and an 1800 gr/mm grating.

### 3.2.5 Adhesion Testing

Adhesion testing was performed per the German technical specification VDI 3198 using a Rockwell C tester and a Nikon stereomicroscope to analyze the indented coatings.

## 3.3 Results and Discussion

### 3.3.1 High Frequency Tribometer Testing

Two amorphous hydrogenated a-C:H DLC coated chilled cast iron and three a-C:H DLC coated SAE 52100 samples were ultrasonically wear tested at 1, 2, and 5N of load and $10^6$, $10^7$, and $10^8$ cycles for a total of nine tests per sample. A conversion of load to contact pressure is given in Table 3.3. To calculate the contact pressure it was assumed that the modulus of the coating was equal to the modulus of steel for both the cast iron and bearing steels.

Table 3.3 Load to contact pressure conversion table

| | | Diamond | Steel |
|---|---|---|---|
| **Young's Modulus** | GPa | 850 | 210 |
| **Poisson's Ratio** | | 0.29 | 0.29 |
| **Radius** | mm | 2.38 | 760 |

| | Load | 1 N | 2 N | 5 N |
|---|---|---|---|---|
| **Mean Contract Pressure** | GPa | 0.70 | 0.88 | 1.20 |
| **Max Contact Pressure** | GPa | 1.05 | 1.32 | 1.80 |

The wear depth scars were then measured using optical interferometry and scanning electron microscopy. A three dimensional optical interferometry image and SEM photomicrograph are shown for representative wear scars from the DLC coated SAE 52100 steel and chilled cast iron samples in Figures 3.3-3.8. A plot of the wear depth results at $10^6$ cycles for the DLC coatings on cast iron and SAE 52100 are shown in Figure 3.9. Only data to $10^6$ cycles are shown as the coating was worn through for the all but five of the samples tested to $10^7$ and $10^8$ cycles. Only data points with depths below the thickness of the coating at $10^6$ cycles are shown. The wear depth appears to

vary linearly with contact pressure for these data. Only a small difference in wear depth of the DLC was observed as a function of the substrate, although this is likely due to error in measuring small wear depths at the lower loads and number of cycles.

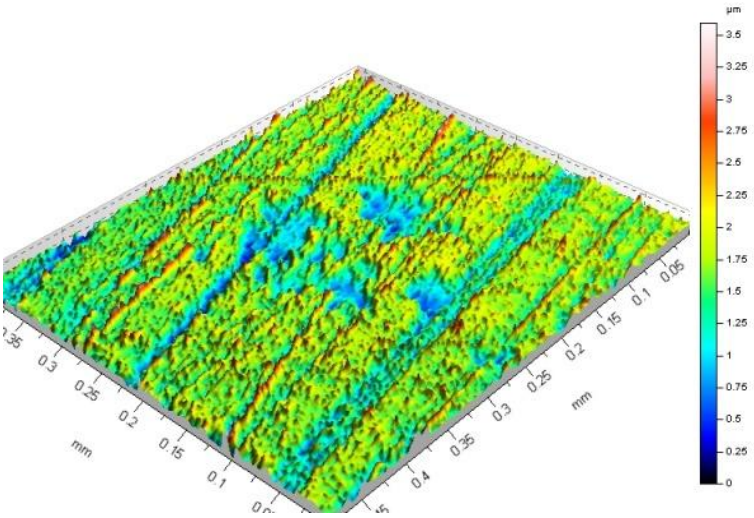


(a)

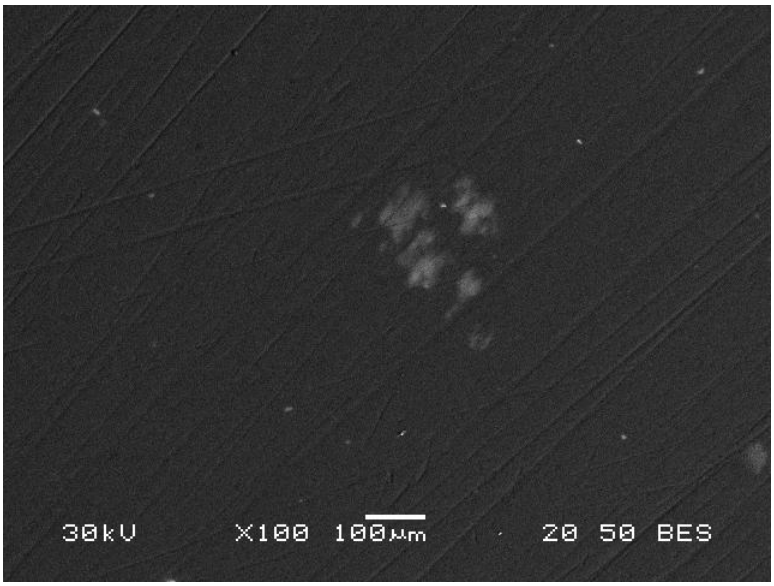


(b)

Figure 3.3 (a) Three dimensional optical interferometry image and (b) SEM image of the wear scars of the DLC coating on the chilled cast iron tested to $10^6$ cycles at a load of 1N.

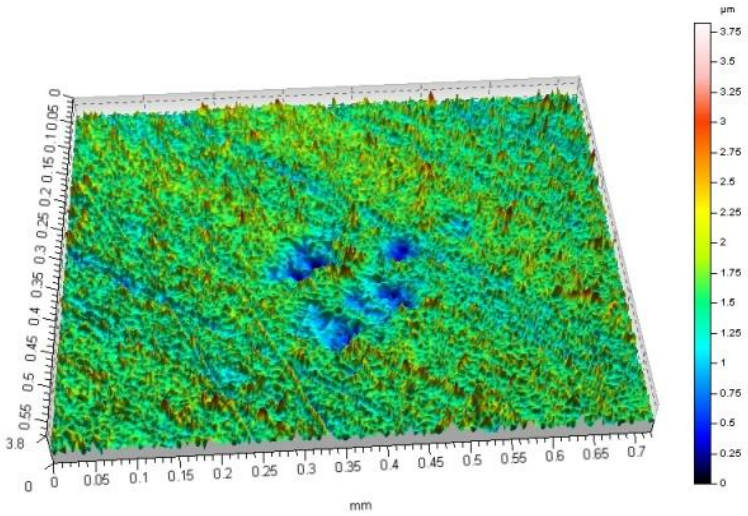


(a)

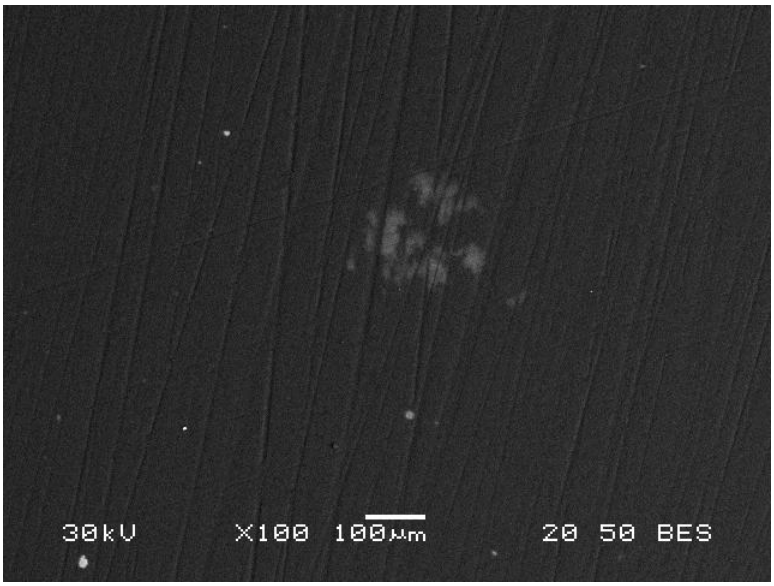


(b)

Figure 3.4 (a) Three dimensional optical interferometry image and (b) SEM image of the wear scars of the DLC coating on the chilled cast iron tested to $10^6$ cycles at a load of 2N.

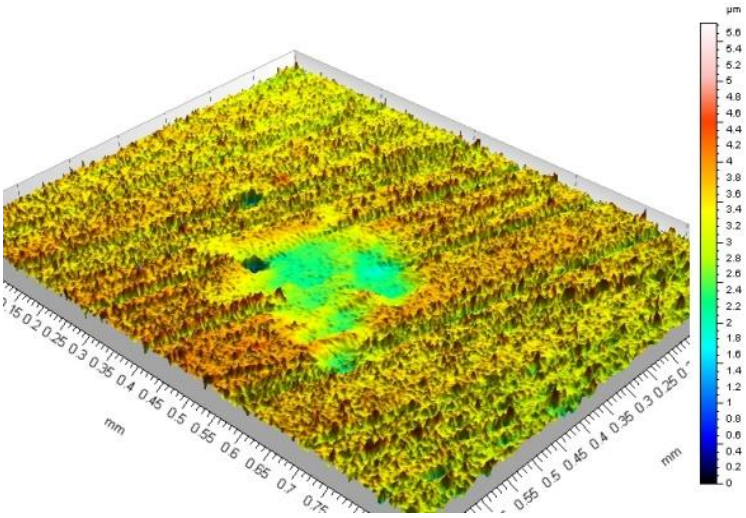


(a)

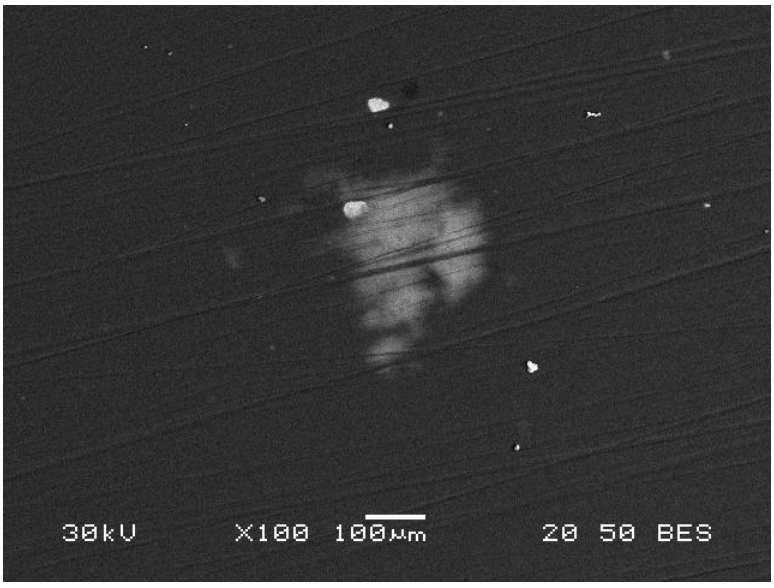


(b)

Figure 3.5 (a) Three dimensional optical interferometry image and (b) SEM image of the wear scars of the DLC coating on the chilled cast iron tested to $10^6$ cycles at a load of 5N.

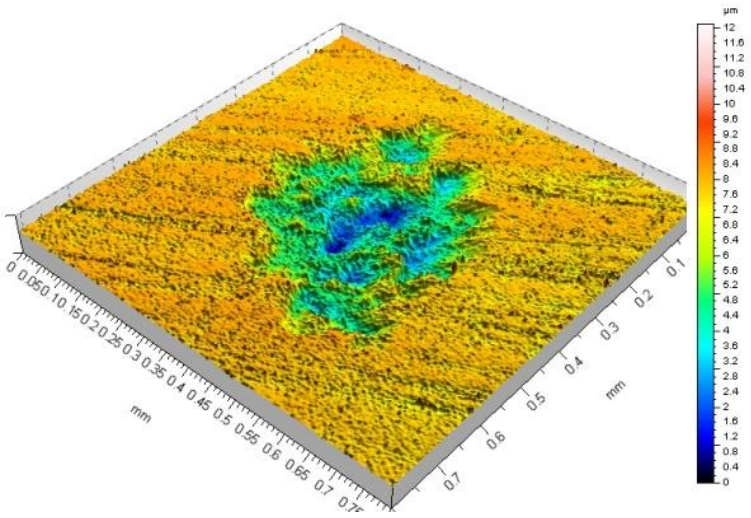


(a)

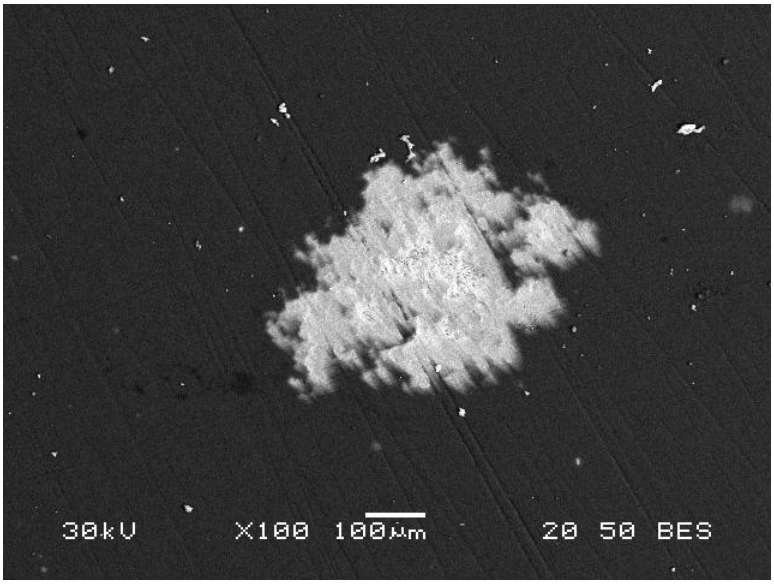


(b)

Figure 3.6 (a) Three dimensional optical interferometry image and (b) SEM image of the wear scars of the DLC coating on the chilled cast iron tested to $10^8$ cycles at a load of 1N.

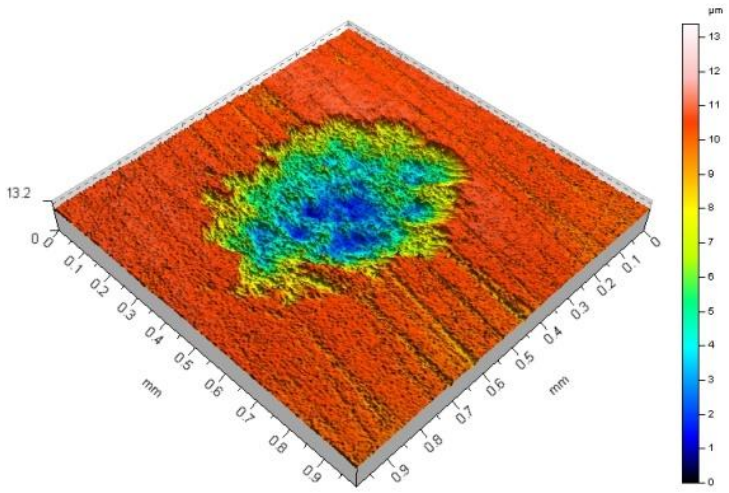


(a)

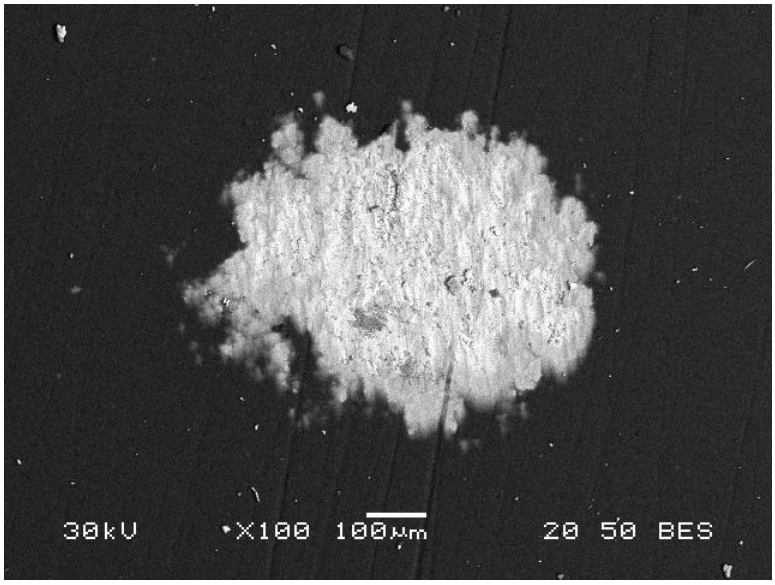


(b)

Figure 3.7 (a) Three dimensional optical interferometry image and (b) SEM image of the wear scars of the DLC coating on the chilled cast iron tested to $10^8$ cycles at a load of 2N.

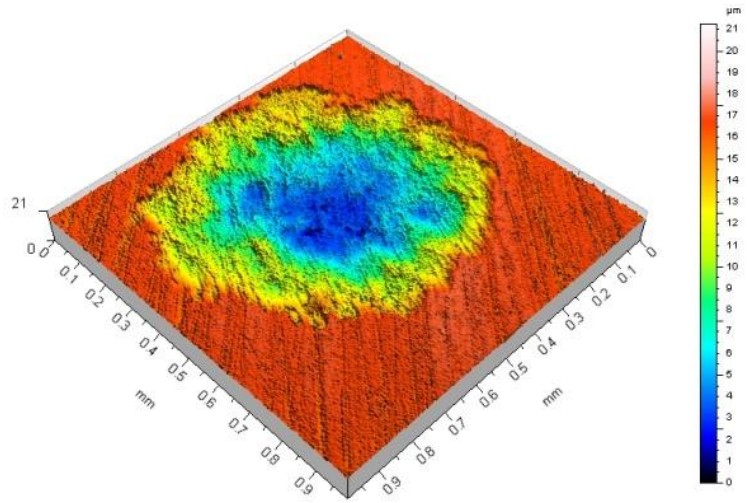


(a)


(b)

Figure 3.8 (a) Three dimensional optical interferometry image and (b) SEM image of the wear scars of the DLC coating on the chilled cast iron tested to $10^8$ cycles at a load of 5N.

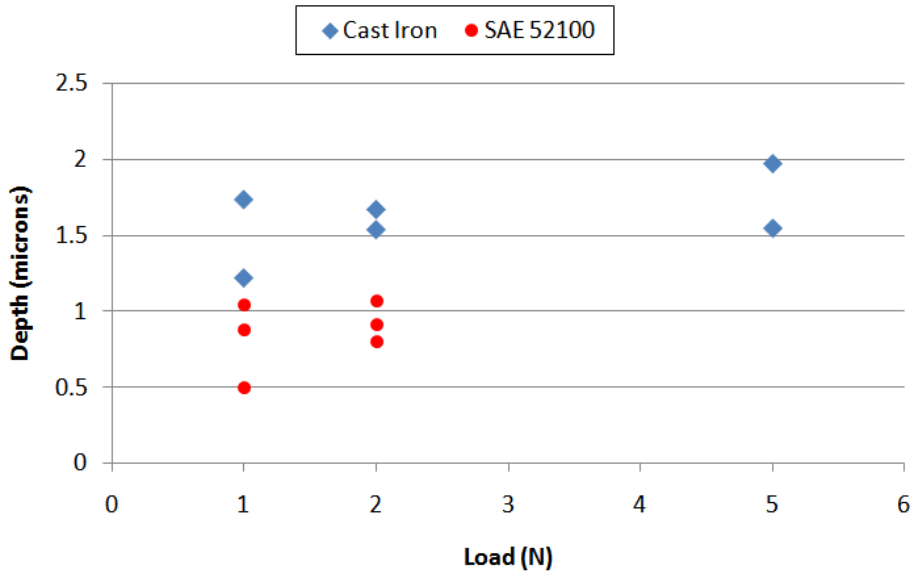


Figure 3.9 DLC wear depth data at $10^6$ cycles for the DLC on cast iron and SAE 52100. The wear depth increases linearly with contact load.

Multi-variable plots of the wear depth at $10^6$, $10^7$, and $10^8$ cycles for all three loads are shown in Figures 3.10 and 3.11. As the coating is penetrated the wear rate increases substantially. The cast iron substrate had a much lower wear rate than the SAE 52100 substrate.

The wear rates for the coatings were calculated using the volume expression for a hemispherical cap given in Appendix A and by setting the variable $t$ to the wear depth. The formula for wear rate is given as equation 3.1 where F is the load in Newtons, $k_{rate}$ is the wear rate expressed in $mm^3/Nm$, $r$ is the radius of the sphere in mm, $N$ is the number of cycles, and $l$ is the length of travel per cycle in m/cycle.

$$k_{rate} = \frac{V_{wear}}{FlN} \qquad (3.1)$$

The mean wear rates for the DLC on chilled cast iron and SAE 52100 for the experimental wear testing were $3.97 \times 10^{-8}$ and $1.45 \times 10^{-8}$ $mm^3/Nm$, respectively. These rates are similar to those reported for a-C:H DLCs [9-11].

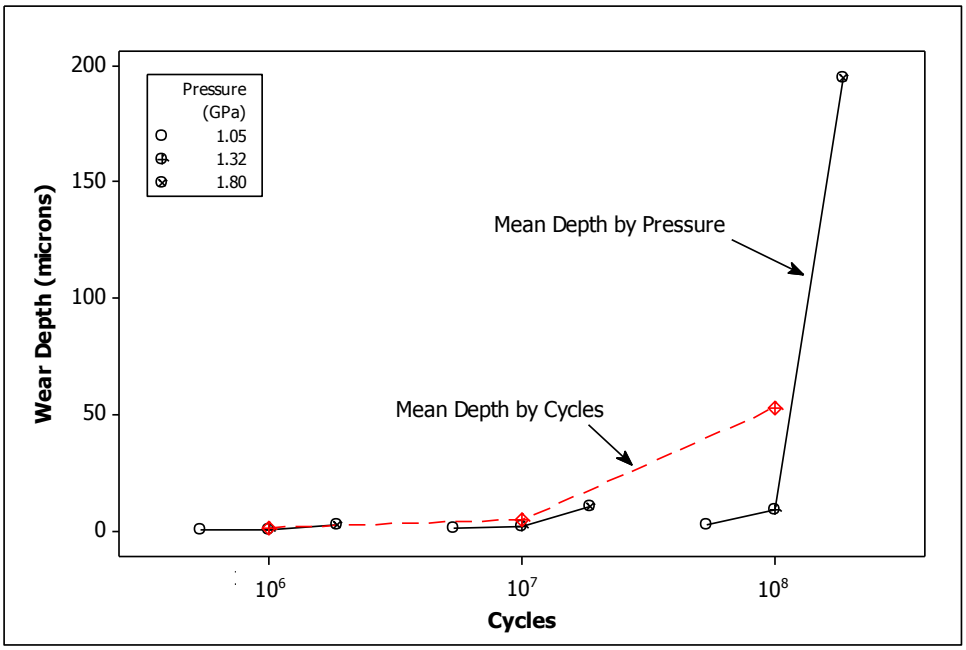


Figure 3.10 Wear depth data for DLC coated SAE 52100 samples as a function of contact pressure and number of cycles. The red hidden line represents the mean wear depth at each level of the factor cycles. The black lines connect the mean values at each contact pressure at a constant number of cycles.

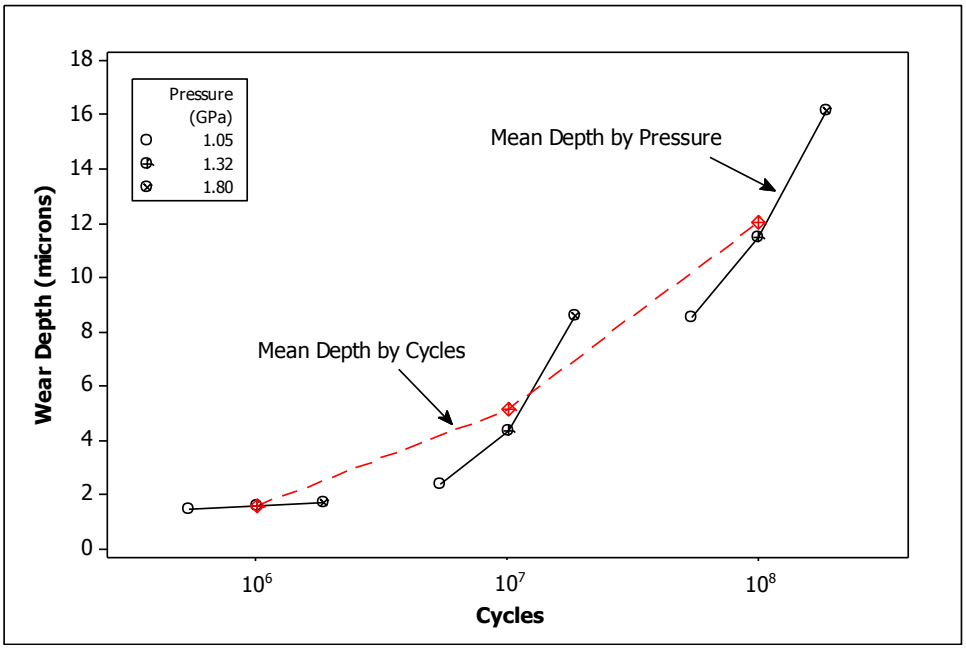


Figure 3.11 Wear depth data for DLC coated chilled cast iron samples as a function of contact pressure and number of cycles. The red hidden line represents the mean wear depth at each level of the factor cycles. The black lines connect the mean values at each contact pressure at a constant number of cycles.

### 3.3.2 Low Frequency Tribometer Testing

Traditional pin-on-disk wear testing was conducted on the same DLC coating that was studied using ultrasonic wear testing. The coating was deposited on both chilled cast iron and hardened SAE 52100 as was done for the very high cycle wear tests. The results of the wear tests are shown in Figures 3.12a, b. The graphs consist of three distinct zones. The first is the shortest and consists of wear on the DLC only. The second consists of continual DLC loss with wear on the steel substrate and the remaining DLC coating. The final zone occurs when the DLC is completely removed from the contact zone and wear is now occurring on the substrate only. These results show that the DLC coating starts to be penetrated around $7x10^4$-$8x10^4$ cycles for all of the tests, with penetration measured at the point where the steady-state coefficient of friction begins to rise. Based on assumed values for the elastic modulus of the DLC coating used in this study, the maximum contact pressure is on the order of 2-3.5 GPa. The wear rate for each test was calculated using the same method used for the very high frequency test results except that the wear volume was modeled as a toroid (Appendix A). The coating thickness was taken to be 2 μm for all samples. The mean wear rate for the DLCs during low cycle wear testing was $2.20x10^{-10}$. This value is very low compared to literature values. Therefore, the wear rate was plotted for both high cycle and low cycle wear in Figure 3.13. In both cases the wear rate decreases due to wear of the pin. As the pin wears the contact pressure decreases according to Hertzian contact mechanics (*F* is the load and E* and R are the effective modulus and radius of curvature of the mating bodies):

$$P_{max} = \left(\frac{6FE^{*^2}}{\pi^3 R^2}\right) \qquad (3.2)$$

Figure 3.13 shows that the low cycle wear data had a substantially larger decrease in wear rate as a function of cycles than did the high cycle wear data. This is due to the fact that the silicon nitride ball was much softer than the synthetic diamond ball. At the high contact loads in the low cycle wear tests, the ball wore rapidly. Assuming that the typical wear rate for a a-C:H DLC is on the order of $10^{-6}$-$10^{-7}$ cycles then the high cycle wear data is only valid from about break-in (~100 cycles) to around 2000 cycles using a silicon nitride ball. At a speed of 500 rpm used for this study, this would be four minutes of valid

testing. For the high cycle wear data the zone of valid data collection would be from about $10^3$ cycles to $10^8$ cycles. Although the usual range of testing for low cycle wear testing would likely increase if a stiffer, stronger ball was used.

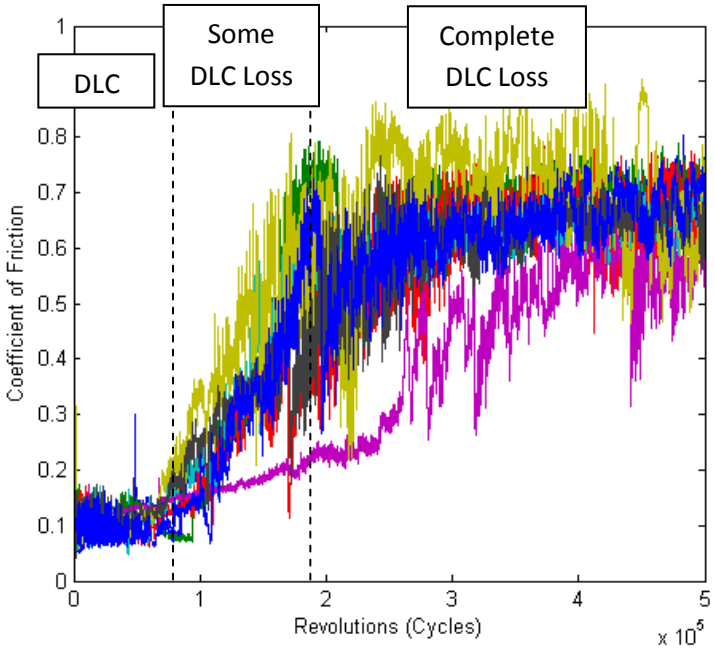


(a)

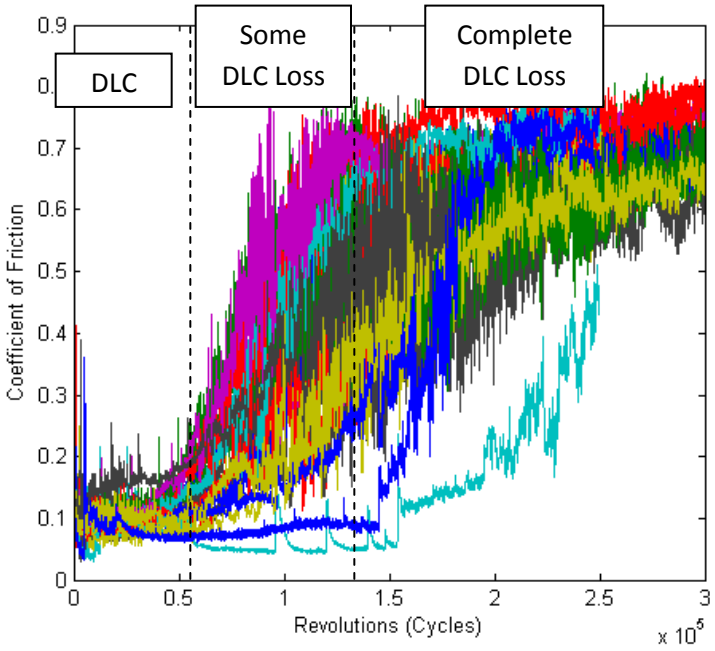


(b)

Figure 3.12 Tribometer pin-on-disk wear test results for a:C:H DLC (a) on SAE 52100 (b) on chilled cast iron.

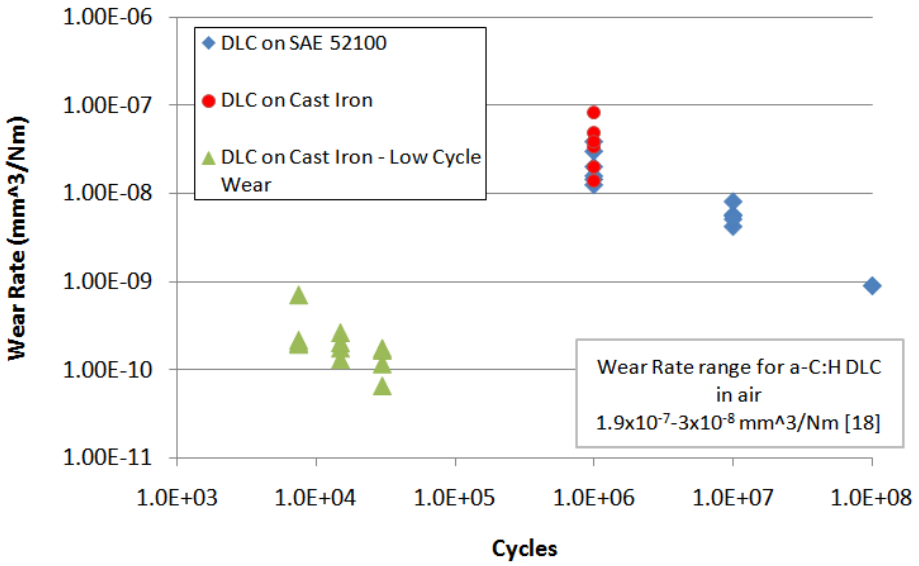


Figure 3.13 Wear rate versus cycles for both the very high cycle wear and low cycle wear) data for DLC coatings on both substrates. The very high cycle wear rates were similar to those in the literature. The wear rates from the low cycle wear data were 1-2 orders of 10 less than the high cycle wear rates. This is mostly due to more ball wear in the softer silicon nitride ball versus the diamond ball used in the high cycle wear testing.

### 3.3.3 Raman Spectroscopy

Raman spectroscopy is a quick and inexpensive method for characterizing DLCs. Carbon materials have three common peaks: G, D, and T at around 1560, 1360 and 1060 $cm^{-1}$, respectively. G is due to the bond stretching of all pairs of $sp^2$ atoms in both rings and chains. D is due to the radial breathing modes (expansion/contraction) of $sp^2$ atoms in rings, and T is due to C-C $sp^3$ vibrations. An example of a a-C:H DLC Raman spectra is given in Figure 3.14. The spectra shape and peak locations changes slightly as a function of the wavelength used in the testing. G peak dispersion is a measure of disordered carbons. The intensity ratio of the D and G peaks [I(D)/I(G)] and the full-width and half max (FWHM) of G are the two other key parameters in Raman measurement. Based on the G dispersion, intensity ratio, and FWHM of the G peak, the density, $sp^3$ content, and percent hydrogen can be determined. Other properties such as modulus, refractive index, and band gap energies can also be empirically derived. As DLCs wear, Raman spectra can help determine the extent of graphitization and hydrogen evolution: key parameters for understanding DLC wear.

Raman spectroscopy was performed on both unworn and worn DLCs. The worn DLC samples came from a worn, but not penetrated spot from a sample tested using the ultrasonic wear system and from a tappet run in an engine where the DLC had separated from some of the substrate (spalled) due to poor adhesion. Testing was performed on the unspalled coating for that sample. The Raman results in Figures 3.15 and 3.16 and Table 3.4 showed no significant difference in the DLC coating on the worn and unworn samples. The D and G peaks were unmoved in the coatings regardless of wear. This is not unprecedented even if a more $sp^2$ – graphite like structure is developing in a transfer film, as it is possible that no transfer film was present at the location in the wear scar where the Raman measurement took place. In order to estimate the $sp^3$ content related to the DLC quality, Spectra 5, 6 and 7 were baseline corrected and band-fitted with two Gaussian-Lorentzian bands at 1560 $cm^{-1}$ (G band) and at 1380 $cm^{-1}$ (D band). From the height ratio of the D and the G bands, it was estimated that the probed spots contained similar amounts of $sp^3$ content at 50-52%; the fraction of $sp^3$ being correlated to coating hardness, modulus, density, and other optical properties.

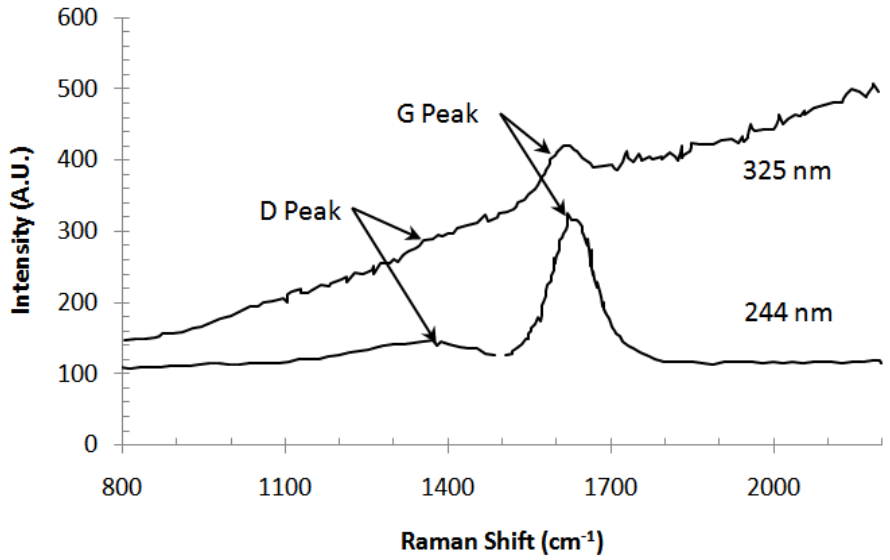

Figure 3.14 Example of Raman spectra for a-C:H DLCs at 325 and 244 nm wavelengths.

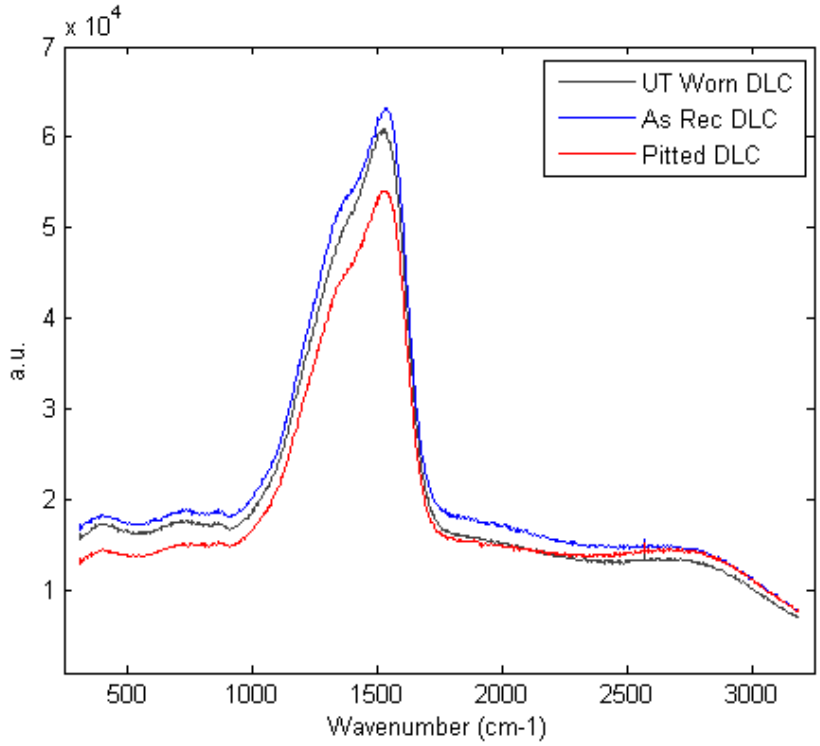


Figure 3.15 Superimposed HeNe laser scans of all three DLC coatings.

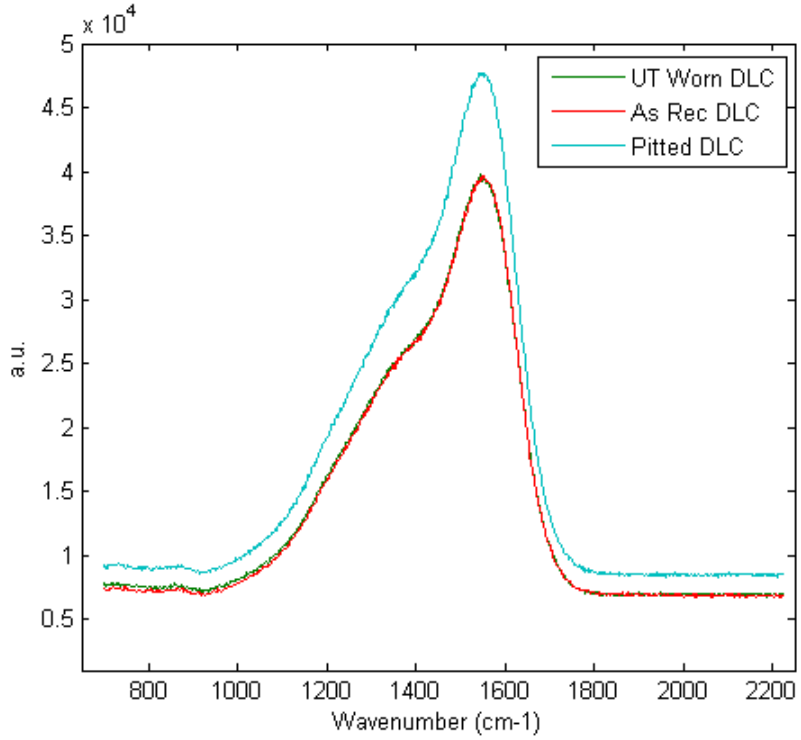


Figure 3.16 Superimposed Argon ion laser scans of all three DLC coatings.

Table 3.4 (a) D and (b) G band data, (c) intensity ratio and estimated $sp^3$ content from the Raman spectroscopy studies

| Sample | D-Band | | | |
|---|---|---|---|---|
| | Peak ($cm^{-1}$) | Width ($cm^{-1}$) | Intensity ($I_D$) | Peak height |
| Field Sample | 1382 | 290 | $5.12x10^6$ | $2.12x10^4$ |
| UT Worn | 1381 | 290 | $4.35x10^6$ | $1.80 x10^4$ |
| Unworn | 1384 | 291 | $4.39x10^6$ | $1.81 x10^4$ |

| Sample | G-Band | | | |
|---|---|---|---|---|
| | Peak ($cm^{-1}$) | Width ($cm^{-1}$) | Intensity ($I_G$) | Peak height |
| Field Sample | 1559 | 131 | $3.19x10^6$ | $2.85x10^4$ |
| UT Worn | 1560 | 131 | $2.63 x10^6$ | $2.36 x10^4$ |
| Unworn | 1561 | 129 | $2.58 x10^6$ | $2.36 x10^4$ |

| Sample | Ratio | Ratio | sp3% |
|---|---|---|---|
| | $I_D/I_G$ | Peak height | |
| Field Sample | 1.61 | 1.00 | 52 |
| UT Worn | 1.66 | 1.00 | 51 |
| Unworn | 1.70 | 1.00 | 50 |

### 3.3.4 Adhesion Testing

The adhesion ratings per VDI 3198 were found to be HF2 for all samples. For the worn engine tappet, the VDI rating was HF4, which is considered to be a borderline adhesion rating. Figure 3.17 shows the visual differences in adhesion ratings HF1-HF6.

### 3.3.5 Summary of Results

No significant difference in the DLC wear depth as a function of cycles or load was observed for the cast iron and steel substrates. A significant difference did exist for the SAE 52100 steel after coating penetration. The wear depth at the higher loads and numbers of cycles was much higher for the steel substrate than the cast iron. Wang et al [12-14] found a similar result for wear of SAE 52100 and SAE 1080 steels, where the wear volume at various contact loads was highest for martensitic forms of both steels and lowest when the microstructure was a lamellar pearlite. In this study, the SAE 52100 had

a tempered martensitic microstructure and the chilled cast iron consisted of lamellar pearlite in a carbide matrix. They concluded that the main difference was due to the lower thermal conductivity of the martensite compared to bainitic or pearlitic microstructures. Thermal conductivity was not measured in this study; however, Wang's theory seems valid in this situation.

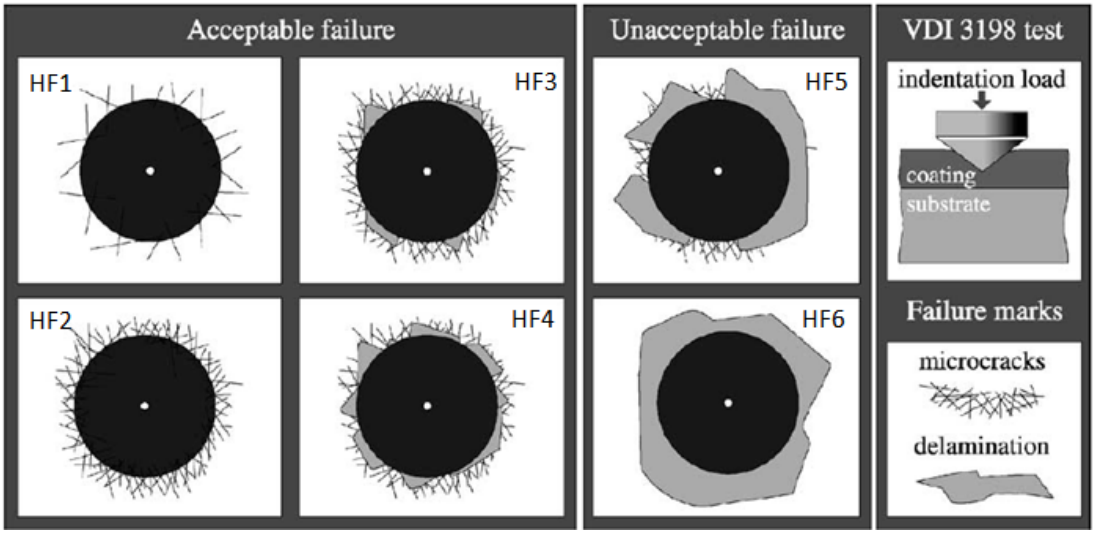


Figure 3.17 Representative pictures of the different adherence ratings per VDI 3198. From N. Vidakis, A. Antoniadis, N. Bilalis, Journal of Materials Processing Technology 143–144 (2003) 481–485.

## 3.4 Modeling the Wear Depth of DLC Coatings

### 3.4.1 Mathematical Model of Wear

A mathematical model was developed to understand the wear depth as a function of the contact pressure and the number of cycles. The wear depth was modeled rather than volume, as depth is a more appropriate design criterion for engineering design using thin films and the density of amorphous thin films can vary.

The model assumes a general form of a power law regression model for the depth of wear $d_{wear}$ versus the number of wear cycles (equation 3.3),

$$d_{wear} = A(N \times C)^{B} \qquad (3.3)$$

"A" can be obtained by using the boundary condition that $d_{wear}$ is equal to the coating thickness at $N_t$ cycles where $N_t$ is defined as the number of cycles to penetrate the coating. Therefore,

$$d_{wear} = t_o = A(N_t \times C)^B, \text{ giving,}$$

$$A = t_o(N_t \times C)^{-B} \qquad (3.4)$$

Combining equations 3.1, 3.3 and 3.4 results in:

$$d_{wear} = t_o \left(\frac{N}{N_t}\right)^B \qquad (3.5)$$

$N_t$ can be determined based on a given wear rate for the material which can be obtained from literature or determined by wear testing. In this work a sphere was used to wear a flat disk using a circular motion for the low cycle wear tests and a reciprocating line motion for the high cycle tests. Therefore, the volume of wear at coating penetration, $V_{wear}$, can be determined from equations 3.5-3.7 where F is the load in Newtons, $k_{rate}$ is the wear rate expressed in $mm^3/Nm$ $r$ is the radius of the sphere, and $\ell$ is the length of travel per cycle. For the low cycle wear $V_{wear}$ will be that of a segment of a toroid which is given in equation 3.6. For the high cycle wear $V_{wear}$ will be that of a segment of an ellipsoid of thickness $t$. In equation 3.6 R is the radius of the toroid. In equation 3.7 $a$ is 30 μm which is half of the total track length for a half cycle. Both equation 3.6 and equation 3.7 are only valid as long as the radius of the ball is greater than the thickness of the coating.

$$V_{Low\ Cycle\ Wear} = 2\pi R\left\{r^2 cos^{-1}\left(\frac{r-t}{r}\right) - (r-t)\sqrt{r^2-(r-t)^2}\right\}, \quad r \geq t \qquad (3.6)$$

$$V_{High\ Cycle\ Wear} = \frac{2\pi}{3} at\sqrt{r^2-(r-t)^2}, \quad r \geq t \qquad (3.7)$$

For the proposed model given in equation 3.3, B is considered to be an experimentally determined fit coefficient on the order of 0.2-0.3, which when combined with equation 3.5 results in the final form of the wear depth up to coating penetration:

$$d_{wear} = t_o \left( \frac{NFk_{rate} l}{V_{wear}} \right)^B \qquad (3.8)$$

### 3.4.2 Comparison of Experimental Data to the Wear Model

To understand the suitability of equation 3.8 and to further understand if ultrasonic wear testing is a valid substitute for traditional tribometry, the calculated wear values were compared to the actual values. As discussed previously, for the high and low cycle wear tests, the wear rate decreased as the number of cycles increased. A similar decrease was seen by other authors [15-17]. It is likely that this is a result of a lower, more stable friction coefficient with time [15-17]. Counterbody wear is also a significant cause of the decreased wear rates in this study, as the balls were not changed out and therefore wore down, especially in the low cycle wear tests. Since no single wear rate was observed for either testing regime a constant rate of $1.45 \times 10^{-8}$ $mm^3/Nm$ and $2.2 \times 10^{-10}$ $mm^3/Nm$ were used for modeling the high cycle and low cycle results, respectively.

For the very high cycle wear results, equation 3.8 was combined with equation 3.7, which with $l_0 = 4a/cycle$ simplifies to:

$$d_{wear} = t_o \left( \frac{6NFk_{rate}}{\pi t \sqrt{r^2 - (r-t)^2}} \right)^B \qquad (3.9)$$

Equation 3.9, calculated with B set equal to 0.26, is shown in Figure 3.18. The model appears to provide a reasonable estimate for DLC wear depths between $10^6$ and $10^7$. It is reasonable to assume that the model would extend to $10^8$ cycles and beyond if the coating could be made thick enough or the load reduced. Using equation 3.9, the number of cycles to coating penetration can be determined by setting $t$ and $d_{wear}$ equal to the coating thickness and solving for $N$.

For the low cycle wear simulation, the wear depth is given as equation 3.10:

$$d_{wear} = t_o \left( \frac{NFk_{rate}}{r^2 cos^{-1}\left(\frac{r-t}{r}\right) - (r-t)\sqrt{r^2 - (r-t)^2}} \right)^B \qquad (3.10)$$

The results for equation 3.3 with B set equal to 0.20, is shown in Figure 3.19. The predicted wear depths were in as close agreement for this simulation as they were for the higher cycle analysis. The main difference in the low cycle wear simulation was that the wear rate was nearly two factors of ten lower.

In both the high and low cycle wear simulations, the equations developed in this paper provide reasonable estimates of the wear depth as a function of contact pressure and cycles under very different testing regimes. Both equations allow for the calculation of the number of cycles to coating penetration using known or easily obtainable parameters. Both test methods provide good analytical approximations for engineering design of hydrogenated DLCs for engine and other high cycle applications. The low cycle wear test is not valid at higher numbers of cycles due to ball wear which leads to non conservative wear results.

## 3.5 Conclusions

1. Ultrasonic wear testing of amorphous-hydrogenated DLC coating on chilled cast iron and SAE 52100 steel was proven to be successful method for determining the number of cycles until coating failure between $10^6$ and $10^8$ cycles and likely beyond.
2. A wear model that reasonably models the wear results was developed. The model can be used for the determination of the number of cycles until coating penetration. The model fit both ultrasonic and classic (low-cycle) tribometer data for wear of DLCs. In the low cycle analysis, the wear rate was nearly two orders of magnitude less than that for the high cycle testing and the literature values for wear of DLCs in air.

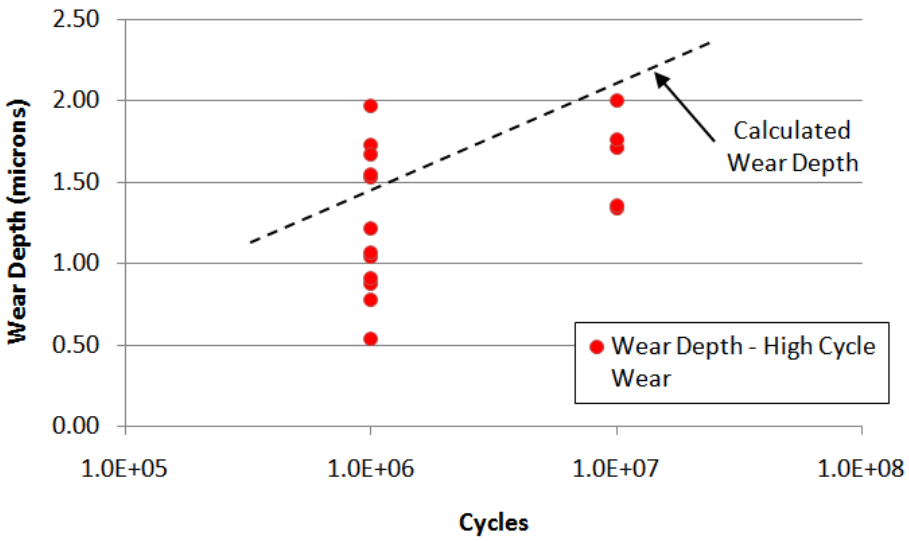


Figure 3.18 Simulated wear curve for the ultrasonic high cycle wear data using equation 3.12. B=0.26 and $k_{rate}$= 1.45x10$^{-8}$ mm3/Nm for the simulation. All DLC wear data were plotted together.

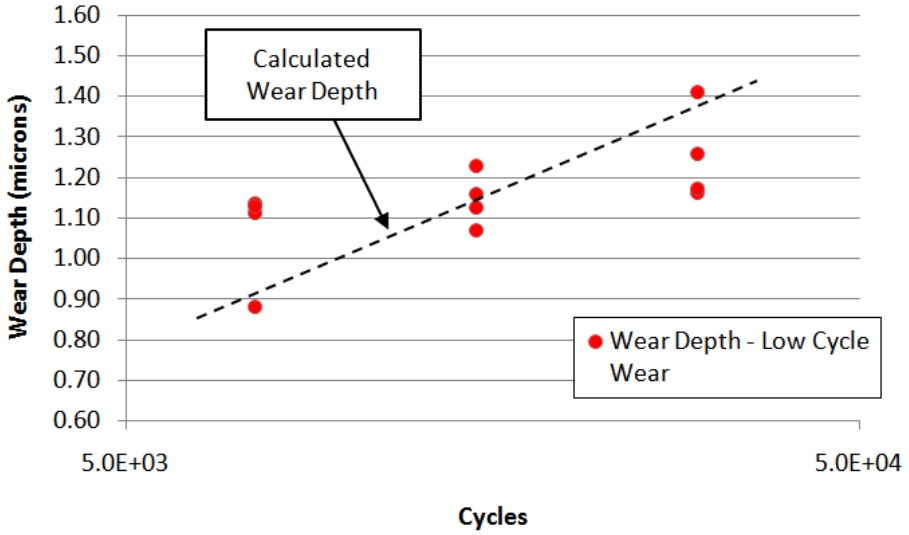


Figure 3.19 Simulated wear curve for the tribometer low cycle wear data. B=0.20 and $k_{rate}$= 2.2x10$^{-10}$ mm3/Nm for the simulation.

## 3.6 References


1. Stern Review on the Economics of Climate Change. Cabinet Office, HM Treasury, (2006).
2. New Science for a Secure and Sustainable Energy Future. US Dept of Energy, (2008)
3. W. Mason, R. Wick. J. Acoustical Society. 23, pp. 209-214, (1951)
4. W. Mason, S. White. Bell System Technical Journal, 31, 3, (1952)
5. B. Blanpain, J. Celis, J. Roos, J. Ebberrink, J. Smeets. Thin Solid Films. 223, pp. 65-71, (1993)
6. K. Schouterden, B. Blanpain, J. Celis, O. Vingsbo. Wear, 181-183, pp. 86-93, (1995)
7. O. Vingsbo, J. Schon. Wear, 162-164, pp. 1129-1138, (1993)
8. D. Spaltmann, M. Hartelt, M. Woydt. Wear, 266, (2009), p 167-174
9. J. Robertson. Materials Science and Engineering R 37, pp. 129-161, (2002)
10. A. Voevodin, A. Phelps, J. Zabinski, M. Donley. Diamond Rel. Mater. 5, pp. 1264-1269, (1996)
11. H. Ronkainen, K. Holmberg, Environmental and Thermal Effects on the Tribological Performance of DLCs, in Tribology of Diamond Like Carbon Films. eds C. Donnet, A. Erdemir. Springer, (2008)
12. Y. Wang, T. Lei, J. Liu. Wear, 231 (1999), p 1-11
13. Y. Wang, T. Lei, J. Liu. Wear, 231 (1999), p 12-19
14. Y. Wang, T. Lei, J. Liu. Wear, 231 (1999), p 20-37
15. M. Hakovirta, J. Vuorinen, X. He, M. Nastasi, R. Schwarz. Applied Physics Letters, Vol 77, No. 15, pp. 2340-2342, (2000)
16. A. Grill. Surface and Coatings Technology. 94-95, pp. 507-513, (1997)
17. T. Scharf, I. Singer. Third Bodies and Tribochemistry of DLC Coatings, in Tribology of Diamond Like Carbon Films. eds C. Donnet, A. Erdemir. Springer, (2008)

## 3.7 Appendix A – Derivation of Equations (3.6) and (3.7)

**Wear volume of a hemispherical cap (partial ellipsoid)**

$$V_{High\ Cycle\ Wear} = \frac{2\pi}{3} at\sqrt{r^2 - (r-t)^2}, \quad r \geq t$$

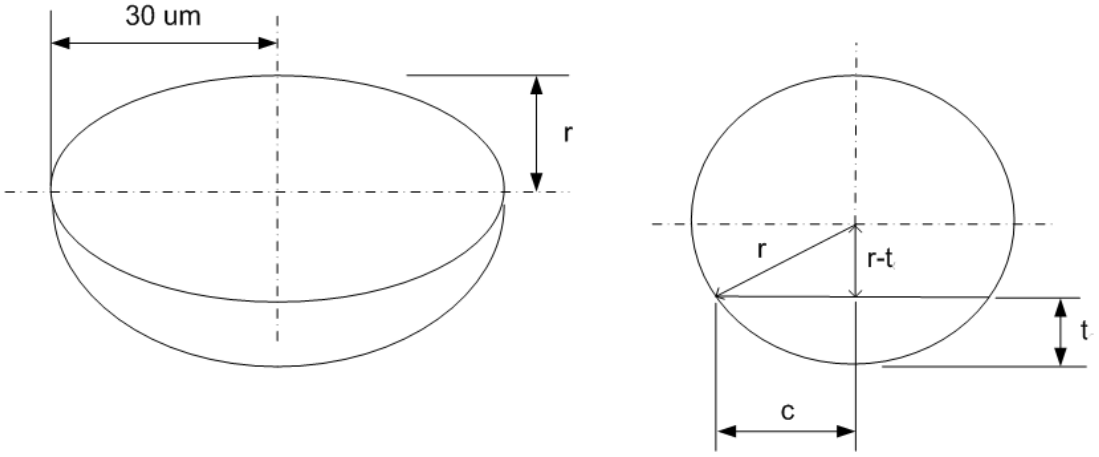


Start with the equation for volume of half of an ellipsoid:

$$V_{High\ Cycle\ Wear} = \frac{2\pi}{3} atc$$

Where *a*, *b*, and *c* are the radii of the principal axes and the height of the ellipsoid. Since *a* is the half length of travel or 30 μm and *t* is the wear depth, we have only to find the value of c, which is easily done using the Pythagorean theorem

$$c = \sqrt{r^2 - (r-t)^2}$$

Therefore,

$$V_{High\ Cycle\ Wear} = \frac{2\pi}{3} at\sqrt{r^2 - (r-t)^2}, \quad r \geq t$$

**Wear volume of a partial toroid**

$$V_{Low\ Cycle\ Wear} = 2\pi R\left\{r^2 cos^{-1}\left(\frac{r-t}{r}\right) - (r-t)\sqrt{r^2-(r-t)^2}\right\}, \quad r \geq t$$

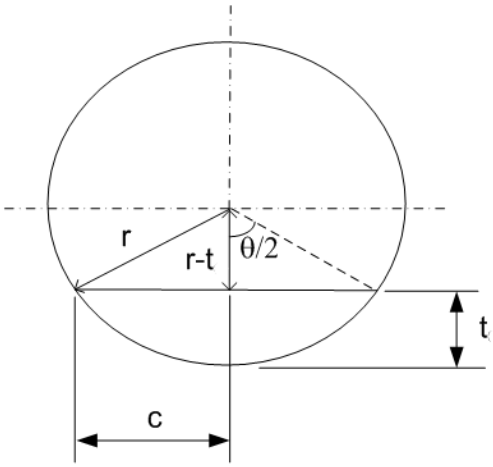


Start with the equation for area of circle segment, which is the area of a circle sector minus the area of the triangle with two sides equal to the radius of the circle.

$$A = A_{sector} - A_{triangle}$$

The area of a circle sector is:

$$A_{sector} = \pi r^2 \frac{\theta}{2\pi}$$

The value of the angle is:

$$\theta = 2cos^{-1}\left(\frac{r-t}{r}\right)$$

The area of the whole triangle (with sides r and r) is:

$$A_{triangle} = \frac{(r-t)}{2}\sqrt{r^2-(r-t)^2}$$

Therefore,

$$A = r^2 cos^{-1}\left(\frac{r-t}{r}\right) - (r-t)\sqrt{r^2-(r-t)^2}$$

Which when multiplied by the length of the toroid gives,

$$V_{Low\ Cycle\ Wear} = 2\pi R\left\{r^2 cos^{-1}\left(\frac{r-t}{r}\right) - (r-t)\sqrt{r^2-(r-t)^2}\right\}, \quad r \geq t$$

Where R is the radius of travel/toroid

# CHAPTER 4

## Laser Hardening of Steel: the Affect of Laser Hardening on Resisting Contact Fatigue in SAE 8620, 4140, and 52100 steels

### 4.1 Introduction

Most camshafts today are made from low to medium carbon steel or ductile chilled iron. For low carbon steels, gas carburizing is used to diffuse enough carbon into the surface of the camshaft lobes and bearing surfaces to allow for a hardening heat treatment resulting in a tempered martensitic case. Laser hardening is a possible alternative to traditional carburizing in that it can achieve a case hardness that meets or exceeds that of carburizing in steels with sufficient carbon content. The processing cycle times and part distortion can also be reduced, as well as the environmental impact.

Research into laser hardening of low alloy steels has been ongoing for more than four decades. In that time, much work has been done to determine optimum laser parameters and the effects of lasers on the microstructure and properties of various steels [1-45]. In laser hardening, a focused or slightly defocused beam is moved across the workpiece with laser power densities sufficient to heat the steel into the austenite region (Figure 4.1a). Because the heating times can be made so brief, grain coarsening can be avoided and the austenitizing times can be made very short, resulting in low distortion of the work piece and the formation of a fully martensitic structure with little retained austenite in easily hardenable steels. Some of the earliest work on laser interaction with steels was published in the late 1960s and early 1970s (Barchukov [1] and Annenkov [2]]. Since then, it has been shown that not only can low-alloy steels with high hardenability be effectively laser hardened, but that plain carbon steels with carbon contents as low as approximately 0.18 wt % can be hardened via a martensitic transformation (Fly et al. [3]). It has been shown by Seaman [4] that the carbon rich austenite surrounding the dissolved or partially dissolved pearlite that is typical of plain carbon, non-hardenable steels can quench out to martensite typical of higher carbon steels. The use of laser hardening has been shown to decrease the wear rates of medium carbon/chromium steels by as much as 150% due to significant increases in hardness and in part to the large residual

compressive stresses that can arise during the laser hardening process [40-45]. Unfortunately, overlapping laser tracks cause mixed compressive and tensile residual stresses across the longitudinal axis of the laser path with the negative effect of increasing crack propagation rates [36-38] and decreasing fatigue strength [3]. The effects that these complex stress fields have on contact fatigue have not been explored extensively. Using Weibull statistical analysis Zhang et al. [44] compared the contact fatigue lives of case hardened versus laser hardened samples of two high chromium steels with 0.17-0.24 wt % C and 0.37-0.344 wt % C, respectively. They found laser hardened steels to be weaker than carburized steels above $4.5x10^6$ cycles due to higher amounts of retained austenite. Below $4.5x10^6$ cycles, the laser hardened samples had longer lives. Other authors focused more on the overall wear rates and did not explore how cracks formed and propagated on the basis of contact load, friction, and plastic deformation resistance of the steel.

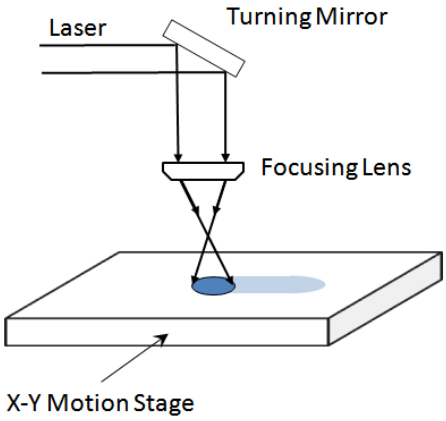


(a)

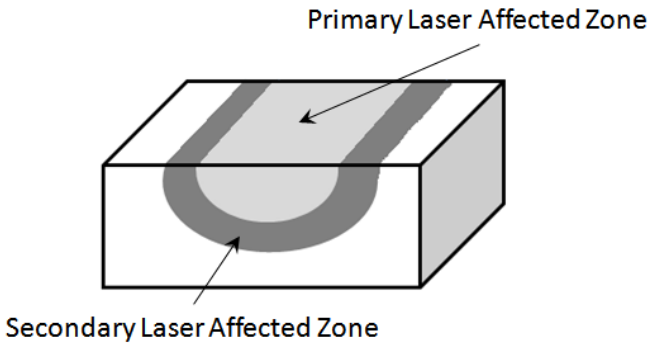


(b)

Figure 4.1 Schematic of the (a) laser heating process and the (b) laser affected zones.

Therefore, this study will investigate both empirically and analytically how laser hardening of various heat treated steels affects the general wear and contact fatigue properties, and controlling mechanisms. The effects of residual stresses between laser tracks will also be studied qualitatively. Finally, optimal steels and heat treatments to provide for an equivalent to conventional gas carburizing will be discussed.

## 4.2 Experimental Methods

### 4.2.1 Design of Experiments

A $2x3^3$ full factorial design of experiments (DOE) with beam size, laser power, and translation speed as variables, was run on SAE 8620 steel using a Rofin-Sinar continuous wave carbon dioxide laser with a $TEM_{00}$ (Gaussian) wave mode. The DOE is shown in Table 4.1. Additional tests using SAE 4140 and SAE 52100 materials were used to determine the combinations of speed and laser power that resulted in adequate hardness and depth of penetration to meet the values typical of carburized SAE 8620 used for camshafts. The pre-laser hardening heat treatments of each steel are given in Table 4.2. The compositions of each steel are given in Table 4.3.

Table 4.1 Details of the DOE factors and levels.

| Material | Beam Size (μm) | Laser Power (W) | Translation Speed (mm/s) | Replicates |
|---|---|---|---|---|
| **SAE 8620** | 790, 820, 910 | 1250, 1500, 1750 | 4.2, 8.5, 12.7 | 2 |
| **SAE 4140** | 680 | 1250, 1500 | 4.2, 8.5, 12.7 | 1 |
| **SAE 52100** | 680 | 1250, 1500 | 4.2, 8.5, 12.7 | 1 |

Table 4.2 Heat treating of the various alloys was accomplished via the following recipes.

| Material | SAE 8620 | SAE 4140 | SAE 52100 |
|---|---|---|---|
| **Normalize** | 3 hrs at 900°C in air, furnace cool | 3 hours at 900°C in air, furnace cool | 3 hours at 900°C in air, furnace cool |
| **Hardening** | | | |
| **Anneal** | 3 hours at 840°C followed by an oil quench | 3 hours at 840°C followed by an oil quench | 3 hours at 840°C followed by an oil quench |
| **Temper** | 260°C for 3 hours | 430°C for 3 hours | 230°C for 3 hours |
| **Annealing** | | | |
| **Anneal** | 3 hours at 885°C, cool to 660°C and hold for 4 hours | 3 hours at 840°C, air cool | |

Table 4.3 Chemical compositions of each steel in wt%. Chemical analysis was made with a Spectro Optical Emission Spectrometer.

| Element | SAE 8620 | SAE 4140 | SAE 52100 |
|---|---|---|---|
| **C** | 0.239 | 0.486 | 1.12 |
| **Si** | 0.232 | 0.207 | 0.215 |
| **Mn** | 0.84 | 0.93 | 0.383 |
| **P** | 0.010 | 0.012 | 0.007 |
| **S** | 0.024 | 0.034 | 0.023 |
| **Cr** | 0.53 | 1.12 | 1.60 |
| **Mo** | 0.178 | 0.219 | 0.0014 |
| **Ni** | 0.451 | 0.02 | 0.059 |
| **Al** | 0.025 | 0.023 | 0.018 |

| | | | |
|---|---|---|---|
| **Co** | 0.006 | 0.002 | 0.004 |
| **Cu** | 0.117 | 0.019 | 0.096 |
| **Nb** | 0.005 | 0.009 | 0.011 |
| **Ti** | 0.001 | 0.000 | 0.000 |
| **V** | 0.003 | 0.006 | 0.0041 |
| **Pb** | <0.003 | <0.003 | <0.003 |
| **Sn** | 0.004 | <0.001 | 0.005 |
| **As** | <0.004 | <0.004 | <0.004 |
| **Zr** | 0.003 | 0.002 | 0.003 |
| **B** | 0.001 | 0.002 | 0.001 |
| **Zn** | 0.011 | <0.001 | <0.001 |
| **Iron** | 97.294 | 96.910 | 96.434 |

### 4.2.2 Wear Testing

Wear testing was performed using a 10 or 30N normal load and a 3.175 mm diameter silicon nitride ball with a Nanovea pin-on-disk tester operating at 500 RPM. All wear testing was performed dry.

### 4.2.3 Hardness Testing

Hardness testing was performed using a Schmadzu microhardness indenter per ASTM E 384 at a 100 gram load for all tests. Many microhardness test data in this paper are either expressed as Vickers hardness numbers or HRC equivalents based on ASTM A307. Macrohardness testing was performed with a Wilson Instruments Series B2000 by Instron tester.

## 4.3 Results

Hardness was a major parameter of interest in the DOE with Vickers hardness results given in Figures 4.2a-c for each steel individually. The different laser affected zones as depicted in Figure 4.1b are noted. Response surface modeling (RSM) of the DOE with the carbon content of the steel, translation speed of the laser, and laser power as control variables was performed; the response variable being the material hardness. RSM models the hardness as a function of the input variables resulting in the form: hardness = $f$ ($x_1$, $x_2$, $x_3$) + $e$. The assumed form of $f$ is a linear polynomial with constants $b_n$ ($y = b_o + b_1x_1 + b_2 x_2 + e$) with all variables being independent and $e$ representing a normal variance of each

hardness result around the sample mean. A graph of the hardness as a function of carbon content and translation speed is shown in Figure 4.3. The percent carbon content was found to have the most significant affect on the mean hardness. A local maximum in the hardness was observed at approximately 0.7% carbon content for all translation speeds.

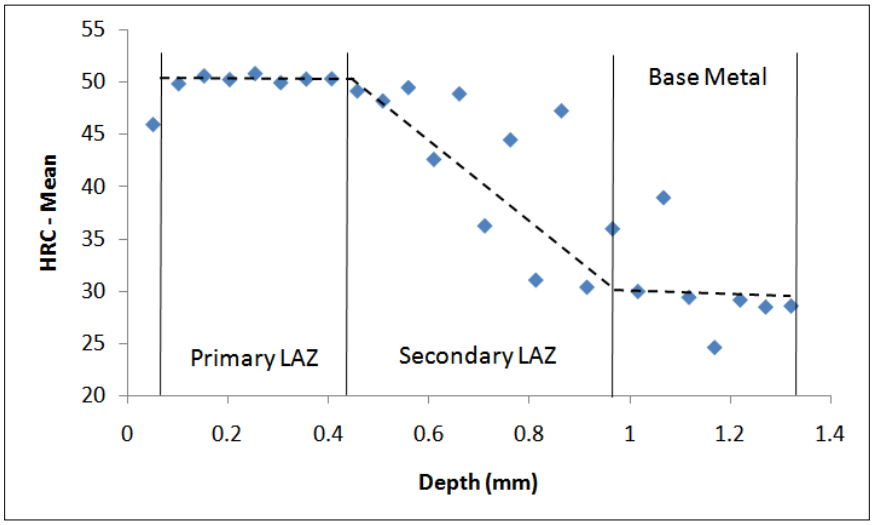


(a)

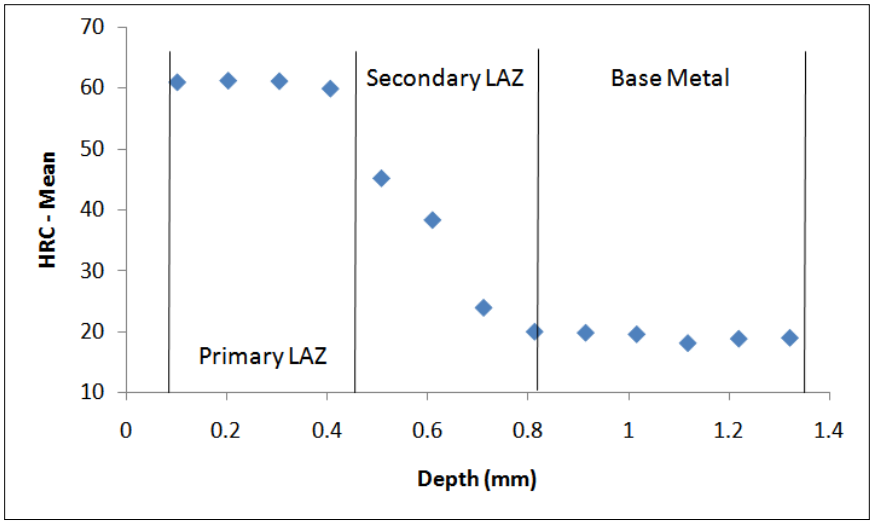


(b)

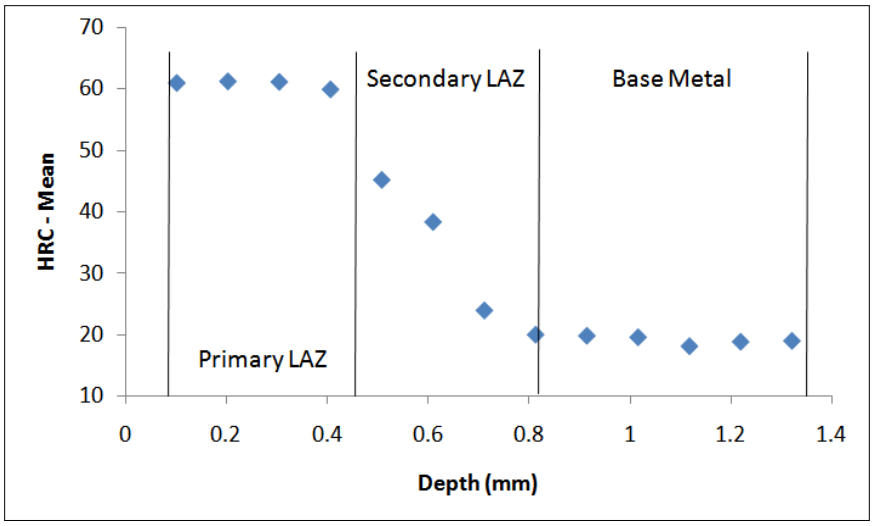


(c)

Figure 4.2 Mean plot for the Vickers hardness traces (converted to HRC) of the (a) SAE 8620 laser hardened samples from the DOE, (b) SAE 4140 samples, (c) SAE 52100 samples. The different laser affected zones are shown as transitions in the hardness.

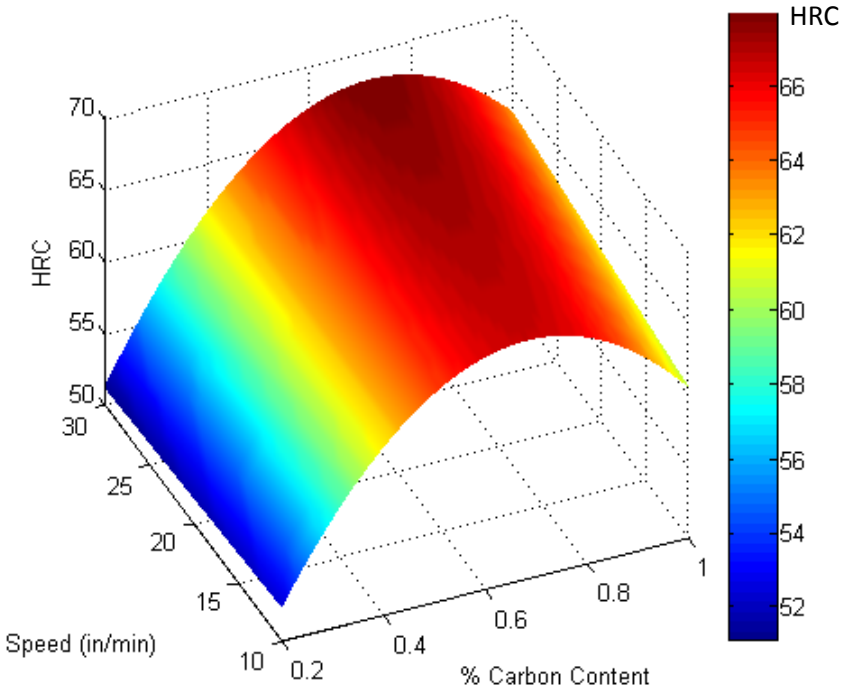


Figure 4.3 Graph of the response surface modeling of the hardness as a function of carbon content and translation speed.

The depth of the laser affected zone (LAZ) measured using light microscopy and a Vickers hardness trace was analyzed from the DOE. The depth of the LAZ was found to be controlled by the power and translation speed with % carbon content having no significant bearing on the depth (Figure 4.4). Beam size was not considered as a factor. Figures 4.4a-c show optical micrographs of an SAE 8620 sample from the DOE processed at a beam size of 790 μm, laser power of 1250 W, and a translation speed of 4.2 mm/s. The microstructure throughout the LAZ of the sample appears to be a lath martensite consistent with lower carbon steels cooled quickly from austenite. Intentional overload fracture through the LAZ, shown in Figures 4.6a-c found a typical ductile-dimple fracture surface with many MnS inclusions present, consistent with hardened ductile steel. In Figure 4.6b the MnS inclusion is shown to have spheriodized during laser process indicating that the temperature was high enough during processing to melt the MnS inclusions.

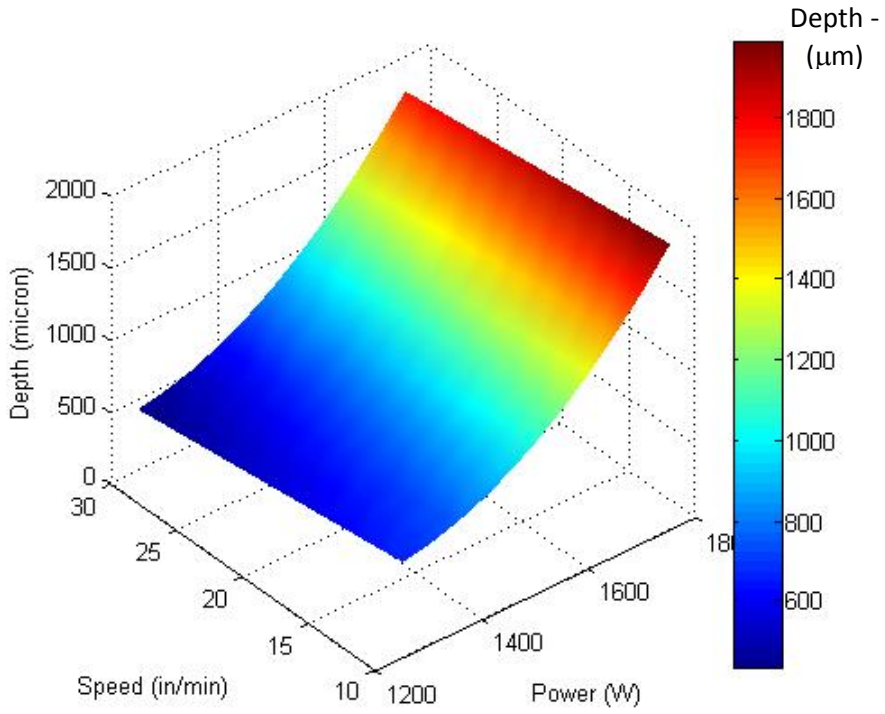


Figure 4.4 Response surface modeling of the depth of the laser-affected zone (HAZ) as a function of translation speed and laser power from the DOE with assumed constant beam size.

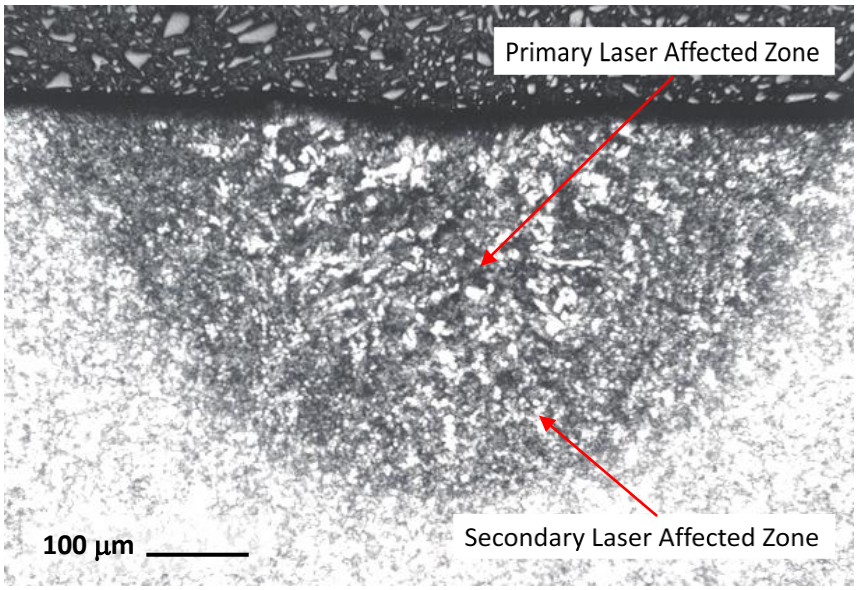
Primary Laser Affected Zone
Secondary Laser Affected Zone
100 µm

(a)

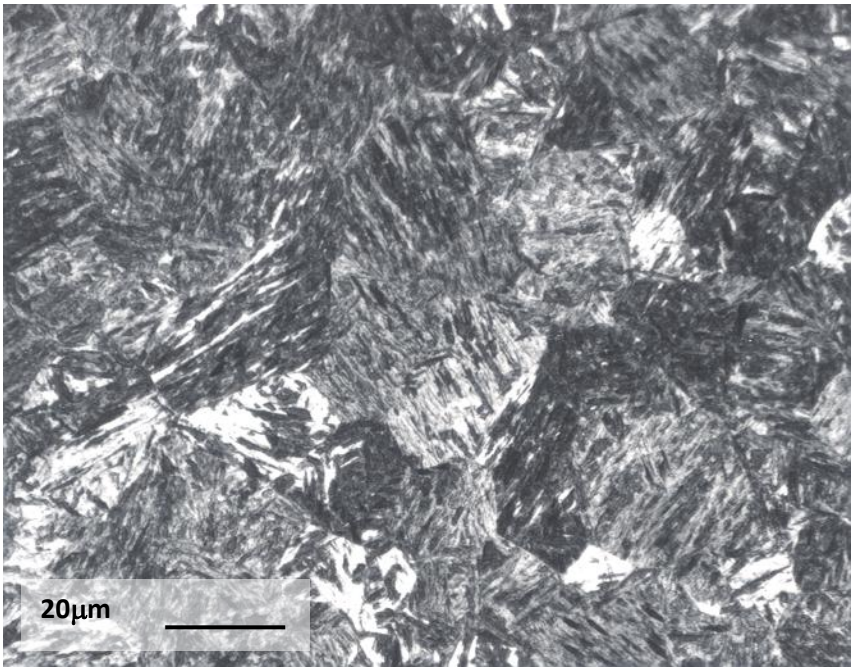
20µm

(b)

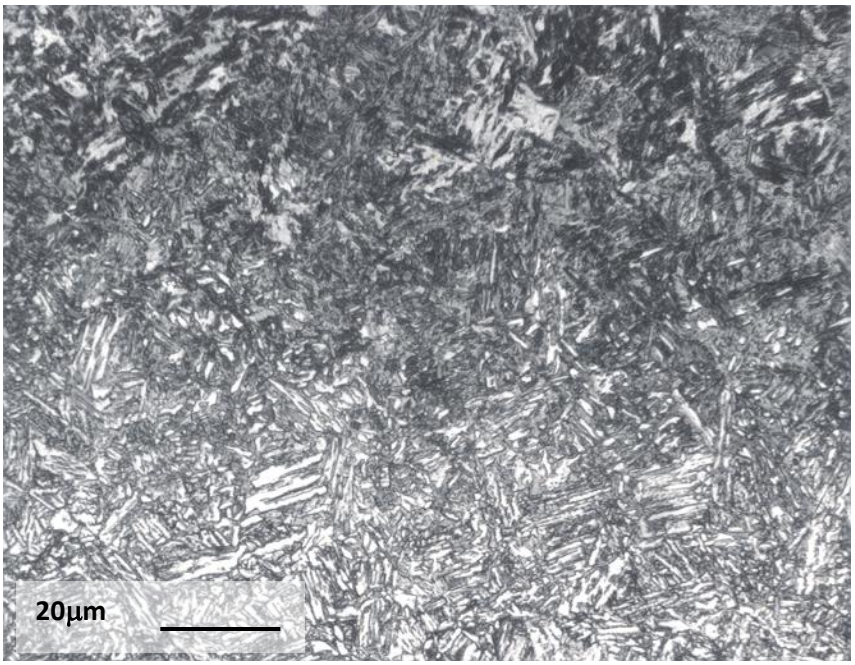


(c)

Figure 4.5 (a-c) Cross-section through the laser track of an SAE 8620 sample from the DOE in the, (b) primary laser hardened zone and (c) secondary laser hardened zone.

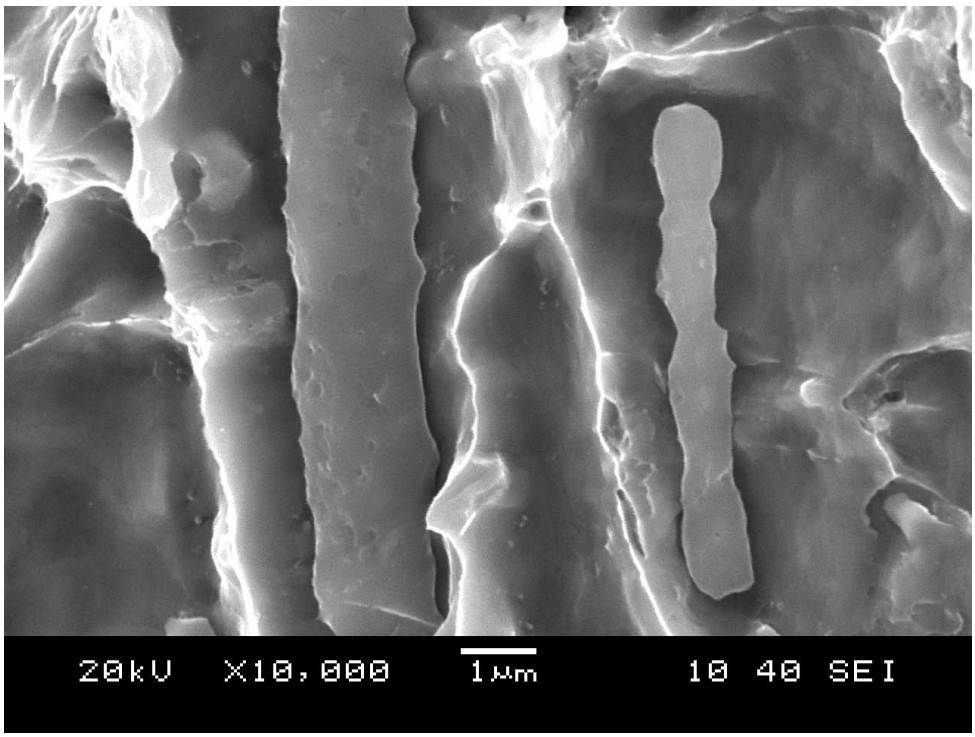


(a)

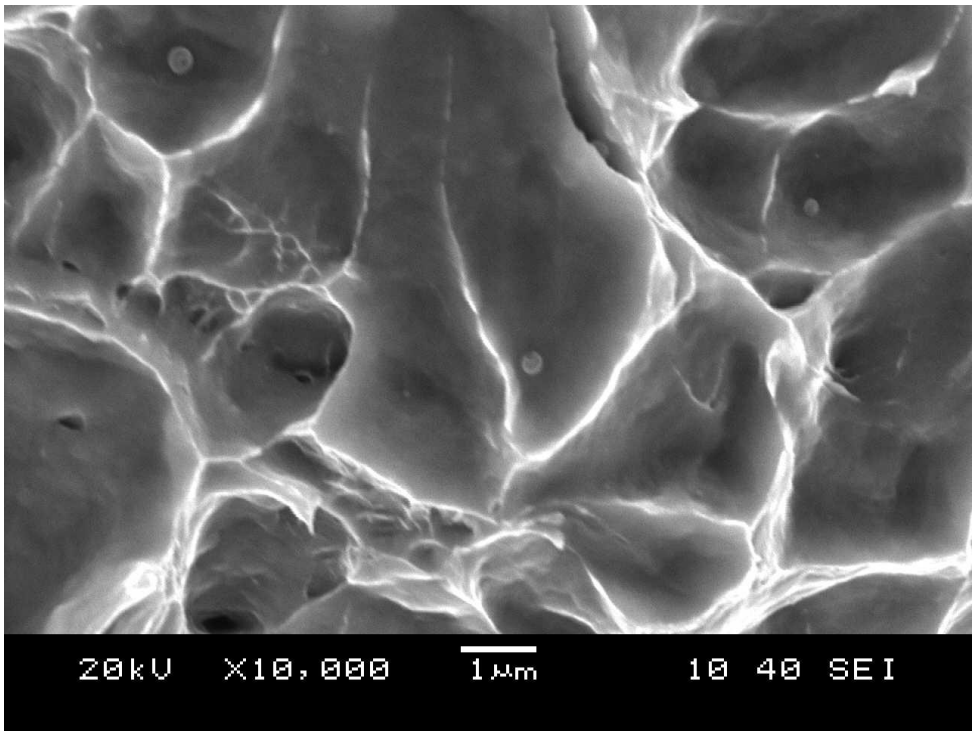


(b)

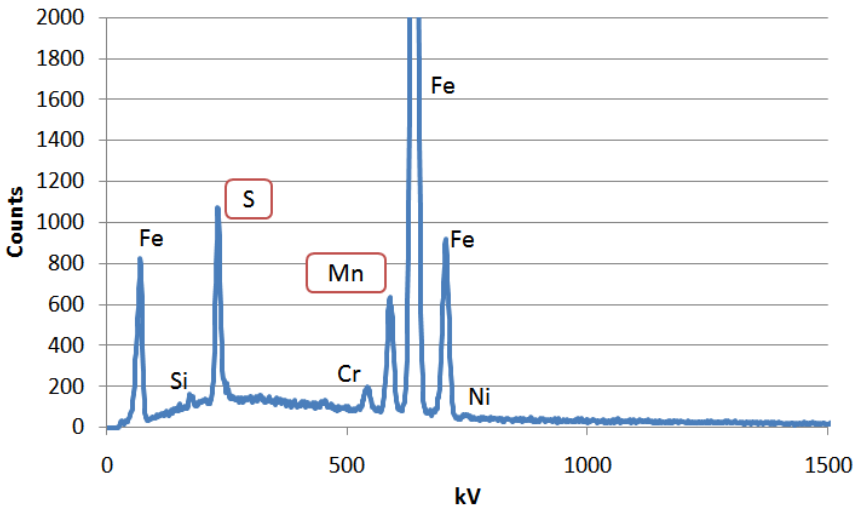


(c)

Figure 4.6 (a) MnS inclusions in the base metal of an SAE 8620 sample prior to laser hardening (b) MnS inclusion after laser hardening, (c) Energy dispersive spectrograph of the inclusion. The iron, chromium, nickel, and silicon are from the steel.

Figures 4.7a-c shows a cross-section through a SAE 4140 sample processed at a beam size of 680 µm, laser power of 1500 W, and a translation speed of 4.2 mm/s. The

microstructure in the LAZ was a lath martensite similar to that seen in the hardened SAE 8620 steel. The martensitic microstructure transitioned into the banded pearlite and ferrite microstructure of the non-laser processed steel. Figures 4.8a-d shows a cross-section through an SAE 52100 sample processed at a beam size of 680 μm, laser power of 1500 W, and a translation speed of 4.2 mm/s. The microstructure consisted of plate martensite with large amounts of retained austenite (white areas in photomicrographs). Two other LAZs were observed (labeled secondary and tertiary). The secondary LAZ consisted of some retained austenite and a pearlite with uniformly distributed carbides microstructure. The tertiary LAZ consisted of was between the pearlite with uniformly distributed carbides microstructure only.

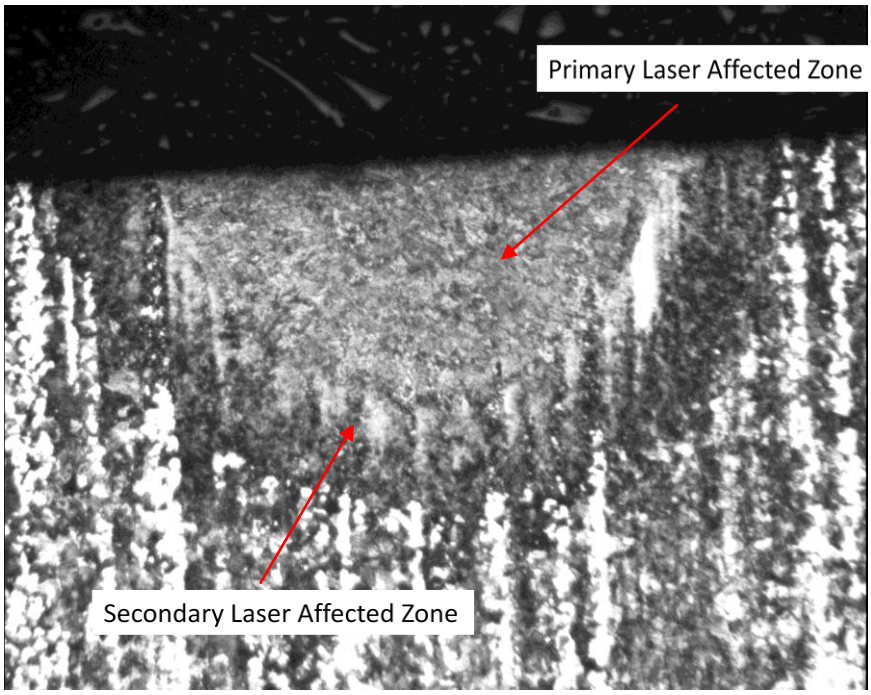


(a)

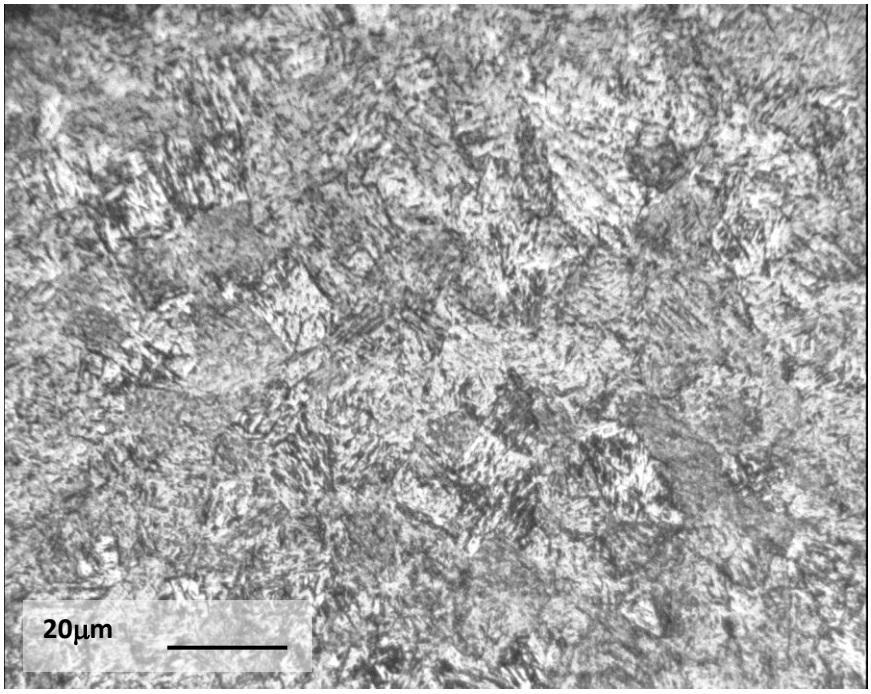


(b)

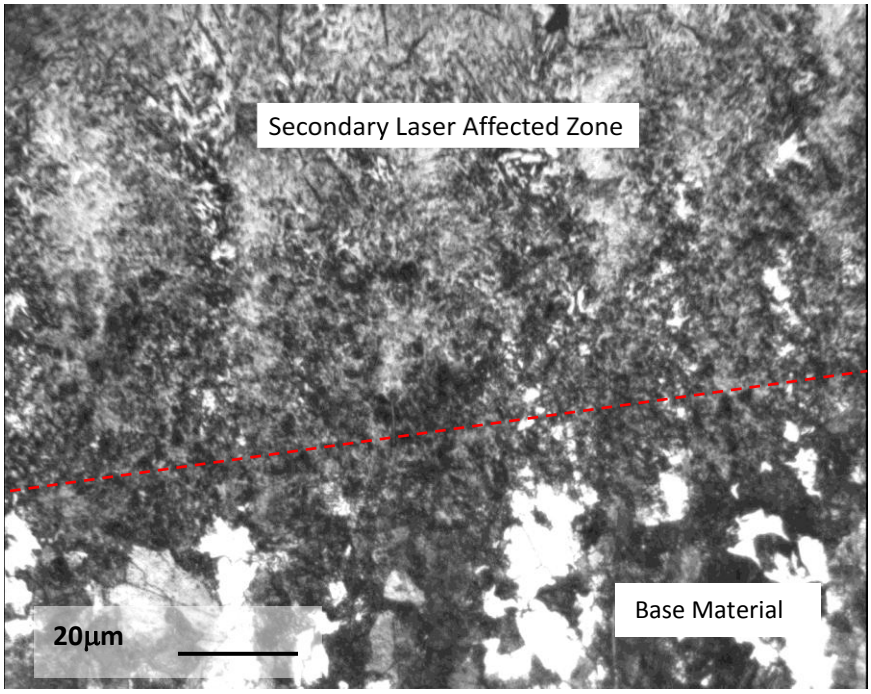


(c)

Figure 4.7 (a-c) Cross section through laser hardened SAE 4140. Martensitic laser hardened zone in a banded pearlite (dark bands) and ferrite (white bands) base microstructure. (b) The secondary LAZ, (c) transition from the secondary LAZ to the banded pearlite/carbide base steel microstructure.

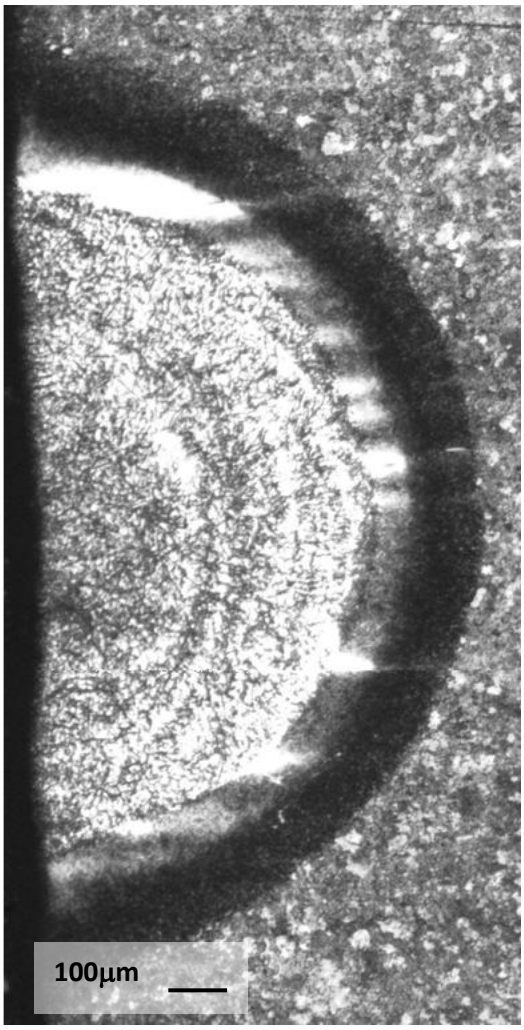


(a)

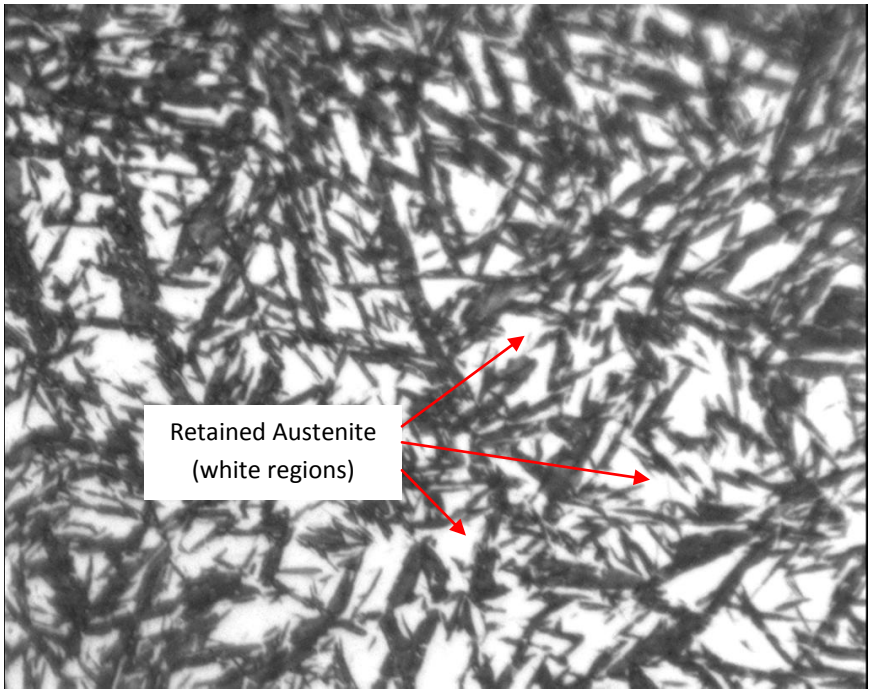
Retained Austenite
(white regions)

(b)

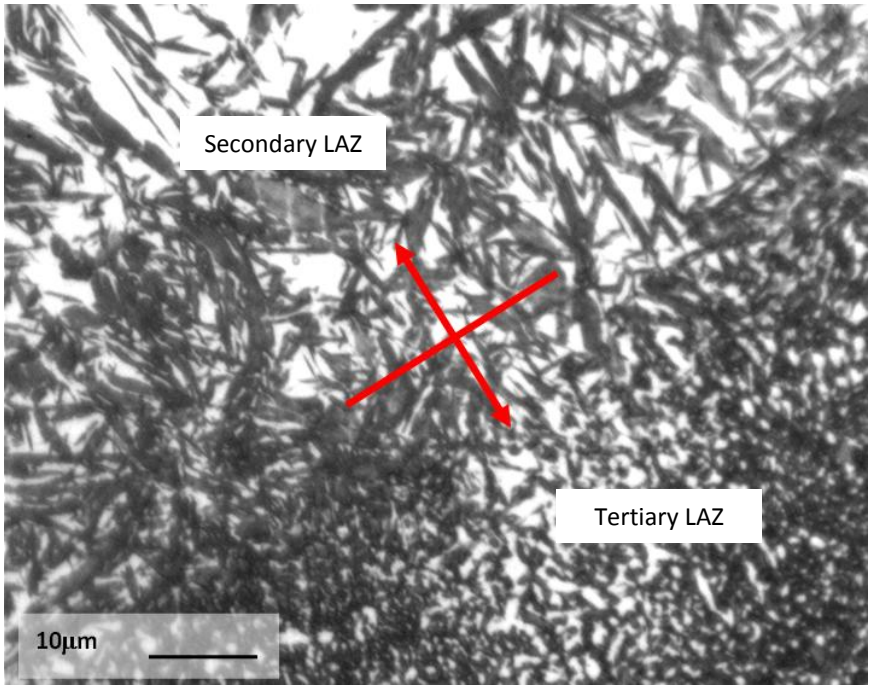
Secondary LAZ
Tertiary LAZ
10µm

(c)

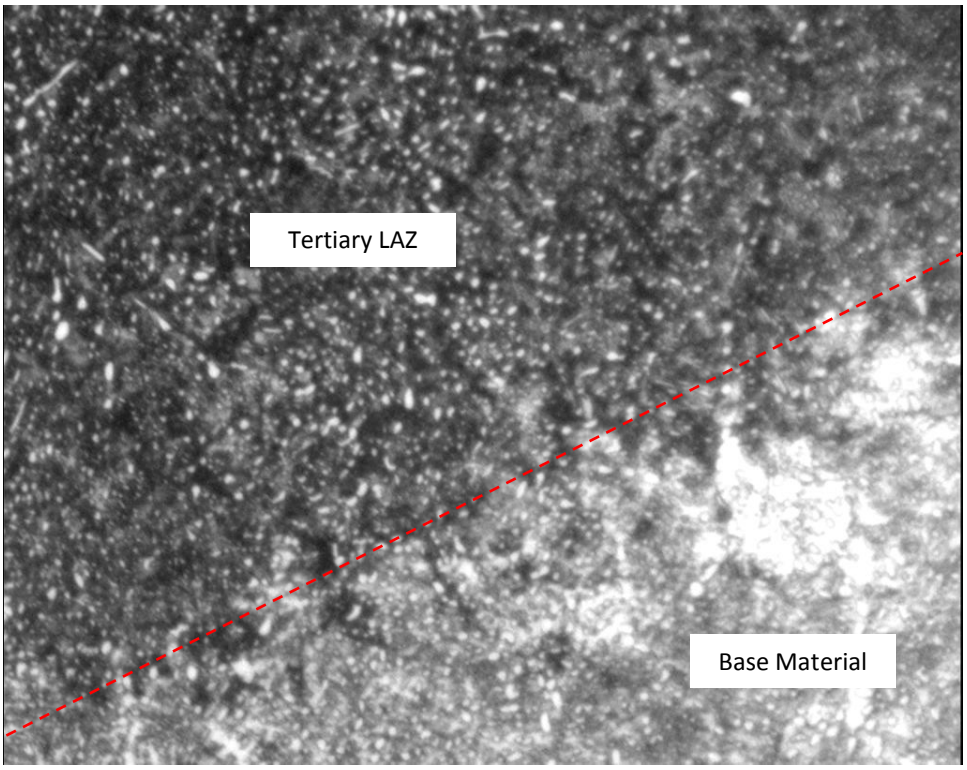


(d)

Figure 4.8 Cross section through an SAE 52100 sample processed at a beam size of 680 μm, laser power of 1500 W, and a translation speed of 4.2 mm/s. The white areas in the laser affected zone in photos (a-c) are retained austenite. The smaller spherical white spots in photo (d) are carbides.

### 4.3.1 Wear Testing

#### 4.3.1.1 General Wear Comparison

Wear testing was performed on the three heat treated steels before and after laser processing. Initial wear testing was performed on samples that were laser heat treated per Figure 4.9. Laser tracks were made at various separation distances to determine if the distance between the tracks affected the degree of wear and the wear mechanism. Figures 4.10a, b are scanning electron microscope (SEM) images of the worn laser tracks and surrounding areas for a normalized and annealed SAE 8620 (8620 N+A) sample run at a translation speed of 0.42 m/s with laser track separation of 1.5 mm. Severe contact fatigue wear, indentified by large plastically deformed wear particles, was observed in the soft non-laser hardened areas outside of the laser tracks. Between the tracks, the wear was significantly less. The wear on the laser lines was less than the non-laser heat treated

areas, consisting mainly of what appeared to be a shallow, plastically driven polishing wear more typical of mild wear seen in harder steels; a comparison to the other steels at the same wear testing parameters are shown in Figures 4.10-4.14. Figures 4.10a-b for normalized and hardened SAE 8620 (8620 N+H) steel show similar results as that seen in the 8620 N+A sample, but with slightly more wear between the tracks. The same was seen for the laser hardened normalized and annealed SAE 4140 shown in Figures 4.12a-b, except for the laser hardened lines which appeared to be less worn than in both SAE 8620 samples. Figures 4.13a-b show the mild wear between and on the laser tracks for normalized and hardened SAE 4140. Similarly, reduced wear was observed in normalized SAE 52100 (Figures 4.4a-b) with severe, contact fatigue driven wear seen outside of the laser hardened zone (Figure 4.14b). The normalized and hardened SAE 52100 steel showed the best wear results in both the laser hardened and non-laser hardened areas as shown in Figures 4.15a-b. Some evidence of severe wear is seen in the non-laser hardened area with only mild polishing wear seen in the laser hardened track and between the tracks. These results suggest that both carbon content and microstructure type play significant roles in the severity of wear in these steels. For all samples, the amount of wear was different not only between the laser tracks and the non-laser treated material, but also in small heat affected zones (secondary laser affected zones as shown in Figure 4.1b) on both sides of the laser track. Examples of this are shown in Figures 4.10-4.15. As the separation distance between laser tracks decreased the total wear damage was observed to decrease for all separation distances. Although residual stresses tend to be tensile toward the primary LAZ boundary, the increased hardness in the laser affected zones most likely had a stronger impact on decreasing the wear than the residual stresses did in increasing wear. For the SAE 52100 steel the amount of wear damage was only significantly reduced for the normalized sample. The hardened sample exhibited little to no difference in wear between the tracks, most likely due to the high hardness in the base material.

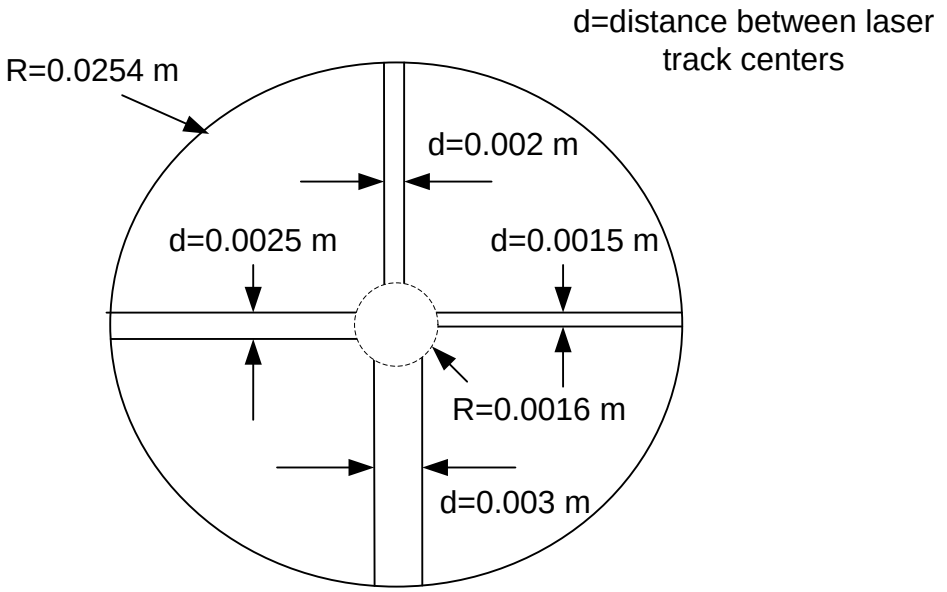


Figure 4.9 Pattern for making laser treated samples with various distances between track centers.

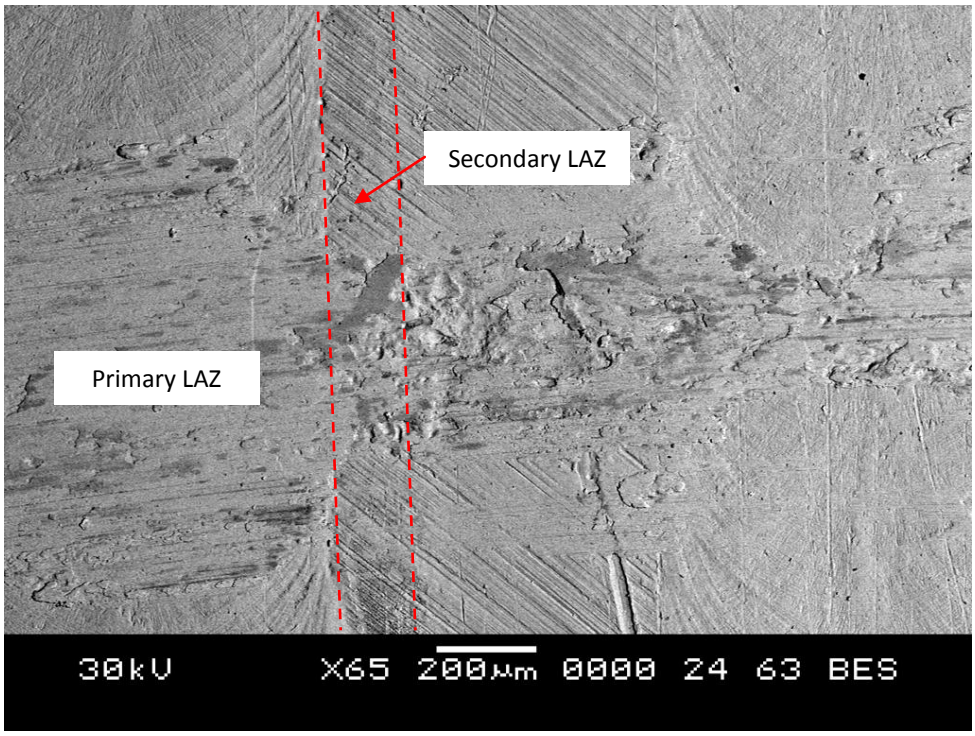


(a)

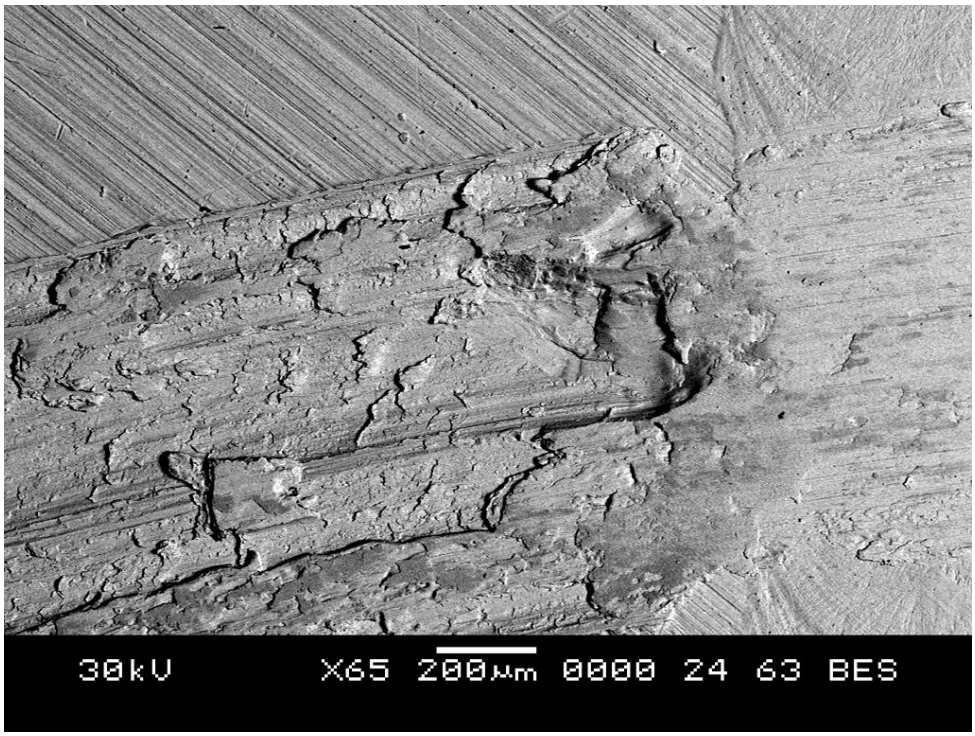


(b)

Figure 4.10 Normalized and annealed SAE 8620 laser heat treated tracks at a 1.5 mm separation distance, wear tested for 5000 cycles at a 0.42 m/s translation speed with a 30N load.

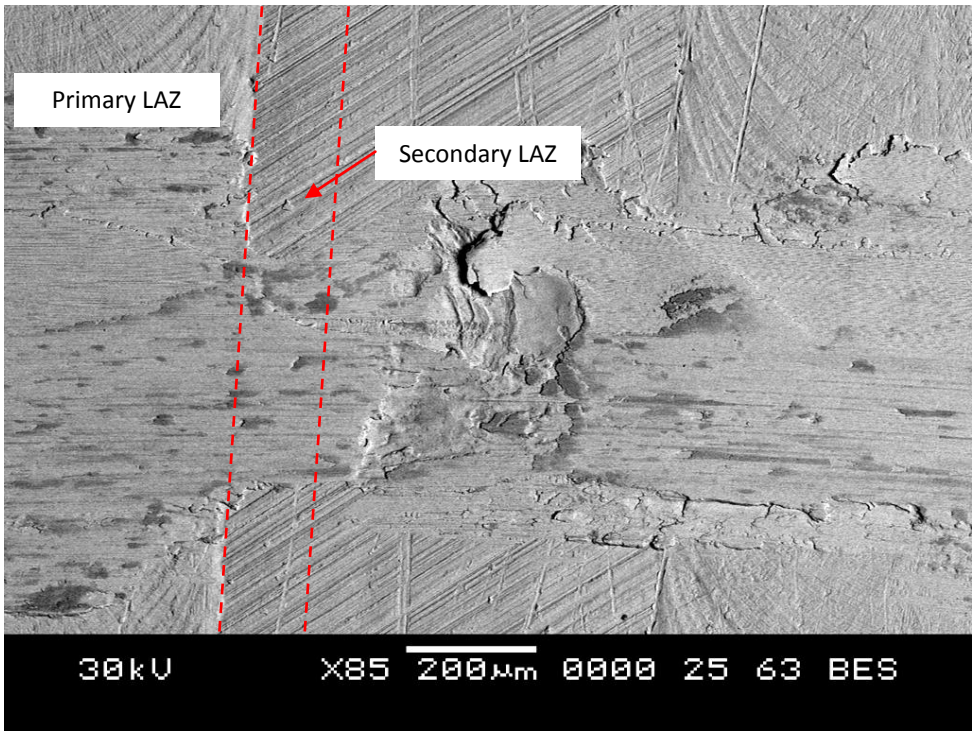


(a)

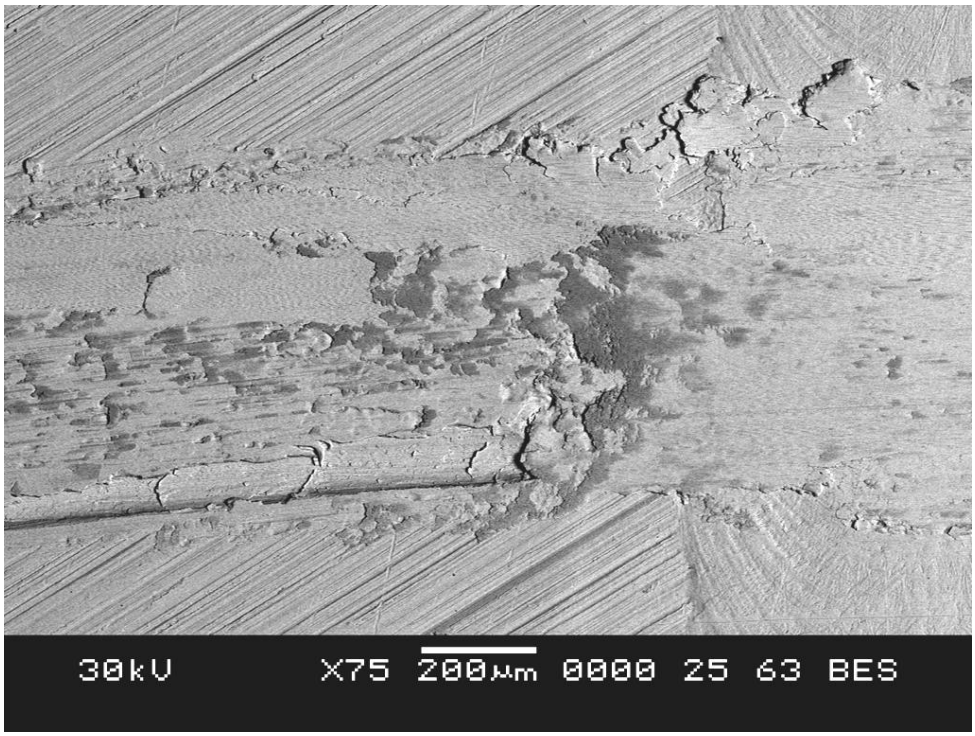


(b)

Figure 4.11 Normalized and hardened SAE 8620, laser heat treated tracks at a 1.5 mm separation distance, wear tested for 5000 cycles at a 0.42 m/s translation speed with a 30N load.

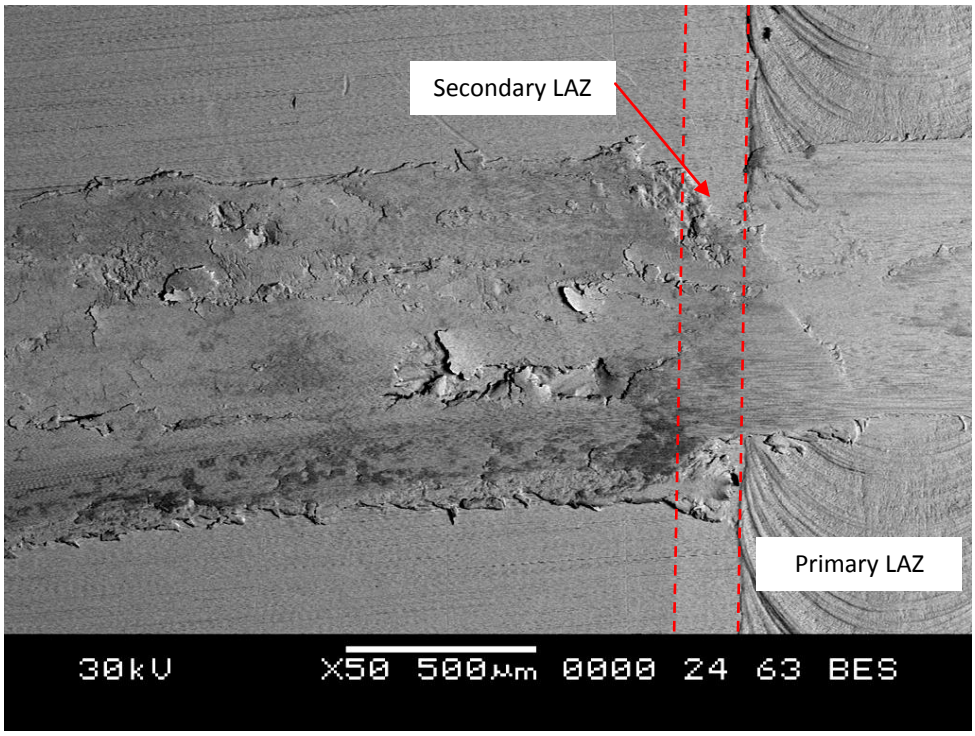


(a)

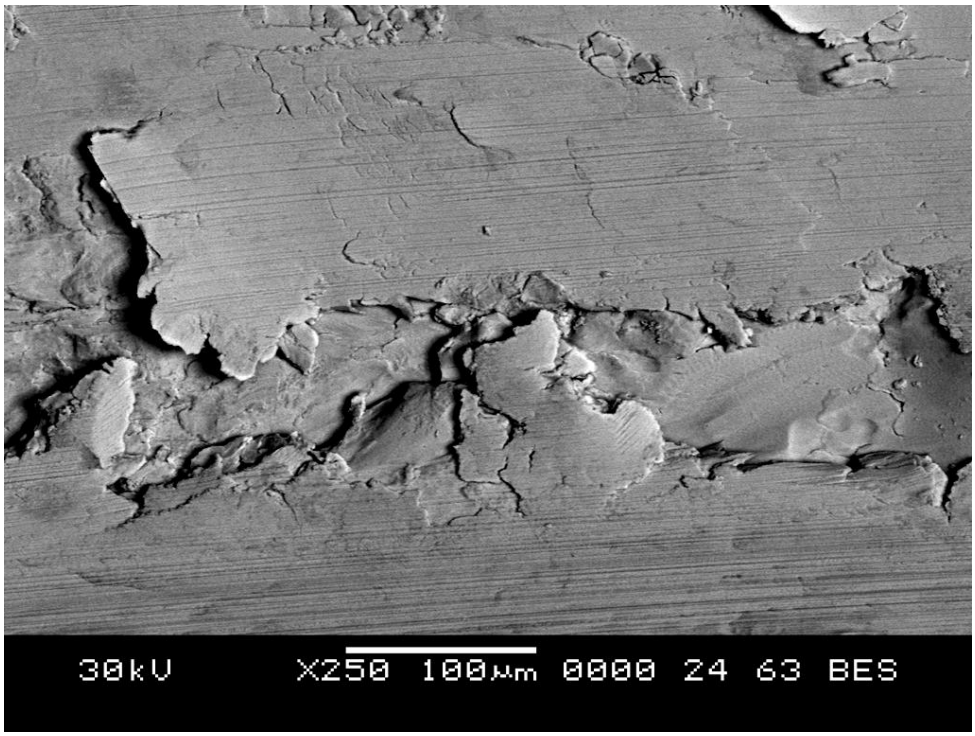


(b)

Figure 4.12 Normalized and annealed SAE 4140, laser heat treated tracks at a 1.5 mm separation distance, wear tested for 5000 cycles at a 0.42 m/s translation speed with a 30N load.

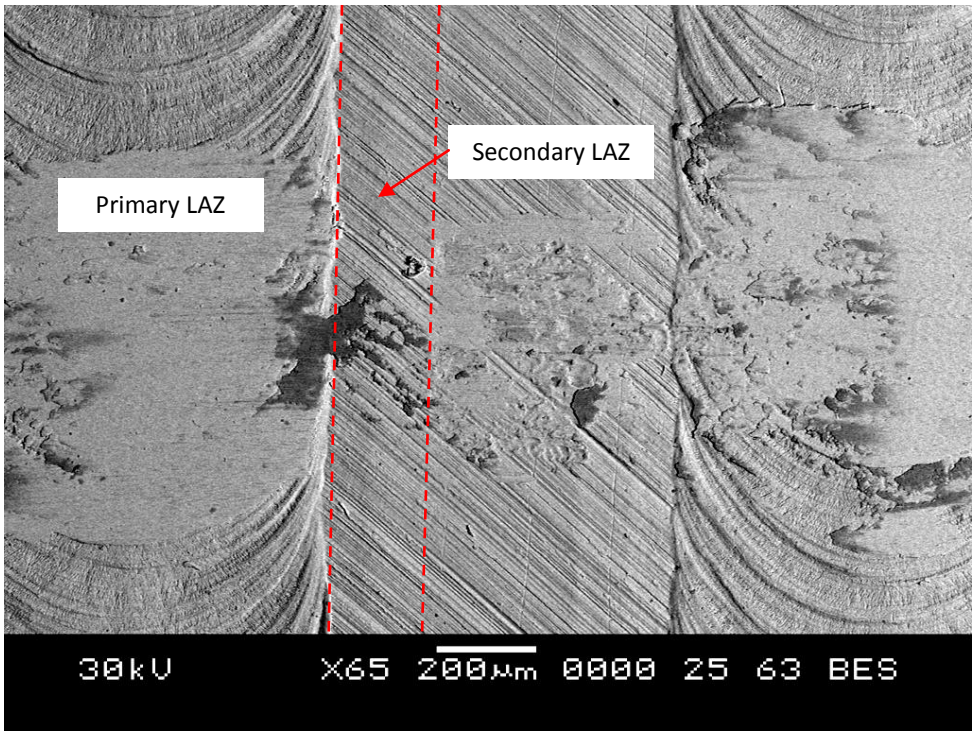


(a)

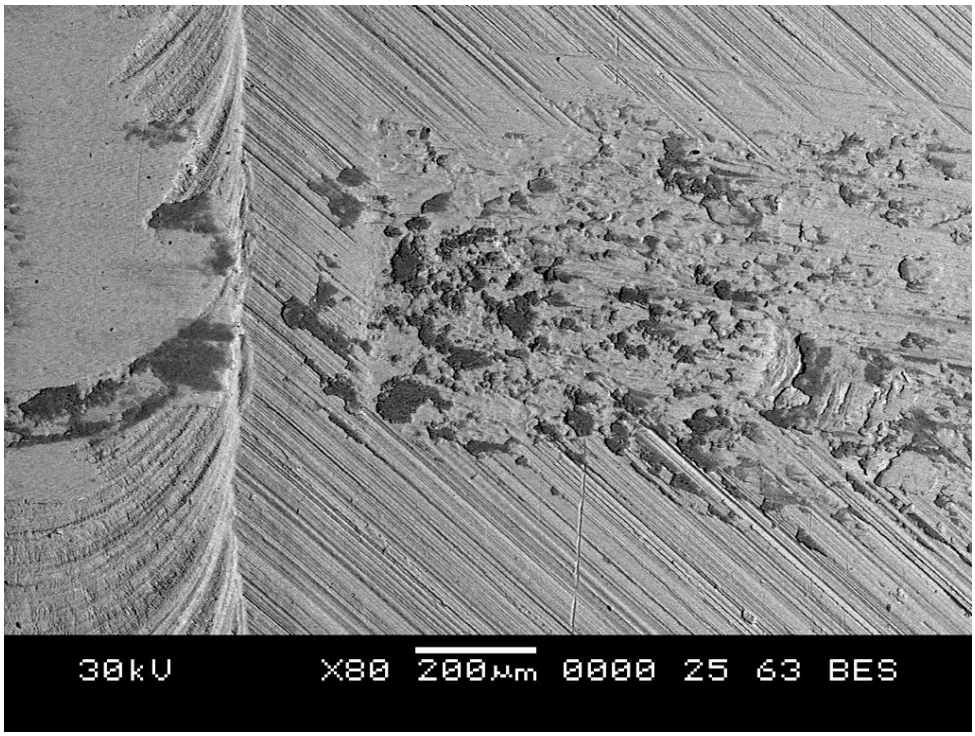


(b)

Figure 4.13 Normalized and hardened SAE 4140, laser heat treated tracks at a 1.5 mm separation distance, wear tested for 5000 cycles at a 0.42 m/s translation speed with a 30N load.

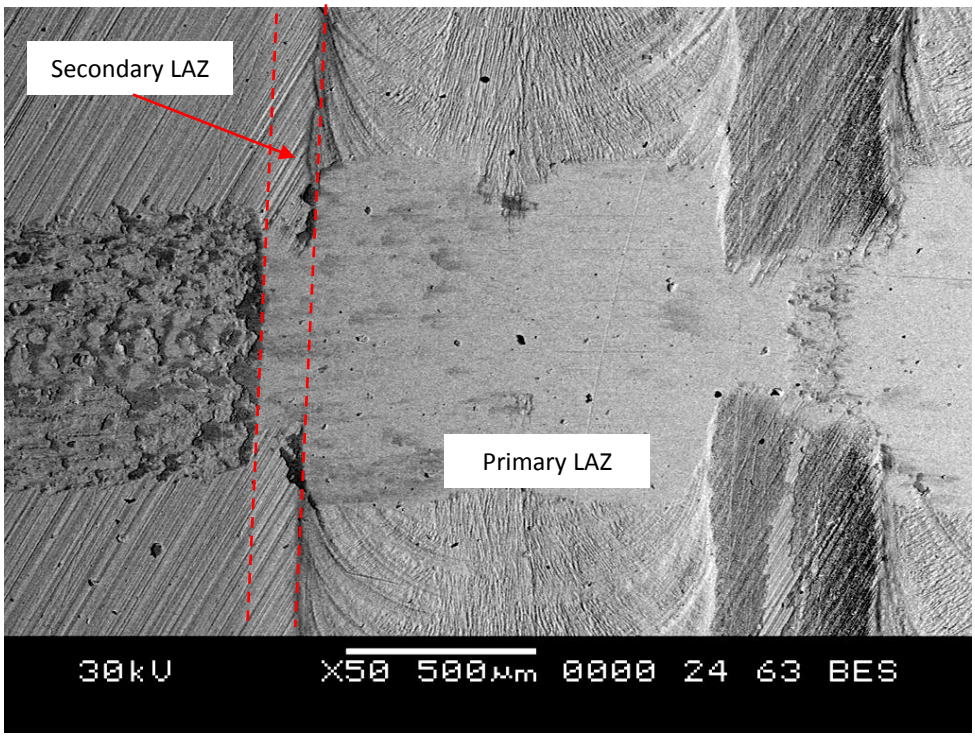


(a)

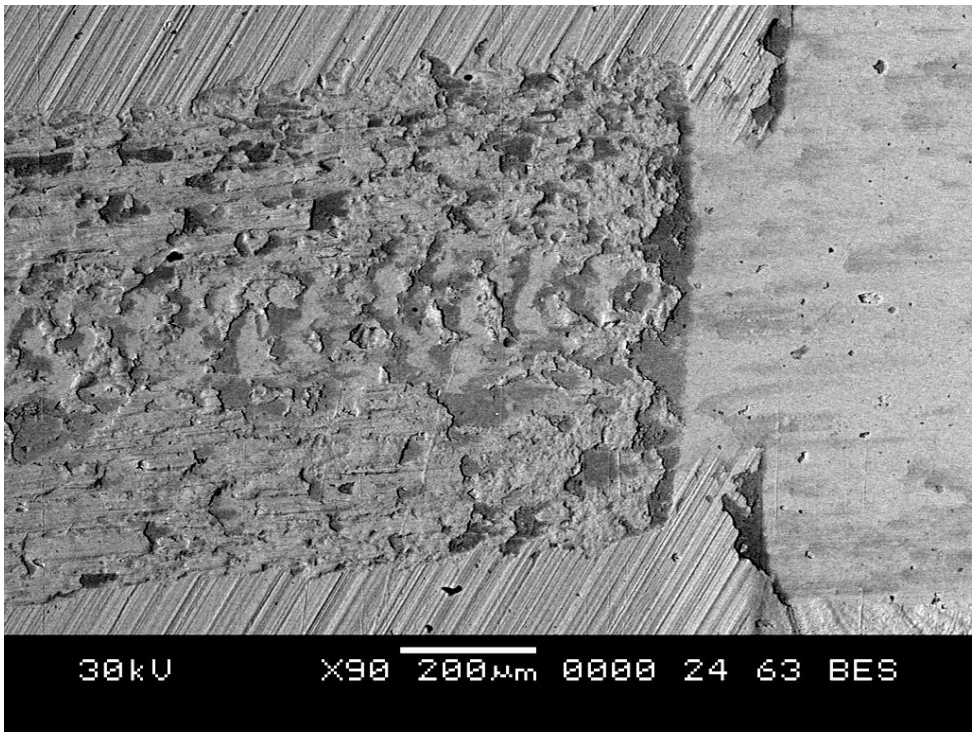


(b)

Figure 4.14 Normalized SAE 52100, laser heat treated tracks at a 1.5 mm separation distance, wear tested for 5000 cycles at a 0.42 m/s translation speed with a 30N load.

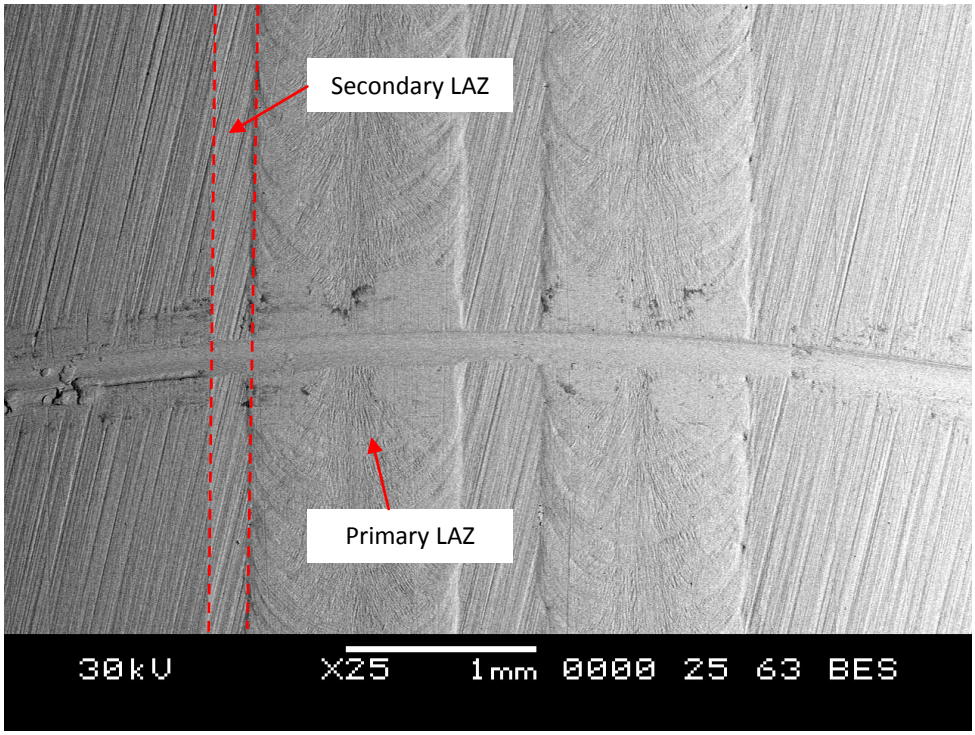


(a)

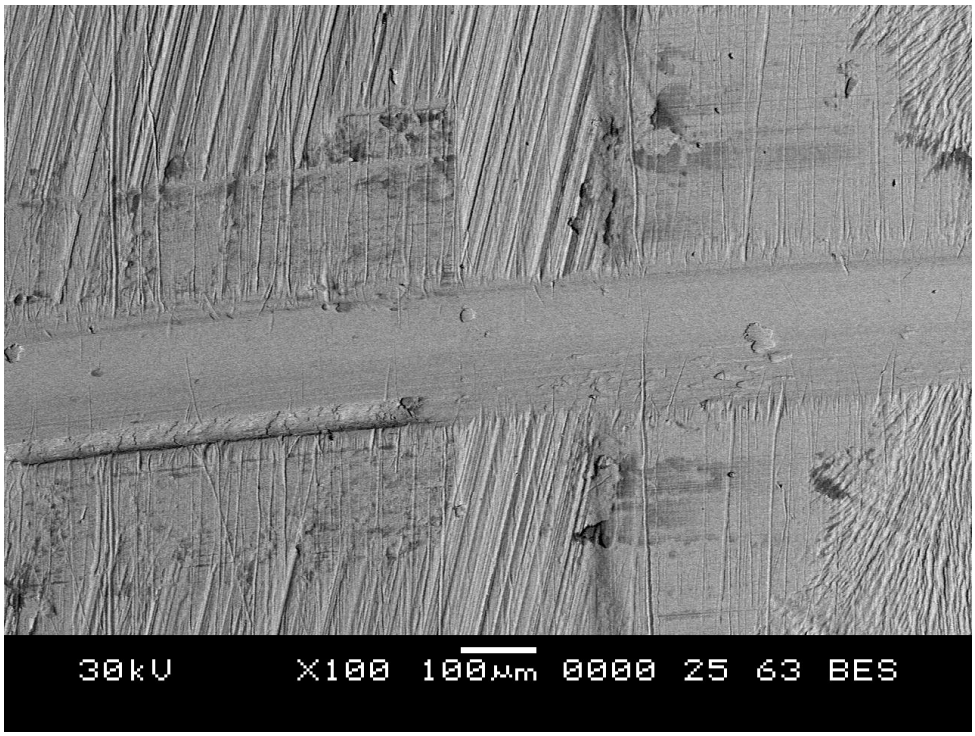


(b)

Figure 4.15 Normalized and hardened SAE 52100, laser heat treated tracks at a 1.5 mm separation distance, wear tested for 5000 cycles at a 0.42 m/s translation speed with a 30N load.

#### 4.3.1.2 Quantitative Wear Analysis

Wear testing was performed on additional samples of normalized, annealed and laser hardened SAE 8620 at 100, 1000, and 5000 cycles at a translation speed of 0.47 m/s and a 30N load. SAE 8620 was chosen as the material to investigate as it is a typical material used for camshafts and gears. SEM images of cross sections through non-laser hardened and laser hardened areas at 100 cycles are shown in Figures 4.16 and 4.17, respectively. Similar photos at 1000 and 5000 cycles are shown in Figures 4.18-4.21. The shear strain in each sample was estimated using taking the tangent of the angle of deformation [52] as shown in Figure 4.22. The shear strain was estimated at a constant depth of 5 μm below each sample surface. For the non-laser hardened area, the shear strain continues to increase in a linear way from approximately 200-300% at 100 cycles to 450% at 5000 (Figure 4.23). The shear strain in the laser hardened area was found to be nearly constant from 100 to 5000 cycles, although this may be due to the difficultly in measuring small changes in shear strain after the surface has work hardened. The $p_{max}/k$ ratio for the non-laser hardened area was 9.0 and 1.9 for the laser hardened area, where $p_{max}/k$ is the maximum contact pressure divided by the shear yield strength of the material which is used to define the shakedown limits of the material as a function of friction. The shear yield strength (k) was equal to $\sigma_{YS}/\sqrt{3}$ where $\sigma_{ys}$ is the tensile yield strength for the non-laser hardened samples. For the laser hardened samples the shear yield strength was taken to be approximately equal to VHN/3, where VHN is the Vickers hardness number. The value of $p_{max}/k$ is important in as it is an indicator of contact fatigue potential. Surfaces experiencing contact loading can fail due to elastic fatigue, elastic/plastic fatigue (elastic shakedown), low-cycle fatigue (plastic shakedown – closed plastic deformation), ratcheting fatigue (open plastic shakedown). The limits of the $p_{max}/k$ space for each of these mechanisms is a function of the coefficient of friction. Therefore, surfaces that have lower shear yield strengths will fail faster due to a higher propensity for plastic deformation at a constant contact stress. The propensity for contact fatigue can be reduced if the lower strength material can form a decreased coefficient of friction which leads to higher elastic and plastic shakedown limits and thus less plastic flow. Therefore,

the non-laser hardened surface with $p_{max}/k$ of 9.0 should exhibit significant plastic deformation from ratcheting and contact fatigue cracking at a very low number of cycles as the $p_{max}/k$ value is above the plastic shakedown limit (see Figure 1.8): exactly what was observed in Figure 4.16. In the laser hardened zone the $p_{max}/k$ of 1.9 would suggest that the surface is likely experiencing plastic deformation possibly due to ratcheting as the mechanisms converge at higher coefficients of friction. As significant plastic deformation was visible in Figures 4.17, 4.19, and 4.21, this is likely the case for these samples.

The shear strain for each samples in both the non-laser hardened and laser hardened samples was measured at 100, 1000, and 5000 cycles using the method of Tyfour [53] as shown in Figure 4.22a. Figure 4.22b shows a schematic of how the shear strain accumulates with cycles of sliding load. The stress distribution in sliding as shown in Figure 1.14, results in an increase in shear strain accumulation unless residual stresses develop to resist further plastic deformation. The non-laser hardened samples saw a small increase in strain from 100 to 5000 cycles, with the laser hardened samples showing a constant shear strain (Figure 4.23).

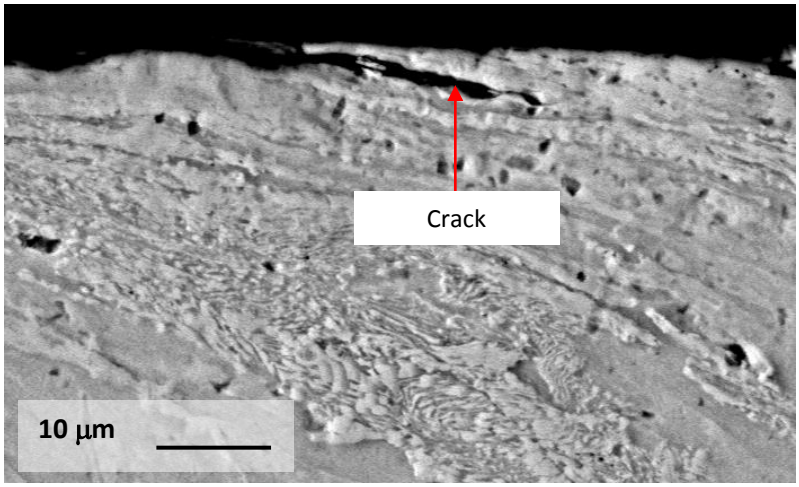


Figure 4.16 Deformed surface after 100 cycles at 30N on a 8620 N+A sample away from the laser hardened zone. Contact fatigue cracks are visible in the upper right of the micrograph (black lines).

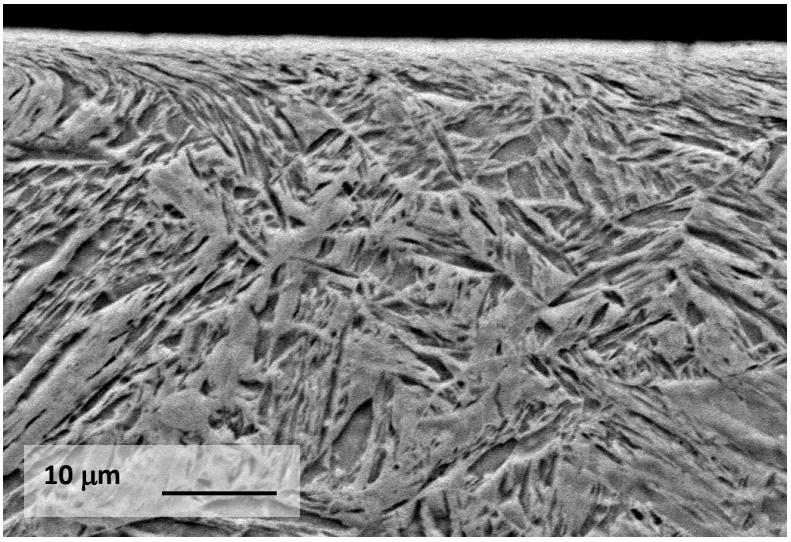


Figure 4.17 Deformed surface after 100 cycles at 30N on a 8620 N+A sample in the laser hardened zone.

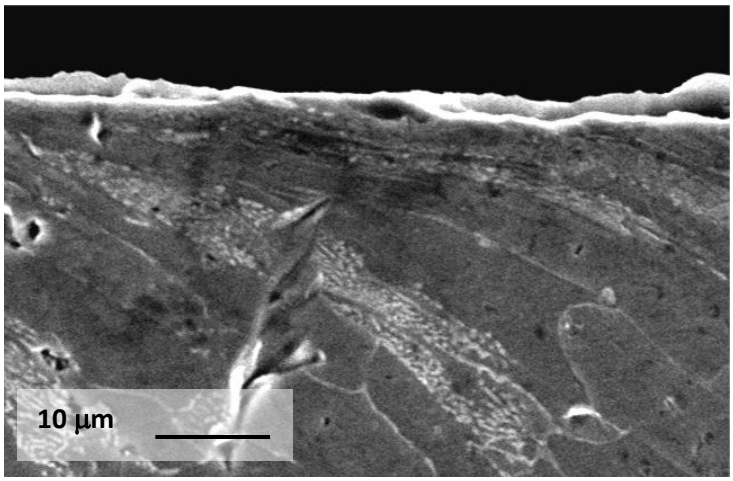


Figure 4.18 Deformed surface region after 1000 cycles at 30N on an 8620 N+A in the non-laser hardened zone.

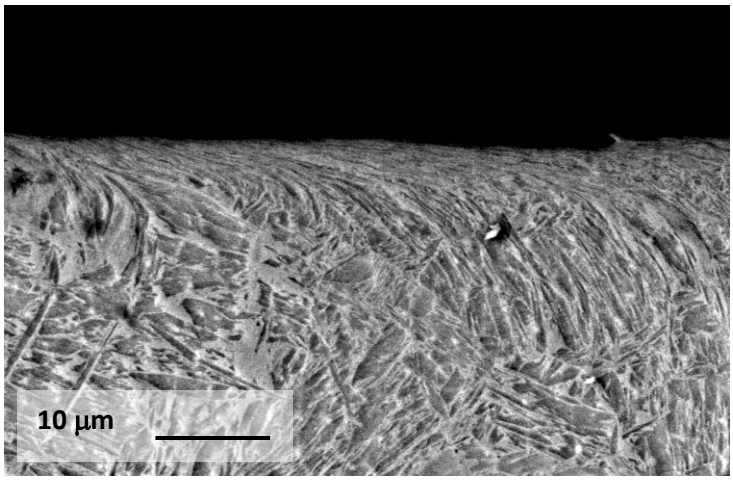


Figure 4.19 Deformed surface region after 1000 cycles at 30N on an 8620 N+A sample in the laser hardened zone.

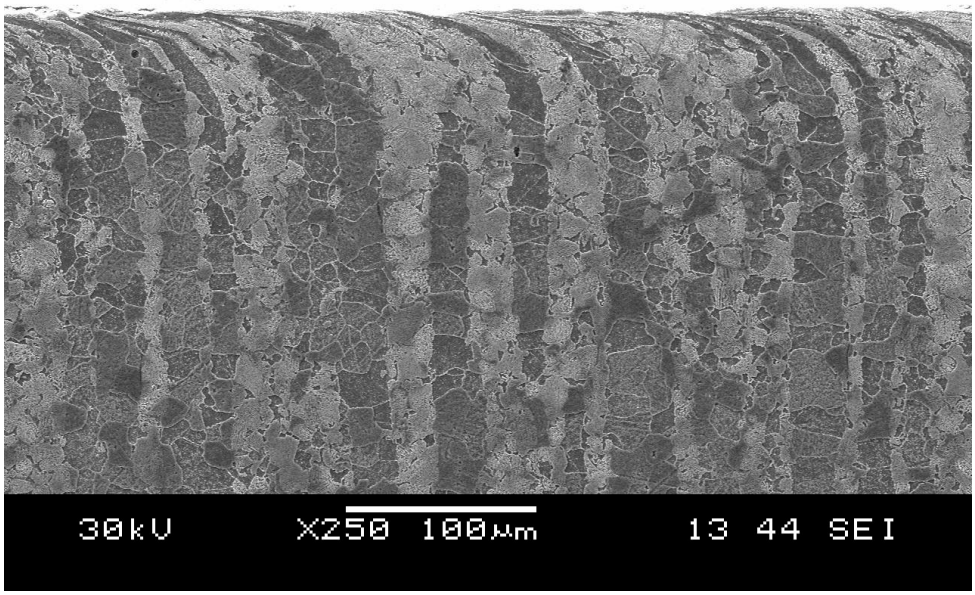


(a)

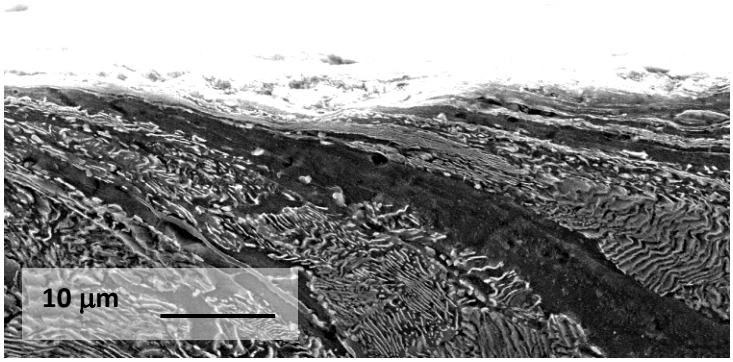


(b)

Figure 4.20 (a, b) Deformed surface region after 5000 cycles at 30N on an 8620 N+A sample in the away from the laser hardened zone.

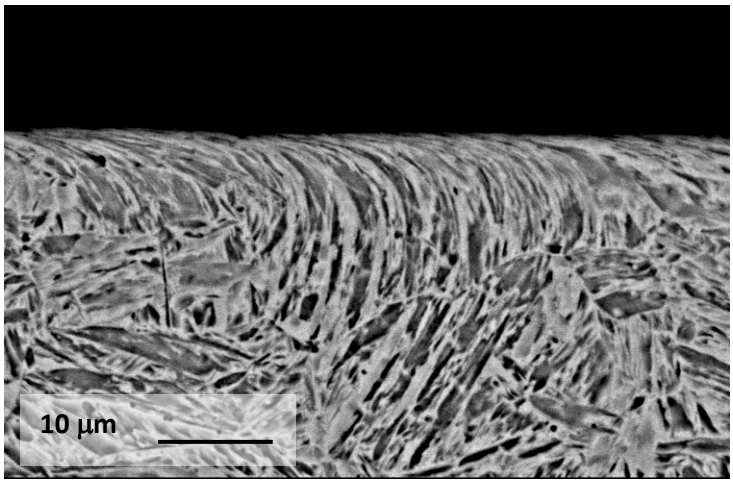


Figure 4.21 Deformed surface region after 5000 cycles at 30N on an 8620 N+A sample in the laser hardened zone.

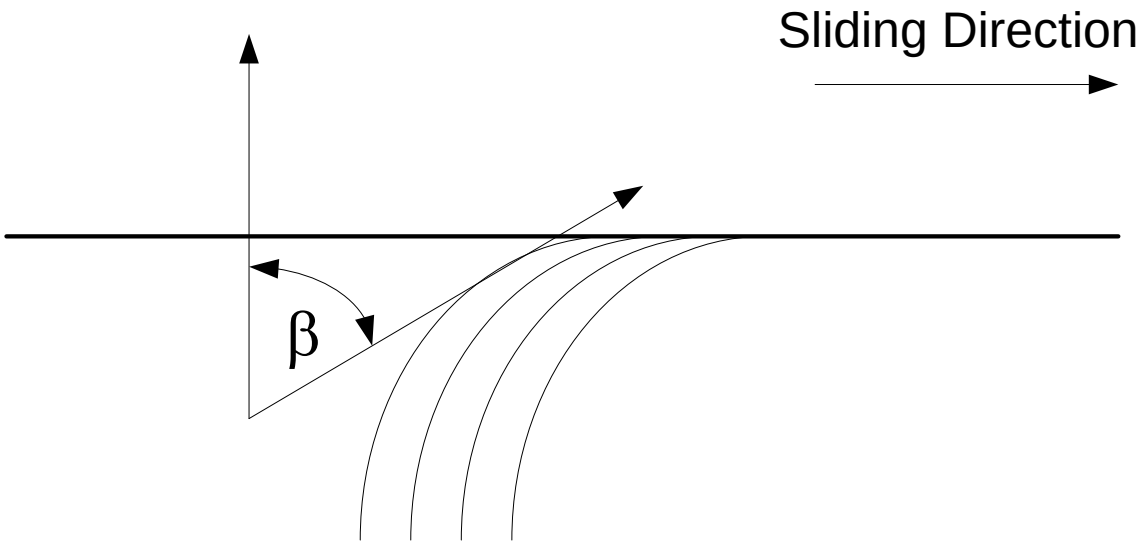


(a)

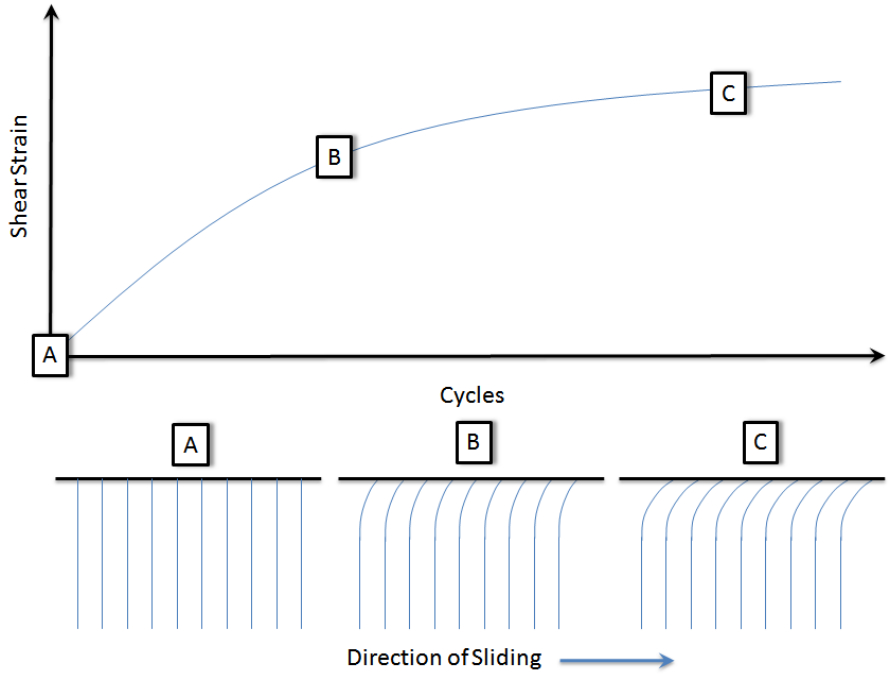


(b)

Figure 4.22 (a) Strain measurement method from [53]. (b) Schematic of shear strain accumulation as a function of cycles in a typical strain hardening steel.

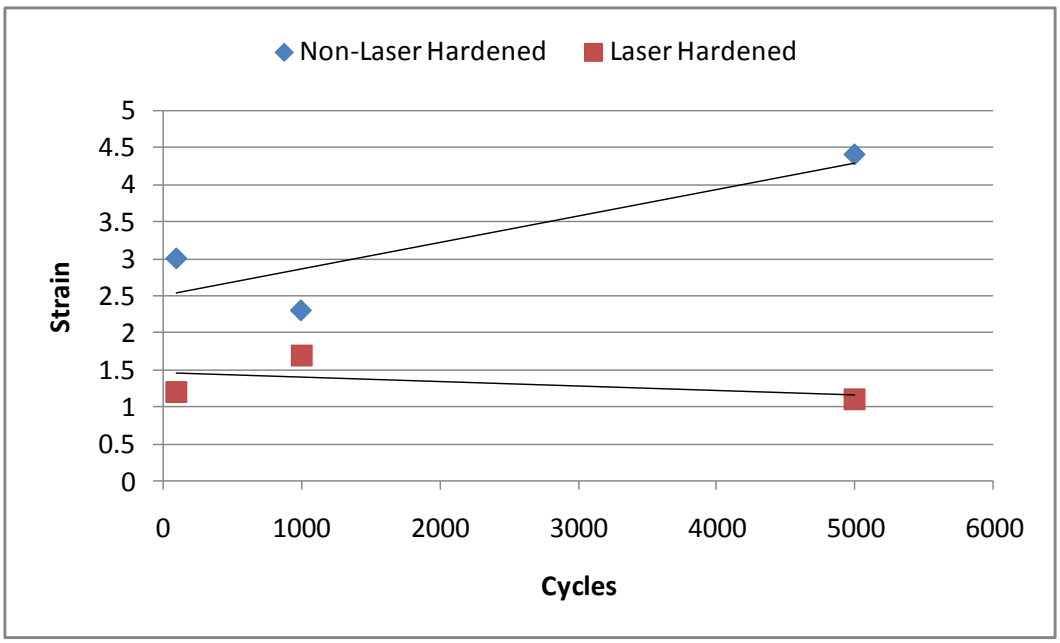


Figure 4.23 Shear strain (tan β) versus cycles for normalized and annealed SAE 8620 steel in both the non-laser hardened and laser hardened state.

#### 4.3.1.3 Wear Analyses on Laser Hardened SAE 8620, 4140 and 52100 with Overlapped Laser Tracks

Additional test samples of SAE 8620, 4140, and 52100 were completely surface laser hardened using a circular laser track pattern at an overlap of 50% and wear tested at a normal load of 10N and a speed of 0.47 m/s for 100, 1000, and 5000 cycles. The coefficient of friction versus the number of cycles for the 5000 cycles samples are shown in Figures 4.24a-b. The large drops in the coefficient of friction represent large wear particles that have come loose from the sample resulting in a third-body transfer layer which temporarily reduces friction. This is typical in spalling during pin-on-disc wear testing, as the large particles act like “banana-peels”, causing a temporary third body wear medium with little friction. Large drops in the coefficient of friction were seen for non-laser hardened samples of normalized SAE 52100 and normalized and hardened SAE 8620 and in the laser hardened normalized and annealed SAE 8620 sample. An absence of a large drop does not mean that no contact fatigue occurred; only that no significant spall occurred that resulted in a large third wear body condition.

Each of the 5000 cycle samples was sectioned, polished and etched in order to measure the total shear strain and depth of plastically deformed material. The results are given in Table 4.4. The shear strain was measured at various depths, at locations where the shear deformation could be closely observed. The strain was approximately 120-230% for all samples, regardless of heat treatment prior to laser hardening, except in both laser hardened SAE 52100 samples, where no noticeable deformation was visible at a magnification of 10,000X using scanning electron microscopy in both secondary and backscattered imaging. It is likely that some plastic deformation is present; however, in the hardened 52100 alloys and the other hardened steels, the deformed layer is difficult to detect at or above 10,000X; also, the fact that the hardened microstructure is martensitic with varying angles of the martensitic lath or plates can make it difficult to distinguish the angle of the deformation and thusly the percent of deformation.

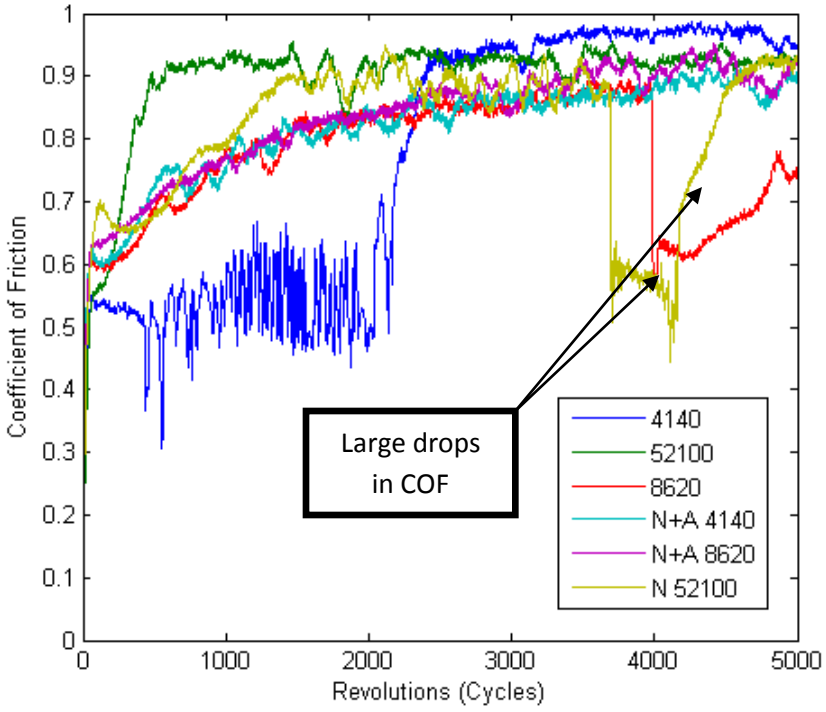


(a)

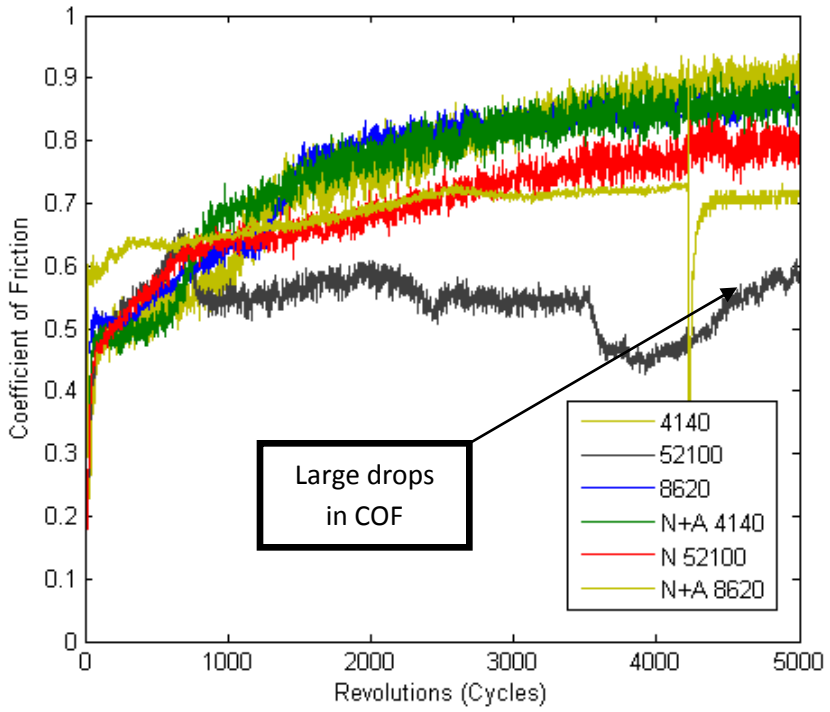


(b)

Figure 4.24 Wear results for (a) non-laser hardened steel, and (b) laser hardened steel samples; all samples were run at a load of 10N and a speed of 0.47 m/s.

Table 4.4 Shear strain data from wear testing of fully laser hardened samples.

| | Cycles | Material | Load (N) | p/k | Shear Strain | Depth (μm) | Hardness # | Hardness (Vickers) |
|---|---|---|---|---|---|---|---|---|
| Not Laser Hardened | 5000 | SAE 52100 N | 10 | 5.44 | 2.1 | 3 | 90 HRB | 192 |
| | 5000 | SAE 52100 N+H | 10 | 2.68 | 1.7 | 2 | 47 HRC | 225 |
| | 5000 | SAE 8620 N+A | 10 | 6.27 | 2.2 | 16 | 72 HRB | 140 |
| | 5000 | SAE 8620 N+H | 10 | 4.38 | 2.3 | 4 | 24 HRC | 261 |
| | 5000 | SAE 4140 N+A | 10 | 7.05 | 2.3 | 8 | 87 HRB | 179 |
| | 5000 | SAE 4140 N+H | 10 | 1.78 | 2.0 | 4 | 44 HRC | 440 |
| | | | | | | | | |
| Laser Hardened | 5000 | SAE 52100 N | 10 | 0.98 | 0* | 0* | 61.4 HRC | 730 |
| | 5000 | SAE 52100 N+H | 10 | 0.98 | 0* | 0* | | |
| | 5000 | SAE 8620 N+A | 10 | 1.33 | 1.7 | 2 | 51.5 HRC | 537 |
| | 5000 | SAE 8620 N+H | 10 | 1.33 | 2.3 | 3 | | |
| | 5000 | SAE 4140 N+A | 10 | 0.97 | 1.9 | 5 | 61.5 HRC | 732 |
| | 5000 | SAE 4140 N+H | 10 | 0.97 | 1.2 | 2 | | |
| # Non laser hardness data was determined from hardness test of the wear disk | | | | | | | | |
| Laser hardness data was determined from the average of a Vickers hardness trace | | | | | | | | |
| *No obvious deformation was observe in SEM up to 10,000X magnification | | | | | | | | |

SEM images of worn areas in both non-laser hardened and laser hardened regions for all six steel and microstructure combinations at 100, 1000, and 5000 cycles are shown in Figures 4.25-4.30. The photos were taken to allow for qualitative determination of whether contact fatigue was occurring. Surface fatigue is defined as extensive macro cracking, examples of which are shown in Figures 1.5 and Figures 4.10b and 4.11b. In Figure 4.25, surface fatigue is seen to begin at 1000 cycles in the non-laser hardened normalized and annealed SAE 8620 and with mostly abrasion wear for all cycles in the laser hardened region. Some small areas of significant surface damage is seen at 5000 cycles in the laser hardened region but this is likely just asperity fatigue typical of the break-in phase. Similar results were observed in the normalized and hardened SAE 8620 shown in Figure 4.26.

The SAE 4140 samples only exhibited fatigue damage in the 1000 and 5000 cycles images in the non-laser hardened region of the normalized and annealed sample (Figure 4.27). Similar results were seen with the SAE 52100 samples, with the only gross contact fatigue being observed by 1000 cycles in the non-laser hardened region of the normalized sample (Figure 4.29). Only some asperity fatigue was seen in the non-laser hardened region of the normalized and hardened sample (Figure 4.30).

The wear types and amounts observed in Figures 4.25-4.30 are consistent with the work of others on general contact fatigue, especially the ratcheting fatigue mechanism [46-52]. Based on the studies of Ponter, Johnson, and Kooper et al. [46-48] all of the samples should be experiencing low-cycle contact fatigue due to ratcheting as their $p_{max}/k$ ratios for a coefficient of friction on 0.6-0.8 are above the plastic shakedown limits. For the laser hardened SAE 52100 samples, the $p_{max}/k$ ratios were approximately 1.0 indicating that only elastic, mild wear should occur, as observed. The laser hardened SAE 8620 and SAE 4140 samples had $p_{max}/k$ ratios of 1.33 and 0.97, respectively. Neither sample exhibited plastically driven contact fatigue with only typical break-in wear observed by 5000 cycles of load. This is what was predicted based on the low $p_{max}/k$ ratios which were below the elastic shakedown limit.

| SAE 8620 Normalized and Annealed | | |
|---|---|---|
| Cycles | Laser Hardened – 51.5 HRC | Non-Laser Hardened – 75 HRB |
| 100 | 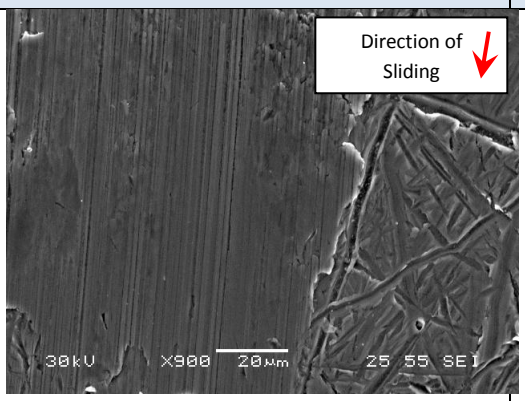  | 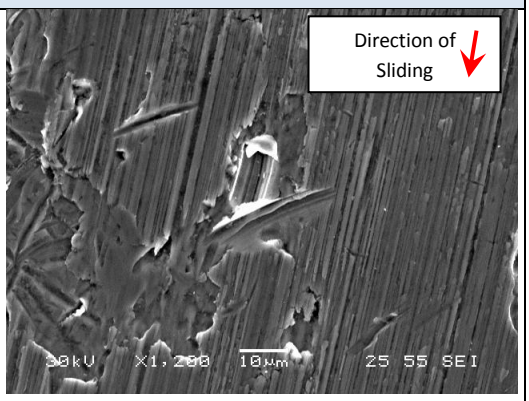  |
| 1000 | 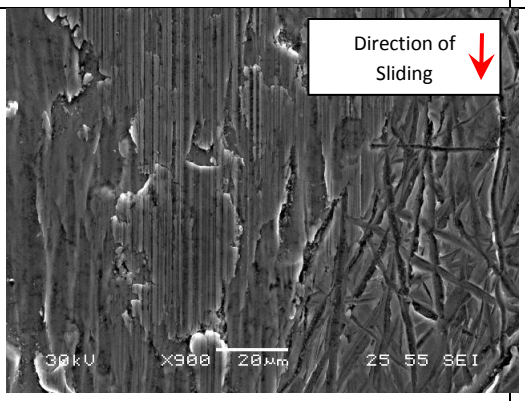  | 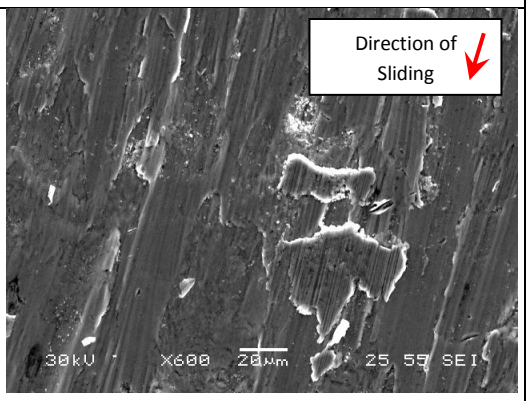  |
| 5000 | 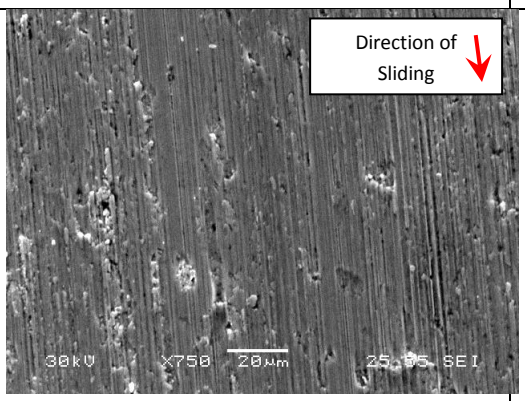  | 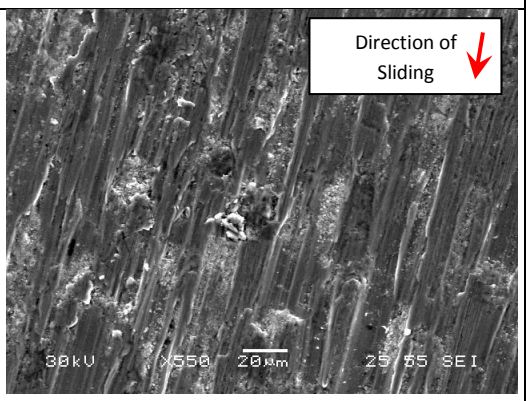  |

Figure 4.25 SEM photomicrographs at 10, 1000, and 5000 cycles of wear for the 10N loaded SAE 8620 normalized and annealed material in laser hardened and non laser hardened zones.

| SAE 8620 Normalized and Hardened | | |
|---|---|---|
| Cycles | Laser Hardened – 51.5 HRC | Non-Laser Hardened – 24 HRC |
| 100 | 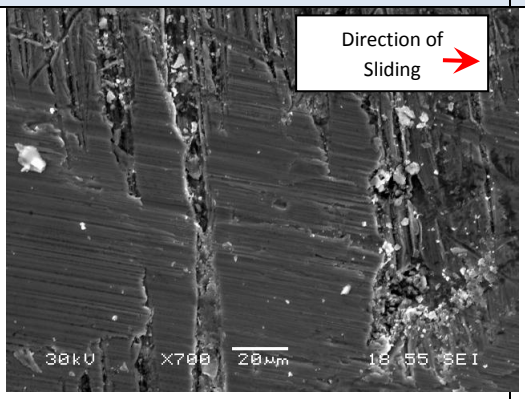  | 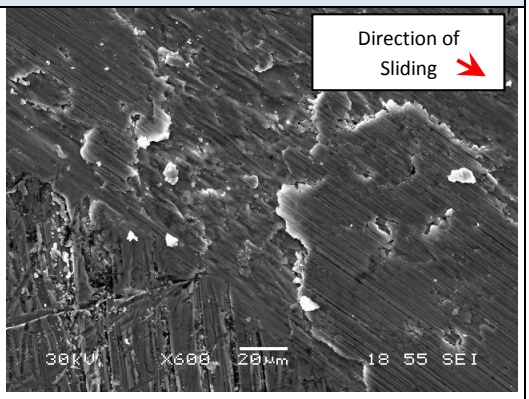  |
| 1000 | 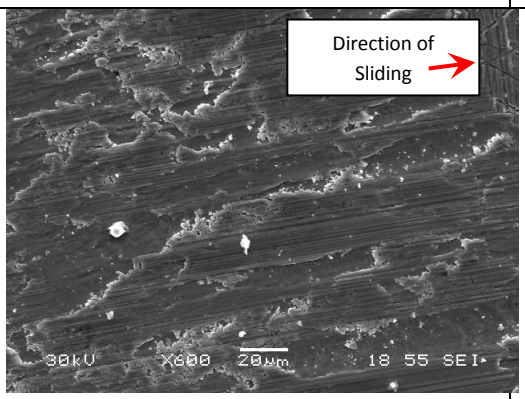  | 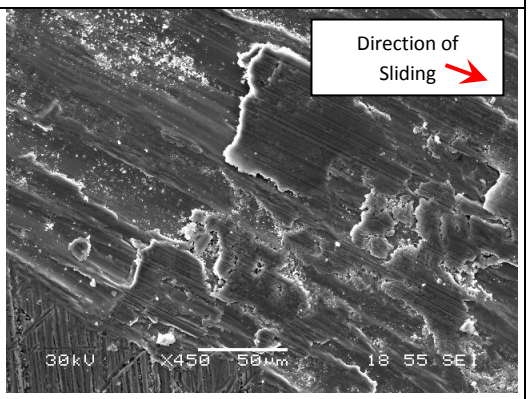  |
| 5000 | 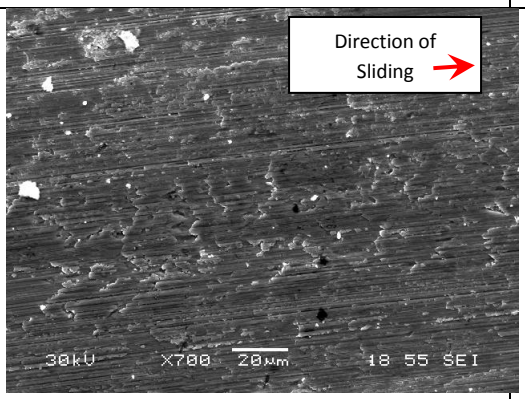  | 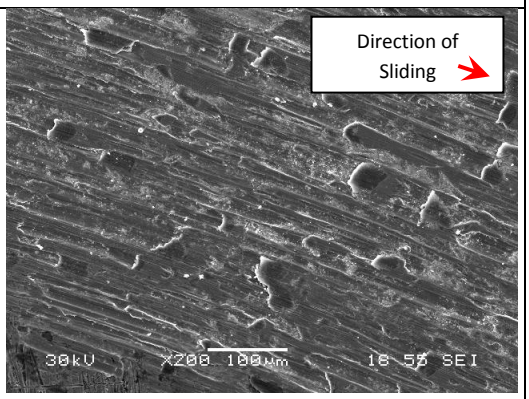  |

Figure 4.26 SEM photomicrographs at 10, 1000, and 5000 cycles of wear for the 10N loaded SAE 8620 normalized and hardened material in laser hardened and non laser hardened zones.

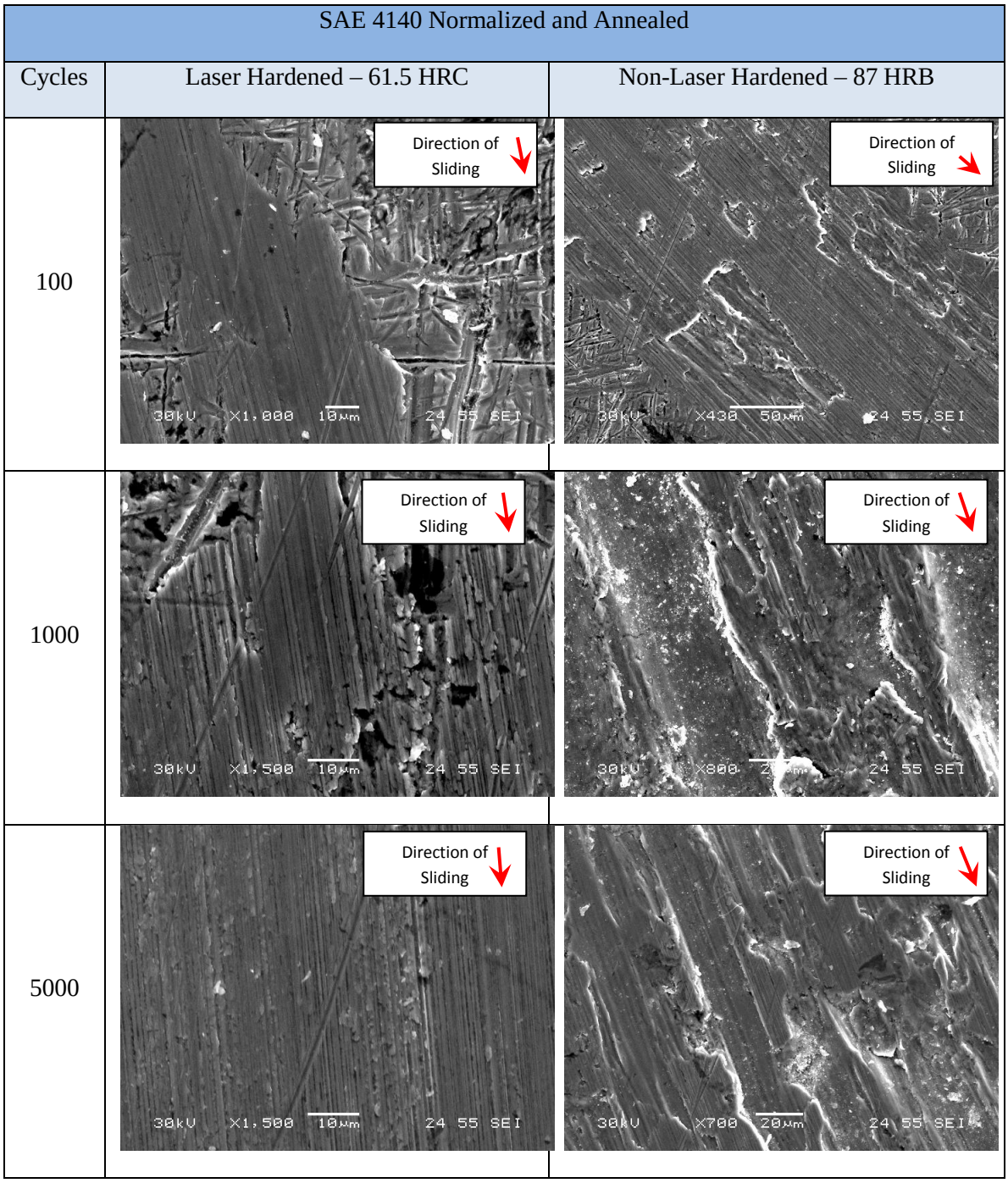


Figure 4.27 SEM photomicrographs at 10, 1000, and 5000 cycles of wear for the 10N loaded SAE 4140 normalized and annealed material in laser hardened and non laser hardened zones.

| SAE 4140 Normalized and Hardened | | |
|---|---|---|
| Cycles | Laser Hardened – 61.5 HRC | Non-Laser Hardened – 44 HRC |
| 100 | 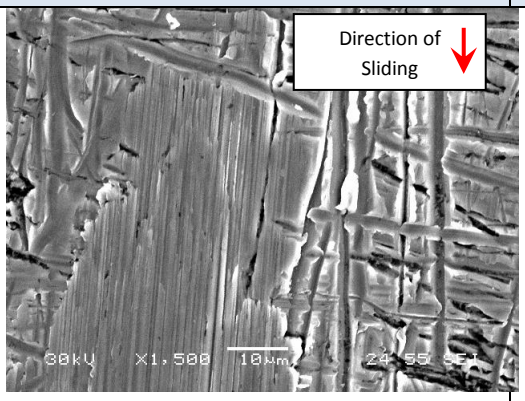  | 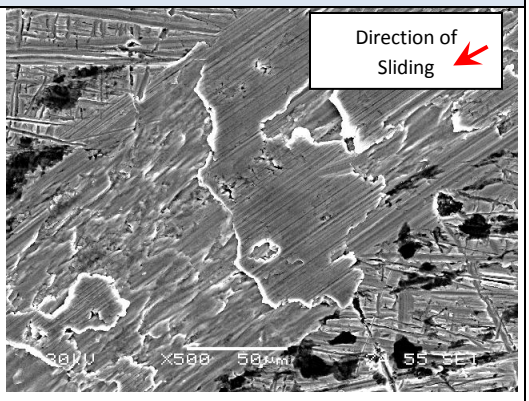  |
| 1000 | 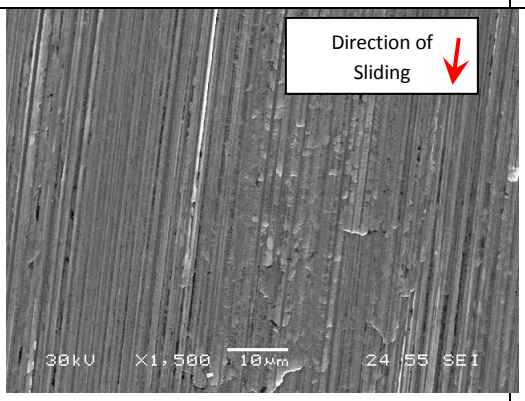  | 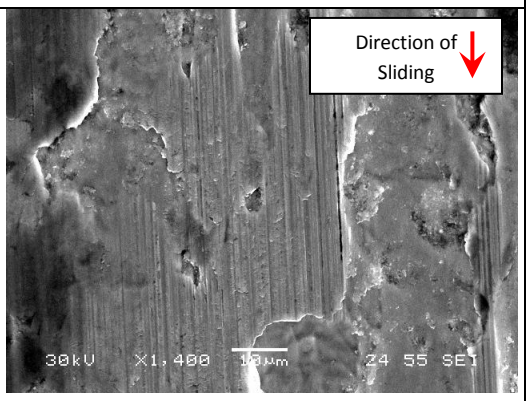  |
| 5000 | 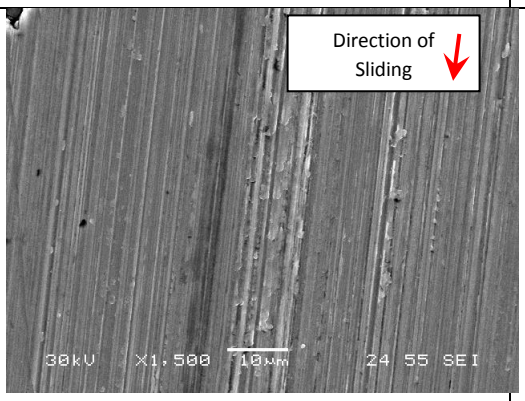  | 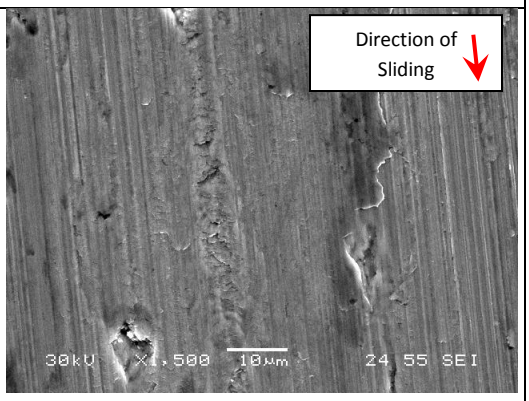  |

Figure 4.28 SEM photomicrographs at 10, 1000, and 5000 cycles of wear for the 10N loaded SAE 4140 normalized and hardened material in laser hardened and non laser hardened zones.

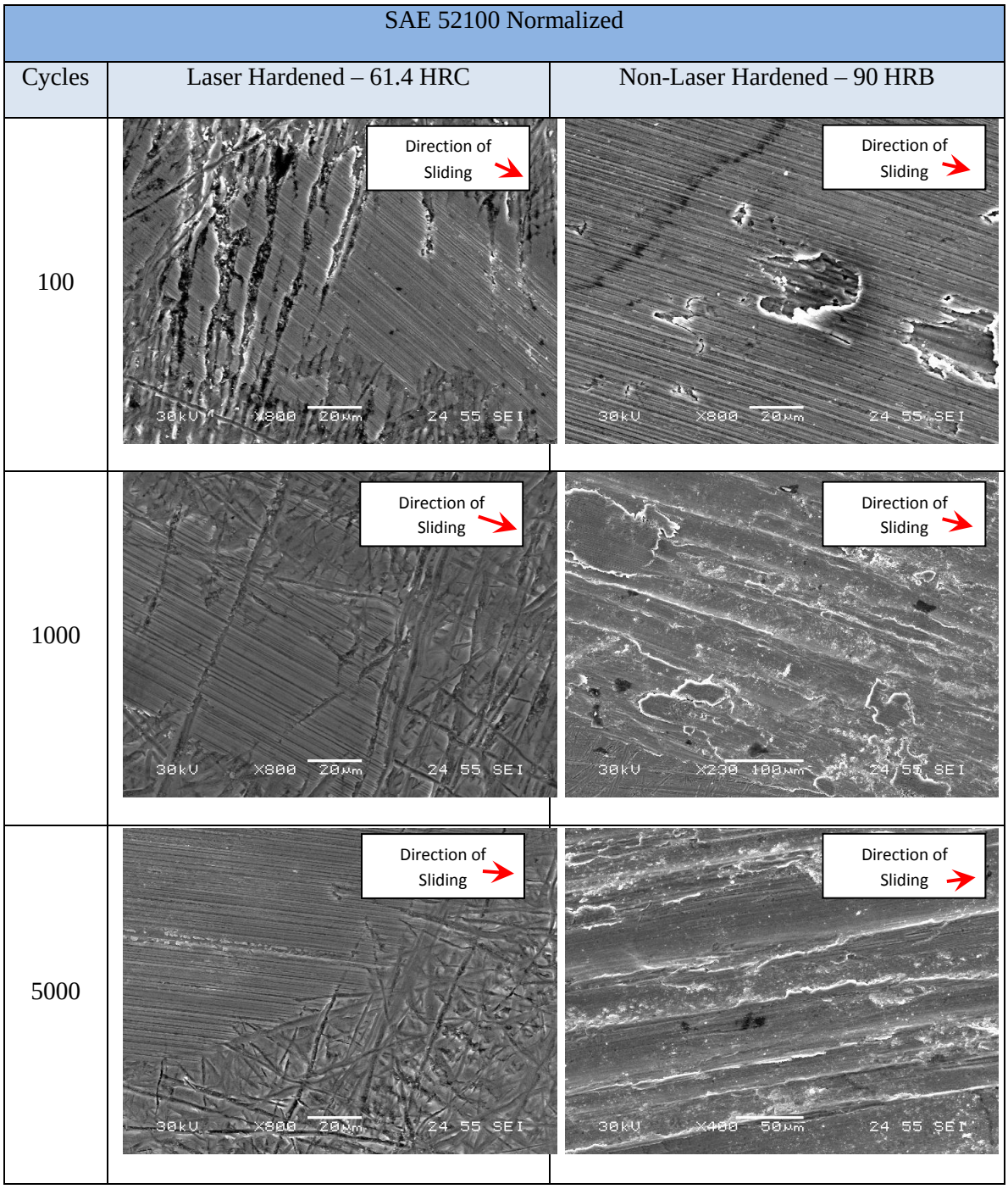


Figure 4.29 SEM photomicrographs at 10, 1000, and 5000 cycles of wear for the 10N loaded SAE 52100 normalized material in laser hardened and non laser hardened zones.

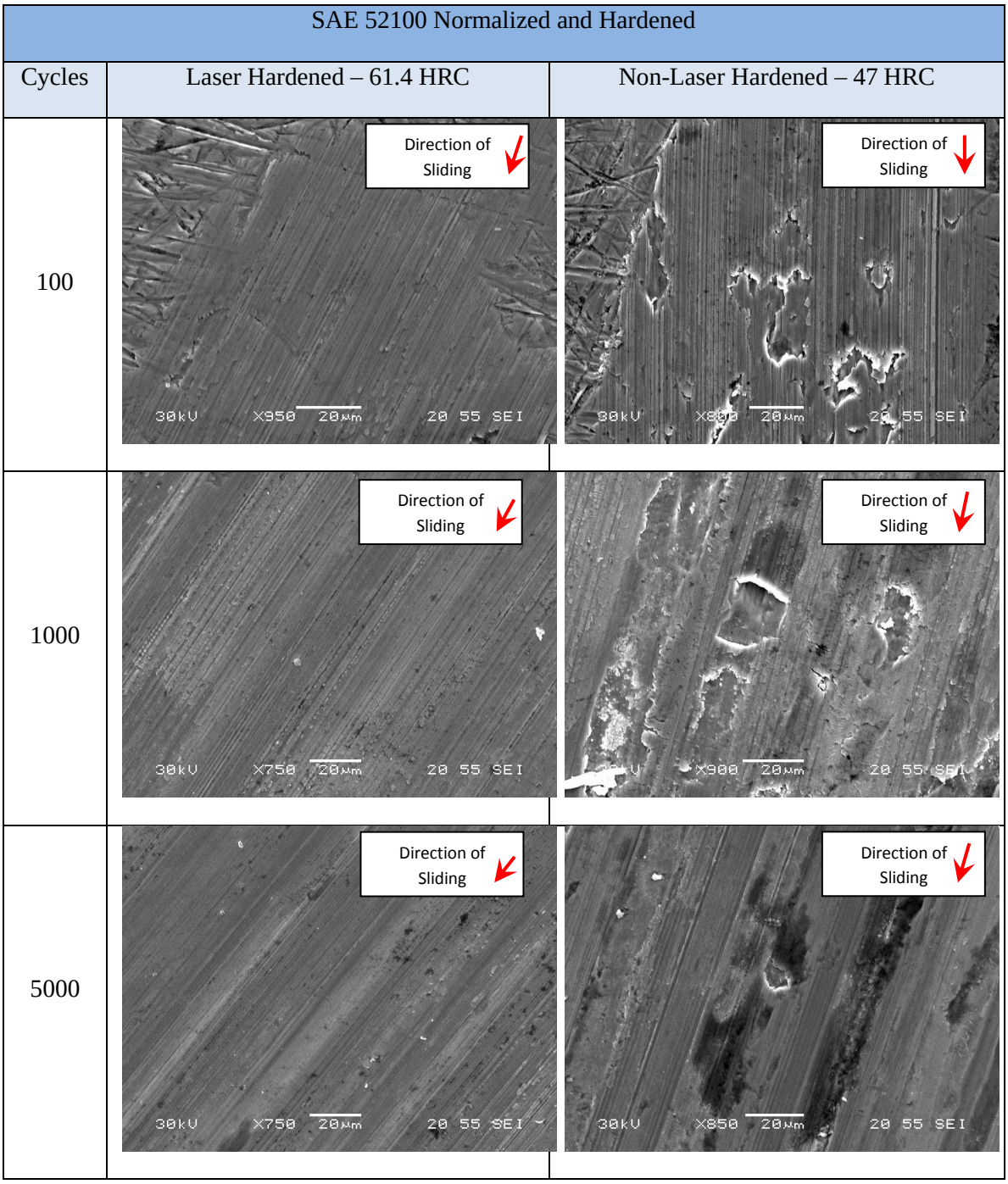


Figure 4.30 SEM photomicrographs at 10, 1000, and 5000 cycles of wear for the 10N loaded SAE 52100 normalized and hardened material in laser hardened and non laser hardened zones.

## 4.4 Discussion

One of the goals of the DOE analysis was to determine if traditional camshaft materials such as SAE 8620 could be suitably laser hardened as a substitute to conventional carburizing. Since SAE 8620 only has approximately 0.2 wt% carbon, it was doubtful as to whether it could be hardened to the 60 HRC level traditionally targeted in carburized camshafts. This was verified in this study which found that the hardness of the SAE 8620 could only reach a maximum hardness level in the low 50 HRC range: the same level found by Yessick and Scherer for SAE 8620 [45] Since hardness is well known to correlate to abrasion/adhesion and contact fatigue wear resistance [54], it is doubtful that laser hardened versions of the material would be suitable as a replacement for carburizing. SAE 4140 and SAE 52100 were also studied and found to harden more than SAE 8620 except that a maximum in the hardness was reached at approximately 0.7 wt% C due to the formation of large amounts of retained austensite. The increase in hardness at the higher carbon content is expected and has been verified by many authors [10, 12, and 16]. Bradley and Kim [17] found that the hardness post laser treatment of SAE 1050 and 5150 was 90 HR15N or 60 HRC. Shiue and Chen [20] achieved hardness values in the upper 50s to low 60s HRC in SAE 4340 with the higher values attained at higher laser translation speeds. Similar hardness values in medium carbon steels were found in [9, 12, 18, 38]. The higher carbon content results in martensitic microstructures with larger crystal lattice distortion (Bain distortion) which results in lower dislocation mobility and higher hardness.

The small dependence of hardness on the laser translation speed seen in Figure 4.3 is opposite of what is typically seen: higher translation speeds equal higher hardness and lower case depths. Higher hardness is a result of higher temperatures developing which leads to a higher austenite temperature and austenite grain size. Autotempering at slower scan rates can also reduce hardness [20]. To better understand this, the data that resulted in the response surface plot were plotted by translation speed and are shown in Figures 4.31a-f. These graphs show that the effect of the translation speed is much more pronounced in the higher carbon content steels, with little to no difference in hardness seen as a function of translation speed in the SAE 8620 steel. Hegge and DeHosson [26] showed similar results in laser studies of hypoeutectoid steel and pure iron. The largest

increase in hardness came when going from 1 to 5 cm/sec translation speed with changing slopes of hardness as a function of speed from 5-50 cm/sec. The 0.20 wt% C steel had the steepest increase in hardness from 5-50 cm/sec with the pure iron showing almost no increase. They found that the hardness varied inversely proportional to the austenite cell width with the boundaries between the subsequent martensitic subgrains hindering dislocation motion. The hardness can also be affected by the amount of martensite formed, which can be controlled by varying the austenite grain size, with larger grains requiring longer diffusion distances for carbon. Also, hardening of a non-homogeneous microstructure such as a banded pearlite/ferrite microstructure will have negative effects on the final hardness, due to the diffusion times required for carbon homogenization to form a uniform martensite [18]. For the SAE 8620 samples examined here, the preexisting microstructure was a banded microstructure consisting of ferrite and pearlite bands. In this study a completely martensitic microstructure formed at all speeds. Therefore, it was likely that initial speed was sufficient to homogenize the carbon in the austenite and form a uniform carbon distribution at all speeds. The difference in the hardness as a function of translation speed was small for the SAE 4140 and 52100 steels. Both microstructures were very similar at all speeds exhibiting a uniform martensitic microstructure for the SAE 4140 samples and a uniform martensite with heavy amounts of retained austenite in the SAE 52100 samples.

The peak in the hardness at approximately 0.7 wt% C is most likely the result of the large amount of retained austenite in the SAE 52100 samples. Fedosov [14] concluded that the principal issues resulting in high amounts of retained austenite from laser hardening are a higher amount of carbide dissolution compared to furnace hardening under standard and a lowering of the martensitic start ($M_s$) temperature in the near surface layers due to up-hill diffusion of carbon raising the carbon content near the sample surface. If the $M_s$ temperature was indeed lowered, cooling for an extended period of time in liquid nitrogen should increase the hardness values of the laser hardened SAE 52100 samples. To test this, a laser hardened sample of SAE 52100 processed at 1500W at a speed of 4.2 mm/s, was cooled in liquid nitrogen for 30 and 60 minutes. The Vickers hardness trace from the surface of the laser hardened zone through the laser hardened zone is shown in Figure 4.32 along with a trace for the non-cooled version of the sample. These data

shown that cooling below the $M_s$ temperature dramatically increased the hardness of the laser hardened zone, indicating a reduction in the amount of retained austenite. This is a strong indication that the $M_s$ temperature at 0.7 wt% C is too low to achieve low amounts of retained austenite during laser hardening, at least within the process parameters of this study.

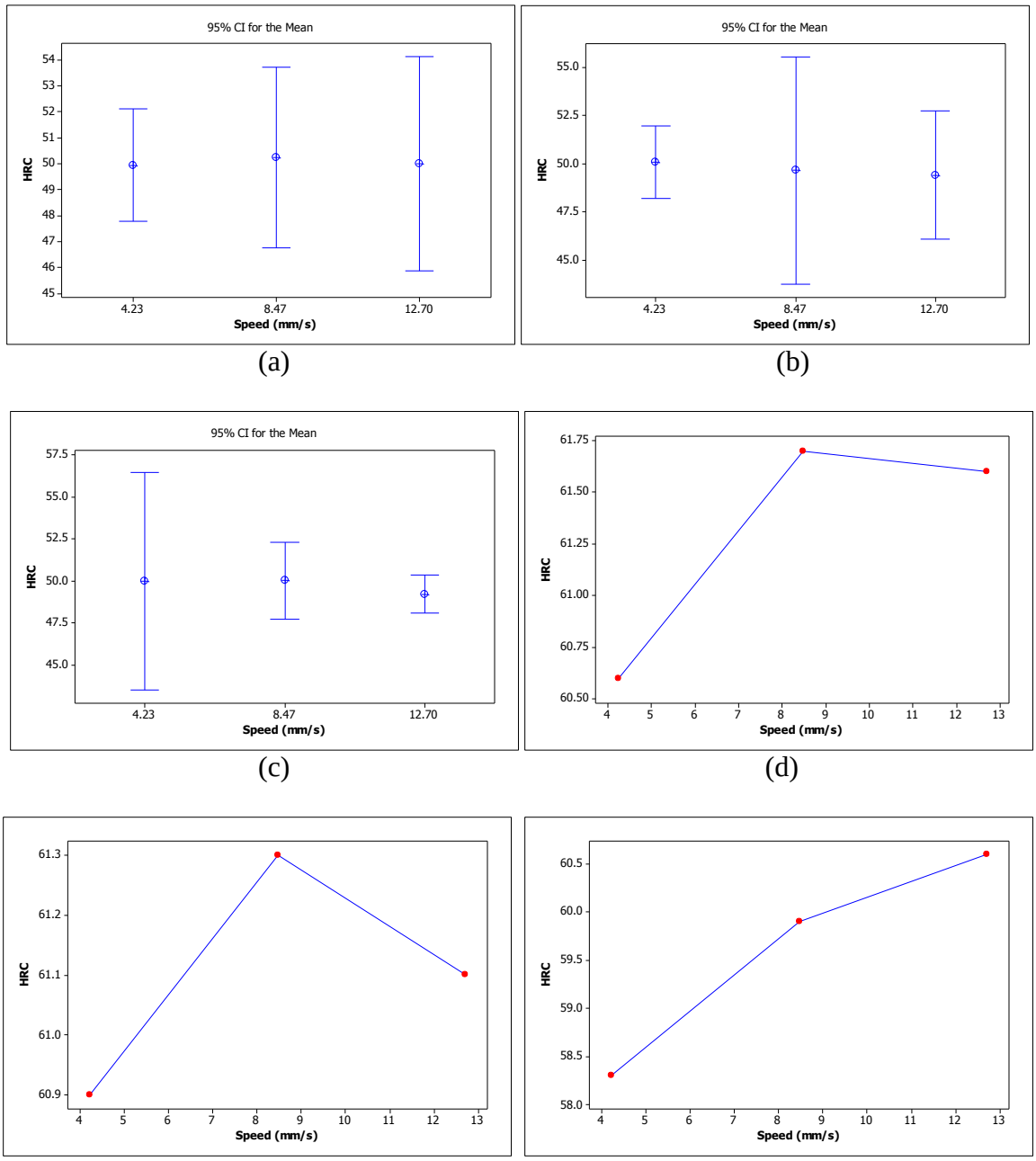


Figure 4.31 Average hardness (HRC) as a function of laser power and alloy, (a) SAE 8620 at 1250W, (b) SAE 8620 at 1500W, (c) SAE 8620 at 1750W, (d) SAE 4140 at 1250W, (e) SAE 4140 at 1250W, (f) SAE 52100 at 1500W.

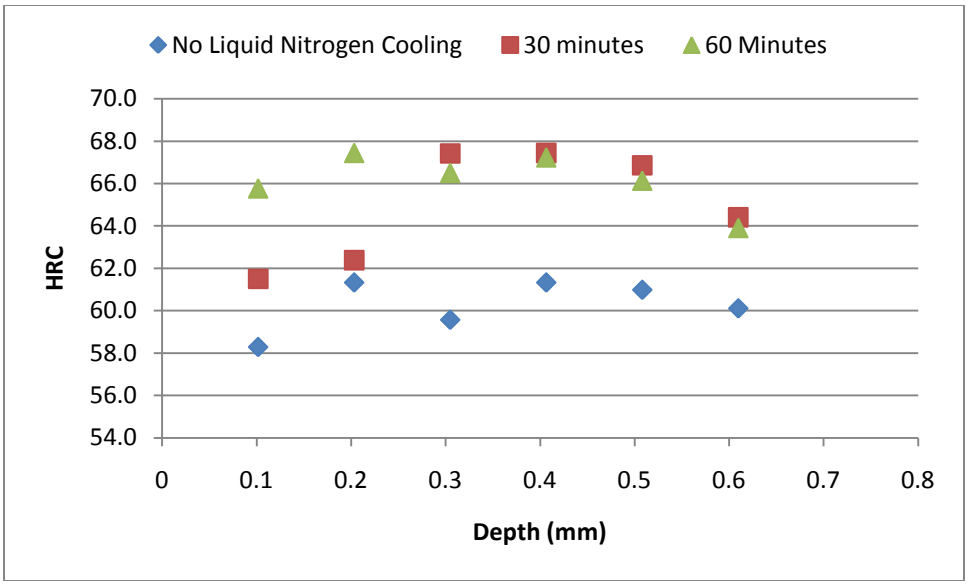

Figure 4.32 Hardness as a function of depth for SAE 52100 before and after 30 and 60 minutes of liquid nitrogen cooling of the laser hardened sample.

### 4.4.1 Quantitative Wear Modeling

#### 4.4.1.1 Contact Fatigue Modeling

The sliding contact of a material can lead to one of four responses as discussed by Tyfour [53] and other authors [51, 52]. The responses are elastic, elastic shakedown, plastic shakedown, or ratcheting. This study assumed that the ratcheting model is most useful for all but the laser hardened samples since the $p_{max}/k$ values for the laser hardened samples were below the plastic shakedown limit. To model ratcheting, the model used by Tyfour et al. [53] as well as Ringsberg et al. [51] based on the work of Kapoor [49-52], was employed. The model is given as

$$Rd = cP_r N \qquad (4.1)$$

where Rd is the accumulated unidirectional plastic shear strain, $P_r$ is the ratcheting load which is the effective (average) load ($p_{max}/k_{eff}$) minus the plastic shakedown limit ($p_{max}/k$ ratio), N is the number of cycles at the given ratcheting load, and c is a constant which is independent of stress and the slope of a linear regression modeling of the shear strain as a function of the net ratcheting load multiplied by the number of cycles at that load. Tyfour found c to be equal to 0.00237 for a BS11 medium carbon (0.52 wt %) steel with a pearlitic microstructure by taking measurements of strain at a constant distance of

0.05mm below the surface. To calculate the value of c for the non-laser hardened normalized and annealed SAE 8620 sample, the strain data from Figure 4.23 can be replotted as strain versus the number of cycles multiplied by the ratcheting load where the ratcheting load was determined by subtracting the actual $p_{max}/k$ value minus the plastic shakedown limit, which is approximately 1.5 at a coefficient of friction of 0.8. The value of c is the slope of the line and was found to be equal to $5x10^{-5}$. At the 10N load used for the samples from which the two c values were calculated, the $p_{max}/k$ value minus the shakedown limit is 4.77 for the non-laser hardened area resulting in 9643 cycles to failure for a shear strain of 2.3 – assuming cracking is has actually occurred at this shear strain. Based on the observation of the surface condition of the non-laser hardened surface in Figure 4.25, the ratcheting equation (equation 2.1) appears to be fairly accurate as obvious contact fatigue cracks (pitting/spalling) were not apparent by 5000 cycles even though the surface was beginning to show surface distress most likely from asperity break-in. The number of cycles to failure for the non-laser hardened, normalized and annealed SAE 8620 sample at a 30N load is 6052 cycles, which is close to 5000 cycles where significant damage was seen in this alloy in Figures 4.11a,b. For the non-laser hardened, normalized and annealed SAE 4140 significant contact fatigue damage was also seen by 5000 cycles. Based on 4.1 at a load of 30N, this surface should fail due to ratcheting fatigue by 5293 cycles assuming the constant c is applicable to this alloy.

The biggest driver of variation in the experimental result from that predicted by equation 4.1 is the difficulty in accurately measuring shear strain in small deformed layers at the sample surface. Especially when the contact area is small, the ability to get repeatable cross-section data is difficult. Another model that may be useful in addition to or as a substitute for equation 4.1 is that created by Clayton and Su [55-57] from a collection of ratcheting data from various steels and extended by Afferente and Ciavarella [58-59]. The model is derived from considerable data and only requires knowledge of the load factor $p_{max}/k$. Afferante et al. extended Clayton and Su's hypothesis that even though complex plasticity models such as the non-linear kinematic, Armstrong-Frederick, and others have been used to describe contact fatigue, knowledge of the hardness or yield limit values are sufficient to model the general ratcheting behavior in metals. They proposed a Wöhler-Basquin curve that interpolates between static failure and a defined

fatigue limit, as used in gear design. They suggest this more simplified engineering approach due to the inherent multivariable complexities of three dimensional sliding wear of materials. They found that the linear statistical correlation was highest in a log-log plot of $p_{max}/k$ versus the number of cycles to spalling instead of $p_{max}$ alone or $p_{max}/HB$, which was the method of Clayton and Su. Their correlation included various steels with yield strengths of 289 to 673 MPa. Their correlation results in the following regression equation:

$$\left(\frac{p_{max}}{k}\right)^{4.69} N = 1.09 \times 10^{8} \qquad (4.2)$$

The equation is based on rolling-contact fatigue with 10% sliding, therefore, it is likely not directly applicable to the results in this study where 100% sliding occurred: equation 4.2 predicts that the non-laser hardened SAE 8620 would fail by 19000 cycles. The difference is the two models is shown in Figure 4.33.

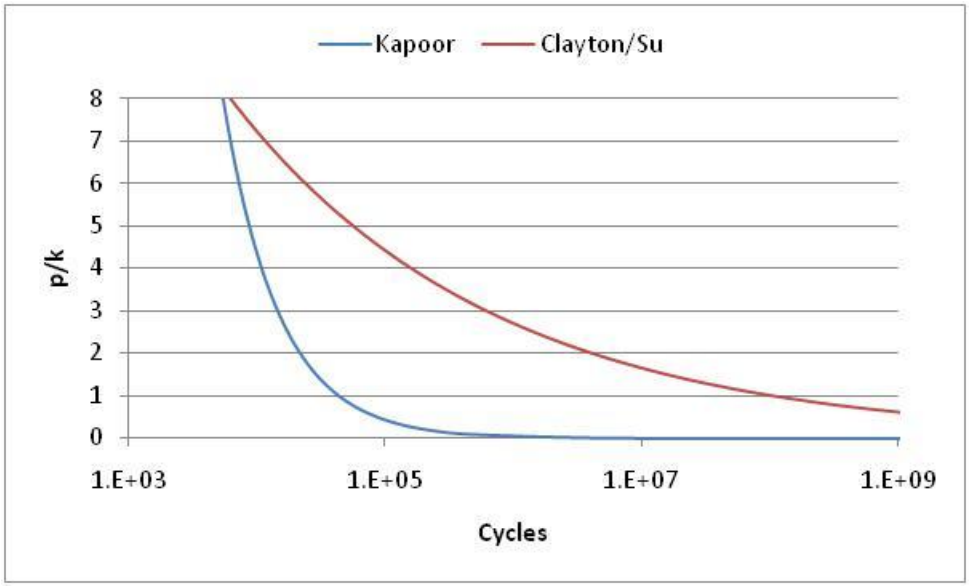


Figure 4.33 Comparison of the Kapoor and Clayton and Su models for contact fatigue. Clayton and Su's model is less conservative because it was derived from data obtained at only 10% of sliding.

The form of equation 4.2 is valuable in that is does not require that the shear strain be measured, but only that the presence of contact fatigue cracking be observed to represent failure. To make equation 4.2 equal to that of Kapoor's for the data from this study, the coefficients would be approximately that shown in equation 4.3.

$$\left(\frac{p_{max}}{k}\right) N = 4400 \qquad (4.3)$$

Obviously, the effect of significant sliding reduces the life of the steels in this study and thus the power law coefficients: 4.69 and $1.09 \times 10^{-8}$ for 10% sliding and 1 and 44000 for 100% sliding. As engineering tools, both equations 4.2 and 4.3, like simple pin-on-disk tribometer tests, are valuable in giving a designer a qualitative idea of the likelihood of failure during the life cycle of the product. In real engineering applications, so many other variables, many of them noise variables, play a role in contact surface degradation of the lifetime of the part. Some of which, such as lubrication condition, rotation speed, break-in, fuel type, vibration, among others can be particularly destructive. Since equation 4.3 requires no empirical strain analysis to solve for N, it should be much more useful. Interestingly in many practical applications, should N be calculated to be large, it is likely that abrasion and/or an adhesive wear mechanism may dominant to the point where the strained surface layer wears faster than it can build up enough cycles to initiate a crack. Under such conditions the classic Archard wear equation, which is widely accepted and easy to use, would likely be better suited for qualitative modeling of the material.

## 4.5 Conclusions

1) The laser processing DOE which included SAE 8620, 4140, and 52100 found a hardness maxima between 0.7-0.8 wt% carbon. This is most likely the result of the attendant decrease in martensitic start and finish temperatures as the carbon content increases, resulting in increased amounts of retained austenite.
2) The carbon content has no significant effect on the laser hardened depth.
3) Both the ratcheting model of Kapoor, and the empirical model of Clayton and Su and extended by Afferente and Ciavarella, provide reasonable semi-quantitative contact fatigue life models for SAE 8620, 4140, and 52100 steels.
4) The percent sliding has a significant effect on reducing the contact fatigue lives of the steel surfaces in this study. This resulted is dramatically reduced coefficients in the power law model of Afferente and Ciavarella.
5) Smaller separation distances between laser tracks decreased the amount of wear although residual stresses are known to be tensile at the track boundaries. This is

likely due to the increased hardness having a stronger positive effect on reducing contact fatigue and abrasion wear than the residual stresses having a negative effect.

## 4.6 References


1. A. Barchukov and L. Mirkin. Materialov. No. 6, pp.126, (1969).
2. V.D. Annenkov, A.P. Barchukov, Yu. Davydov, A.A. Zhukov, A.N. Kokura, M.A. Krishtal, and A.A. Uglov. Ibid. No. 2, pp. 38, (1974).
3. D.E. Fly, J.T. Black, and B. Singleton. Journal of Laser Applications. Vol. 8. pp. 89-93, (1996).
4. F. D. Seaman and D.S. Gnanamuth. Metal Progress. pp. 179, 1975.
5. P. De la Cruz, M. Oden, and T. Ericsson. Int. J. Fatigue. Vol. 20, No. 5. pp. 389-398, 1998.
6. W. Steen. Met. Technology. Vol. 6, No. 12. pp. 456-462, 1979.
7. H. Kawasumi. Source Book on Application of Laser in Metalworking. ASM, Metals Park, OH, 1981. pp. 185-194.
8. E.A. Dubrovskaya, C.V. Kopetskii, V.S. Kraposhin, and I.V. Rodin. Metal Sci. Heat Treat. Vol. 28. No. 9. pp. 658-663.
9. W. Li, K.E. Easterling, and M. Ashby. Acta Metall. Vol 34. No. 8. pp. 1533-1543.
10. J. Benedek, A. Shachrai, L. Levin. Case Hardening of Steel by a CO2 Laser Beam. Optics and -Laser Technology, pp 247-253, (1980).
11. J.H. Ouyang, Y.T. Pei, X.D. Li, T.C. Lei. Effect of Tempering Temperature on Microstructure and Sliding Wear Property of Laser Quenched Cr13 Steel. Wear 177, pp 203-208, (1994)
12. S.J. Na and Y.S. Yang. Influence of Heating Rate on the Laser Surface Hardening of a Medium Carbon Steel. Surface and Coatings Technology, 34, pp 319-330, (1988)
13. A.I. Katsamas, G.N. Haidemenopoulos. Laser-Beam Carburizing of Low-Alloy Steels. Surface and Coatings Technology, 139, pp 183-191, (2001)
14. S.A. Fedosov. Laser beam hardening of carbon and low alloyed steels: Discussion of increased quantity of retained austenite. Journal of Materials Science, 34, pp 4259-4264, (1999)
15. T. Ericcson, S.C. Yao, and M. Melander. 4th Int. Congress on Heat Treatment of Materials. pp 702-733, 1985.

16. M. Cantello, M. Bianco, A. Zambon, B. Badan and E. Ramous, Laser surface hardening of high carbon and chromium steels. SPIE Vol 1810, Gas Flow and Chemical Lasers, (1992).
17. J.R. Bradley and S. Kim. Laser transformation hardening of a high-purity iron-carbon-chromium alloy. Scripta Met, vol23, pp 131-136, (1989)
18. M.F. Ashby and K.E. Easterling. The transformation hardening of steel surfaces by laser beams-I hypo-eutectoid steels. Acta Metall, vol. 32, no. 1, pp 1935-1948, (1984)
19. R.A. Ganeev. Low-power laser hardening of steels. Journal of Materials Processing Technology. 121, pp 414-419, (2002).
20. R.K. Shiue and C. Chen. Microstructural observations of the laser-hardened 1045 steel. Scripta Met, vol. 25, pp. 1889-1894. (1991)
21. P.A. Molian and W.E. Wood. Non-equillibrium phases in laser-processed Fe-0.2wt%C-20wt.%Cr alloys. Materials Science and Engineering, 60, pp. 241-245, (1983).
22. B.A. van Burssel, J. Noordhuis, and J.Th. M. De Hosson. Reduction of the tensile stress state in laser treated materials. Scripta Met, vol. 25, pp. 1719-1724, (1991)
23. P.A. Molian. Structural characterization of laser-processed molybdenum steel. Materials Science and Engineering, 58, pp. 175-180, (1983).
24. A. Hussain, R. Akhtar, S. Shahdin and M. Ashraf Atta, Surface hardening of steel with a low power laser. 11th International School on Quantum Electronics: Laser Physics and Applications, Peter A. Atanasov, Stefka Cartaleva, Editors, Proceedings of SPIE Vol. 4397 (2001)
25. M.H. McCay, N.B. DaHotre, J.A. Hopkins, and T.D. McKay. The influence of metals and carbides during laser surface modification of low alloy steel. Journal of Materials Science. 34, pp. 5789-5802 (1999).
26. H.J. Hegge and J. Th. M. De Hosson. The relationship between hardness and laser treatment of hypo-eutectoid steels. Scripta Met. Vol. 21., pp. 1737-1742, (1987)
27. M. Tayal and K. Mukherjee. Thermal and microstructural analysis for laser surface hardening of steel. J. Appl. Phys, 75 (8), pp. 3855-3862, (1994).

28. D.I. Pantelis, E. Bouyiouri, N. Kouloumbi, P. Vassiliou, and A. Koutsomichalis. Wear and corrosion resistance of laser surface hardened structural steel. Surface and Coatings Technology, 298, pp. 125-134, (2002).
29. X.M. Zang, H.C. Man, and H.D. Li. Wear and friction properties of laser surface hardened En31 steel. Journal of Materials Processing Technology, 69, pp. 162-166, (1997).
30. H. De Beurs, and J. Th. M. De Hosson. Scripta Met. Vol. 21, pp. 627-632, (1987)
31. H.B. Singh, S.M. Copley, and M. Bass. Fatigue Resistance of laser heat-treated 1045 carbon steel. Met Trans A, 12A (1), pp 138-140, (1981).
32. K. Obergfell, V. Schulze, and O. Vohringer. Classification of microstructural changes in laser hardened steel surfaces. Materials Science and Engineering A355, pp 348-356, (2003).
33. L. W. Tsay and Z. W. Lin. Effect of laser beam radiation on fatigue crack propagation in AISI 4150 steel. Fatigue and Fracture of Engineering Materials and Structures. 21, pp. 1549-1558, (1998).
34. P. De la Cruz, M. Oden, and T. Ericsson. Effect of laser hardening on the fatigue strength and fracture of a B-Mn steel. Int. J. Fatigue, Vol. 20, No. 5, pp. 389-398, (1998).
35. J.L. Doong, T.J. Chen and Y.H. Tan. Effect of laser surface hardening on fatigue crack growth rate in AISI-4130 steel. Engineering Fracture Mechanics, Vol. 33, No. 3, pp. 483-491, (1989).
36. M.S. Devgun and P.A. Molian. Experimental study of laser heat-treated bearing steel. Journal of Materials Processing Technology, 23, pp. 41-54, (1990)
37. J. Kusinski and G. Thomas. L. Proc. SPIE, Vol. 668. No. 150, 1986.
38. J. Benedek, A. Shachrai, L. Levin. Case Hardening of Steel by a $CO_2$ Laser Beam. Optics and Laser Technology. (1980)
39. V.K. Semenchenko. Surface Phenomena in Metals and Alloys. Addison-Wesley. Reading, MA. 1962.
40. Y.S. Yang and S. J. Na. A Study of Residual Stresses in Laser Surface Hardening of a Medium Carbon Steel. Surface and Coatings Technology, 38, (1989) pp 311-324.

41. M.R. James, D.S. Gnanamuthu, and R.J. Moores. Mechanical State of Laser Melted Surfaces. Scripta Met, vol. 18, pp. 357-361, (1984)
42. Y.S. Yang and S. J. NA. Residual Stresses in Laser Surface Hardening of Large Areas. Surface and Coatings Technology, 42, pp 165-174, 1990
43. B.A. Van Brussel, H.J. Hegge, and J Th. M. De Hosson. Development of Residual Stress and Surface Cracks in Later Treated Low Carbon Steel. Scripta Met, Vol 25, pp 779-784, 1991
44. H. Zhang, Y. Shi, C. Y. Xu and M. Kutsuna. Surface Engineering 2004 Vol. 20 No. 2, pp. 117-120, 2004
45. M. Yessick, R. Scherer, SME Technical Paper MR76-570, 1975
46. A. Bower and K. Johnson. The influence of strain hardening on cumulative plastic deformation in rolling and sliding contact. J. Mech. P. Solids, 37, 4, pp. 471-493, (1989)
47. A. Ponter, A.D. Hearle, and K. Johnson. Application of the kinematical shakedown theorem to rolling and sliding point contacts. J. Mech. Phys. Solids, 33, 4, pp. 339-362. 1985
48. A.F. Bower. Cyclic Hardening Properties of Hard-Drawn Copper and Rail Steel. J. Mech. Phys. Solids., vol 37, No. 4, pp. 455-470. 1989.
49. A. Kapoor. A Re-Evaluation of the Life to Rupture of Dutile Metals by Cyclic-Plastic Strain. Fatigue and Fracture of Eng. Materials and Structures. Vol. 17, No. 2, pp. 201-219. 1994.
50. A. Kapoor. A Re-Evaluation of the Life to Rupture of Dutile Metals by Cyclic-Plastic Strain. Fatigue and Fracture of Eng. Materials and Structures. Vol. 17, No. 2, pp. 201-219. (1994).
51. J. Ringsberg, M. Loo-Morrey, B. Josefson, A. Kapoor, and J. Beynon. Prediction of fatigue crack initiation for rolling contact fatigue. International Journal of Fatigue, 22, pp. 205-213. 2000
52. A. Kapoor and F.J. Franklin. Tribological Layers and the Wear of Ductile Metals. Wear, 245, pp. 204-215. (2000)
53. W. Tyfour, J. Beynon, A. Kapoor. Wear, 197, pp. 255-265, (1996)
54. J. Archard. Journal of Applied Physics. 24, 8, pp. 981-988, (1953)

55. X. Su, P. Clayton. Ratchetting strain experiments with a pearlitic steel under rolling/sliding contact. Wear, 205 (1-2), pp. 137-143. (1997)
56. X. Su, P. Clayton. Wear, 197, pp. 137-144. (1996)
57. P. Clayton, X. Su, Wear, 200, pp. 63-73. (1996)
58. L. Afferrante, M. Ciavarella, G. Demelio, Wear, 256, pp. 329-334. (2004)
59. M. Ciavarella, F. Monno. Tribology International, 43, pp. 2136-2144, (2010)

# CHAPTER 5

## Conclusions and Recommendations

This dissertation sought to develop a design methodology for improving contact fatigue resistance of commercial steels. The wear behavior of laser hardened surfaces and hydrogenated diamond-like-carbon (DLC) coatings was explored, as well as the very high cycle fatigue behavior of coated materials. Specifically, the following questions were addressed:

1. What is the influence on very high cycle fatigue life and the dominant fatigue mechanisms for a hardened SAE 52100 with the following coatings: layered CrN and hydrogenated diamond-like-carbon or an electroless nickel-phosphorus-polytetrafluoroethylene infused coating? How do the coatings affect the axial stress-life fatigue limit of the steel? Can the mechanisms controlling axial fatigue be related to the mechanisms and controlling variables in elastic contact fatigue?

2. Does coating a SAE 52100 and a chilled cast iron with a layered CrN and hydrogenated diamond-like-carbon increase the contact fatigue life of the materials? If so, by what mechanisms?

3. Is it possible to use ultrasonic wear testing to simulate contact lifetimes on the order of $10^8$ cycles SAE 52100 steel and chilled cast iron coated with a layered CrN and hydrogenated-amorphous hydrogenated diamond-like-carbon? Will the results from the tester allow for the development of a quantitative-empirical model for wear depth calculation that can also predict wear for traditional tribometers?

4. How does laser hardening affect the contact fatigue resistance of SAE 8620, 4140, or 52100 steels with various pre-heat treatments? What differences or similarities exists that help define the mechanisms and the roles of substrate microstructure, composition and hardness?

## 5.1 Conclusions

*What is the influence on very high cycle fatigue life and the dominant fatigue mechanisms for a hardened SAE 52100 with the following coatings: layered CrN and hydrogenated diamond-like-carbon or an electroless nickel-phosphorus-polytetrafluoroethylene infused coating? How do the coatings affect the axial stress-life fatigue limit of the steel? Can the mechanisms controlling axial fatigue be related to the mechanisms and controlling variables in elastic contact fatigue?*

The addition of coatings of diamond like carbon and electroless nickel with polytetrafluoroethylene to hardened and tempered SAE 52100 bearing steel had no effect on the axial fatigue life in the very high cycle fatigue regime. Fatal fatigue cracks initiated at small inclusions and the behavior was dependent on inclusion type. The influence of inclusion type was rationalized on the basis of differences in the crack driving force for very small cracks that could arise from residual stresses. This was corroborated by differences in the apparent stress intensity values at the transition from the FGA to the fisheye feature, and the absence of such differences in apparent stress intensity at the fish-eye/overload interface. Thus, the difference in calculated stress intensity value and that consistent with the transition described above was attributed to the inclusion type. Smaller Ti(C,N) inclusions have higher effective stress intensities than would be described by the Murakami equation, which only accounts for inclusion size.
A correction factor can be added to the Murakami equation to account for inclusion type as well as inclusion size. However, above $2 \times 10^9$ cycles the correction factor approaches zero. On the other hand, Chapetti's and Liu et al modeling methods, both of which allow for inclusion type correction accurately predicted the fatigue strength of the failed coated SAE 52100 samples.

Finally, the use of extreme value statistical methods such as the Gumbel distribution suggested by Murakami are very useful in accounting for extreme sized inclusions and volume of material stressed. The use of this method could be very helpful for design engineers trying to control failure rates to maintain a reliable product in contact mechanical design. By calculating the volume of stressed material experiencing contact

loading, the Murakami method can allow for a direct, statistical link of inclusion type and geometry to contact fatigue life.

> *Does coating a SAE 52100 and a chilled cast iron with a layered CrN and hydrogenated diamond-like-carbon increase the contact fatigue life of the materials? If so, by what mechanisms?*

The amorphous-hydrogenated DLC coating on chilled cast iron and SAE 52100 steel reduced the wear rate relative to that of the uncoated materials. The DLC coating provided higher shakedown limits due to the lower friction inherent to the coating. The DLC coating was also significantly harder (stronger) than the base material, which reduces the $p_{max}/k$ value by increasing the shear yield strength. This results in an elastic response to a contact load that would otherwise result in racheting contact fatigue as described by Ponter et al and Kapoor.

> *Is it possible to use ultrasonic wear testing to simulate contact lifetimes on the order of $10^8$ cycles SAE 52100 steel and chilled cast iron coated with a layered CrN and hydrogenated-amorphous hydrogenated diamond-like-carbon. Will the results from the tester allow for the development of a quantitative-empirical model for wear depth calculation that can also predict wear for traditional tribometers?*

Ultrasonic wear testing of amorphous-hydrogenated DLC coating on chilled cast iron and SAE 52100 steel was proven to be a successful method for determining the number of cycles until coating failure between $10^6$ and $10^8$ cycles.

A wear model that includes sliding thermal effects as well as thermodynamics consistent with the wear mechanism for DLCs was formulated based on empirical results from ultrasonic wear testing to $10^8$ cycles. The model provided a good fit for both ultrasonic and classic tribometer wear behavior for DLC-coated steels.

*How does laser hardening affect the contact fatigue resistance of SAE 8620, 4140, or 52100 steels with various pre-heat treatments? What differences or similarities exists that help define the mechanisms and the roles of substrate microstructure, composition and hardness?*

The wear behavior of SAE 8620, 4140, and 52100 in the heat treated and heat treated plus laser hardened condition was conducted. From the DOE analysis a hardness maxima for the laser treated surface was predicted to be between 0.7-0.8 wt% carbon. This maxima is likely the result of the attendant decrease in martensite start and finish temperatures as the carbon content increases, which leads to increased amounts of retained austenite. The carbon content had no significant affect on the depth of laser hardening.

SAE 8620 and 4140 steels in the non-laser hardened condition exhibited severe contact fatigue dominated wear. The SAE 52100 exhibited severe to very little wear depending on the hardness of the non-laser hardened material. Contact fatigue likely results from ratcheting due to the asymmetric contact loading indicative of sliding contact and the high $p_{max}/k$ ratios in the study for the softer microstructures of the 8620 and 4140 steels. The high $p_{max}/k$ ratios put the softer surfaces above the plastic shakedown limit where ratcheting fatigue is known to occur.

Further wear studies suggested that both the ratcheting model of Kapoor, and the empirical model of Clayton and Su and extended by Afferente and Ciavarella, provide reasonable semi-quantitative contact fatigue life models for SAE 8620, 4140, and 52100 steels. Increases in the percent sliding significantly reduce the contact fatigue lives of the steel surfaces. This resulted is dramatically reduced coefficients in the power law model of Afferente and Ciavarella.

Smaller separation distances between laser tracks decreased the amount of wear, even though residual stresses are known to be tensile at the track boundaries. This is likely due to the positive effects of an increased hardness outweighing the negative effects of tensile residual stresses.

Overall, wear in these alloys is controlled by ratcheting contact fatigue for $p_{max}/k$ ratios above the plastic shakedown limit. Laser hardening primarily increased the hardness as well as homogenizing the microstructure in all three steels tested, resulting in reduced $p_{max}/k$ ratios and thus lower wear rates.

## 5.2 Contact Mechanical Design Criteria

The cracked cam surface shown in Chapter 1 resulted from ratcheting contact fatigue. The results of this dissertation supports the theories of Ponter et al, and Kapoor that ratcheting fatigue is the principal mechanism controlling wear due to contact fatigue at $p_{max}/k$ ratios of approximately 2 at high levels of friction (>0.5) or around 5 at friction coefficients of 0.2 or lower.

Therefore, to design a contact fatigue resistant metal the following design steps should be considered.

1. Considering the $p_{max}/k$ ratio, lower values can be achieved by reducing the contact load, decreasing the elastic moduli of the contacting materials, as well as increasing the contact radius to increase the contact area. The $p_{max}/k$ ratio can also be reduced by using higher shear strength materials such as hardened steels (e.g. bearing or tool steels) or by the use hard thin films.
2. The effects of materials features such as porosity, inclusions, oxide films, etc, need to be considered as they can be the location of crack initiation even in contact loading with small contact areas. In this dissertation it was shown that inclusions and their type can strongly affect the axial fatigue of bearing steels. Since contact stress can be considered a multidimensional stress analog to axial loading, the inclusion size and type effect on contact fatigue life needs to be understood. Using inclusion size and size density in contact mechanical design has been the norm in bearing design for many years and inclusion type is not normally considered. However, using Murakami's method corrected for inclusion type, the effects of inclusion

types on fatigue life in both axial and contact loading can be more realistically considered in design.

3. Ultrasonic wear test instrumentation has been demonstrated as a viable method to evaluate the wear behavior for high cycles of load in much shorter test time compared to conventional test methods. The technicque is therefore useful in reducing testing costs and time as well as providing a quality validation method and can provide accelerated methods to evaluate the behavior of hard thin film (low $p_{max}/k$ values) in reducing wear by contact fatigue.

## 5.3 Recommendations for Future Work

Based on the findings of the present study, the following recommendations are made for future work in this area.

1) Because of the difficulty in accurately measuring strain evolution in sliding contact leading to contact fatigue, especially in high hardness steels, it would be valuable to develop a non-destructive technique for measuring the strain accumulation at the surface of contact as a function of the number of cycles in real-time. This would also allow for accurate measurement of the total strain to failure for use in Kapoor's ratcheting model, low-cycle fatigue models, as well as multi-axial fatigue models.
2) As found by Wang et al, it appears that non-martensitic steels have better wear properties at high contact stresses. Generally, it is assumed that the higher energy consumption of bainitic and pearlitic microstructures play a significant role in this difference. Also, the higher thermal conductivity of non-martensitic microstructures has been cited as a significant factor. However, it is still not clear if lower hardness microstructures are better and if they are, why? A more extensive study of the plasticity/low cycle fatigue properties of different steel microstructures at elevated temperatures under sliding and/or rolling conditions is needed.
3) The work of Clayton and Su was very helpful in creating highly correlated empirical models relating the $p_{max}/k$ load factor to number of cycles to failure. Therefore, there exists a need for more empirical data across different steels and

steel microstructures to understand the applicability of their empirical model. If these empirical studies can be tied to accurate measurements of surface strain to failure, a more complete understanding of how the existing empirical models and multiaxial fatigue and ratcheting models support one another. Also, the role of sliding and its affect on contact fatigue life needs to be studied further. As most of the ratcheting fatigue methods stem from research in rolling contact fatigue, little data exist to understand how the introduction of sliding contact changes the boundary conditions on which ratcheting models are built and used.

4) The wear of DLC coatings at high numbers of wear cycles was successfully measured and modeled in this dissertation. There exists a need for more empirical data on the atomistic/nano-level evolution of wear debris in DLC coatings and how that mechanisms leads to macroscopic wear.
5) The affect of lubricants on hydrogenated-DLC wear in engines and other applications has been studied to some degree, however, there exists a need to understand how different lubricants and fuels affect DLC wear, especially when diesel, JP8, or JET-A fuels are used.